Magnetic coupling between liquid ³He and solid insulators (Review)

V. V. Naletov, M. S. Tagirov, and D. A. Tayurskiĭ*

Kazan State University, ul. Kremlevskaya 18, 42008 Kazan, Russia
(Submitted November 16, 2001; revised January 14, 2002)

Theoretical and experimental results are presented on the magnetic coupling between liquid ³He (in the normal phase) and single crystals and fine powders of insulating Van Vleck paramagnets and their diamagnetic analogs. © *2002 American Institute of Physics.*
[DOI: 10.1063/1.1480236]

INTRODUCTION

Research on the phenomena occurring at interfaces between two physically dissimilar media and, in particular, on transport processes across them is among the fundamental problems of modern physics. One such problem is that of the magnetic coupling between liquid ³He and a solid substrate. The anomalously small thermal resistance (the Kapitsa resistance) at the boundary between liquid ³He and cerium manganese nitrate at $T = 10$ mK, observed more than 30 years ago,[1,2] stimulated active research on the magnetic properties of liquid ³He at interfaces with solids. Of course, in studies of this kind one needs to know both the physical properties of the two components and the state of the interface.

Research on the properties of the quantum Fermi liquid—liquid ³He—is of interest from the standpoint of both basic science and applications. Being a natural Fermi liquid, liquid ³He is a unique experimental object for checking many theoretical ideas of modern physics. For example, the discovery of superfluidity in liquid ³He in 1971[3] has made it possible to check such ideas of modern theoretical physics as the simultaneous existence of several broken symmetries in the system, topological defects of the order-parameter field, etc.[4] On the other hand, superfluid liquid ³He is a system with anisotropic superfluidity and studying its properties may lead to a deeper understanding of the physics of superconductivity, processes in the early universe, and the nature of neutron stars (see Ref. 5, for example).

The unique property of liquid ³He, liquid ⁴He, and their mixtures to remain in the liquid state (at the saturated vapor pressure) all the way down to absolute zero, due to the large zero-point vibrations of the atoms, makes them indispensable working substances in low-temperature physics. Here, of course, knowledge of the heat-transfer processes between these quantum liquids and solid substances plays an important role. In the case of liquid ³He one of the possible channels of heat transfer is magnetic coupling—the transfer of energy between the magnetic degrees of freedom of a solid and the nuclear spin system of liquid ³He.

Various substances were chosen as solid substrates for the magnetic coupling studies (powdered insulators, powdered metals, and glasses). Among the extremely promising substances for studying the magnetic channel of energy transfer from liquid ³He to a solid and vice versa are insulating Van Vleck paramagnets. Magnetic coupling effects in such systems were first observed in the Laboratory of Magnetic Radio Spectroscopy of Kazan State University.[6,7]

A special class of solid-state magnets—Van Vleck paramagnets—has been studied for quite a long time. The strong hyperfine interaction makes these substances extremely interesting from the standpoint of studying electronic–nuclear magnetism. The magnetic field induced at the nucleus of the rare-earth Van Vleck ion is by many times higher than the external applied magnetic field, so that the nuclear magnetic resonance (NMR) frequencies in such systems occupy an intermediate position between the ordinary NMR frequencies and the electron paramagnetic resonance (EPR) frequencies, and one can therefore speak in terms of a so-called "enhanced" NMR. Intermetallic Van Vleck paramagnets ordinarily have cubic symmetry, while the symmetry of the majority of insulating Van Vleck paramagnets is lower than cubic, so that they are characterized by anisotropy of the effective gyromagnetic ratio of the nuclei of the Van Vleck ions.[8] An extremely strong dependence of the NMR frequencies on the direction of the applied magnetic field makes it possible to achieve coincidence of the resonance frequencies of the nuclear spins of the Van Vleck ions and of the liquid ³He, i.e., to observe a resonant magnetic coupling. Here we note that such resonant coupling has been observed experimentally for only one of the insulating Van Vleck paramagnets—thulium ethyl sulfate,[6] and then everything depended on the state of the crystalline surface (this crystal does not tolerate prolonged vacuumization) and, as a consequence, the results were not completely reproducible. In experiments with an analogous insulating Van Vleck paramagnet, the thulium double fluoride LiTmF₄, the crystalline surface of which is more stable against external agents, the resonant magnetic coupling effect was not observed.[7] However, there is no doubt as to the existence of such an effect, since Richardson and co-workers[9] observed an analogous effect five years later: the resonant magnetic coupling of the nuclear spins of nitrogen ¹⁴N and liquid ³He. In those experiments the resonance conditions were achieved through the presence of a zero splitting and the small gyromagnetic ratio of the nuclear spins of nitrogen ($I=1$) in comparison with those of ³He ($I=1/2$), which do not have a zero splitting. Thus there is an unarguable need for a comprehensive, in-depth study of the surface of the solid substrate and the external influences leading to a change of its state.

It is of particular interest to study the properties of insulating Van Vleck paramagnets at high magnetic fields and at

ultralow temperatures (see review[10]) and to investigate the magnetic coupling between them and liquid ^{3}He under these conditions. Such studies are of interest from an applied as well as a fundamental standpoint. For example, only under such conditions can one obtain a highly polarized (spin) state of liquid ^{3}He. Spin-polarized Fermi systems are a special state of matter and possess new and extremely nontrivial properties that may shed light on many fundamental problems of modern physics.[11–25] On the other hand, the promising applications of hyperpolarized gaseous ^{3}He in medicine[26–32] moves the question of the mechanisms for polarization of a Fermi system from the purely scientific sphere to that of applied problems.

Two main methods are now used to obtain highly polarized liquid ^{3}He:

1) optical pumping[33,34] of gaseous ^{3}He followed by rapid liquefaction;[34]

2) polarization of solid ^{3}He by the "brute force" method at ultralow temperatures and high magnetic fields, followed by rapid melting.[35–37]

Another possible method of polarizing liquid ^{3}He might be the transfer of a highly polarized state of the magnetic moments of a solid to the nuclear spins of liquid ^{3}He by means of magnetic coupling. Thus it is unquestionably of interest to study the possibility of using the dynamic polarization of the nuclei of a solid substrate to obtain a high polarization of the nuclear spins of liquid ^{3}He.

Finally, knowledge of the physical state of the liquid ^{3}He–solid interface plays an important role in the problem of magnetic coupling. At sufficiently low temperatures a film of solid ^{3}He several atomic layers thick exists at the interface with the solid on account of the rather high adsorption potential, and the magnetism of this film plays a key role in processes of magnetization transfer from the liquid ^{3}He to the solid. Furthermore, the solid surface itself has physical properties different from those of the bulk. Studying these properties could no doubt improve our understanding of the nature of the magnetic coupling between liquid ^{3}He and a solid substrate.

All of what we have said above pointed to the need for a comprehensive study of magnetic coupling processes between liquid ^{3}He and a solid substrate, including studies of the media themselves and the phenomena occurring directly at their interface. In this review we set forth the main results of our experimental and theoretical studies of the properties of liquid ^{3}He in contact with an insulating Van Vleck paramagnet—the thulium double fluoride LiTmF$_4$—and its diamagnetic analog LiYF$_4$. In Sec. 1 of this review we briefly summarize the data obtained in studies of the magnetic coupling of liquid ^{3}He with various solid substrates. Section 2 is devoted to presenting the main experimental and theoretical data obtained in the study of the magnetic coupling of liquid ^{3}He in contact with crystals and fine powders of LiTmF$_4$ and LiYF$_4$. We conclude this review with a summary of the main results.

1. MAGNETIC COUPLING BETWEEN LIQUID ^{3}He AND A SOLID SUBSTRATE

The question of magnetic coupling between liquid ^{3}He and a solid substrate first arose in 1965 after a series of

experiments by Abel and co-workers[1] on measurement of the heat capacity of liquid ^{3}He at low temperatures revealed anomalies in the temperature dependence of the heat capacity of liquid ^{3}He. We note that in actuality this question has a longer history: it was established back in the papers by Romer[38,39] that the walls of the container had an effect on the relaxation of the spins of liquid ^{3}He. From an analysis of the manner in which thermal equilibrium is established between liquid ^{3}He and the cerium–magnesium nitrate Mg$_3$La$_2$(NO$_3$)$_{12}$·24H$_2$O:Ce^{3+} (CMN), which was used in the experiments of Abel[1] for cooling and measuring the temperature of liquid ^{3}He, an experimental value of the thermal resistance at the liquid ^{3}He–CMN boundary was calculated for temperatures of 2–15 mK.[2] The value obtained was anomalously small and was not described in the framework of the Kapitza theory of thermal (phonon) resistance. Kapitza's theory of acoustic resistance between liquid ^{3}He and a solid was refined by Bekarevich and Khalatnikov[40] and by Gavoret.[41] Its essence is that in view of the substantial difference of the phonon velocities in the solid and in liquid ^{3}He, only a tiny fraction of them (10^{-5}) penetrate from the liquid into the solid substrate. Here it is assumed that for $T < 0.1$ K the energy of the phonons of the solid is transferred to collective zero-sound modes in liquid ^{3}He. For the Kapitsa resistance, given by

$$R_K = \left(\frac{\partial \dot{Q}}{\partial T} \right)^{-1}, \tag{1.1}$$

where $\dot{Q}$ denotes the heat flux through a unit area of the liquid ^{3}He–solid boundary, the theory of Ref. 42, with the contribution of transverse zero sound taken into account, gives a temperature dependence of the form $R_K \sim T^{-3}$:

$$R_K = \frac{15\hbar^3 \rho_s v_T^3}{2\pi^2 \rho_l k_B^4 T^3 (a_1 c_{L0} + a_2 c_{T0}) F}. \tag{1.2}$$

Here ρ_s and ρ_l denote the densities of the solid and liquid ^{3}He, respectively, v_T is the velocity of transverse phonons in the solid, c_{L0} and c_{T0} are the velocities of longitudinal and transverse zero sound in normal liquid ^{3}He, and F is a function of the densities and velocities of photons of the solid and of liquid ^{3}He. The parameters a_1 and a_2 have values of the order of unity and are expressed in terms of the parameters F_0 and F_1 of the Landau theory of the Fermi liquid.

In 1968 Wheatley[43] first proposed a qualitatively new approach for describing the anomalously small thermal resistance at the boundary between ^{3}He and a solid.[1,2] In that paper it was assumed that, in addition to the phonon mechanism of energy transfer across the liquid ^{3}He–CMN boundary there exists a spin mechanism, and energy can be transferred directly from the spin system of CMN (Ce^{3+}: $g_\parallel = 0.25$, $g_\perp = 1.84$)[44] to the spin system of liquid ^{3}He. At temperatures below 20 mK the spin mechanism becomes dominant over the phonon mechanism. Those papers laid the groundwork for a new direction of basic research on surface effects in ^{3}He–solid systems. There have been a great many papers devoted to the study of magnetic coupling effects between the nuclear spins of liquid ^{3}He and the magnetic moments in the solid substrate, where various substances, differing in chemical composition and in the physical state

(polymers, powders, glasses, single crystals, etc.), have chosen for the latter. However, in spite of the intensive research over the course of thirty years, a complete understanding of the mechanism for magnetic coupling has not been achieved. The data of different experiments are often in disagreement with one another, and in some cases magnetic coupling at the liquid ^{3}He–solid interface is not observed at all. On the whole, the research on the magnetic coupling between liquid ^{3}He and solids can be roughly classified into two groups:

1) studies of the magnetic coupling between the nuclear spins of liquid ^{3}He and the electronic magnetic moments of the solid;[45–55]

2) studies of the magnetic coupling between the nuclear spins of liquid ^{3}He and the nuclear magnetic moments of the solid.[56–72]

In respect to the value of the effective gyromagnetic ratio, Van Vleck paramagnetism occupies an "intermediate" position between ordinary electronic and nuclear magnetism (see Ref. 10, for example), and therefore a third group can be added to the above classification: studies of the magnetic coupling of the nuclear spins of liquid ^{3}He and the polarizational magnetic moments of solid-state Van Vleck paramagnets.[6,7,73,74]

While this problem and all the proposed approaches to studying it cannot be explored completely in this review article, let us briefly discuss the present state of the problem. First of all, we note that observations of a direct "resonant" coupling between nuclear spins of liquid ^{3}He and the magnetic moments of a solid are quite rare, and a large role in the process of magnetization exchange between liquid ^{3}He and a solid substrate is played by a film of solid ^{3}He adsorbed on the substrate surface (this question and the properties of the film are discussed in detail in Refs. 75 and 76).

The "bulk" (three-dimensional) and "surface" (two-dimensional) forms of solid ^{3}He are splendid model objects for studying spin-ordering processes. For this reason there has been very wide range of experimental studies of the properties of surface ^{3}He (various materials have been used for substrates: Mylar, graphite, Grafoil, silver powder, Vycor porous glass, etc.).

The "bulk" form of ^{3}He has a tendency toward antiferromagnetic ordering, with a temperature of the transition to the antiferromagnetic state of the order of 1.1 mK.

The characteristics of adsorbed ^{3}He vary, depending on the number of atoms found on the surface of the substrate. It has been shown by neutron diffraction methods and from measurements of the heat capacity that the first adsorbed monolayer appears as a solid-state film. This is because the ^{3}He surface atoms are acted on by van der Waals forces exerted by the substrate. These forces have a rather short-range potential that decays rapidly with distance from the substrate. The typical values[49,77,78] of the adsorption potential are as follows: the ground state of the ^{3}He atom adsorbed on graphite is characterized by a localization energy of 136 K, and the first excited state, by 64 K. The difference between them represents the delocalization energy: 72 K. The energy of delocalization from the second atomic layer of adsorbed ^{3}He is considerably less—of the order of 10 K. These values show how strongly the adsorbed ^{3}He is held by the substrate. The motion of the ^{3}He atoms in the adsorbed film at liquid

helium temperature occurs by the quantum tunneling of ^{3}He atoms.

The magnetic properties of the adsorbed ^{3}He and the change of those properties with increasing number of atoms in the adlayer have been well studied.[79–81] The magnetization of ^{3}He obeys the Curie–Weiss law:

$$M = \frac{CH_0}{T - \Delta},\qquad(1.3)$$

where Δ is the Weiss constant and C is the Curie constant. At small numbers of molecules on the surface of the substrate it has a tendency toward antiferromagnetic ordering ($\Delta < 0$). With increasing number of ^{3}He molecules in the layer the magnetic properties change to ferromagnetic. The constant J of the exchange interaction that leads to the ferromagnetic ordering can be estimated from the relation $J \approx 3\Delta$. Since Δ for a ^{3}He monolayer is of the order of 3 mK, the exchange interaction constant is around 10 mK. When the thickness of the adlayer is increased further, the properties of the first monolayer are affected strongly, since the density of this monolayer increases under the influence of the higher-lying ^{3}He layers. As a result, when more than 3 layers are stacked, all of the adsorbed ^{3}He can be characterized as ferromagnetic, with a Weiss temperature $\Delta = 0.5$ mK. Its properties do not change as the layer thickness is increased further.

In Ref. 61 a direct interaction mechanism was proposed for ^{3}He–^{19}F (DLX-6000). The authors showed that magnetization transfer between the two Zeeman reservoirs occurs via the modulation of the ^{3}He–^{19}F dipole–dipole interaction by quantum tunneling (quantum motion) of ^{3}He atoms in the adlayer. All other types of motion in a potential with such a value are forbidden at liquid helium temperatures. Therefore, it becomes necessary to consider the influence of the magnetism of the adsorbed ^{3}He on the properties of the liquid ^{3}He in the case when the contribution of the surface atoms is substantial (porous glass, graphite, fine powders).

Numerous experiments measuring the magnetization of ^{3}He in porous systems (where the ^{3}He atoms are found in a restricted geometry in the space of the pores) have shown that the value of the magnetic susceptibility of such systems can be characterized by the expression[59]

$$\chi = \frac{(1-f)}{T_F^{**}} + \frac{fC}{T - \Delta}.\qquad(1.4)$$

The first term describes the temperature-dependent contribution of the Pauli susceptibility of a degenerate ^{3}He Fermi liquid (at temperatures $T < T_F^{**}$, where $T_F^{**} \sim 0.5$ K is the Fermi temperature), and the second term is the contribution to the susceptibility of the adlayer of ferromagnetic ^{3}He; f is the surface-atom fraction. For different porous substrates the Weiss temperature varies in the range 0.2–0.8 mK. In the case when a small amount of ^{4}He is added to the ^{3}He the solid-state layer disappears. This is because the adsorption coefficient of ^{4}He is considerably larger than that of ^{3}He.[49]

To explain the experimental results on the magnetic relaxation of liquid ^{3}He in the DLX-6000 sample, Hammel and Richardson proposed a model for the relaxation of liquid ^{3}He via the solid-state film of adsorbed ^{3}He.[82] The model is based on three hypotheses: **a**) all of the liquid ^{3}He relaxes via the surface film of adsorbed ^{3}He (this is completely obvious,

since the relaxation time of "bulk" liquid ^{3}He is around 1000 s; Refs. 38 and 39); **b**) the solid surface ^{3}He and bulk liquid ^{3}He exchange magnetization over a time much shorter than the relaxation time of adsorbed ^{3}He (liquid ^{3}He has a high coefficient of spin diffusion, $D = 10^{-4}$ cm^2/s); c) the relaxation time of ^{3}He in the adlayer is independent of temperature (the temperature independence is due to the fact that only quantum exchange is allowed in the adsorbed ^{3}He). Since the magnetic susceptibility of the system is described by expression (1.4), the authors have obtained a linear temperature dependence for the magnetic relaxation time of liquid ^{3}He at temperatures below the Fermi temperature. Such a relaxation mechanism might possibly be manifested at very low temperatures and in systems for which the ratio of surface atoms to atoms belonging to the "bulk" liquid is not so small.

At liquid helium temperatures the magnetization of the adlayer (and, hence, its magnetic heat capacity) is negligible in comparison with the magnetization of the "bulk" liquid ^{3}He. We note here that studies of the properties of the ^{3}He adlayer are ordinarily studied on a substrate with a quite uniform surface. If the real shape of the surface of fine powders is taken into account (see, e.g., Ref. 83), one can expect a substantial change in the properties of the ^{3}He adlayer. In particular, it can be assumed that extremely strong nonuniformities of the surface will lead to a weakening of the correlation between the magnetic moments of the adsorbed ^{3}He atoms, and this will be manifested in a decrease of the magnetization and magnetic heat capacity.

All of the evidence adduced above indicates that the model of Ref. 82 is incapable of explaining the relaxation of the entire bulk of liquid ^{3}He via the adlayer at helium temperatures, where the thickness of this layer is extremely small. In this situation an energy reservoir with substantially greater heat capacity is needed for relaxation of the liquid ^{3}He. Such a reservoir might, for example, be a system of paramagnetic defect centers arising on the solid surface. This again shows the need for a detailed study of the surface of the solid substrate and its role in the relaxation processes of liquid ^{3}He.

However, in the presence of extremely strong inhomogeneities on the solid surface an additional channel for the relaxation of the magnetization of liquid ^{3}He appears, due to the substantial change of the character of the motion of the atoms of liquid ^{3}He in pores on the surface of the solid and in the space between particles of fine disperse powders.

Summing up all we have said above, we note that in studying the phenomena occurring at an interface between liquid ^{3}He and a solid, the solid substrate is ordinarily taken in the form of powders, porous amorphous materials, or porous polymers, i.e., samples with a well-developed surface. Obviously, the use of such disordered systems as powdered solids in experiments makes it harder to interpret the experimental data and may wash out some manifestations of the magnetic coupling of the nuclear spins of liquid ^{3}He with the magnetic moments of the solid. Therefore, for interpreting the experimental data on the magnetic relaxation of liquid ^{3}He in contact with a solid, the following three factors must be taken into consideration:

1) the existence of magnetic moments (electronic or nuclear) in the solid which is in contact with the liquid ^{3}He;

2) the influence of the solid-state adlayers of ^{3}He;

3) the bounded motion of the ^{3}He atoms, limited by the size of the pores on the solid surface and the size of the interparticle space.[84]

2. MAGNETIC COUPLING BETWEEN LIQUID ^{3}He AND THE INSULATING VAN VLECK PARAMAGNET LiTmF$_4$ AND ITS DIAMAGNETIC ANALOG LiIYF$_4$

Of all the members of the class of insulating Van Vleck paramagnets, the thulium ethyl sulfate (TmES) and thulium double fluoride (LiTmF$_4$) crystals are the most-studied at the present time. Both have a comparatively high (axial) symmetry and are characterized by strong anisotropy of the γ tensor of the ^{169}Tm nuclei, which have spin-1/2, making it unnecessary to take into account quadrupolar effects in the magnetic relaxation. Together, these properties make the two materials extremely attractive from the standpoint of comparison of the experimental results with the theoretical predictions and calculations for the spin kinetics of liquid ^{3}He in contact with a crystalline surface. As we have said, the TmES single crystal was used in the first experiments,[6] which revealed the existence of resonant magnetic coupling of the ^{169}Tm nuclei with the nuclei of a thin film (0.1 mm) of liquid ^{3}He coating the whole surface of a cylindrical sample of TmES ($h = 3$ mm, $d = 3$ mm). For better reproducibility of the results, in all of the subsequent experiments the chemically stable compound LiTmF$_4$ was used. Moreover, it was initially hoped that changing from single-crystal samples of thulium double fluoride to magnetically oriented LiTmF$_4$ powders, whose magnetic properties are analogous to those of the LiTmF$_4$ single crystal but which have the very important advantage of possessing a well-developed crystalline surface.[7] In a certain sense those hopes have been realized: anisotropy of the relaxation of the longitudinal magnetization of the ^{3}He nuclei has been observed for liquid ^{3}He found in the pores of magnetically oriented LiTmF$_4$ powders with particle sizes <57 μm, <20 μm, $2-4$ μm, and <1 μm. However, those experiments did not provide direct proof of the influence of cross-relaxation.

Analysis of the experimental results obtained for TmES single crystals and magnetically oriented LiTmF$_4$ powders led to the conclusion that there is a need for studies in an extremely simple geometry of the liquid ^{3}He volume and with a controlled surface quality. With this goal, in Ref. 84 we studied the magnetic relaxation of liquid ^{3}He in contact with crystals of the Van Vleck paramagnet LiTmF$_4$ containing nuclear magnetic moments of ^{169}Tm, with a gyromagnetic ratio close to that of ^{3}He, and its diamagnetic analog LiYF$_4$. Because of the small boundary surface between the crystal and the liquid ^{3}He, the influence of the solid-state ^{3}He adlayers can be eliminated from consideration, and the use of a single crystal with a special surface treatment[85] made it possible to reduce the influence of heterogeneities to a minimum.

We also note that the majority of studies on the magnetic relaxation of ^{3}He at a contact with a solid have been done at very low temperatures (<0.1 K). At such temperatures liquid ^{3}He is a degenerate Fermi liquid, and its kinetic properties can be described in the framework of the Landau theory
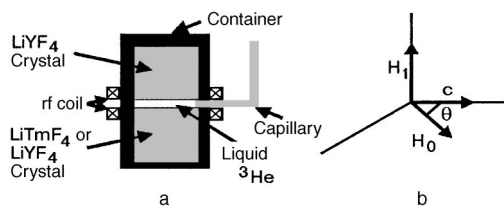
FIG. 1. Experimental cell (a) and the geometry of the magnetic fields (b).[84]

of the Fermi liquid in the language of elementary excitations. For example, the elementary process of relaxation of the longitudinal magnetization consists in the decay of a spin wave with zero wave vector into two spin waves with oppositely directed nonzero wave vectors.

At temperatures between 1.5 and 3 K, at which the measurements were made in our experiments, liquid ^{3}He is a nondegenerate quantum liquid for which Landau theory is unsuitable, and it has a number of interesting properties due to the large energy of zero-point vibrations.[86–89] At these temperatures it is apparently necessary to take into account the influence of the real motion of the atoms on the magnetic relaxation.[84]

2.1. NMR of liquid ^{3}He in contact with diamagnetic LiYF$_4$ crystals

Figure 1 shows a diagram of the experimental cell used in our experiments[84] for measuring the pulsed NMR of liquid ^{3}He. Two single crystals (LiTmF$_4$–LiYF$_4$ and LiYF$_4$–LiYF$_4$) of cylindrical shape (6.0 mm in diameter and 6.0 mm in height) were tightly inserted in a cylindrical container of Stycast 1266A epoxy resin, with the c axis of the crystal directed perpendicular to the axis of the cylinder. ^{3}He from a stainless-steel capillary was condensed in the 100 μm plane-parallel gap between the carefully polished surfaces of the single crystals. In the experiments with pure ^{3}He the impurity of the more-common isotope ^{4}He did not exceed 0.04%. The static magnetic field $\mathbf{H}_0$ was oriented in the plane of the gap in one case parallel to the c axis and in the other case perpendicular to it. According to the EPR data, the LiTmF$_4$ crystal contained paramagnetic impurities of Nd^{3+} (0.023% in relation to the Tm^{3+} ions) and Gd^{3+} (0.007%). In the LiYF$_4$ crystal the impurity concentrations were 3–4 times lower.

For liquid ^{3}He in contact with the diamagnetic LiYF$_4$ crystals the longitudinal T_1 and transverse T_2 relaxation times of the nuclear spins are observed to be quite short:

$$T_1 = 7 \text{ s}, \quad T_2 = 5.8 \text{ ms} \quad \text{at} \quad T = 1.5 \text{ K}. \tag{2.1}$$

It is noteworthy that for the isotropic bulk liquid ^{3}He in the macroscopic gap between crystals the longitudinal and transverse relaxation times differ by three orders of magnitude.

Let us first analyze the transverse relaxation. Such a short decay time of the transverse magnetization of the ^{3}He nuclei cannot be caused solely by magnetic field gradients in the gap between crystals. Since the diamagnetic crystals LiYF$_4$ do not contain intrinsic electronic magnetic moments capable of creating a macroscopic field near the boundary of the crystal, and the paramagnetic impurity content in our samples is small, only two possible sources of these gradi-

ents remain: **a**) nonuniformity of the field of the electromagnet; **b**) magnetic fields of F centers localized at the surface of the crystal.[90,91] For comparison of the transverse relaxation times of the ^{3}He nuclei found in the gap between the LiYF$_4$–LiYF$_4$ and LiYF$_4$–LiTmF$_4$ crystals, measurements of T_2 were made at identical values of the nonuniformity of the external magnetic field. This made it possible to isolate the various contributions to T_2.

The measured value of the longitudinal relaxation rate is unexpectedly large for the given experimental conditions. In order of magnitude this relaxation rate is only an order of magnitude smaller than the relaxation rate of liquid ^{3}He observed in experiments in which liquid ^{3}He is found in contact with solid particles of submicron dimensions,[7] and two orders of magnitude larger than the longitudinal relaxation rate of the nuclei of bulk liquid ^{3}He,[38,39] where the magnetization of ^{3}He relaxes through a modulation of the dipole–dipole interactions by the diffusive motion. In our case the magnetization of the nuclei of liquid ^{3}He can be transferred either to a Zeeman reservoir of paramagnetic impurities or into a reservoir of exchange motions of the ^{3}He atoms in the solid film adsorbed on the surface of the crystal.[82] As to the latter factor, the surface of our crystals is immeasurably smaller than the surface area of all of the solid particles bordering the liquid ^{3}He in the experiments with powders, but the observed relaxation rates are not so strongly different; we may therefore neglect the influence of the solid ^{3}He layers.

Let us estimate the possible influence of paramagnetic impurity ions contained in the crystals on the longitudinal relaxation of liquid ^{3}He. For thermal contact to be present between the paramagnetic impurity ions and the ^{3}He nuclei (flips of the nuclear spins of ^{3}He due to fluctuations of the magnetization of the impurity atoms), it is necessary that the heat capacities C_{He} and C_{imp} of the ^{3}He and of the impurity ions obey a definite relationship:

$$C_{\text{He}} T_1^{-1} = C_{\text{imp}} T_{1,\text{imp}}^{-1}. \tag{2.2}$$

Calculations show that at the given impurity concentrations and for any reasonable value of the spin–lattice relaxation rate $T_{1,\text{imp}}^{-1}$, relation (2.2) cannot be satisfied even in order of magnitude. A similar conclusion can be reached for paramagnetic F centers located on the surface of the crystal—their concentration is much lower than the concentration of these centers on the crystalline surface of the particles of the fine powder.[91]

Thus these two mechanisms do not explain the observed value of the longitudinal relaxation rate. Since the measured value is quite close to the value of the longitudinal relaxation rate of the nuclei of liquid ^{3}He in contact with powdered solids,[7] it is reasonable to look for an explanation of our experiments in those processes which occur near the surface of the LiYF$_4$ crystals. A single crystal and a powder of single-crystal particles have in common that even after treatment the single crystal still has surface inhomogeneities not more than 100 Å in size, and such inhomogeneities are, of course, also present on the surface of the single-crystal particles, only in the latter case, since the total surface of the particles is larger than the surface of the single crystal, there are more of these inhomogeneities (see the results of atomic-force microscopy and NMR cryoporimetry in Ref. 91). It is
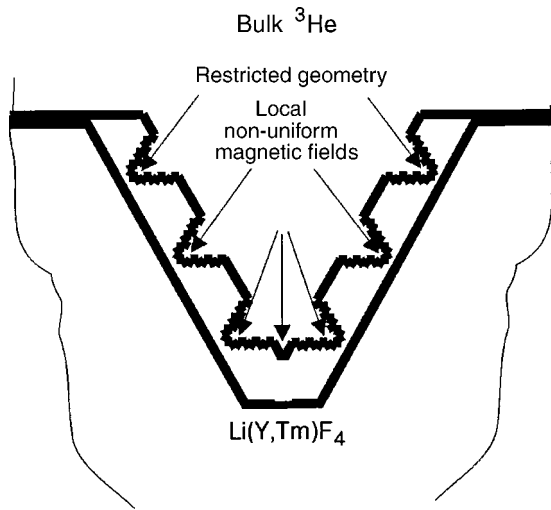
Bulk ^{3}He

FIG. 2. Possible form of the structure of a microcrack on the surface of a crystal (the profile of the surface is in the form of a Koch curve).

reasonable to suppose that these microcracks have a fractal character, as in the case of cracks on the surfaces of metals.[92] A possible form of these heterogeneities is illustrated in Fig. 2; let us call them "fractal pits." Then the following mechanism of longitudinal relaxation is entirely realistic: the magnetization of the nuclei of the bulk liquid ^{3}He, owing to diffusion processes, is rapidly (in a time of the order of T_2) transferred to the ^{3}He nuclei located in the microcracks, where, as was shown in Ref. 84 (see below), the influence of the restricted geometry alters the spectrum composition of the diffusive motion and relaxation occurs through a modulation of the dipole–dipole interactions by the motion of the ^{3}He atoms. This same mechanism of longitudinal relaxation occurs in powdered LiYF$_4$ (sample V in Ref. 7).

2.2. Relaxation of the nuclei of liquid ^{3}He in contact with LiYF$_4$–LiTmF$_4$ crystals

Replacing one of the diamagnetic LiYF$_4$ crystals by a crystal of the Van Vleck paramagnet LiTmF$_4$ leads to a substantial increase in the rates of both transverse and longitudinal relaxation of the nuclear magnetization of the liquid ^{3}He. Moreover, the relaxation parameters of liquid ^{3}He begin to exhibit anisotropy, which reflects the magnetic properties of the substrate. The results obtained for the temperature,
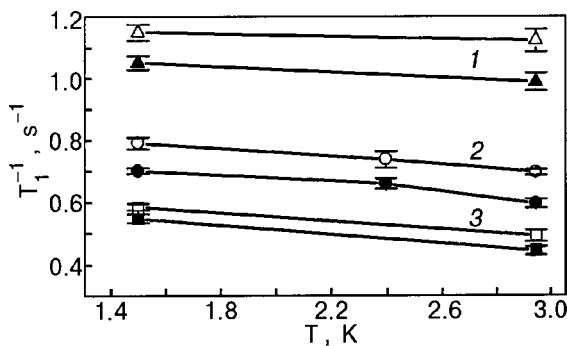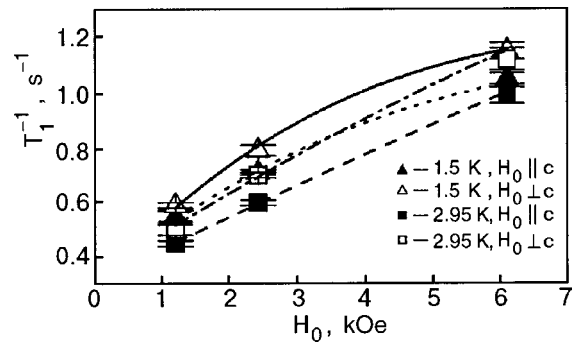

FIG. 4. Longitudinal relaxation rate of the nuclei of liquid ^{3}He versus the value of the magnetic field H_0 in the gap between LiYF$_4$ and LiTmF$_4$ crystals at different temperatures and magnetic field orientations.[84]

field, and concentration dependences of the longitudinal relaxation rates of the nuclei of liquid ^{3}He in the gap between LiYF$_4$–LiTmF$_4$ crystals are presented in Figs. 3–5.

In all of the experiments done under the same conditions as for the LiYF$_4$–LiYF$_4$ system (the width of the spin echo at half maximum is 30 μs at a field of 2.4 kOe), the evolution of the transverse magnetization could be described by the expression

$$\frac{M(2\tau_1)}{M(0)} = \exp\left[-\left(\frac{2\tau_1}{T_2}\right)^n\right], \tag{2.3}$$

where $M(2\tau_1)$ is the amplitude of the spin echo in the case of a delay τ_1 between the $\pi/2$ and π probe pulses. As we see from Table I, measurements reveal the presence of an additional source of magnetic field gradients, but this source does not affect the integral width of the spin echo. Our calculations show that the Van Vleck magnetization of the LiTmF$_4$ crystal cannot produce the required magnetic field in the gap between LiYF$_4$–LiTmF$_4$ crystals. The maximum calculated value of the nonuniformity of the magnetic field at a distance of 5 μm is 0.5 Oe at 1 cm. It is reasonable to assume that the sources of these local magnetic field gradients are the paramagnetic defect ions Tm^{3+} located on the walls of the microcracks.[90,91] The different values of the transverse relaxation rate of the nuclei of liquid ^{3}He for perpendicular and parallel orientations of $\mathbf{H}_0$ are evidence of anisotropy of the magnetic susceptibility of the paramagnetic defect centers Tm^{3+}. Let us consider how the proposed mechanism might
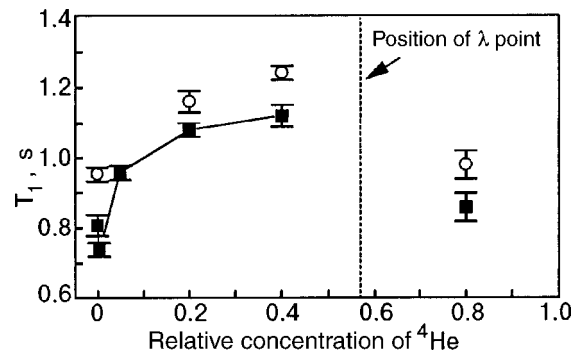

FIG. 3. Temperature dependence of the longitudinal relaxation rate of the nuclei of liquid ^{3}He in the gap between crystals LiYF$_4$–LiTmF$_4$ for H_0 =6.1 (*1*), 2.4 (*2*), and 1.19 kOe (*3*). The unfilled symbols correspond to $\mathbf{H}_0 \perp c$, the filled symbols to $\mathbf{H}_0 \| c$.[84]

FIG. 5. Dependence of the longitudinal relaxation rate of the nuclei of liquid ^{3}He on the concentration of ^{4}He in the gap between crystals LiYF$_4$–LiTmF$_4$; temperature $T=1.5$ K, NMR frequency 19.8 MHz; $\mathbf{H}_0 \| c$ (○), $\mathbf{H}_0 \perp c$ (■).[84]

TABLE I. Parameters of the transverse relaxation of the nuclear spins of liquid ^{3}He.

Samples	Parameter	$T = 1.5$ K		$T = 2.95$ K	
		$\mathbf{H}_0 \parallel c$	$\mathbf{H}_0 \perp c$	$\mathbf{H}_0 \parallel c$	$\mathbf{H}_0 \perp c$
LiYF$_4$–LiTmF$_4$	T_2, ms	5.47(6)	1.74(3)	4.5(1)	1.40(3)
	n	2.4(1)	2.2(1)	2.3(1)	2.1(4)
LiYF$_4$–LiYF$_4$	T_2, ms	5.8(3)		–	
	n	1			

explain the temperature and field dependences of the longitudinal relaxation rates of the liquid ^{3}He nuclei. We note that the observed temperature and field dependences cannot be described in the framework of the conventional approaches: relaxation into a reservoir of spin–spin interactions of paramagnetic impurities, direct transfer of magnetization from the nuclei of liquid ^{3}He to the resonant nuclei of the substrate, relaxation into a reservoir of exchange motions of ^{3}He atoms in the solid adlayer. The latter mechanism is not effective because of the small size of the contact surface between the ^{3}He and the crystal. The only nuclei to which the ^{3}He spins can transfer their magnetization directly in our experiments are the ^{169}Tm nuclei, the spin–lattice relaxation rate of which falls off with decreasing temperature (see Fig. 6). Furthermore, the magnetic heat capacity of the nuclei of the surface Van Vleck ions Tm^{3+} is insufficient to bring about thermal contact. As to the relaxation via paramagnetic impurities, not only is the surface concentration of these impurities low, but this mechanism also gives the opposite temperature and field dependences.[93] The most probable relaxation mechanism is the following. As in the experiments with the diamagnetic crystals LiYF$_4$–LiYF$_4$, the magnetization of the nuclei of the bulk liquid ^{3}He rapidly diffuses to the ^{3}He nuclei located in direct proximity to the surface of the LiTmF$_4$ crystal. Relaxation of the longitudinal magnetization is brought about by the motion of the ^{3}He atoms in microcracks on the surface, as in the case of diamagnetic crystals. However, this motion in a restricted geometry (in the "fractal pits") occurs under conditions of a large local magnetic-field
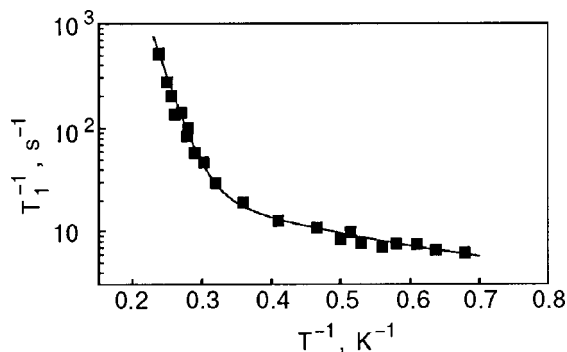
nonuniformity created by paramagnetic defect ions of thulium located in the walls of the pits. On the one hand, the presence of these nonuniformities leads to acceleration of the nuclear spin relaxation of ^{3}He in these pits. (A somewhat similar situation was considered in Ref. 94 — longitudinal relaxation of the magnetization of particles moving in a random fluctuating magnetic field. As a result of this motion the relaxation rate increased with increasing field and decreasing temperature. Such a tendency is also observed in our experiments. However, direct use of this model here is impossible, since, first, the fields of the paramagnetic defect ions are strongly anisotropic, and second, liquid ^{3}He has a number of special properties, which were mentioned above.) On the other hand, the nuclear spins of these ^{3}He atoms located in such nonuniformities of the magnetic fields have different Zeeman frequencies, which makes the exchange of magnetization between these atoms difficult. Thus the efficiency of this mechanism will be determined by the competition between two processes: acceleration of the relaxation in the magnetic-field nonuniformities, and the exchange of magnetization between ^{3}He atoms in the near-surface layer.

In the framework of the proposed mechanism one can also interpret the data on the relaxation of the longitudinal magnetization of ^{3}He nuclei in ^{3}He–^{4}He mixtures (Fig. 5). The admixture of ^{4}He leads to a situation in which predominantly ^{4}He atoms are found in the microcracks because of the different values of the van der Waals interactions with the atoms of the walls of the substrate. Therefore, the penetration of ^{3}He atoms into microcracks becomes increasingly difficult with increasing ^{4}He concentration, and the longitudinal relaxation rate of ^{3}He decreases. We note that the concentration dependence of T_1^{-1} (Fig. 5) is very reminiscent of the adsorption curve of ^{4}He in ^{3}He–^{4}He mixtures.[49] Upon transition to the superfluid state the diffusion coefficient of ^{3}He atoms increases, so that the transfer of magnetization from the bulk ^{3}He atoms to the near-surface ones is strongly accelerated, and the relaxation rate of ^{3}He increases practically to the values measured in pure ^{3}He.

2.3. Relaxation of ^{3}He nuclei on the surface of crystals and magnetically oriented powders

Both in the studies discussed and in experiments with fine powders[7] it has been observed that the relaxation of the longitudinal magnetization of ^{3}He in contact with the surface of the Van Vleck paramagnet LiTmF$_4$ occurs more rapidly than in the same experiments using the diamagnet LiYF$_4$. This is convincing evidence of the existence of magnetic coupling between ^{3}He and the substrate, so that for generalization of the experimental data it makes sense to summarize the most important feature of the relaxation of ^{3}He in magnetically oriented powders of LiTmF$_4$ at $T = 1.5$ K, which are reflected in the following relations (the number in parentheses denote the size of the powder particles, the subscripts $\parallel$ and $\perp$ denote the direction of the external field relative to the c' axis, which is the axis of predominant orientation of the powder particles):

$$T_{1\parallel} \ll T_{1\perp}, \tag{2.4}$$

$$T_{1\parallel}(<20\ \mu\text{m}) \approx T_{1\parallel}(<1\ 1\mu\text{m}) \ll T_{1\parallel}(2-4\ \mu\text{m}), \tag{2.5}$$

FIG. 6. Temperature dependence of the longitudinal relaxation rate of ^{169}Tm nuclei in a LiTmF$_4$ single crystal in the orientation $\mathbf{H}_0 \parallel c$. The solid line was calculated by the formula $T_1^{-1} = 3.4T^{1.5} + 4 \times 10^7 \exp(-47.5/T)$, where the first term is due to relaxation of the thulium nuclei via paramagnetic impurities, and the second term is due to fluctuations of the hyperfine magnetic field produced by the $4f$ shell of the Tm^{3+} ion; the argument of the exponential function is in good agreement with the energy of the first excited doublet in the LiTmF$_4$ crystal.[84]

$$T_{2\|}(<1 \ \mu m) = 12 \ \mu s \ll T_{2\perp}(<1 \ \mu m). \qquad (2.6)$$

We see that the time T_1 decreases substantially only for $\mathbf{H}_0 \| c'$ and only in samples containing a large number of particles of submicron size and, consequently, have a well-developed surface. In this case the relaxation time T_2 also turns out to be small. In a sample containing particles smaller than 1 μm the time $T_{2\|}$ turns out to be even smaller than for ^{19}F nuclei in CaF_2 (Ref. 93). Since the magnetic moments of the ^3He nuclei are smaller than those of fluorine, and the distances between them cannot be smaller than the distance between ^{19}F spins in CaF_2, it must be assumed that the relaxation of the transverse magnetization of ^3He in a sample containing submicron particles of $LiTmF_4$ will occur not only because of the dipole–dipole interaction of the nuclear spins of ^3He with one another but also because of the effect of the fluctuating magnetic fields created by the paramagnetic centers at the substrate surface. Moreover, when one considers the extremely strong influence on the relaxation of the ^3He nuclei ($T_{2\|}(<1 \ \mu m) = 12 \ \mu s$), it must be assumed that the source of these fluctuating fields is from paramagnetic centers located in the immediate vicinity of the surface of the crystalline powder particles. Our experiments show that native impurities such as Nd^{3+}, Gd^{3+}, and other rare-earth ions are incapable of causing the observed effects, and it therefore seems to us that more likely candidates for the role of acceptors are Tm^{3+} ions, which are located just near the surface in sites with highly distorted symmetry and have large magnetic moments.

Thus a decisive role in the magnetization transfer process is played by the ^3He surface atoms, which are well coupled to the subsurface system of paramagnetic centers of the crystal. Of course, this channel of nuclear relaxation of bulk ^3He can operate only under the condition of a rapid exchange of energy between the bulk and near-surface ^3He atoms, i.e., in the presence of spin diffusion. In a field $\mathbf{H}_0 \perp c'$ the Van Vleck magnetization of $LiTmF_4$ is extremely large, and therefore in the space between powder particles the nuclear spins of the liquid ^3He come under the influence of a highly nonuniform field (the gradients reach 100 Oe/pore size). A consequence of this should be a spread of Larmor frequencies of the nuclear spins of ^3He and a breaking of the coupling between ^3He nuclei in the bulk and in the immediate vicinity of the surface. Apparently, it is this circumstance that is reflected in the observed properties [see Eqs. (2.4) and (2.6)]. We note that in a recent paper[97] the features of the magnetic relaxation of liquid ^3He were also explained by taking into consideration the diffusive motion of the ^3He atoms near the surface.

Obviously, in the powder experiments it is necessary to take into account the role of the solid adlayer of ^3He on the developed surface of the samples. This raises the question of the relation between the contributions to the longitudinal relaxation rate of ^3He nuclei from quantum exchange at the surface of the substrate and from relaxation in microcracks. Unfortunately, the data available from powder experiments prior to the start of this study were insufficient to permit reaching final conclusions as to the role of the solid film. For example, in experiments with the coarsest powder ($<57 \ \mu m$) an admixture of the ^4He isotope did not lead to an increase of T_1, indicating that the relaxation due to ex-

change is ineffective in this case. On the other hand, in the experiments of Ref. 57 it was reliably established that a solid films of ^4He (1–2 monolayers) substantially slows the recovery of the longitudinal magnetization. Apparently, the cause of the disagreement of these results is rooted in the fact that the surface of the sample containing the coarsest particles is insufficiently large.

2.4. Nuclear magnetic relaxation of liquid ^3He in water-filled pores of a fine $LiYF_4$ powder

For further study of the influence of surface paramagnetic defect centers on the magnetic relaxation of the nuclei of liquid ^3He we made experimental measurements of the temperature dependence of the longitudinal relaxation time T_1 of the ^3He nuclei for different degrees of filling of the microcracks on the crystalline surface by molecules of distilled water.[83] Fine powders of $LiYF_4$ were placed in a Pyrex glass ampoule with a filling factor of 0.5 and were then pumped down for several days. At a certain time they were brought into contact with saturated water vapor at room temperature. After being removed from the volume containing the saturated water vapor, the sample came to an equilibrium state over several hours. The degree of filling of the microcracks by water was monitored by the NMR cryoporometry method described in Ref. 83. The value of the longitudinal relaxation rate of the nuclear spins of the liquid ^3He at each temperature was determined from 50 values of the amplitude of the free-induction decay signal for different delay times τ between the rf probe pulses ($\pi/2$-τ-$\pi/2$).

Figure 7 shows the temperature dependence of the longitudinal relaxation rate of the liquid ^3He nuclei in contact with "dry" $LiYF_4$ powder.[98] Although the temperature dependence obtained is weak, the sign of the derivative is clearly opposite to that which is observed in the earlier studies of magnetic coupling and in our experiments on the magnetic relaxation of liquid ^3He in contact with $LiYF_4$–$LiTmF_4$ single crystals (Fig. 3), where the longitudinal relaxation rate was proportional to the magnetization of the magnetic moments of the solid and, consequently, decreased with increasing temperature. To understand the cause of such a fundamental change in the temperature dependence, let us write an expression for the thermal contact of the nuclear spin system of liquid ^3He and the solid substrate in the framework of the relaxation model which we proposed above:

$$C_{He}T_{1,meas}^{-1} = C_{He,bulk}T_{1,diff}^{-1} + C_{He,restr}T_{1,restr}^{-1}, \qquad (2.7)$$

where

$$C_{He} = C_{He,bulk} + C_{He,restr} \qquad (2.8)$$

is the total magnetic heat capacity of the nuclear spins of liquid ^3He, consisting of two terms pertaining to ^3He atoms of the bulk and to atoms found in a restricted geometry in microcracks on the crystalline surface (restr); $T_{1,meas}$ is the measured relaxation time, $T_{1,diff}$ is the characteristic time for transfer of longitudinal magnetization of the nuclear spins of liquid ^3He from the atoms of the bulk liquid to atoms found in a restricted geometry in microcracks on the crystalline surface, and $T_{1,rest}$ is just the relaxation time of the nuclear magnetization of the liquid ^3He atoms found in these microcracks. This time can be governed by several mechanisms:
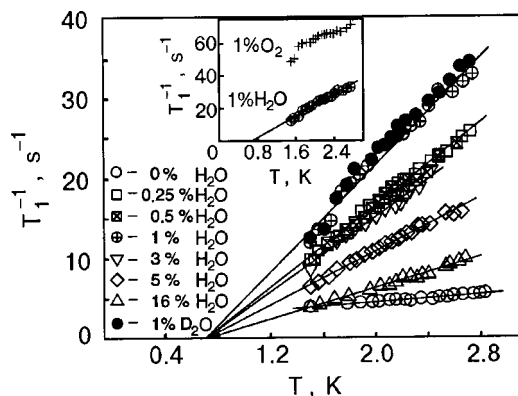
FIG. 7. Temperature dependence of the longitudinal relaxation rate of the nuclear spins of liquid ^{3}He in pores of a "dry" (0% H$_2$O) micron powder of LiYF$_4$ (○) and in pores filled with distilled water and deuterated water, with various degrees of filling of the voids by water molecules (in percent of the total volume of the voids in the sample). The inset shows a comparison of the relaxation rates of liquid ^{3}He at 1% filling of the voids of the sample with H$_2$O and O$_2$ molecules.[98]

1) direct transfer of magnetization to the magnetic moments of the solid substrate having close values of the Larmor frequencies (see, e.g., Ref. 56); this mechanism is most efficient when the frequencies coincide completely (see, e.g., Refs. 6 and 72);

2) relaxation of the longitudinal magnetization in strongly fluctuating local magnetic fields produced by paramagnetic defect centers on the surfaces of microcracks;

3) relaxation due to fluctuations of the local fields in the quantum exchange of ^{3}He atoms on the solid surface;[82] clearly, at temperatures above 1 K this mechanism has a low efficiency because of the small number of adsorbed ^{3}He atoms;

4) relaxation in a restricted geometry due to substantial changes of the spectral characteristics of the diffusive motion; according to our calculations,[84] this mechanism should give a temperature-independent contribution (if the temperature dependence of the diffusion coefficient is neglected) to the measured relaxation rate.

It follows from Eq. (2.7) that in the single-crystal experiments discussed above, the "bottleneck" in the process is the relaxation of the magnetization near the surface, because of the small percentage of the ^{3}He atoms found in the microcracks. In terms of the character of the temperature and field dependences (Figs. 3 and 4) we can conclude that the dominant relaxation mechanism is the second of those mentioned above. Indeed, the growth of the magnetization of paramagnetic defect centers with temperature or magnetic field leads to enhancement of the amplitude of the fluctuating magnetic fields, and that accelerates the relaxation process.

In experiments with fine powders, the results of which are presented in this Section, the percentage of the ^{3}He atoms found in the microcracks is large because of the well-developed crystalline surface of the micron-size powder particles. However, because of the large local magnetic fields in the microcracks the Larmor frequencies of the nuclear spins of the liquid ^{3}He atoms in the microcracks differ rather substantially from the Larmor frequency of the nuclear spins of the bulk liquid ^{3}He. Here it is clear that in such a situation the "bottleneck" in the relaxation will be transfer of magne-

tization from the bulk liquid to the nuclear spins of ^{3}He in the microcracks. Therefore, the growth of the magnetization of the paramagnetic defect centers, owing to the decrease in temperature, will further increase the mismatch of the Larmor frequencies and, as a consequence, slow the relaxation process for the longitudinal magnetization. Here there is a rather large temperature-independent contribution to the relaxation rate from the mechanism of relaxation in the restricted geometry.

Summarizing what we have said above, we can say that the data of these experiments confirmed our hypothesis that the efficiency of the magnetic relaxation of liquid ^{3}He at a contact with a solid substrate is governed by the competition between two processes: acceleration of the relaxation in non-uniform magnetic fields, and the exchange of magnetization between atoms of liquid ^{3}He.

In all the experiments investigating the magnetic relaxation of the nuclear spins of liquid ^{3}He in the water-filled pores of finely powdered LiYF$_4$, the evolution of the longitudinal magnetization has been described well by a single exponential. These results are presented by the unfilled symbols in Fig. 7. A comparison of these curves with the data obtained from measurements of the relaxation rate of the nuclei of liquid ^{3}He in contact with "dry" LiYF$_4$ powder shows that, while in the case of the dry powder the temperature dependence is rather weak, even a low degree of filling of the microcracks with H$_2$O molecules leads to an increase in the rate of magnetic relaxation of liquid ^{3}He and to a strong linear temperature dependence of the Curie–Weiss type, with a characteristic temperature $T_C = 0.7$ K. Such behavior of $T_1^{-1}(T)$ indicates that the water molecules play a substantial role, both in "crowding out" the liquid ^{3}He atoms from microcracks and also in the magnetism of the surface. An extremely low filling of the microcracks with water is reflected primarily in a lessening of the mismatch of the Larmor frequencies, since the rapidly relaxing atoms of liquid ^{3}He are crowded out of the regions with the largest nonuniformities of the local magnetic fields by water molecules. Increasing the concentration of water molecules further leads to a substantial decrease in the magnetic heat capacity of the rapidly relaxing atoms of liquid ^{3}He [see Eq. (2.7)]. The increase of the slope of the temperature dependence of the rate of longitudinal relaxation of liquid ^{3}He when the concentration of the water molecules is increased from 0.25% to 1% indicates that the aforementioned mismatch of the Larmor frequencies decreases, i.e., there is a decrease in the spatial fluctuations of the local magnetic fields in the microcracks on the surface. This fact can be explained by the appearance of certain correlations between the magnetic moments of the defect centers. It is therefore reasonable to assume that the paramagnetic defect centers,[90,91] which are concentrated on the surface, form exchange-coupled magnetic pairs or clusters in which the exchange interaction comes about through the transfer of spin density via the molecular orbitals of oxygen in the water molecules. This is indicated by the fact that the pattern of the temperature dependence of the relaxation rate is remains unchanged when deuterated water is used instead of ordinary water (the filled symbols in Fig. 7). Increasing the temperature leads to a decrease of the magnetization of these exchange-coupled
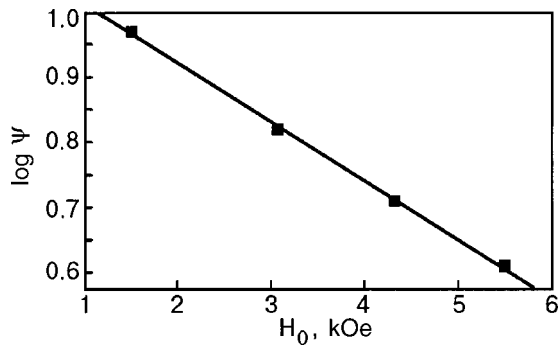
FIG. 8. Field dependence of the slope of the $T_1^{-1}(T)$ curve at $T = 1.5$ K for 0.5% filling of the voids of the sample by H_2O molecules.[98]

FIG. 9. Temperature dependence of the longitudinal relaxation rate of the nuclear spins of liquid ^{3}He in the pores of a micron powder of LiYF$_4$ for various concentrations of the ^{3}He–^{4}He mixture.[83] The vertical dotted lines show the positions of the λ points for the superfluid mixtures.

pairs and, consequently, to an increase of the rate of relaxation of the nuclear magnetization of liquid ^{3}He. An additional argument supporting our ideas about the pattern of magnetic relaxation of liquid ^{3}He in contact with a crystalline surface is the field dependence of the slope of the $T_1^{-1}(T)$ curve at $T = 1.5$ K and 0.5% filling of the microcracks with water molecules (see Fig. 8). Increasing the magnetic field, which suppresses the correlations between the paramagnetic defect centers, leads to growth of the spatial inhomogeneities of the local magnetic fields in the microcracks and to a decrease in the relaxation rate. At this stage of the investigation there is no possibility of obtaining quantitative estimates of the characteristic temperature for such magnetically coupled pairs or of establishing the structure of the clusters because of the lack of detailed information about the wave functions of the paramagnetic defect centers. However, the experimental value obtained, $T_C = 0.7$ K, lies within reasonable limits with allowance for the two-dimensional character of the distribution of defect centers and their concentration on the surface.[91] According to our calculations,[84] the relaxation mechanism in the restricted geometry is most efficient for pore sizes less than 50 Å. It is therefore unsurprising that in the experiments with water-filled pores the temperature-independent contribution to the magnetic relaxation rate is absent, and the extrapolation of the temperature dependence in Fig. 7 gives the same characteristic temperature for all of the curves.

If the magnetic relaxation mechanism described above, which works through the formation of exchange-coupled pairs or clusters, is correct, then replacing the diamagnetic water molecules with paramagnetic oxygen molecules (this actually means covering the entire surface of the microcracks by a solid-state film of oxygen, which is possibly found in a magnetically ordered state) should smooth out the spatial fluctuations of the local magnetic fields and increase the longitudinal relaxation rate. Indeed, such an acceleration, by more than a factor of two, is observed in the experiment (inset to Fig. 7).

The whole set of experimental data—the temperature, field, and concentration dependences of the rate of relaxation of the longitudinal magnetization of the nuclear spins of liquid ^{3}He—can be described by the formula

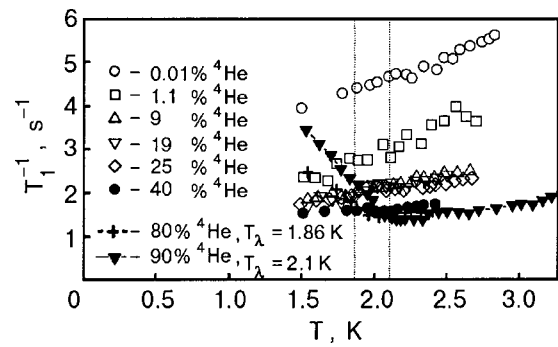$$T_1^{-1} = A + \frac{T - T_C}{CH_0}, \qquad (2.9)$$

where H_0 is the magnetic field, and C is a coefficient containing information about both the magnetic properties of the surface paramagnetic centers and the magnetic interactions of the nuclear spins of the liquid ^{3}He with them. The constant term A describes the contribution of the relaxation mechanism in the restricted geometry.

2.5. Nuclear magnetic relaxation of liquid ^{3}He in ^{3}He–^{4}He quantum mixtures filling the pores of a fine LiYF$_4$ powder

In the previous Subsection we discussed the results of research on the magnetic relaxation of liquid ^{3}He in powers of a fine LiYF$_4$ powder in which the nanocracks are partially filled with water, which was in the solid state under the conditions of the experiment. It is no doubt of interest to replace the classical liquid by a quantum liquid. The difference in the adsorption energies of the helium isotopes (^{3}He and ^{4}He) allows one to fill the nanocracks by ^{4}He atoms in a controllable manner. Figure 9 shows the temperature dependence of the longitudinal relaxation time of liquid ^{3}He for different ^{3}He–^{4}He quantum mixtures.[83] Increasing the concentration of the diamagnetic liquid ^{4}He leads to a monotonic decrease of the relaxation rate on account of a decrease of the constant A in formula (2.9) and to a weakening of the temperature dependence. Behavior of this sort becomes understandable if it is taken into account that when ^{3}He atoms are crowded out of the nanocracks by ^{4}He atoms, the fraction comprised of rapidly relaxing ^{3}He nuclear spins decreases. This sort of behavior was noticed in our experiments with LiYF$_4$ single crystals. Increasing the ^{4}He concentration further leads to an increase in the temperature of the transition to the superfluid state of the quantum mixture, e.g., at concentrations of 80% and 90% one has $T_\lambda = 1.86$ and 2.1 K, respectively, which lie within the investigated temperature interval 1.5–3 K. Below the critical temperature of the superfluid transition, the diffusion coefficient and, accordingly, the probability of penetration of ^{3}He atoms into the nanocracks increase, and that leads to acceleration of the magnetic relaxation.

2.6. On the possibility of using insulating Van Vleck paramagnets for dynamic polarization of liquid ³He

It was mentioned in the Introduction that spin-polarized liquid ³He is at the present time obtained by two main methods:

— polarization of solid ³He by the "brute force" method, followed by rapid melting;[35–37]

— optical pumping[33,34] of gaseous ³He, followed by rapid liquefaction.[34]

The first of these methods requires very low temperatures ($T < 10^{-2}$ K) and high magnetic fields in view of the small value of the nuclear magnetic moment. Although solid ³He can be quite strongly polarized under those conditions, even a very small heat leak can cause the sample to be heated and very strongly depolarized. The subsequent rapid melting gives spin-polarized liquid ³He, but the spin polarization in the liquid relaxes to its equilibrium value in a few minutes. The second method involves the use of rather powerful sources of electromagnetic radiation and also yields a high spin polarization, but for gaseous ³He with a rather low density, so that the subsequent liquefaction yields an extremely small amount of polarized ³He. Therefore, it is of interest to consider methods of direct polarization of liquid ³He.

Spin-polarized ³He–⁴He quantum mixtures (with a polarization of the liquid ³He of up to 20%) can be obtained in a circulating dilution refrigerator.[99,100]

Dynamic methods of polarization can also be used to obtain a highly spin-polarized state of liquid ³He. In Sec. 1 we mentioned the use of paramagnetic centers in fluorocarbons for transfer of the spin polarization to liquid ³He at saturation of the electron spin resonance.[62] The possibility of using powders of solid insulators (charcoal) for this purpose was demonstrated in Refs. 101 and 102, and the possibility of achieving dynamic polarization of liquid ³He by employing the spin resonance of electrons injected into the liquid by a strong electric potential was considered in Ref. 103.

Our studies of the properties of insulating Van Vleck paramagnets at high magnetic field and of the magnetic coupling between them and liquid ³He suggest that these substances may be used for dynamic polarization of the nuclei of liquid ³He.[104] From the theoretical and experimental results presented above, it follows that for dynamic polarization with the use of Van Vleck paramagnets there are two types of magnetic moments that can be used:

1) electronic–nuclear magnetic moments of Van Vleck ions found in the bulk of the crystal or of the crystalline powder grains;

2) paramagnetic defect centers formed on the crystalline surface of insulating Van Vleck paramagnets.

The first of these magnetic moments have a pronounced anisotropy of the gyromagnetic ratio, making it possible to vary their Larmor frequency by varying the orientation of the external magnetic field. At high magnetic fields the Van Vleck ions in the bulk of the crystal are quite highly polarized and, furthermore, they are distributed regularly in the sites of the crystal lattice. The experimental observation of high-frequency EPR due to transitions between the ground and excited levels of these ions[10,105] holds the hope that the saturation of these transitions might be used for polarization of the nuclear spins of ³He in contact with insulating Van Vleck paramagnets. One of the possible channels for the transfer of magnetization may be the dynamic polarization of the nuclear spins of the ligands due to saturation of the high-frequency EPR and the subsequent transfer of magnetization under conditions of resonant magnetic coupling. However, this sort of transfer is influenced considerably by paramagnetic defect centers located on the crystalline surface. From this standpoint, to bring about the efficient polarization of liquid ³He with the use of insulating Van Vleck paramagnets it is necessary to conduct an experimental search for methods of obtaining crystals and powders with an atomically smooth surface in order to avoid the formation of defect centers.

On the other hand, the paramagnetic surface defect centers are found in the immediate vicinity of atoms of liquid ³He, so that it seems extremely attractive to use saturation of the EPR of these centers for polarization of the nuclear spins of ³He, particularly since a controlled variation of the magnetic properties of the surface centers has an extremely large influence on the kinetic parameters of the spin system of liquid ³He.[83,98] Therefore, it appears extremely promising to go forward with a detailed study of the magnetic properties of paramagnetic surface defect centers.

CONCLUSION

Let us summarize the main results of the theoretical and experimental studies of the magnetic relaxation of the nuclear spins of liquid ³He in contact with single crystals and fine powders of the insulating Van Vleck paramagnet LiTmF₄ and its diamagnetic analog LiYF₄.

We first of all showed that the coupling of the bulk ³He with a magnetic substrate is effected through the ³He atoms on and near the surface of the crystal (in microcracks on the surface of the powder grains and single crystals). The theoretical model proposed in Ref. 84 for describing the influence of the restricted geometry of the surface microcracks on the magnetic relaxation of liquid ³He made it possible to understand the basic experimental relationships and to reveal the different channels of magnetic relaxation of the nuclear spins of liquid ³He in contact with insulating powders of LiYF₄. On the basis of such an analysis it was demonstrated experimentally that by making controlled changes in the magnetic properties of the surface of the solid substrate, one can control the relaxation parameters of liquid ³He. It was also established that the quantum liquid (³He) can be used as a probe for studying the magnetic properties of a solid surface at low and ultralow temperatures. Finally, it is predicted that insulating Van Vleck paramagnets can be used for dynamic polarization of the nuclear spins of liquid ³He.

310   Low Temp. Phys. **28** (5), May 2002

Naletov *et al.*

*E-mail: dtayursk@mi.ru

[1] W. R. Abel, A. C. Anderson, W. C. Black, and J. C. Wheatley, Phys. Rev. Lett. **15**, 875 (1965).

[2] W. R. Abel, A. C. Anderson, W. C. Black, and J. C. Wheatley, Phys. Rev. Lett. **16**, 273 (1966).

[3] D. D. Osheroff, W. J. Gully, R. C. Richardson, and D. M. Lee, Phys. Rev. Lett. **29**, 920 (1979).

[4] G. E. Volovik, *Exotic Properties of Superfluid Helium 3*, World Scientific (1992).

[5] G. E. Volovik, Proceedings of the National Academy of Sciences of the United States of America (PNAS) **96**, 6042 (1999).

[6] A. V. Egorov, F. L. Aukhadeev, M. S. Tagirov, and M. A. Teplov, JETP Lett. **39**, 584 (1984).

[7] A. V. Egorov, O. N. Bakharev, A. G. Volodin, S. L. Korableva, M. S. Tagirov, and M. A. Teplov, Zh. Éksp. Teor. Fiz. **97**, 1175 (1990) [Sov. Phys. JETP **70**, 658 (1990)].

[8] L. K. Aminov and M. A. Teplov, Usp. Fiz. Nauk **147**, 49 (1985) [Sov. Phys. Usp. **28**, 762 (1985)].

[9] F. W. Van Keuls, T. J. Gramila, L. J. Friedman, and R. C. Richardson, Physica B **165−166**, 717 (1990).

[10] M. S. Tagirov and D. A. Tayurskiĭ, Fiz. Nizk. Temp. **28**, (2002) [Low Temp. Phys. **28**, 147 (2002)].

[11] C. Lhuillie and F. Laloe, J. Phys. (Paris) **4**, 239 (1979).

[12] B. Castaing and P. Nozieres, J. Phys. (Paris) **4**, 257 (1979).

[13] P. Nozieres, Physica B **126**, 212 (1984).

[14] H. R. Glyde and S. I. Hernadi, Phys. Rev. B **29**, 3873 (1984).

[15] I. A. Fomin, JETP **81**, 347 (1997).

[16] A. E. Meyerovich and A. Stepaniants, J. Low Temp. Phys. **106**, 653 (1997).

[17] I. A. Fomin, JETP Lett. **65**, 749 (1997).

[18] O. Buu, A. C. Forbes, A. S. van Steenbergen, S. A. J. Wiegers, G. Remenyi, L. Puech, and P. E. Wolf, J. Low Temp. Phys. **11**, 311 (1998).

[19] O. Buu, A. C. Forbes, L. Puech, and P. E. Wolf, J. Low Temp. Phys. **11**, 381 (1998).

[20] B. Cowan, W. J. Mullin, and S. Tehrani-Nasab, Physica B **284−288**, 176 (2000).

[21] B. Villard, P. J. Nacher, and G. Tastevin, Physica B **284−288**, 178 (2000).

[22] B. Villard and P. J. Nacher, Physica B **284−288**, 180 (2000).

[23] O. Buu, L. Puech, and P. E. Wolf, Physica B **284−288**, 182 (2000).

[24] O. Buu, L. Puech, and P. E. Wolf, Physica B **284−288**, 184 (2000).

[25] P. E. Wolf, O. Buu, and L. Puech, Physica B **284−288**, 186 (2000).

[26] H. Middleton, R. D. Black, B. Saam, G. D. Cates, G. P. Cofer, R. Guenther, W. Happer, L. W. Hedlund, G. A. Johnson, K. Juvan, and J. C. Swartz, Magn. Reson. Med. **33**, 271 (1995).

[27] R. D. Black, H. L. Middleton, G. D. Cates, G. P. Cofer, B. Driehuys, W. Happer, W. L. Hedlund, G. A. Johnson, and M. D. Shattuck, Radiology **199**, 867 (1996).

[28] P. Bachert, L. R. Schad, M. Bock, M. V. Knopp, M. Ebert, T. Grossmann, W. Heil, G. Hofmann, R. Surkau, and E. W. Otten, Magn. Reson. Med. **36**, 192 (1996).

[29] H. E. Moller, X. J. Chen, M. S. Chawla, B. Driehuys, L. W. Hedlund, and G. A. Johnson, J. Mater. Res. **135**, 133 (1998).

[30] F. Kober, B. Koenigsberg, V. Belle, M. Viallon, J. L. Leviel, A. Delon, A. Ziegler, and M. Decorps, J. Mater. Res. **138**, 308 (1999).

[31] G. Tastevin, Phys. Scr. **86**, 46 (2000).

[32] P. J. Nache and G. Tastevin, Physica B **284−288**, 2053 (2000).

[33] E. Stolz, M. Meyerhoff, N. Bigelow, M. Leduc, P. J. Nacher, and G. Tastevin, Appl. Phys. B: Laser Opt. **63**, 629 (1996).

[34] M. Leduc, P. J. Nacher, G. Tastevin, and E. Courtade, Hyperfine Interact. **127**, 443 (2000).

[35] M. Chapellier, G. Frossati, and F. B. Rasmussen, Phys. Rev. Lett. **42**, 904 (1979).

[36] S. A. J. Wiegers, P. E. Wolf, and L. Puech, Phys. Rev. Lett. **66**, 2895 (1991).

[37] G. Frossati, J. Low Temp. Phys. **111**, 521 (1998).

[38] R. H. Romer, Phys. Rev. **115**, 1415 (1959).

[39] R. H. Romer, Phys. Rev. **117**, 1183 (1960).

[40] I. L. Bekarevich and I. M. Khalatnikov, Zh. Éksp. Teor. Fiz. **39**, 1699 (1960) [Sov. Phys. JETP **12**, 1187 (1961)].

[41] J. Gavoret, Phys. Rev. A **157**, 721 (1965).

[42] I. A. Fomin, Zh. Éksp. Teor. Fiz. **54**, 1881 (1968) [Sov. Phys. JETP **27**, 1010 (1968)].

[43] J. C. Wheatley, Phys. Rev. **165**, 304 (1968).

[44] S. A. Altshuler and B. M. Kozyrev, *Electron Paramagnetic Resonance in Compounds of Transition Elements*, Halsted, New York (1975), Nauka, Moscow (1972).

[45] A. J. Leggett and M. Vuorio, J. Low Temp. Phys. **3**, 359 (1970).

[46] J. H. Bishop, D. W. Cutter, A. C. Mota, and J. C. Wheatley, J. Low Temp. Phys. **1**, 379 (1973).

[47] W. C. Black, A. C. Mota, J. C. Wheatley, J. H. Bishop, and P. M. Brewster, J. Low Temp. Phys. **4**, 391 (1971).

[48] M. Jutzler and A. C. Mota, Physica B **107**, 553 (1981).

[49] K. Thompson, J. Low Temp. Phys. **32**, 361 (1981).

[50] S. Saito, Physica B **107**, 555 (1981).

[51] O. Avenel, M. P. Berglund, R. G. Gylling, N. E. Phillips, A. Vetleseter, and M. Vuorio, Phys. Rev. Lett. **31**, 76 (1973).

[52] T. Perry, K. DeConde, J. A. Sauls, and D. L. Stein, Phys. Rev. Lett. **48**, 1831 (1982).

[53] S. Saito, T. Nakayama, and H. Ebisawa, Phys. Rev. B **31**, 7475 (1985).

[54] Y. Hu, G. J. Stecher, T. J. Gramila, and R. C. Richardson, Phys. Rev. B **54**, 9639 (1996).

[55] R. Konig, Th. Hermannsdorfer, and I. Batko, Phys. Rev. Lett. **8**, 4787 (1987).

[56] L. J. Friedman, P. J. Millet, and R. C. Richardson, Phys. Rev. Lett. **47**, 1078 (1981).

[57] L. J. Friedman, T. J. Gramila, and R. C. Richardson, J. Low Temp. Phys. **55**, 83 (1984).

[58] P. C. Hammel, M. L. Roukes, Y. Hu, T. J. Gramila, T. Mamiya, and R. C. Richardson, Phys. Rev. Lett. **51**, 2124 (1983).

[59] R. C. Richardson, Physica B **126**, 298 (1984).

[60] M. Chapellier, L. Sniadower, G. Dreyfus, H. Alloul, and J. Cowen, J. Phys. (Paris) **45**, 1033 (1984).

[61] A. Schuhl, F. B. Rasmussen, and M. Chapellier, J. Low Temp. Phys. **57**, 483 (1984).

[62] A. Schuhl, S. Maegawa, M. W. Meisel, and M. Chapellier, Phys. Rev. Lett. **54**, 1952 (1985).

[63] S. Maegawa, A. Schuhl, M. W. Meisel, and M. Chapellier, Europhys. Lett. **1**, 83 (1986).

[64] S. Maegawa, A. Schuhl, M. W. Meisel, and M. Chapellier, Jpn. J. Appl. Phys. **26−3**, 323 (1987).

[65] A. Schuhl, S. Maegawa, M. W. Meisel, and M. Chapellier, Jpn. J. Appl. Phys. **26−3**, 333 (1987).

[66] A. Schuhl, S. Maegawa, M. W. Meisel, and M. Chapellier, Jpn. J. Appl. Phys. **26−3**, 325 (1987).

[67] Q. Geng, M. Olsen, and F. B. Rasmussen, J. Low Temp. Phys. **74**, 369 (1989).

[68] D. R. Swanson, D. Candela, and D. O. Edwards, Jpn. J. Appl. Phys. **26−3**, 313 (1987).

[69] I. S. Solodovnikov and N. V. Zavaritskiĭ, JETP Lett. **56**, 162–165 (1992).

[70] I. S. Solodovnikov and N. V. Zavaritskiĭ, Zh. Éksp. Teor. Fiz. **106**, 489 (1994) [JETP **79**, 267 (1994)].

[71] R. W. Singerman, F. W. Van Keuls, and R. C. Richardson, Phys. Rev. Lett. **72**, 2789 (1994).

[72] F. W. Van Keuls, R. W. Singerman, and R. C. Richardson, J. Low Temp. Phys. **96**, 103 (1994).

[73] D. A. Tayurskii and M. S. Tagirov, Appl. Magn. Reson. **6**, 587 (1994).

[74] N. Mizutani, H. Suzuki, and M. Ono, Physica B **165−166**, 523 (1990).

[75] D. A. Tayurskiĭ, Dep. VINITI 04.05.94, No. 1084–V94 (1994).

[76] H. Godfrin and R. E. Rapp, Adv. Phys. **44**, 113 (1995).

[77] B. Brami, F. Joly, and C. Lhuillier, J. Low Temp. Phys. **94**, 63 (1994).

[78] M. G. Richards, J. Phys. (Paris) **39**, C6-1342 (1978).

[79] H. Godfrin, Can. J. Phys. **65**, 1430 (1987).

[80] A. Fukushima, S. Ogawa, and Y. Okuda, J. Low Temp. Phys. **88**, 483 (1992).

[81] R. E. Rapp and H. Godfrin, Phys. Rev. B **47**, 12004 (1993).

[82] P. C. Hammel and R. C. Richardson, Phys. Rev. Lett. **52**, 1441 (1984).

[83] A. V. Klochkov, V. V. Naletov, M. S. Tagirov, D. A. Tayurskii, A. N. Yudin, M. R. Zhdanov, R. Sh. Zhdanov, A. A. Bukharaev, and N. I. Nurgazizov, Appl. Magn. Reson. **19**, 199 (2000).

[84] V. V. Naletov, M. S. Tagirov, D. A. Tayurskiĭ, and M. A. Teplov, Zh. Éksp. Teor. Fiz. **108**, 577 (1995) [JETP **81**, 311 (1995)].

[85] R. Yu. Abdulsabirov, S. L. Korableva, V. A. Sakharov, and M. S. Tagirov, Poverkhnost': Fiz., Khim., Mekh. **10−11**, 125 (1994).

[86] A. F. Andreev, JETP Lett. **28**, 556 (1978).

[87] A. M. Dyugaev, Zh. Éksp. Teor. Fiz. **87**, 1232 (1984) [Sov. Phys. JETP **60**, 704 (1984)].

[88] A. M. Dyugaev, Zh. Éksp. Teor. Fiz. **89**, 1220 (1985) [Sov. Phys. JETP **62**, 703 (1985)].

[89] A. M. Dyugaev, J. Low Temp. Phys. **78**, 79 (1990).

[90] A. V. Klochkov, V. V. Naletov, M. S. Tagirov, D. A. Tayurskiĭ, M. A.

Teplov, V. N. Efimov, and G. V. Mamin, JETP Lett. **62**, 585 (1995).

[91] A. V. Klochkov, S. P. Kurzin, I. R. Mukhamedshin, D. R. Nabiullin, V. V. Naletov, H. Suzuki, I. Kh. Salikhov, M. S. Tagirov, D. A. Tayurskii, and R. Sh. Zhdanov, Appl. Magn. Reson. **14**, 525 (1998).

[92] E. Louis, F. Guinea, and F. Flores, in *Fractals in Physics*, edited by L. Pietronero and E. Tosatti [North-Holland, Amsterdam (1986), p. 117; Mir, Moscow (1988)].

[93] A. Abragam and M. Gol'dman, *Nuclear Magnetism: Order and Disorder* [Clarendon Press, Oxford (1982); Mir, Moscow (1984)].

[94] N. F. Fatkullin, Zh. Éksp. Teor. Fiz. **101**, 1561 (1992) [JETP **74**, 833 (1992)].

[95] A. Abragam, *The Principles of Nuclear Magnetism* [Clarendon Press, Oxford (1961); Izd. Inostr. Lit., Moscow (1963)].

[96] D. Vollhardt and P. Wolfle, Phys. Rev. Lett. **47**, 190 (1981).

[97] A. S. van Steenbergen, S. A. J. Wiegers, P. E. Wolf, J. A. Perenboom, and J. C. Maan, Phys. Rev. B **58**, 925 (1998).

[98] A. V. Klochkov, V. V. Naletov, M. S. Tagirov, and D. A. Tayurskiĭ, JETP Lett. **69**, 539 (1999).

[99] A. Rodrigues and G. Vermeulen, J. Low Temp. Phys. **108**, 103 (1997).

[100] A. Roni and G. Vermeulen, J. Low Temp. Phys. **121**, 761 (2000).

[101] S. A. Langer, K. D. DeConde, and D. L. Stein, J. Low Temp. Phys. **57**, 249 (1984).

[102] L. W. Engel and K. D. DeConde, Phys. Rev. B **33**, 2035 (1986).

[103] A. Dyugaev, I. Wagner, and Yu. Ovchinnikov, JETP Lett. **59**, 640 (1994).

[104] M. S. Tagirov and D. A. Tayurskiĭ, JETP Lett. **61**, 672 (1995).

[105] H. P. Moll, J. van Toll, P. Wyder, M. S. Tagirov, and D. A. Tayurskii, Phys. Rev. Lett. **77**, 3459 (1996)

Translated by Steve Torstveit

SUPERCONDUCTIVITY, INCLUDING HIGH-TEMPERATURE SUPERCONDUCTIVITY

Anisotropy of the critical current and the guided motion of vortices in a stochastic model of bianisotropic pinning. II. Observed effects

V. A. Shklovskij*

Institute of Theoretical Physics, National Research Center "Kharkov Physicotechnical Institute," ul. Akademicheskaya 1, 61108 Kharkov, Ukraine and V. N. Karazin Kharkov National University, pl. Svobody 4, Kharkov 61077 Kharkov, Ukraine

A. A. Soroka

Institute of Theoretical Physics, National Research Center "Kharkov Physicotechnical Institute," ul. Akademicheskaya 1, 61108 Kharkov, Ukraine

A simple and clear relationship between the anisotropy of the current density j_c and the guided motion of vortices along the basal planes of a bianisotropic potential is established on the basis of a physical analysis of experimentally observed effects. This relationship is expressed in the form a diagram of the possible dynamical states of the vortex ensemble on the (j_x, j_y) plane. A theoretical analysis of the nonlinear resistive responses in the "rotating current" scheme, which has been used to investigate the anisotropy of the pinning in a number of experimental studies, is given for the first time. The most typical behaviors of the various resistive responses are presented graphically. © *2002 American Institute of Physics.* [DOI: 10.1063/1.1480237]

1. NONLINEAR G EFFECT

Continuing the investigations begun in Ref. 1, we consider the vortex dynamics in a bianisotropic pinning model and the associated resistive properties on the basis of the bianisotropic pinning potential introduced there. We use the dimensionless parameters introduced in that paper.[1]

Bianisotropic pinning, like simple anisotropic pinning,[2] has the peculiarity that the direction of the external driving force $\mathbf{F}_L$ acting on a vortex does not coincide with the direction of its velocity $\mathbf{v}$ (for isotropic pinning $\mathbf{F}_L \| \mathbf{v}$ if the Hall effect is neglected). Nonlinear dependences of the pinning viscosities on the current and temperature bring about both corresponding nonlinear transitions from the full pinning regime [in which the vortex motion with respect to both systems of pinning centers occurs in the thermally activated flux flow (TAFF) regime] into one of the guiding (G) regimes, and also nonlinear transitions from the latter to the isotropic regime, in which the influence of pinning by both systems of pinning centers can be neglected.

The function $\cot\beta = -\rho_\perp/\rho_\|$ used in Ref. 3 for describing the G effect has the following form in our model:

$$\cot\beta = \frac{(1 - \nu_x/\nu_y)\cot\alpha}{1 + (\nu_x/\nu_y)\cot^2\alpha} = -\frac{(1 - \nu_y/\nu_x)\tan\alpha}{1 + (\nu_y/\nu_x)\tan^2\alpha}, \quad (1)$$

where $\rho_\|$ and $\rho_\perp$ are the longitudinal and transverse magnetoresistivities, and β is the angle between the vortex velocity vector $\mathbf{v}$ and the current density vector $\mathbf{j}$ (see Fig. 1 of Ref. 1). The G effect is expressed the more strongly the greater

the noncoincidence of the directions of $\mathbf{F}_L$ and $\mathbf{v}$, i.e., the smaller the angle β. Here it is possible that $\cot\beta \gg 1$, i.e., $\rho_\perp \gg \rho_\|$.

We note that in the X and Y geometries $\beta(\alpha=0) = \beta(\alpha=\pi/2) = \pi/2$, since in both cases the Lorentz force is directed parallel to one of the systems of pinning centers and perpendicular to the other. To investigate the sensitivity of the value of the angle β to small deviations of the angle α from the values 0 and $\pi/2$, corresponding to the Y and X geometries, we write the derivatives $d\beta/d\alpha$ at $\alpha=0$ and $\alpha=\pi/2$ in the linear approximation in α:

$$\left.\frac{d\beta}{d\alpha}\right|_{\alpha=0} = 1 - \frac{\nu_y(0,\tau)}{\nu_x(j,\tau)}, \quad \left.\frac{d\beta}{d\alpha}\right|_{\alpha=\pi/2} = 1 - \frac{\nu_x(0,\tau)}{\nu_y(j,\tau)}. \quad (2)$$

As we see from Eq. (2), the formulas for the derivative $d\beta/d\alpha$ in the Y and X geometries are mutually symmetric with respect to permutation of the indices of the function ν, and in both geometries $d\beta/d\alpha$ depends on both the current and temperature. For $j \to 0$ the value and sign of the derivative in both geometries depends on the ratio $\nu_x(0,\tau)/\nu_y(0,\tau)$. For $\tau=0$ we have $(d\beta/d\alpha)|_{\alpha=0} = (d\beta/d\alpha)|_{\alpha=\pi/2} = 1$. Under the conditions $j \to \infty$ and/or $\tau \to \infty$, corresponding to the isotropic regime of free flux flow (the FF regime), when the influence of both systems of pinning centers on the pinning can be neglected, $d\beta/d\alpha = 0$, as might have been expected, since in this regime the angle $\beta = \pi/2$ and is independent of the direction of the current relative to the pinning center.

The evolution of the vortex dynamics with changes in current and temperature can be represented most transparently with the aid of a diagram of the dynamical states on the
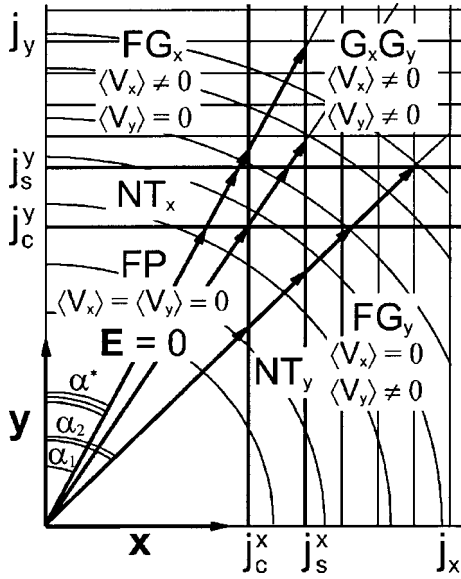
FIG. 1. Diagram of the dynamical states of the vortex system (the Hall effect is neglected) on the plane (j_x,j_y); here j_c^x, j_s^x and j_c^y, j_s^y are the principal critical currents and saturation currents along the vectors $\mathbf{x}$ and $\mathbf{y}$ of the pinning anisotropy, FP is the full pinning region, NT_x is the region of the nonlinear transition between the linear TAFF and FF regimes of vortex motion in the direction of the vector $\mathbf{x}$ (conditional on the pinning by a system of pinning centers parallel to the $0y$ axis), NT_y is the region of the nonlinear transition in the direction of the vector $\mathbf{y}$ (conditional on the pinning by a system of pinning centers parallel to the $0x$ axis), FG_x is the region of guided motion of the vortices along the $0x$ axis, FG_y is the region of guided motion of the vortices along the $0y$ axis, G_xG_y is the region of free flux flow. The circular arcs 1–7 described by the end of the vector $\mathbf{j}$ on the diagram of dynamical states correspond qualitatively to the characteristic of curves 1–7 of the function $\rho(\alpha)$ in Fig. 10, thus explaining their features.

$(j_x,\ j_y)$ plane (see Fig. 1). The first quadrant of the plane of this figure is divided by the lines $j_x=j_c^x$, $j_y=j_c^y$ and $j_x=j_s^x$, $j_y=j_s^y$ into several regions, corresponding to all of the different possible dynamical states of the vortex system in this model. The end of the vector $\mathbf{j}$, which has coordinates $j\sin\alpha$, $j\cos\alpha$, falls in one of these regions, depending on the values of j and α. We denote by α^* ($\tan\alpha^*=j_c^x/j_c^y$) the critical angle formed by the ray passing through the origin and the point of intersection of the lines $j_x=j_c^x$ and $j_y=j_c^y$. In Fig. 1 the region FP corresponds to the full-pinning (FP) regime, since here $j_x<j_c^x$, $j_y<j_c^y$ and TAFF vortex dynamics is realized in respect to both systems of pinning centers. The region NT_x (NT stands for nonlinear transition) corresponds to the regime of nonlinear transition between the linear TAFF and FF regimes of vortex motion in the direction of the vector $\mathbf{x}$ (this nonlinear transition regime is conditional on the pinning by the system of pinning centers parallel to the $0y$ axis); here $j_c^y<j_y<j_s^y$ $[j_c^y(\alpha)<j<j_s^y(\alpha)]$. The analogous region NT_y corresponds to the regime of nonlinear transition in the direction of the vector $\mathbf{y}$ (conditional on the pinning by the system of pinning centers parallel to the $0x$ axis); here $j_c^x<j_x<j_s^x$ $[j_c^x(\alpha)<j<j_s^x(\alpha)]$. The region FG_x, which is shaded by horizontal lines, corresponds to the regime of guided motion of the vortices along the pinning centers parallel to the $0x$ axis (the FG_x regime), $\langle\mathbf{v}\rangle_{FG_x}\|\mathbf{x}$; here $j_x<j_c^x$, $j_y>j_s^y$ $[j_s^y(\alpha)<j<j_c^x(\alpha)]$. The region FG_y, which is shaded by vertical lines, corresponds to the regime of guided motion of the vortices along the pinning centers par-

allel to the $0y$ axis (the FG_y regime), $\langle\mathbf{v}\rangle_{FG_y}\|\mathbf{y}$; here $j_x>j_s^x$, $j_y<j_c^y$ $[j_s^x(\alpha)<j<j_c^y(\alpha)]$. Finally, the region G_xG_y, shaded by both horizontal and vertical lines, corresponds to the regime of free magnetic flux flow with respect to both systems of pinning centers, and, consequently, to an isotropic resistive response (the G_xG_y regime); $\langle\mathbf{v}\rangle_{G_xG_y}\|\mathbf{F}_L$; here $j_x>j_s^x$, $j_y>j_s^y$ $[j>j_s^x(\alpha),\ j>j_s^y(\alpha)]$.

Using Fig. 1, it is easy to trace the sequence of dynamical regimes through which a vortex system passes as the current is increased at a fixed temperature and fixed angle α. We note that an additional source of dissipation arises at the boundary of the regions corresponding to the linear (FP, FG_x, FG_y, G_xG_y) and nonlinear (NT_x, NT_y) regimes of vortex dynamics, giving rise to kinks on the observed current dependence of $\rho_\|$ and $\rho_\perp$ at values of the current density $j_c^x(\alpha)$, $j_c^y(\alpha)$, $j_s^x(\alpha)$, and $j_s^y(\alpha)$. In the general case the maximum number of such kinks on the $\rho_\|(j)$ and $\rho_\perp(j)$ curves is equal to four, and the minimum number is two (e.g., in the cases $\alpha=0$ and $\alpha=\pi/2$). The number of kinks is determined by the angle α; it decreases if the line of the current density vector passes through points of intersection of the boundary lines of the regions.

Let us turn our attention to particular limiting cases $j_c^x(p,\varepsilon_x,\tau)\ll j_c^y(p,\varepsilon_y,\tau)$ and $j_c^x(p,\varepsilon_x,\tau)\gg j_c^y(p,\varepsilon_y,\tau)$, for which the bianisotropic character of the pinning reduces to a uniaxial anisotropic one over a wide range of current densities and angles α.[4] In fact, for $j_c^x\ll j_c^y$ in the interval $j_c^x/\sin\alpha<j<j_c^y/\cos\alpha$ the pinning is weakened in the direction of the $0y$ axis in the presence of strong pinning along the $0x$ axis, and for $j_c^y\ll j_c^x$ in the interval $j_c^y/\cos\alpha<j<j_c^x/\sin\alpha$ the pinning in the direction of the $0x$ axis is weakened in the presence of strong pinning along the $0y$ axis, i.e., in these cases the pinning is effective for only one of the mutually orthogonal systems of pinning centers in the corresponding intervals of current density and angle α, while pinning on the other system of pinning centers is absent. A simple example of such a situation is the case $p\gg1$ (or the opposite, $p\ll1$) at zero temperature, when $j_c^x=p^{-1}\ll j_c^y=p$ $(j_c^x\gg j_c^y)$, respectively).

The dynamical state of the system can be described directly using formula (1). The guiding regimes will exist in the limiting cases when the function $R=\nu_x/\nu_y$ or $R^{-1}=\nu_y/\nu_x$ can be treated as a small parameter. The limit of the function R for $j\to0$, if the terms proportional to positive integer powers of the parameter τ are neglected, has the form

$$R_0=\exp[(1-p^2)p^{-1}\tau^{-1}]p^2k^2[(1-\varepsilon k)/(1-\varepsilon/k)] \quad (3)$$

for $\tau\ll p,\ p^{-1},\ (k/\varepsilon-1),\ [(k\varepsilon)^{-1}-1]$. Formula (3) describes a weak (in respect to the magnitude of the resultant velocity) G effect which arises on account of the competition between the vortex velocity components perpendicular to the both sets of pinning centers; these velocity components are associated with the TAFF dynamics at low temperatures and currents (FP region). It is easy to see that $\cot\beta\approx\cot\alpha$ ($\beta\approx\alpha$) for $R_0\ll1$, $\tan^2\alpha$ and $\cot\beta\approx-\tan\alpha$ ($\beta\approx\pi/2+\alpha$) for $R_0^{-1}\ll1$, $\cot^2\alpha$ (with accuracy to R_0 and R_0^{-1}, respectively). It follows from formula (3) that a decisive role in determining which of these cases is realized is played by the value of the parameter p in comparison with unity, as that determines the sign of the argument of the exponential function. The
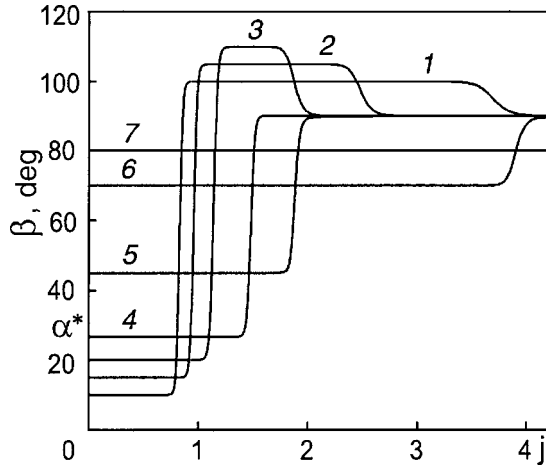
FIG. 2. Dependence of $\beta(j)$ for different values of the angle α [deg]: 10 (*1*), 15 (*2*), 20 (*3*), 27 (*4*), 45 (*5*), 70 (*6*), and 80 (*7*) for $p=1.4$, $\tau=0.01$, $\varepsilon=0.001$, $k=1$; $\alpha^*=27°$.

FIG. 3. Curves of $\beta(\tau)$ for different values of the angle α [deg]:10 (*1*), 20 (*2*), 30 (*3*), 45 (*4*), 60 (*5*), 70 (*6*), and 80 (*7*) for $p=1.4$, $j=1.2$, $\varepsilon=0.001$, $k=1$; $\alpha^*=27°$.

condition $p>1$ corresponds to the case $\beta\approx\alpha$, and the condition $p<1$ to the case $\beta\approx\pi/2+\alpha$ (the function R_0 is proportional to the factor $\exp(\pm c)$ for $|1-p|\approx c\tau$, where the value of c must be determined by the condition $R_0\ll1$ or $R_0^{-1}\ll1$ for realization of the G effect). The physical reason for realization of one of these cases is the unequal depths of the potential wells U_{x0} and U_{y0}: it is energetically favorable for the vortices to localize in the potential wells with the greater depth and to move along them under the influence of an external force, overcoming the potential barriers of the wells with the smaller depth. In the case $p=1$ for $j\to0$ we have $\nu_x\equiv\nu_y$, from which we get $\cot\beta\equiv0$ and, hence, with increasing current density the angle β changes from the value $\beta(j=0)\equiv\pi/2$, independently of the angle α.

The G effect is strongly expressed when FF vortex dynamics is realized along one of the anisotropy directions of the system while TAFF dynamics is realized along the other. This occurs under the conditions $\nu_x\simeq1$, $\nu_y\ll1$, which give $R^{-1}\ll1$, $\beta\approx\pi/2+\alpha$, which corresponds to the FG$_x$ regime (the region $j_x<j_c^x$, $j_y>j_s^y$), and under the conditions $\nu_x\ll1$, $\nu_y\simeq1$, which give $R\ll1$, $\beta\approx\alpha$, corresponding to the FG$_y$ regime (the region $j_x>j_s^x$, $j_y<j_c^y$). If the FF dynamics is realized along both anisotropy directions, i.e., $\nu_x\simeq1$, $\nu_y\simeq1$, then $\cot\beta\approx0$, $\beta\approx\pi/2$ ($\beta\to\pi/2$ in the limit $j\to\infty$), and a practically isotropic regime in the region G$_x$G$_y$ is realized ($j_x>j_s^x$, $j_y>j_s^y$).

The vortex dynamics nonlinear in the current and temperature is illustrated in Figs. 2 and 3, which show the functions $\beta(j)$ and $\beta(\tau)$ for a number of values of the angle α [we note that the critical angle is related to the parameter p by the relation $\alpha^*\approx\arctan(p^{-2})$]. As we see from the $\beta(j)$ curves, the arrangement of the linear regimes (where $\beta\approx$const), the values of the angle β in them, and the values of the critical currents and saturation currents correspond to our above analysis of the diagram of the dynamical states. Indeed, the current intervals corresponding to the FP regime ($j<j_c^y(\alpha)$ for $\alpha<\alpha^*$ and $j<j_c^x(\alpha)$ at $\alpha>\alpha^*$) are wider for values of α which are closer to α^*. The current intervals corresponding to the strong G effect, i.e., the FG$_x$ regime ($j_s^y(\alpha)<j<j_c^x(\alpha)$) and the FG$_y$ regime ($j_s^x(\alpha)<j<j_c^y(\alpha)$) are wider for values of α which are farther from α^* (for α
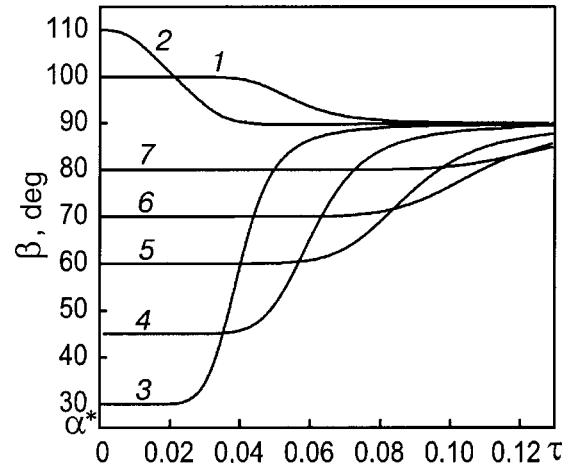
$=\alpha^*$ there are no G-effect regions; the transition from the FP regime occurs directly to the regions of the nonlinear NT$_x$ and NT$_y$ regimes). Let us consider the interval of values of the angle β corresponding to intervals of current density in which transitions nonlinear in the current occur between linear regimes of vortex dynamics (the "amplitudes" of the nonlinear transitions for angle β). It can be shown that in the case $p>1$ (see Fig. 2) the amplitudes of the nonlinear transitions for angle β (denoted $\Delta\beta$ with subscripts indicating the corresponding pairs of regimes linear in the current, between which the particular nonlinear transition occurs) have the values: $\Delta\beta_{FP\to FG_x}=\pi/2$, $\Delta\beta_{FG_x\to G_xG_y}=\alpha$ for $\alpha<\alpha^*$ (see curves *1*, *2*, and *3* in Fig. 2) and $\Delta\beta_{FP\to FG_y}=0$, $\Delta\beta_{FG_y\to G_xG_y}=\pi/2-\alpha$ and $\alpha>\alpha^*$ (see curves *5*, *6*, and *7*; on curve *7* the transition FG$_y\to$G$_x$G$_y$ is not reflected, since it occurs at values of j that fall outside the field of the figure). Analogously, in the case $p<1$ the amplitudes of the nonlinear transitions for the angle β have the values: $\Delta\beta_{FP\to FG_x}=0$, $\Delta\beta_{FG_x\to G_xG_y}=\alpha$ for $\alpha<\alpha^*$ and $\Delta\beta_{FP\to FG_x}=\pi/2$, $\Delta\beta_{FG_x\to G_xG_y}=\pi/2-\alpha$ for $\alpha>\alpha^*$. In the case $p=1$, $\lim_{j\to0}\beta$ $=\pi/2$ the vortices are localized on that system of pinning centers which makes an acute angle with the Lorentz force. If $\alpha=45°$, then $\beta\equiv90°$, even though, generally speaking, this state is unstable with respect to the angle α.

The diagram of dynamical states can also be used for analysis of the temperature dependence of β at a fixed current density in the temperature region where the concept of critical currents and saturation currents have physical meaning [taking into account that the parameters depending implicitly on τ vary weakly in those temperature intervals which correspond to singularities of the function $\nu(\tau)$; Ref. 4]. With increasing temperature the probability that the vortices will break away from the pinning centers (depinning) under the influence of the thermal fluctuations increases, and at a certain temperature the the pinning of vortices at pinning centers can be neglected. The vortex depinning temperature $T_{dep}(j,\alpha,p,\varepsilon,k)$ is most simply defined as the value at which the dynamics of the vortex system passes into the FF regime at the given parameters j, α, p, ε, and k. Then the condition

of applicability of the diagram of dynamical states for the temperature dependences of the observed quantities has the form $T \ll T_{\text{dep}}$. It can be said that as the temperature increases, the values of the critical currents decrease and the values of the saturation currents increase until these concepts become undefined. This change in the critical currents and saturation currents leads a deformation of the dynamical regions on the diagram of states, and that makes it possible to describe the influence of temperature on these quantities in a transparent way. The functions $\beta(\tau)$ in Fig. 3 for a number of angles α correspond to the case $p > 1$, $k = 1$ and $j_s^x < j < j_c^y$. With the help of the diagram (see Fig. 1) it is easy to understand why it is that for curves *1* and *2* in Fig. 3 one has $\beta(\tau = 0) = \pi/2 + \alpha$, which corresponds to the FP regime of vortex dynamics (region FP on the diagram), while for the remaining curves $\beta(\tau = 0) \equiv \alpha$, which corresponds to the FG$_y$ regime (region FG$_y$ on the diagram). We see that rotation of the current vector alters the dynamical state of the system at zero temperature. It should be emphasized that at zero temperature the dynamical regime at fixed j and α is essentially determined by the value of j in relation to the critical and saturation current densities; this, in turn, determines the characteristic form of the $\beta(\tau)$ curves. With increasing temperature (at $T \sim T_{\text{dep}}$) the vortex system passes nonlinearly into the isotropic regime ($\lim_{\tau \to \infty} \beta \equiv \pi/2$).

Let us examine the experimental dependence obtained in Ref. 5 for $\theta_E(\alpha)$, where θ_E is the angle between the $0y$ axis and the electric field vector **E** measured at fixed values of the current density and temperature. Taking into account that in the xy coordinate system the magnetoresistivity components are $\rho_x = \rho_{xx} \sin \alpha = \nu_y \sin \alpha$, $\rho_y = \rho_{yy} \cos \alpha = \nu_x \cos \alpha$, we obtain the following simple relation: $\tan \theta_E(\alpha) = \rho_x/\rho_y = (\nu_y/\nu_x) \tan \alpha$, or

$$\theta_E(\alpha) = \arctan(R^{-1} \tan \alpha). \tag{4}$$

It follows from (4) that the period of the function $\theta_E(\alpha)$ is equal to $\pi/2$. If A is the argument of the arctangent function in formula (4), then $\theta_E \approx A$ for $A \ll 1$, while $\theta_E \approx \pi/2 - A^{-1}$ for $A \gg 1$. One more important limiting case is realized in the case $\nu_y/\nu_x \approx 1$, which always holds when the pinning has become isotropic. Indeed, by using an expansion of the functions ν_x and ν_y in powers of $1/j$, we find that in the case $j \gg \max[p/\cos \alpha, \, 1/(p \sin \alpha)]$ we have $\nu_y/\nu_x \approx 1$ to an accuracy of $\max[\varepsilon k/(p \sin \alpha j)^2, \, (\varepsilon/k)(p/\cos \alpha j)^2]$. Then in the region of angles α restricted by the conditions $\cos \alpha \gg p/j$, $\sin \alpha \gg 1/(pj)$, we have the relation $\tan \theta_E \approx \tan \alpha$ to the same accuracy.

Figure 4 shows curves of the function $\theta_E(\alpha)$ for a series of values of the current density j. We see that the $\theta_E(\alpha)$ curves have characteristic limiting segments $\theta_E \approx 0$, $\theta_E \approx \pi/2$ and $\theta_E \approx \alpha$, situated in accordance with the indicated conditions for the angle α as a function of j and p and connected by nonlinear transition segments. The velocity vector of the vortex system is directed perpendicular to the electric field vector, and this implies that the segments $\theta_E \approx 0$ and $\theta_E \approx \pi/2$ of the curves correspond to the FG$_x$ and FG$_y$ regimes of guided motion of the vortices. The intermediate segment $\theta_E \approx \alpha$ (if present) corresponds to isotropization of the system (the G$_x$G$_y$ regime) due to suppression of the potential barriers of the pinning planes. In an analogous
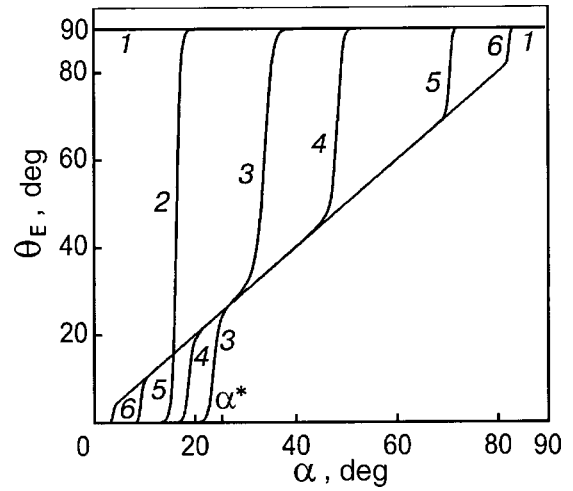

FIG. 4. Curves of $\theta_E(\alpha)$ for different values of the parameter j: 0.5 (*1*), 1 (*2*), 1.6 (*3*), 2 (*4*), 4 (*5*), and 10 (*6*) for $p = 1.4$, $\tau = 0.01$, $\varepsilon = 0.001$, $k = 1$; $\alpha^* = 27°$.

way one can analyze the series of curves of the function $\theta_E(\alpha)$ for a number of different values of the parameter τ. For example, the series of curves for the set of parameters $p = 1.4$, $\varepsilon = 0.001$, $k = 1$, $j = 0.1$ and a number of values of τ (0.05, 0.1, 0.12, 0.14, 0.17, 0.3) is a set of monotonically increasing, convex-upward curves, the degree of convexity of which decreases with increasing τ. At the minimum value of τ we have $\theta_E(\alpha) \approx \pi/2$, which corresponds to the FG$_y$ regime. At the maximum value of τ we have $\theta_E(\alpha) \approx \alpha$, i.e., a complete isotropization of the system occurs on account of the effect of thermal fluctuations on the vortices. Thus the function $\theta_E(\alpha)$ can be used to clearly track the change in the regimes of vortex dynamics as a function of the angle α with the other parameters fixed, and its behavior corresponds completely to the general description of the dynamics of a vortex system on the basis of the diagram of dynamical states.

Let us consider the behavior of the observed magnetoresistivities $\rho_\parallel$ and $\rho_\perp$. The final analytical formulas for them in the given bianisotropic pinning potential (formula (19) of
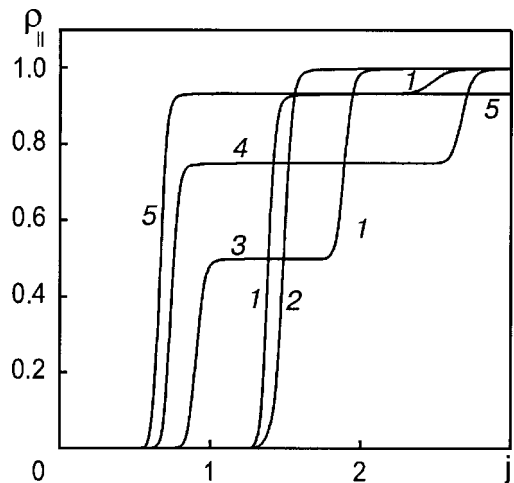

FIG. 5. Curves of $\rho_\parallel(j)$ for different values of the angle α [deg]: 15 (*1*), 27 (*2*), 45 (*3*), 60 (*4*), and 75 (*5*) for $p = 1.4$, $\tau = 0.01$, $\varepsilon = 0.001$, $k = 1$; $\alpha^* = 27°$.
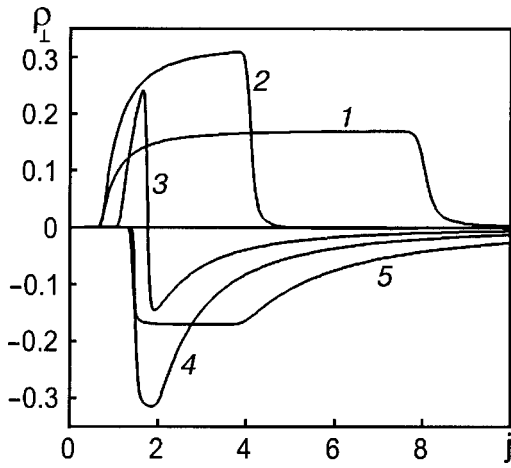
FIG. 6. Curves of $\rho_\perp(j)$ for different values of the angle α [deg]: 10 (*1*), 20 (*2*), 53 (*3*), 70 (*4*), and 80 (*5*) for $p=0.7$, $\tau=0.01$, $\varepsilon=0.1$, $k=0.1$; $\alpha^* =64°$.
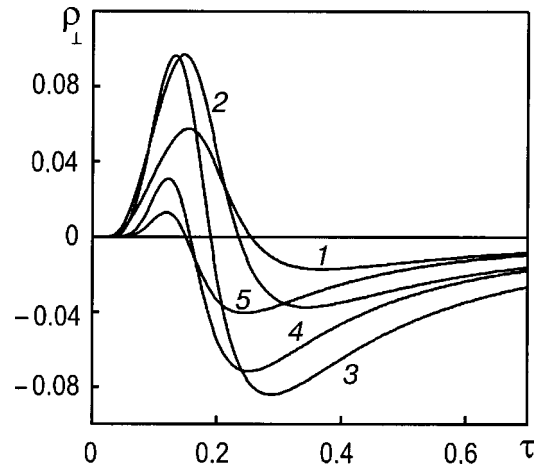

FIG. 8. Curves of $\rho_\perp(\tau)$ for different values of the angle α [deg]: 10 (*1*), 20 (*2*), 45 (*3*), 70 (*4*), and 80 (*5*) for $p=0.65$, $j=0.4$, $\varepsilon=0.1$, $k=0.1$; $\alpha^* =67°$.

Ref. 1) are obtained by substituting the values of the functions $\nu_{x,y}$ calculated according to formula (20) of Ref. 1 into formula (18) of that paper. On the basis of the investigated properties of the functions $\nu_{x,y}$ and the features of the vortex dynamics, it is straightforward to explain the resistivity curves $\rho_{\|,\perp}(j)$ and $\rho_{\|,\perp}(\tau)$. The linear limit in formulas (18) of Ref. 1 is realized in that region of currents and temperatures which corresponds to the TAFF and FF regimes, while the region of nonlinearity of the current and temperature dependences of $\rho_{\|,\perp}$ is that interval of j and τ in which at least one of the functions $\nu_x(j)$, $\nu_y(j)$ and $\nu_x(\tau)$, $\nu_y(\tau)$, respectively, is nonlinear. Figures 5–8 illustrate the current and temperature dependences of the magnetoresistivities $\rho_{\|,\perp}$ for a number of fixed values of the parameters τ, j, p, and the angle α. These curves clearly reveal the above-discussed nonlinear current and temperature dynamics of the vortices in a system with bianisotropic pinning. The limiting linear parts of these curves at low currents and temperatures correspond to the FP regime, while at high currents and/or temperatures, to the $G_x G_y$ regime. The intermediate parts that are linear in the current or temperature correspond to one of the

FG$_x$ or FG$_y$ regimes. The values of the magnetoresistivities $\rho_\|$ and $\rho_\perp$ in these linear regimes are easily obtained using formulas (18) of Ref. 1, since the limiting values of the functions ν_x and ν_y are known. The parts corresponding to the nonlinear transitions with respect to current in the functions $\rho_\|(j)$ and $\rho_\|(j)$ (see Figs. 5 and 6) are easily established from the values of the critical and saturation current densities (for known values of the parameters p, τ, ε, and k, which determine those currents) on the diagram of dynamical states. The transition to the nonlinear regime on the temperature dependences of $\rho_\|$ and $\rho_\perp$ (see Figs. 7 and 8) is due to the temperature-induced depinning of vortices under the influence of thermal fluctuations. For $T \gtrsim T_{\text{dep}}$ the temperature-induced depinning leads to isotropization of the system as a result of the establishment of the FF regime of vortex dynamics. We stress that the characteristic form of the curves of the temperature dependence of $\rho_\|$ and $\rho_\perp$ is essentially determined by the value of j in relation to the set of critical and saturation current densities at fixed angle α. In Fig. 7 for $\rho_\|(\tau)$, the value of the current density $j < j_c^x(\alpha)$, $j_c^y(\alpha)$, $j_s^x(\alpha)$, $j_s^y(\alpha)$ for all values of the angle α, and $\rho_\|(\tau=0) =0$, since at zero temperature the vortex system is found in the FP regime. Let us vary the value of j while leaving the rest of the parameters the same, and consider the case $j_s^x < j=1.2 < j_c^y$ (then we obtain the set of parameters used in Fig. 3 for the function $\beta(\tau)$). This will lead to a qualitative change of the function $\rho_\|(\tau)$, starting at some angle α. In fact, for $\alpha > \alpha^*$ and a given value of j the end of the vector **j** falls in the FG$_y$ region on the diagram (see Fig. 1), and it is easily shown that that will lead to the appearance of linear segments on the $\rho_\|(\tau)$ curves, the temperature width of which and the value of the resistivity of which grow with increasing angle α. In an analogous way one can analyze the features of the temperature dependence of $\rho_\perp$ in Figs. 8 and 9. The curves in Fig. 8 are nonmonotonic and have two maxima, which are opposite in the sign of the function $\rho_\perp(\tau)$ and which go to zero at some values of τ. The limit $\rho_\perp(\tau =0)=0$ for all curves is due to the fact that the FP regime is realized at zero temperature for the given value of the current at any angle α. The limit $\rho_\perp \to 0$ at $\tau \to \infty$ is reached in general regardless of the values of the fixed parameters and is
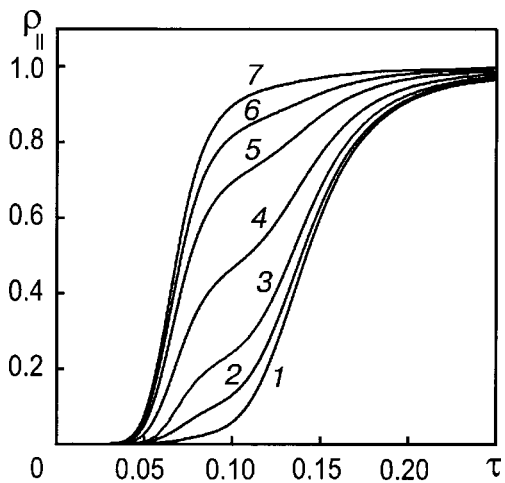

FIG. 7. Dependence of $\rho_\|(\tau)$ for different values of the angle α [deg]: 10 (*1*), 20 (*2*), 30 (*3*), 45 (*4*), 60 (*5*), and 70 (*6*) for $p=1.4$, $j=0.1$, $\varepsilon =0.001$, $k=1$; $\alpha^*=27°$.
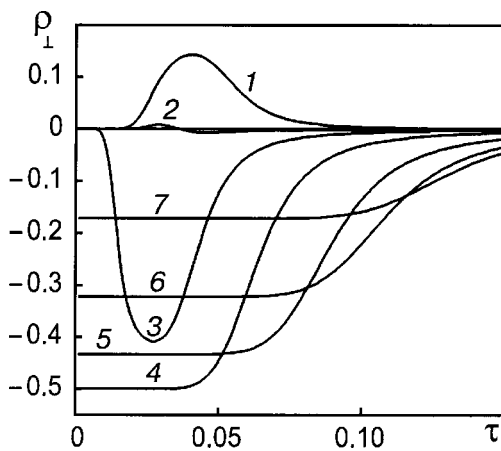
FIG. 9. Curves of $\rho_\perp(\tau)$ for different values of the angle α [deg]: 10 (*1*), 20 (*2*), 30 (*3*), 45 (*4*), 60 (*5*), 70 (*6*), and 80 (*7*) for $p=1.4$, $j=1.2$, $\varepsilon=0.001$, $k=1$; $\alpha^*=27°$.

explained physically by the coincidence of the directions of the velocity vector of the vortex system and the Lorentz force vector upon the establishment of the FF regime on account of temperature-induced depinning of the vortices. Figure 9 shows some different types of functions $\rho_\perp(\tau)$, the difference being due to the fact that the dynamical state corresponding to zero temperature changes as the angle α changes. Curves *1* and *3* are bell-shaped curves with maxima of different sign, curve *2*, intermediate between them, has a form like the curves in Fig. 8, and curves *4–7* are monotonically increasing and have linear segments whose width in temperature increases and whose absolute value (the magnetoresistance $\rho_\perp$ is negative for them) decreases with increasing angle α.

Let us pay particular attention to the fact that the magnetoresistance $\rho_\parallel$ is a monotonic function of the current and temperature. It is seen from formula (18) of Ref. 1 that the monotonically increasing functions ν_x and ν_y appear with the same sign in the expression for the longitudinal magnetoresistance. In contrast, the functions ν_x and ν_y appear in the magnetoresistance $\rho_\perp$ in the form of a difference, and therefore the curves of $\rho_\perp$ as a function of current and temperature can change sign at certain values of the corresponding fixed parameters (see Figs. 6, 8, and 9). Physically this is due to the change in sign of the vortex velocity component parallel to the current density vector as a result of a competition of G effects related to each of the systems of parallel pinning centers and the predominance of one of the regimes FG_x or FG_y in certain intervals of values of the current density and temperature.

We also make note of the circumstance that the substitutions $p \rightarrow 1/p$ and $k \rightarrow 1/k$ reduce to a coordinate transformation and, accordingly, to the appearance of symmetry of the functions under study for complementary angles. For example, for values reciprocal to p or k and at the complementary angles, the functions $\beta(j)$ and $\beta(\tau)$ are symmetric with respect to the line $\beta=90°$, the $\theta_E(\alpha)$ curves are centrosymmetric about the point $(45°, 45°)$, the functions $\rho_\perp(j)$ and $\rho_\parallel(\tau)$ are symmetric about the line $\rho_\perp=0$, and the curves of $\rho_\parallel(j)$ and $\rho_\parallel(\tau)$ coincide. The cases $p=1$ and $k=1$ are de-

generate and give the indicated forms of symmetry for the corresponding angles.

2. RESISTIVE RESPONSE IN A ROTATING CURRENT SCHEME

An experimental study of the vortex dynamics in $YBa_2Cu_3O_{7-\delta}$ crystals with unidirectional twin planes was recently done using a modified rotating current scheme in Refs. 5 and 6. In that scheme it was possible to pass current in an arbitrary direction in the *ab* plane of the sample by means of four pairs of contacts placed in the plane of the sample. Two pairs of contacts were placed as in the conventional four-contact scheme, and the other two pairs were rotated by 90° with respect to the first (see the illustration in Fig. 1 of Ref. 5). By using two current sources connected to the outer pair of contacts, one can continuously vary the direction of the current transport in the sample. By simultaneously measuring the voltage in the two directions, one can determine directly the direction and magnitude of the average velocity vector of the vortices in the sample as a function of the direction and magnitude of the transport current density vector. This made it possible to obtain the angular dependence of the resistive response on the direction of the current with respect to the pinning planes on the same sample. The experimental data of Refs. 5 and 6 attest to the anisotropy of the vortex dynamics in a certain temperature interval which depends on the value of the magnetic field. In Ref. 5 a rotating current scheme was used to measure the polar diagrams of the total magnetoresistivity $\rho(\alpha)$, where $\rho=(\rho_x^2+\rho_y^2)^{1/2}$ is the absolute value of the magnetoresistivity, ρ_x and ρ_y are the x and y components of the magnetoresistivity in an xy coordinate system, and α is the angle between the current direction and the $0y$ axis (parallel to one of the systems of pinning centers). In the case of a linear anisotropic response the polar diagram of the resistivity is an ellipse, as can easily be explained. In the case of a nonlinear resistive response the polar diagram of the resistivity is no longer an ellipse and has no simple interpretation.

In this Section we carry out a theoretical analysis of the polar diagrams of the magnetoresistivity ρ in the general nonlinear case in the framework of a stochastic model of bianisotropic pinning. This type of angular dependence $\rho(\alpha)$ is informative and convenient for theoretical analysis. For a sample with specific internal characteristics of the pinning (such as p, ε, and k) at a given temperature and current density the function $\rho(\alpha)$ is contained by the resistive response of the system in the entire region of angles α and makes it possible to compare the resistive response for any direction of the current with respect to the system of mutually orthogonal planar pinning centers. In addition, in view of the symmetric character of the $\rho(\alpha)$ curves, their measurement makes it possible to establish the spatial orientation of the system of planar pinning centers with respect to the boundaries of the sample if this information is not known beforehand.

As in the previous cases, the main features of the $\rho(\alpha)$ curves in the investigated stochastic model of bianisotropic pinning can be understood with the aid of the diagrams of dynamical states of the vortex system (see Fig. 1). Now for analysis of the $\rho(\alpha)$ curves we imagine that the vector **j** is
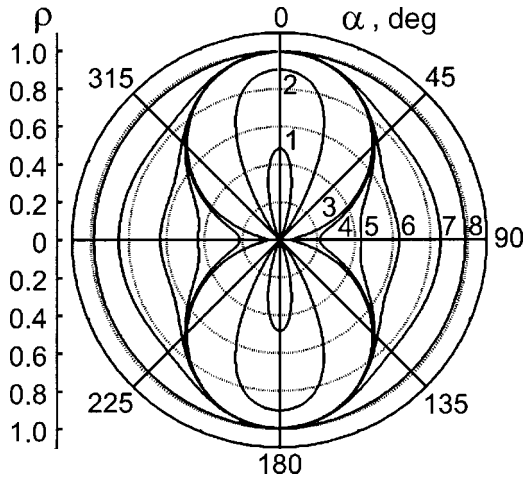
FIG. 10. Series of graphs of the function $\rho(\alpha)$ for a sequence of values of the parameter j: 0.66 (*1*), 1 (*2*), 1.34 (*3*), 1.43 (*4*), 1.48 (*5*), 1.7 (*6*), 2 (*7*), 3 (*8*) for $p=1.4$, $\tau=0.01$, $\varepsilon=0.001$, $k=1$; $\alpha^*=27°$.
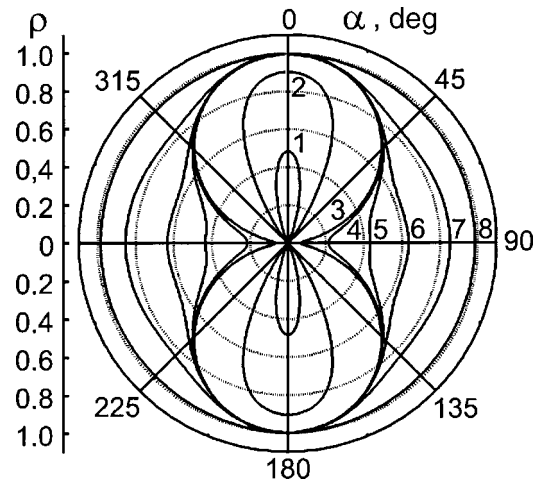
FIG. 11. Series of graphs of the function $\rho(\alpha)$ for a sequence of values of the parameter τ: 0.013 (*1*), 0.02 (*2*), 0.07 (*3*), 0.08 (*4*), 0.09 (*5*), 0.1 (*6*), 0.12 (*7*), 0.2 (*8*) for $p=0.7$, $j=0.6$, $\varepsilon=0.001$, $k=1$; $\alpha^*=64°$.

rotated continuously from an angle $\alpha=\pi/2$ to $\alpha=0$. Here the end of the vector **j**, which falls in some one region of the diagram, indicates the corresponding dynamical state. The characteristic form of the $\rho(\alpha)$ curves will obviously be determined by the sequence of dynamical regimes through which the vortex system passes as the current vector is rotated. By virtue of the symmetry of the problem, the $\rho(\alpha)$ curves can be obtained in all regions of angles α from the parts in the first quadrant.

We recall that in respect to the two systems of pinning centers it is possible to have the linear TAFF and FF regimes of vortex dynamics and regimes of nonlinear transitions between them. The regions of nonlinear transitions are determined by the corresponding values of the pairs of critical and saturation current densities. The regime of vortex dynamics at a given angle α and current density j is determined by the value of j in relation to a sequence of values of the current density (see Fig. 1):

$$j_c^y(\alpha)<j_s^y(\alpha)<j_c^x(\alpha)<j_s^x(\alpha) \quad \text{for} \quad \alpha<\alpha^*,$$

$$j_c^x(\alpha)<j_s^x(\alpha)<j_c^y(\alpha)<j_s^y(\alpha) \quad \text{for} \quad \alpha>\alpha^*.$$

The whole diversity of $\rho(\alpha)$ curves at fixed parameters τ, p, ε, and k is due to the influence of the set of values of these parameters on the values j_c^x, j_s^x, j_c^y, and j_s^y, which shape the diagram of dynamical states, and also the value of the current density j, which determines the sequence of states of the vortex system on the diagram as the current is rotated.

Let us consider the characteristic curves of $\rho(\alpha)$. Figures 10 and 11 show plots of $\rho(\alpha)$ for series of values of the parameters j and τ, respectively. The transformation with changing values of the parameter j or τ is clearly seen. Let us analyze Fig. 10 in detail. Here we have considered the case $j_c^y/j_c^x=\cot\alpha\approx U_{pa}/U_{pb}=p^2\approx2\neq1$; $\varepsilon_x=\varepsilon_y=0.001$ and $\tau=0.01$, the principal critical currents and saturation currents satisfy the inequalities $j_c^x<j_s^x<j_c^y<j_s^y$. The qualitative form of the $\rho(\alpha)$ plots depends on where the values of the components of the current density vector **j** lie with respect to this sequence of currents. In Fig. 10, curves *1* and *2* of the function $\rho(\alpha)$ have the shape of a Figure 8 drawn out along

the $0x$ axis. When the angle α changes from $\pi/2$ to 0 the function $\rho(\alpha)$ falls off monotonically from $\rho(\pi/2)=\rho_x(\pi/2)=\nu_y(j,\tau,\varepsilon_y)$ to $\rho(0)=\rho_y(0)=\nu_x(j,\tau,\varepsilon_x)$ [on curve *1* $j_c^x<j<j_s^x$, $j<j_c^y$, and on curve *2* $j>j_s^x$, $j<j_c^y$]. On curve *3* a second Figure 8 appears, with its axis oriented perpendicular to that of the first (i.e., parallel to the $0y$ axis); here $j>j_s^x$, $j_c^y<j<j_s^y$. On this curve, in a small region of angles in the neighborhood of α^* between the large and small lobes, the end of the vector **j** falls in the FP region of the diagram of dynamical states ($j\sin\alpha<j_c^x$, $j\cos\alpha<j_c^y$). Curve *4* corresponds to the case when the free flux flow regime is realized both for **j**$\|0x$ and **j**$\|0y$, $j>j_s^x$, $j>j_s^y$ (as for the other curves). In addition, here the current density vector **j** does not fall in the FP region for any value of α ($j\sin\alpha>j_c^x$, $j\cos\alpha>j_c^y$). On curve *5* one can see the broadening of the lobes of the Figure 8, while the overall dependence remains qualitatively unchanged. On curve 6, bulges at which $\rho(\alpha)\approx1$ have appeared along the edges of the lobes of the vertical Figure 8. This is due to the fact that in the region of angles corresponding to these bulges the vortex dynamics goes to a saturation regime with respect to both systems of pinning centers ($j\sin\alpha>j_s^x$, $j\cos\alpha>j_s^y$), as in the region of angles α around the values $\alpha=0$, $\pi/2$. Further increase in the current density (see curves *7* and *8*) leads to a gradual smoothing of the nonmonotonicity of the $\rho(\alpha)$ curve and ultimately to complete isotropization of the resistive response on account of the complete suppression of pinning on the two systems of pinning centers. The diagram of dynamical states (Fig. 1) shows circular arcs described by the end of the vector **j** (curves *1–7*). They show the possible sequences of dynamical regimes of the vortex system as the current density vector is rotated, and they are in qualitative correspondence with the characteristic curves *1–7* of the function $\rho(\alpha)$ in Fig. 10 and explain the features of those curves.

In an analogous way one can analyze the $\rho(\alpha)$ curves for the case when the inequality of the principal critical currents and saturation currents is due to a difference in the concentrations of the mutually orthogonal pinning centers ($k\neq1$) with equal depths of their potential wells ($p=1$); the same can be done for the general case of arbitrary p, k, and

ε. The behavior of the curves in Fig. 11 reflects the temperature dynamics of the vortex system. At low temperatures, within the domain of definition of the concepts of critical and saturation currents, the form of the $\rho(\alpha)$ curves can be explained on the basis of the diagram of dynamical states (see Fig. 1). With increasing temperature there first occurs a gradual elongation of the curves, which have the form of a Figure 8 extended along the $0y$ axis, on account of a decrease in the values of the critical current densities and an increase in the values of the saturation currents. Then, when the temperature approaches the depinning temperature, there is a gradual smearing and transformation of the curves into circles, which is due to the isotropization of the pinning at high temperatures. The qualitative form of the curves in Fig. 11 depends substantially on the fixed value of the parameter j, since it determines the sequence of dynamical regimes on the state diagram as the current density vector is rotated (e.g., taking a value $j = 1.43$, we obtain a curve analogous to curve *4* in Fig. 10).

Thus in the framework of the bianisotropic pinning model, all of the characteristic features of the $\rho(\alpha)$ curves obtained in a rotating current scheme can be explained qualitatively and quantitatively on the basis of the diagram of dynamical states of the vortex system.

3. CONCLUSION

The experimental realization of the model studied here can be based on both naturally occurring[7] and artificially created[8] systems with bianisotropic pinning structures. In a number of limiting cases, the anisotropy of the pinning in those structures is equivalent to the anisotropy of certain perforated[9,10] and "meshlike" regular planar structures[11,12] and is also close to the real anisotropy of a new generation of long polycrystalline high-current ribbons of HTSC epitaxial films with low-angle grain boundaries, deposited on biaxially ordered grain-oriented metallic ribbon substrates by RABITS (rolling assisted biaxially aligned textured substrate) and other similar technologies (see the Materials of the IWCC-10, cited in Ref. 13).

The proposed model has made it possible for the first time (as far as we know) to give a consistent description of the anisotropic current- and temperature-induced depinning of vortices for an arbitrary direction relative to the anisotropy axes and to link it clearly with the motion of vortices along these axes. In the framework of this model one can successfully analyze theoretically certain observed resistive responses which are used for studying anisotropic pinning in a number of new experimental techniques[5,6] [the $\theta_E(\alpha)$ curve described by formula (4); the polar diagram of $\rho(\alpha)$]. Nonlinearity of the vortex dynamics with respect to current is due to the nonlinear character of the dependence of the values of the potential barriers of the pinning centers on the external force acting on the vortices; the nonlinearity of the vortex dynamics with respect to temperature, on the other hand, is due to nonlinear temperature dependence of the probability that a vortex will escape from the potential wells of the pinning centers. A quantitative description of the nonlinear resistive properties of the bianisotropic superconducting system under study is done in the framework of the stochastic model on the basis of the Fokker–Planck equations.

The main nonlinear components of the problem are the probability functions for the vortices to overcome the potential barriers corresponding to the systems of pinning centers, $\nu_{x,y}(j,\tau,\alpha,p,\varepsilon,k)$ (the arguments of which include both the "external" parameters j, τ, α and the "internal" parameters p, ε, k, which describe the intensity and anisotropy of the pinning). As can be seen from formula (18) of Ref. 1, the magnetoresistivities $\rho_{\|,\perp}(j,\tau)$ are linear combinations of the experimentally measured functions ν_x and ν_y in the XY geometries and, hence, they can easily be explained on the basis of the properties of the latter. In those cases when the bianisotropic pinning reduces to uniaxial anisotropic pinning, the corresponding functions $\rho_{\|,\perp}(j,\tau)$ can be found in Ref. 4.

The diagram of the dynamical states of the vortex system is a convenient and efficient tool for the qualitative understanding and quantitative analysis of the curves obtained. First, it clearly shows the origin of the anisotropy of the critical currents and saturation currents and their role in the vortex dynamics in the entire range of angles α. The influence of the "internal" parameters p, ε, k and the temperature (the parameter τ) on the observed dependence is easily explained qualitatively by considering their influence on the values of the current densities j_c^x, j_s^x, j_c^y, and j_s^y, which shape the state diagram. With increasing τ the basal critical current densities j_c^x and j_c^y decrease and the basal saturation current densities j_s^x and j_s^y increase, so that the FP region on the diagram narrows and the NT region widens. With increasing ε both pairs of basal current densities, j_c^x, j_c^y and j_s^x, j_s^y increase, since the functions ν_x and ν_y decrease monotonically with increasing ε; however, the growth of the second pair of current densities occurs considerably faster than the first, and, as a result, a widening of the NT regions and a less significant widening of the FP region occur. The parameters p and k describe the anisotropy of the bianisotropic pinning potential and determine the anisotropy of the critical and saturation current densities. It is easy to see that increasing the parameter p and/or decreasing the parameter k lead to a decrease in the values of the pairs of critical and saturation current densities j_c^x and j_s^x and to an increase in the values of the other pair j_c^y and j_s^y. Here the NT_x region is shifted upward, the NT_y region is shifted to the left, and the FP region accordingly becomes narrower and longer. Second, the state diagram can easily be used to establish the dynamical state of the vortex system in relation to the magnitude and direction of the transport current density (specified by the parameter j and angle α). Finally, it permits analysis of the evolution of the vortex dynamics upon a change in the magnitude or direction of the current vector.

The basic relationships analyzed in this paper—the observed magnetoresistivity $\rho_{\|,\perp}(j,\tau)$, the functions $\beta(j,\tau)$ and $\theta_E(\alpha)$ describing the nonlinear G effect, and the polar diagrams of the total magnetoresistivity $\rho(\alpha)$—give a clear idea of the role of anisotropy of the critical currents in the dynamics of the guided motion of vortices in the presence of bianisotropic pinning in the framework of the stochastic model investigated here.

*E-mail: Valerij.A.Shklovskij@univer.kharkov.ua

[1] V. A. Shklovskij and A. A. Soroka, Fiz. Nizk. Temp. **28**, 365 (2002) [Low Temp. Phys. **28**, 254 (2002)].

[2] V. A. Shklovskij, Fiz. Nizk. Temp. **23**, 1134 (1997) [Low Temp. Phys. **23**, 853 (1997)].

[3] V. V. Chabanenko, A. A. Prodan, V. A. Shklovskij, A. V. Bondarenko, M. A. Obolenskii, H. Szymczak, and S. Piechota, Physica C **314**, 133 (1999).

[4] V. A. Shklovskiĭ, A. A. Soroka, and A. K. Soroka, Zh. Éksp. Teor. Fiz. **116**, 2103 (1999) [JETP **89**, 1138 (1999)].

[5] H. Pastoriza, S. Candia, and G. Nieva, Phys. Rev. Lett. **83**, 1026 (1999).

[6] G. D'Anna, V. Berseth, L. Forro, A. Erb, and E. Walker, Phys. Rev. B **61**, 4215 (2000).

[7] J. Z. Wu and W. K. Chu, Phys. Rev. B **49**, 1381 (1994).

[8] G. Koren, E. Polturak, N. Levy, G. Deutscher, and N. D. Zakharov, Appl. Phys. Lett. **73**, 3763 (1998).

[9] A. Castellanos, R. Wordenweber, G. Ockenfuss, A. V. D. Hart, and K. Keck, Appl. Phys. Lett. **71**, 962 (1997).

[10] J.-Y. Lin, M. Gurvitch, S. K. Tolpygo, A. Bourdillon, S. Y. Hou, and Julia. M. Phillips, Phys. Rev. B **54**, 12717 (1996).

[11] M. J. Van Bael, K. Temst, V. V. Moshchalkov, and Y. Bruynseraede, Phys. Rev. B **59**, 14674 (1999).

[12] V. V. Moshchalkov, M. Baert, V. V. Metlushko, E. Rosseel, M. J. Van. Bael, K. Temst, and Y. Bruynseraede, Phys. Rev. B **57**, 3615 (1998).

[13] V. A. Shklovskij and A. A. Soroka, in *Proceedings of the 10th International Workshop on Critical Currents (IWCC-2001)*, June 4–7, 2001, edited by Ch. Jooss, Göttingen, Germany, p. 58.

Translated by Steve Torstveit

Galvanomagnetic effects in the normal state of high-T_c metal oxides in a model two-band superconductor with a narrow band (level) near the Fermi boundary

V. P. Galaĭko and E. N. Bratus'*

B. Verkin Institute for Low Temperature Physics and Engineering, National Academy of Sciences of Ukraine, pr. Lenina 47, 61103 Kharkov, Ukraine
(Submitted December 21, 2001)
Fiz. Nizk. Temp. **28**, 460–468 (May 2002)

The research of V. P. Galaiko, Fiz. Nizk. Temp. **19**, 123 (1993) [Low Temp. Phys. **19**, 87 (1993)] on electronic orbital effects in samples of a high-T_c superconductor (Y–Ba–Cu–O) in the normal state is continued for the case of dc galvanomagnetic effects. The conductivity tensor, resistivity, and Hall coefficient are calculated. The results agree qualitatively with experiment. © *2002 American Institute of Physics.* [DOI: 10.1063/1.1480238]

This article is a continuation of Ref. 1, which explored the various experimental consequences of a previously proposed model[2,3] in which a high-T_c superconductor (HTSC) is treated as a two-band superconductor with a narrow band (level) near the Fermi boundary. The essence of the model is that, owing to exchange of singlet pairs of electrons, Cooper pairing arises between the level and the wide band of immobile electrons, in which case the critical temperature T_c of the superconducting transition turns out to be only quadratically small in the coupling constant, in contrast to the BCS theory, in which it is exponentially small. In Ref. 1 it was additionally taken into account (over and above Refs. 2 and 3) that, owing to the characteristic "doping" of HTSC metal oxides (for purposes of achieving the maximum T_c; in the case of Y–Ba–Cu–O compounds this is doping with oxygen), HTSC systems should be treated as crystalline solutions of substitution. From the standpoint of electronic properties this means that they are "dirty" superconductors with a large number of impurity scattering centers.

In Ref. 1 the scattering on these "impurities" was taken into account phenomenologically, by introducing in the Hamiltonian of the electron system an interaction with randomly distributed impurities, the matrix elements of which described both intraband and interband transitions in scattering. In the model a suitable technique was developed for averaging the physical quantities over the random coordinates of the impurities, and various consequences of the model were examined. As in conventional superconductors, the influence of impurities on the thermodynamic characteristics of the system turn out to be small ("Anderson's theorem"), unlike the kinetic characteristics. As the most important characteristic, the electrical conductivity of an HTSC sample in the normal state was calculated as a function of temperature and frequency. It was found that, in spite of the crudity of the model, the results of the theory agree qualitatively with experiment[4] for characteristic frequencies of 10^5 s^{-1}. A detailed comparison of the theory with experiment was made in Ref. 5.

The main features of these results are: a) a linear temperature dependence of the resistivity at zero frequency, which is typical of all HTSC compounds; b) a nonmonotonic dependence of the resistivity on frequency and temperature, which was first observed in Ref. 4: a maximum of the resistivity at a certain frequency, and a change in sign of the temperature derivative of the resistivity (a transition from a linear temperature dependence to a so-called "semiconductor trend"). According to the model,[1] these features are due to the fact that the scattering of mobile electrons in the wide band on impurities, owing to the exchange of singlet pairs with the narrow band, is of a resonance character, so that at a certain energy the frequency of collisions with impurities goes to zero, and an anomalously large contribution to the conductivity from these electrons appears. In reality this contribution is limited by the width of the resonance, which cannot be calculated in the framework of the model,[1] since the latter does not take into account the strong antiferromagnetic correlations of the localized electrons and, possibly, other interactions. The width of the resonance is put into the theory phenomenologically, and the parameters of the theory are determined from a comparison with experiment.

Despite this shortcoming, one can nevertheless expect that to the extent that one is talking about orbital effects that do not break the singlet symmetry, the model should agree, at least qualitatively, with experiment. From this standpoint it is of interest to consider the Hall effect and conductivity in the presence of a static magnetic field H, when the role of the orbital frequency is played by the Larmor frequency of gyration of the mobile electrons on closed orbits, $\omega_H = eH/mc$, in a plane perpendicular to the magnetic field. The present paper is devoted to a calculation of the conductivity tensor for this case and to a comparison of the results of the theory with experiment. In view of the frequent references to the formulas and notation from Ref. 1, we shall denote the formulas of that paper as $(\ldots)^1$, where the ellipsis in parentheses stands for the formula number from Ref. 1.

The conductivity tensor is calculated as in Ref. 1 in the temperature Green's function technique with analytical continuation to the region of real frequencies for the linear response of the system.[6,7] We start from the expression for the conductivity tensor $\sigma_{\alpha\beta}$ $(j_\alpha = \sigma_{\alpha\beta}E_\beta)$ analogous to $(60)^1$–$(62)^1$, in terms of the temperature correlation function in the coordinate (more precisely, band–site) representation, conjugate to the band–quasimomentum representation:

$$\sigma_{\alpha\beta}(\mathbf{R},\mathbf{R}';\omega) = -\frac{2}{i\omega}\left(\frac{e}{v_0}\right)^2 T\sum_{\omega_n} \mathrm{Tr}(\hat{v}_\alpha(\mathbf{R})G(\omega_+)$$

$$\times\hat{v}_\beta(\mathbf{R}')G(\omega_-))|_{iv_{n0}\to\omega+i0}, \qquad (1)$$

$$\omega_n = \pi T(2n+1), \quad \omega_+ = \omega_n, \quad \omega_- = \omega_n - \nu_{n0},$$

$$\nu_{n0} = 2\pi T n_0 \quad (k_B = 1, \quad \hbar = 1),$$

where $\mathbf{R}$ stands for the coordinates of the lattice sites, v_0 is the volume of the unit cell of the crystal, and $\hat{v}_\alpha(\mathbf{R})$ is the velocity operator.

Unlike $(60)^1$–$(62)^1$, in Eq. (1) we have taken into account a number of simplifying circumstances. The coefficient 2 takes into account states with isotopic spin $\sigma_z = -1$ in "electron–hole" space (in the normal state this is the doubling on account of spin). We have dropped the so-called "diamagnetic" contribution to the current, which automatically vanishes in the order to which the calculation of the trace and summation over the discrete frequencies ω_n were done in Ref. 1. A more important remark concerns the averaging over impurities of the tensor product of Green's functions, $(G\times G)_{\mathrm{average}}$, which reduces to summation of the "ladder" diagrams of perturbation theory (see Ref. 1). In the case of the normal skin effect this average decomposes into a product of averages: $(G\times G)_{\mathrm{average}} = G_{\mathrm{average}}\times G_{\mathrm{average}}$. It can be shown that this result is preserved in the presence of a static magnetic field in the quasiclassical approximation, and in expression (1) the averaged Green's functions are understood. Here, since in the narrow band the velocities of the electrons are zero, G actually denotes the diagonal (with respect to the band index) matrix element $G_{jj'}$, which describes mobile electrons in the wide band.

These functions were calculated in Ref. 1 (formulas $(20),^{1)}$ (24)–(26), and (64) of that paper). In contrast to these formulas, in the present case it is necessary to take into account that the spectral decomposition of the Green's functions is carried out not with respect to the quasimomentum and plane waves, which describe the free motion of the electrons, but with respect to the quantum numbers of the Landau spectrum and the corresponding quasiclassical wave functions for electrons in a magnetic field. However, it is not hard to see that when the inequalities

$$\omega_H \ll T_c \ll \frac{1}{\tau} \ll \varepsilon_F \qquad (2)$$

hold (these will be important later on; here τ is the mean free time of the electrons, and $\varepsilon_F = p_F^2/2m = mv_F^2/2$ is the Fermi energy, of the order of the width of the band of mobile electrons), the scheme[1] of averaging the Green's functions over impurities and the overall structure of the expressions for the averaged Green's function remain as before. Here the thermodynamic parameters of the model (the critical temperature T_c [Eq. (57)],[1] the hybridization parameter d of the branches of the spectrum [Eq. $(30)^1$], and the energy ξ_0 of the local level [Eq. (37)][1] retain their significance and, what is of particular practical importance, the analytical formulas for the mass operators $M(\omega_n)$, $L(\omega_n)$ as functions of the discrete frequency ω_n are preserved. This is almost obvious. In view of the local nature of the scattering potential of the impurities and the inequalities $l = v_F\tau \ll r_H = v_F/\omega_H$ (l is the

mean free path, and r_H is the Larmor radius of the orbits of the electron in the magnetic field), in the quasiclassical approximation the electrons move almost as free particles in the intervals between collisions with impurities.

Thus the problem addressed in this paper is to take into account the influence of the Landau spectrum on a kinetic characteristic—the conductivity tensor. According to the Wannier construction,[8] in a magnetic field $\mathbf{H}=\mathrm{curl}\ \mathbf{A}$ smoothed over atomic distances, the kinetic energy operator for mobile electrons is written

$$H_0(\mathbf{R},\mathbf{R}') = \frac{1}{N_0}\sum_{\mathbf{p}} \xi\left(\mathbf{p} - \frac{e}{c}\mathbf{A}\left(\frac{\mathbf{R}+\mathbf{R}'}{2}\right)\right)$$

$$\times\exp[i\mathbf{p}\cdot(\mathbf{R}-\mathbf{R}')]. \qquad (3)$$

where N_0 is the number of lattice sites, and $\xi(\mathbf{p})$, the kinetic energy of the free electrons measured from the chemical potential $\mu\approx\varepsilon_F$, is a periodic function of the quasimomentum $\mathbf{p}$. The summation over quasimomentum in (3) and everywhere below is done over nonequivalent states, i.e., within a cell of the reciprocal lattice. The corresponding velocity operators $\hat{v}_\alpha(\mathbf{R})$ have the form

$$\hat{v}_\alpha(\mathbf{R})(\mathbf{R}_1,\mathbf{R}_2) = \delta_{\mathbf{R}(\mathbf{R}_1+\mathbf{R}_2)/2}\frac{1}{N_0}$$

$$\times\sum_{\mathbf{p}} \frac{\partial}{\partial p_\alpha}\xi\left(\mathbf{p} - \frac{e}{c}\mathbf{A}(\mathbf{R})\right)$$

$$\times\exp[i\mathbf{p}\cdot(\mathbf{R}_1-\mathbf{R}_2)]. \qquad (4)$$

In view of the qualitative character of the model, in order to emphasize the effect of magnetic field on the conductivity tensor, we neglect the orthorhombic anisotropy of the Y–Ba–Cu–O crystals, with axes a, b, c (x, y, z, respectively) and, moreover, to simplify the subsequent calculations we assume that $\xi(\mathbf{p}) = \mathbf{p}^2/2m - \varepsilon_F$ within the symmetric ($\xi(\mathbf{p}) = \xi(-\mathbf{p})$) cell of the reciprocal lattice. Then for a magnetic field directed along the c (or z) axis, in the Landau gauge $\mathbf{H} = (0,0,H)$, $\mathbf{A} = (0,Hx,0)$ the wave functions, as can easily be checked, have the form:

$$\psi_{n,p_y,p_z}(\mathbf{R}) = \psi_{n,p_y}(x)\frac{\exp[i(p_y y + p_z z)]}{\sqrt{N_y N_z}} \qquad (5)$$

(N_y and N_z are the numbers of lattice sites along the y and z axes), with the Landau spectrum

$$\xi(n,p_z) = n\omega_H + \frac{p_z^2}{2m} - \varepsilon_F, \qquad (6)$$

where $n>0$ is an integer. The normalized quasiclassical wave functions $\psi_{n,p_y}(x)$ are nonzero in the interval between the turning points on the orbit and have the form

$$\psi_{n,p_y}(x) = \left(\frac{2a\omega_H}{\pi|v_x(x)|}\right)^{1/2}\sin\int^x p_x(x')dx'\ \theta$$

$$\times\left(r_H^2(n) - \left(\frac{cp_y}{eH} - x\right)^2\right), \qquad (7)$$

$$\frac{cp_y}{eH} - r_H(n)$$

where a is the lattice period along the x axis, cp_y/eH plays the role of the x coordinate of the center of the circular orbit in the (x,y) plane, $r_H(n)$ is the radius of the orbit, and

$$p_x(x)=mv_x(x)=\frac{eH}{c}\left[r_H^2(n)-\left(\frac{cp_y}{eH}-x\right)^2\right]^{1/2}>0,$$

$$r_H(n)=\frac{c}{eH}\sqrt{2mn\omega_H}. \qquad (8)$$

In formula (7) the support of the wave function $\psi_{n,p_y}(x)$ is explicitly separated out; with quasilocal accuracy; in view of the exponentially rapid decay of the wave function beyond the turning points, it reduces to the singular θ function.

The wave functions (5) and (7) satisfy the completeness and orthogonality relations. Therefore the spectral decomposition of the total Green's functions in expression (1), with allowance for the interband interaction in the self-consistent field approximation[1] and for scattering on impurities, is written, in view of what was said above, as

$$G(\mathbf{R}_1,\mathbf{R}_2;\omega_{\pm})=\sum_{\lambda}\psi_{\lambda}(\mathbf{R}_1)G_{\lambda}(\omega_{\pm})\psi_{\lambda}^*(\mathbf{R}_2), \qquad (9)$$

$$\lambda=(n,p_y,p_z),$$

$$G_{\lambda}(\omega_{\pm})=\left(n\omega_H+\frac{p_z^2}{2m}-\varepsilon_F-i\omega_{\pm}-L(\omega_{\pm})\right)^{-1}, \qquad (10)$$

where the function $L(\omega_n)$ is given by formulas [(24), (25), and (64)][1].

By definition, the trace in expression (1) is given by the sum

$$(\mathrm{Tr})_{\alpha\beta}(\mathbf{R},\mathbf{R}')$$

$$=\frac{1}{N_0^2}\circ\sum\circ\left\{v_{\alpha}\left(\mathbf{p}_1-\frac{e}{c}\mathbf{A}(\mathbf{R})\right)\delta_{\mathbf{R},(\mathbf{R}_1+\mathbf{R}_2)/2}\right.$$

$$\times\exp[i\mathbf{p}_1\cdot(\mathbf{R}_1-\mathbf{R}_2)]\psi_{\lambda}(\mathbf{R}_2)G_{\lambda}(\omega_+)\psi_{\lambda}^*(\mathbf{R}_3)$$

$$\times v_{\beta}\left(\mathbf{p}_2-\frac{e}{c}\mathbf{A}(\mathbf{R}')\right)\delta_{\mathbf{R}',(\mathbf{R}_3+\mathbf{R}_4)/2}$$

$$\left.\times\exp[i\mathbf{p}_2\cdot(\mathbf{R}_3-\mathbf{R}_4)]\psi_{\lambda'}(\mathbf{R}_4)G_{\lambda'}(\omega_-)\psi_{\lambda'}^*(\mathbf{R}_1)\right\},$$

$$v_{\alpha}(\mathbf{p})=\frac{\partial\xi(\mathbf{p})}{\partial p_{\alpha}}. \qquad (11)$$

The symbol $\circ\Sigma\circ$ denotes summation over all variables in expression (11) except for $\mathbf{R}$, $\mathbf{R}'$, and $\omega_{\pm}$. We note that, in view of the translational symmetry, this expression actually depends on the difference $\mathbf{R}-\mathbf{R}'$, and its Fourier transform should be calculated according to the representation

$$\int\frac{d^3q}{(2\pi)^3}\exp[i\mathbf{q}\cdot(\mathbf{R}-\mathbf{R}')](\ldots).$$

In what follows we let $\mathbf{q}\to0$ on account of the normal skin effect.

Evaluation of the trace over the y and z variables does not present any difficulty, since, according to formulas (5) and (9), one is dealing with the evaluation of sums of prod-

ucts of normalized wave functions. The values of these sums are determined by the completeness and orthogonality relations:

$$\frac{1}{N_y}\sum_{p_y}\exp[ip_y(y_1-y_2)]=\delta_{y_1,y_2},$$

$$\frac{1}{N_y}\sum_{y}\exp[iy(p_{1y}-p_{2y})]=\delta_{p_{1y},p_{2y}}$$

and analogously for the variable z. Here, because of the presence of the Kronecker deltas $\delta_{\mathbf{R},(\mathbf{R}_1+\mathbf{R}_2)/2}$ and $\delta_{\mathbf{R},(\mathbf{R'}_3+\mathbf{R}_4)/2}$ in expression (11), it is convenient to make the change of variables

$$\frac{y_1+y_2}{2}=Y'_1,\quad y_1-y_2=Y_1,\quad \frac{y_3+y_4}{2}=Y'_3,$$

$$y_3-y_4=Y_3,\quad \frac{z_1+z_2}{2}=Z'_1,\quad z_1-z_2=Z_1,$$

$$\frac{z_3+z_4}{2}=Z'_3,\quad z_3-z_4=Z_3,$$

where the Jacobian of the transformation has a unit modulus. Evaluation of the desired sums over the variables y and z leads to the expression

$$\delta_{p_{1y},(p_y+p'_y)/2}\delta_{p_{2y},(p_y+p'_y)/2}\delta_{p_{1z},(p_z+p'_z)/2}\delta_{p_{2z},(p_z+p'_z)/2}.$$

Now making the change of variables

$$\frac{p_y+p'_y}{2}=\mathcal{P}_y;\quad p_y-p'_y=q_y;\quad \frac{p_z+p'_z}{2}=\mathcal{P}_z;$$

$$p_z-p'_z=q_z;\quad p_y=\mathcal{P}_y+\frac{1}{2}q_y;\quad p'_y=\mathcal{P}_y-\frac{1}{2}q_y;$$

$$p_z=\mathcal{P}_z+\frac{1}{2}q_z;\quad p'_z=\mathcal{P}_z-\frac{1}{2}q_z$$

and converting the remaining sums $\underset{\mathcal{P}_yq_y\mathcal{P}_zq_z}{\Sigma\Sigma\Sigma\Sigma}$ into integrals,

$$\sum_{\mathcal{P}_y}\sum_{q_y}\to\left(\frac{N_ya_y}{2\pi}\right)^2\int\int d\mathcal{P}_ydq_y,$$

$$\sum_{\mathcal{P}_z}\sum_{q_z}\to\left(\frac{N_za_z}{2\pi}\right)^2\int\int d\mathcal{P}_zdq_z$$

(a_y and a_z are the lattice periods along the y and z axes), we take the integral

$$\int\int\frac{dq_ydq_z}{(2\pi)^2}\exp[iq_y(y-y')+iq_z(z-z')](\ldots).$$

In the limit $(q_y q_z)\to0$ we obtain the following result from Eq. (11) $(\mathcal{P}_y,\mathcal{P}_z\to\equiv p_y,p_z)$:

$$(\mathrm{Tr})_{\alpha\beta}(x,x')=\left(\frac{a_ya_z}{N_x}\right)^2\int\int\frac{dp_ydp_z}{(2\pi)^2}$$

$$\circ\sum\circ\left\{v_{\alpha}\left(p_{1x},p_y-\frac{eHx}{c},p_z\right)\delta_{x,(x_1+x_2)/2}\right.$$

$$\times\exp[ip_{1x}(x_1-x_2)]\psi_{n,p_y}(x_2)G_{n,p_z}(\omega_+)$$

$$\times \psi_{n,p_y}(x_3) v_\beta\left(p_{2x},p_y-\frac{eHx'}{c},p_z\right)$$

$$\times \delta_{x',(x_3+x_4)/2}$$

$$\times \exp[ip_{2x}(x_3-x_4)]\psi_{n',p_y}(x_4)G_{n',p_z}(\omega_-)$$

$$\times \psi_{n',p_y}(x_1)\bigg\}. \tag{12}$$

Evaluation of the trace over the x variable is a more complicated matter. We start by eliminating the Kronecker deltas $\delta_{x,(x_1+x_2)/2}$, $\delta_{x',(x_3+x_4)/2}$ in Eq. (12) by making the change of variables

$$\frac{x_1+x_2}{2}=X_1,\ \ x_1-x_2=X_1';\ \ \frac{x_3+x_4}{2}=X_3,$$

$$x_3-x_4=X_3'.$$

As a result, Eq. (12), after a shift $p_y\to p_y+eHx'/c$, takes the form [see Eqs. (7) and (8) for $\psi_{n,p_y}(x)$; here $X=x-x'$]:

$$(\mathrm{Tr})_{\alpha\beta}(X)=\left(\frac{a_y a_z}{N_x}\right)^2\left(\frac{2a\omega_H}{\pi}\right)^2\sum_{n,k}\int\int\frac{dp_y dp_z}{(2\pi)^2}$$

$$\circ\sum\circ\bigg\{\exp[ip_{4x}X_1'+ip_{2x}X_3']$$

$$\times\frac{\sin\alpha\sin\beta\sin\gamma\sin\delta}{\sqrt{|v_x^\alpha v_x^\beta v_x^\gamma v_x^\delta|}}\theta_\alpha\theta_\beta\theta_\gamma\theta_\delta v_\alpha$$

$$\times\left(p_{1x},p_y-\frac{eHX}{c},p_z\right)v_\beta(p_{2x},p_y,p_z)$$

$$\times G_{n,p_z}(\omega_+)G_{n-k,p_z}(\omega_-)\bigg\}, \tag{13}$$

where for brevity we have introduced the following notion for the integrals:

$$X-\frac{cp_y}{eH}-\frac{1}{2}X_2' \qquad -\frac{cp_y}{eH}+\frac{1}{2}X_3'$$

$$\alpha=\frac{eH}{c}\int_{-r_H(n)}dx''\sqrt{r_H^2(n)-x''^2},$$

$$\beta=\frac{eH}{c}\int_{-r_H(n)}dx''\sqrt{r_H^2(n)-x''^2},$$

$$-\frac{cp_y}{eH}-\frac{1}{2}X_3' \qquad X-\frac{cp_y}{eH}+\frac{1}{2}X_1' \tag{14}$$

$$\gamma=\frac{eH}{c}\int_{-r_H(n-k)}dx''\sqrt{r_H^2(n-k)-x''^2},$$

$$\delta=\frac{eH}{c}\int_{-r_H(n-k)}dx''\sqrt{r_H^2(n-k)-x''^2}.$$

The other notion is clear from formula (7).

In expression (13) we must explicitly take into account the quasiclassical character of the electron motion, i.e., the rapid oscillations of $\psi_{n,p_y}(x)$ over a length $\lambda_F\sim 1/p_F\ll l$ $\ll r_H$, and also the large values of the quantum number n $\sim\varepsilon_F/\omega_H$. This is achieved by expanding the integrals

(14)—the arguments of the sines in expression (7)—in series in the variables X_1', X_3', and $k=n-n'$ and choosing suitable combinations of the exponentials $e^{\pm i\alpha}e^{\pm i\beta}e^{\pm i\gamma}e^{\pm i\delta}$ $\times\exp[i(p_{1x}X_1'+p_{2x}X_3')]$ in the products of wave functions $\psi_{n,p_y}(x)$ such that the rapid oscillations are "quenched" in them and such that they give a nonzero contribution to expression (13) to leading order in the small parameters. We see from formula (14) that for this it is necessary to take the combinations $\alpha-\delta$ and $\beta-\gamma$, which can then be combined with arbitrary signs.

Expanding the integrals (14) to terms linear in in X_1', X_3', and k, we obtain

$$\alpha-\delta=-\mathcal{P}_1 X_1'+kI_1,\ \ \beta-\delta=\mathcal{P}_2 X_3'+kI_2, \tag{15}$$

$$\mathcal{P}_1=\frac{eH}{c}\left[r_H^2(n)-\left(X-\frac{cp_y}{eH}\right)^2\right]^{1/2},$$

$$\mathcal{P}_2=\frac{eH}{c}\left[r_H^2(n)-\left(\frac{cp_y}{eH}\right)^2\right]^{1/2}, \tag{16}$$

$$X-\frac{cp_y}{eH} \qquad\qquad -\frac{cp_y}{eH}$$

$$I_1=\int_{-r_H(n)}\frac{dx''}{\sqrt{r_H^2(n)-x''^2}},\ \ I_2=\int_{-r_H(n)}\frac{dx''}{\sqrt{r_H^2(n)-x''^2}}. \tag{17}$$

The summation of the exponentials in expression (13) over the variables X_1' and X_3' gives the following group of terms, as can easily be seen from formulas (15)–(17):

$$\frac{N_x^2}{16}\{\delta_{p_{1x},\mathcal{P}_1}\delta_{p_{2x},-\mathcal{P}_2}\exp[ik(I_1+I_2)]$$

$$+\delta_{p_{1x},\mathcal{P}_1}\delta_{p_{2x},\mathcal{P}_2}\exp[ik(I_1-I_2)]$$

$$+\delta_{p_{1x},-\mathcal{P}_1}\delta_{p_{2x},-\mathcal{P}_2}\exp[-ik(I_1-I_2)]$$

$$+\delta_{p_{1x},-\mathcal{P}_1}\delta_{p_{2x},\mathcal{P}_2}\exp[-ik(I_1+I_2)]\}. \tag{18}$$

We substitute this group of terms (18) into expression (13) and do the summation over p_{1x} and p_{2x}. The resulting expression for $(\mathrm{Tr})_{\alpha\beta}(X)$ must be Fourier transformed with respect to the difference $x-x'=X$ by operating with $\int dX e^{-iq_x X}(...)$, after which one should let $q_x\to 0$. Next, since the characteristic frequencies $\omega_H\ll\varepsilon_F$, the summation over the quantum number n can be replaced by an integral over the variable ξ (6): $\omega_H\sum_n\to\int_{-\infty}^{\infty}d\xi$. Here, since the integral over ξ is concentrated in a small neighborhood near the Fermi boundary, the values of p_z are restricted to the interval $-p_F<p_z<p_F$, and with the same accuracy the radius of the orbit (8) is written in the form

$$r_H^2(p_z) = \left(\frac{c}{eH}\right)^2 (p_F^2 - p_z^2). \tag{19}$$

In order to eliminate the support $\theta(r_H^2(p_z) - (X - cp_y/eH)^2)\,\theta(r_H^2(p_z) - (cp_y/eH)^2)$ in formula (13) and to do the integration over the variables X, p_y, and p_z, we make the following change of variable, which corresponds to the classical dynamics of the electron in a magnetic field:

$$X - \frac{cp_y}{eH} = r_H(p_z)\cos\varphi, \quad \frac{cp_y}{eH} = r_H(p_z)\cos\varphi_0;$$

$$\frac{\partial(X, p_y)}{\partial(\varphi, \varphi_0)} = \begin{vmatrix} -r_H\sin\varphi, & -r_H\sin\varphi_0 \\ 0, & -\dfrac{eH}{c}r_H\sin\varphi_0 \end{vmatrix}$$

$$= \frac{eH}{c}r_H^2\sin\varphi\sin\varphi_0, \tag{20}$$

where φ and φ_0 are the phases specifying the position of the electron on the orbit. In view of the positivity of $\mathcal{P}_1$, $\mathcal{P}_2$, I_1, and I_2 in Eqs. (16) and (17), the integration over phases can be done over a half period $(-\pi, 0)$: $\int_{-\pi}^0\int_{-\pi}^0 d\varphi\,d\varphi_0$ from the "left" turning point to the "right" one. The values of these quantities, according to formulas (16), (17), and (20), are

$$\mathcal{P}_1 = -\frac{eH}{c}r_H(p_z)\sin\varphi, \quad \mathcal{P}_2 = \frac{eH}{c}r_H(p_z)\sin\varphi_0,$$

$$I_1(\varphi) = \pi + \varphi, \quad I_2(\varphi) = -\varphi_0. \tag{21}$$

The further integration over p_z and evaluation of the trigonometric integrals over phases φ and φ_0 in expression (13) are elementary. It is convenient to normalize the tensor $\sigma_{\alpha\beta}$ to the Drude–Lorentz conductivity $\sigma_0 = ne^2\tau/m$, where $n = p_F^3/3\pi^2$ is the density of conduction electrons. Taking formulas (19)–(21) into account, we obtain the following expressions for the nonzero components of the desired tensor, $\sigma_{\alpha\beta} = \sigma_{\alpha\beta}(\mathbf{q}, \omega)|_{\mathbf{q}\to 0}$:

$$\frac{\sigma_{xx}}{\sigma_0} = \frac{\sigma_{yy}}{\sigma_0} = -\frac{1}{i\omega\tau}T\sum_{\omega_n}\sum_k \frac{1}{2}(\delta_{k,1} + \delta_{k,-1})$$

$$\times \int d\xi\, G_\xi(\omega_+)G_{\xi - k\omega_H}(\omega_-)\big|_{i\nu_{n0}\to\omega + i0}, \tag{22}$$

$$\frac{\sigma_{xy}}{\sigma_0} = -\frac{\sigma_{yx}}{\sigma_0} = \frac{1}{i\omega\tau}T\sum_{\omega_n}\sum_k \frac{1}{2i}(\delta_{k,1} - \delta_{k,-1})$$

$$\times \int d\xi\, G_\xi(\omega_+)G_{\xi - k\omega_H}(\omega_-)\big|_{i\nu_{n0}\to\omega + i0},$$

$$\sigma_{zz} = (\sigma_{xx} = \sigma_{yy})|_{\omega_H = 0}. \tag{23}$$

The components σ_{xz}, σ_{yz}, σ_{zy}, and σ_{zx} vanish because the integrands are odd with respect to p_z. Owing to the selection rules, in the sums over the integers k that specify transitions from orbit to orbit as a result of collisions with impurities, formulas (22) and (23) satisfy the Onsager symmetry relations with respect to a change in sign of the magnetic field. The component σ_{zz} is equal to the conductivity in zero magnetic field and will be of no further interest.

Equations (22) and (23) require an analytical continuation to the upper half plane with respect to the real frequency ω: $i\nu_{n0}\to\omega + i0$; we do this by the technique pointed out in Ref. 7: we represent the Green's function $G(\omega_n)$ by an integral of the Cauchy type:

$$G_\xi(\omega_n) = \int_{-\infty}^\infty \frac{d\varepsilon}{2\pi i}\frac{\chi(\varepsilon)}{\varepsilon - i\omega_n},$$

$$\chi_\xi(\varepsilon) = G_\xi(\omega_n)\big|_{i\omega_n\to\varepsilon + i0} - G_\xi(\omega_n)\big|_{i\omega_n\to\varepsilon - i0}$$

$$= (\xi - \varepsilon - L_+(\varepsilon))^{-1} - (\xi - \varepsilon - L_-(\varepsilon))^{-1}.$$

The value of the sum over the discrete frequencies ω_n is determined by the well-known expansion of the hyperbolic tangent in simple fractions and is equal to

$$T\sum_{\omega_n}\frac{1}{(\varepsilon_+ - i\omega_n)(\varepsilon_- - i\omega_n + i\nu_{n0})}$$

$$= \frac{1/2[\tanh(\varepsilon_+/2T) - \tanh(\varepsilon_-/2T)]}{\varepsilon_+ - \varepsilon_- - i\nu_0};$$

$$\varepsilon_\pm = \varepsilon \pm \frac{\varepsilon'}{2}.$$

Thus, according to formulas (22) and (23), we need to evaluate the integral

$$\frac{1}{i\omega\tau}\int\int\frac{d\varepsilon\,d\varepsilon'}{(2\pi i)^2}\frac{1/2[\tanh(\varepsilon_+/2T) - \tanh(\varepsilon_-/2T)]}{\varepsilon' - \omega - i0}$$

$$\times \int d\xi\,\chi_\xi(\varepsilon_+)\chi_{\xi - k\omega_H}(\varepsilon_-), \tag{24}$$

in terms of which the principal components of the conductivity tensor, σ_{xx} (22) and σ_{xy} (23), are expressed. In formula (24), after integration of the spectral densities over the variable ξ,

$$\int d\xi\,\chi_\xi(\varepsilon_+)\chi_{\xi - k\omega_H}(\varepsilon_-) = -2\pi i[(\varepsilon' - k\omega_H$$

$$+ L_+(\varepsilon_+) - L_-(\varepsilon_-))^{-1}$$

$$+ (-\varepsilon' + k\omega_H + L_+(\varepsilon_+)$$

$$- L_-(\varepsilon_-))^{-1}] \tag{25}$$

a rapidly convergent integral over the variable ε' appears. Therefore, having in mind the limit $\omega\to 0$, we can expand the difference of the hyperbolic tangents in powers of ε' and, after performing the integration over ε', set $\omega = 0$:

$$-\frac{1}{i\tau}\int_{-\infty}^\infty\frac{d\varepsilon}{4T\cosh^2(\varepsilon/2T)}\frac{1}{-k\omega_H + L_+(\varepsilon) - L_-(\varepsilon)}. \tag{26}$$

The difference $L_+(\varepsilon) - L_-(\varepsilon)$ has the form [Eq. (67)][1]

$$L_+(\varepsilon) - L_-(\varepsilon) = \frac{1}{\tau}\left(1 + \frac{\delta}{\xi_0 - \varepsilon}\right)^2, \tag{27}$$

where the parameters of the model are given in Eqs. [(37), (57), (30), and (67)][1]:

$$\xi_0 = T \ln \frac{1-k}{1+k}; \quad T_c \sim \lambda^2 \varepsilon_F \frac{k}{\dfrac{1+k}{\ln \dfrac{1+k}{1-k}}};$$

$$d \sim \lambda c u_{12}; \quad \delta = \frac{|d|^2 u_{22}}{u_{11} u_{22} - |u_{12}|^2}; \tag{28}$$

where k is the degree of filling of the narrow band ($-1 < k < 1$), c is the impurity concentration, $u_{jj'}$ are the matrix elements of the scattering potential of the impurities ($u < \varepsilon_F$), and λ is a small interband coupling constant. These quantities satisfy the inequality

$$\lambda \ll 1, \quad \delta \ll d, \quad \delta \ll \xi_0 \sim T_c, \tag{29}$$

which must be taken into account together with inequalities (2).

Let us separate out in the integrand of (26) the asymptotic form for high energies and the resonance term:

$$\frac{1}{-k\omega_H + L_+(\varepsilon) - L_-(\varepsilon)} = \frac{1}{-k\omega_H + i/\tau}$$

$$+ \left(\frac{1}{-k\omega_H + L_+(\varepsilon) - L_-(\varepsilon)} \right.$$

$$\left. - \frac{1}{-k\omega_H + i/\tau} \right). \tag{30}$$

As is easily seen from formula (27), the resonance term converges rapidly with respect to energies and in zero magnetic field $\omega_H = 0$ gives an infinite contribution to the conductivity tensor at the energy $\varepsilon = \xi_0 + \delta$. We introduce phenomenologically a Lorentzian width of the resonance according to the rule

$$\frac{1}{(\varepsilon - \xi_0 - \delta)^2} \rightarrow \frac{1}{(\varepsilon - \xi_0 - \delta)^2 + \nu_0^2}, \quad \nu_0 \ll \delta.$$

Integrating over energy in (26) and collecting together formulas (22)–(30), we obtain the final expressions for the components of the conductivity tensor:

$$\frac{\sigma_{xx}}{\sigma_0} = \frac{\sigma_{yy}}{\sigma_0} = 1 + \frac{\pi(1-k^2)}{4T} \operatorname{Re} \frac{\delta^2}{\sqrt{\nu_0^2 - i\omega_H \tau \delta^2}}, \tag{31}$$

$$\frac{\sigma_{xy}}{\sigma_0} = -\frac{\sigma_{yx}}{\sigma_0} = \tau\omega_H + \frac{\pi(1-k^2)}{4T} \operatorname{Im} \frac{\delta^2}{\sqrt{\nu_0^2 - i\tau\omega_H \delta^2}},$$

$$\sqrt{1} = 1. \tag{32}$$

The resistivity tensor $\rho_{\alpha\beta} = (\sigma^{-1})_{\alpha\beta}$.

Let the current be directed along the x axis: $j_x \equiv j$, $j_y = 0$, $E_x \equiv E$. Defining the resistivity and Hall coefficient as

$$\rho = \frac{E}{j} = \frac{\sigma_{xx}}{\sigma_{xx}^2 + \sigma_{yy}^2}; \quad R_H = \frac{E_y}{jH} = \frac{\sigma_{xy}}{[\sigma_{xx}^2 + \sigma_{yx}^2]H},$$

we find for these quantities

$$\frac{\rho}{\rho_0} = \left(1 + \frac{\varepsilon}{t} \operatorname{Re} \frac{1}{\sqrt{1-i\Omega}} \right) \left[\left(1 + \frac{\varepsilon}{t} \operatorname{Re} \frac{1}{\sqrt{1-i\Omega}} \right)^2 \right.$$

$$\left. + \left(\tau\omega_H + \frac{\varepsilon}{t} \operatorname{Im} \frac{1}{\sqrt{1-i\Omega}} \right)^2 \right]^{-1}, \quad \rho = 1/\sigma_0, \tag{33}$$

$$\tau\omega_H \frac{R_H}{R_{H0}} = \left(\tau\omega_H + \frac{\varepsilon}{t} \operatorname{Im} \frac{1}{\sqrt{1-i\Omega}} \right) \left[\left(1 + \frac{\varepsilon}{t} \operatorname{Re} \frac{1}{\sqrt{1-i\Omega}} \right)^2 \right.$$

$$\left. + \left(\tau\omega_H + \frac{\varepsilon}{t} \operatorname{Im} \frac{1}{\sqrt{1-i\Omega}} \right)^2 \right]^{-1}, \tag{34}$$

where $R_{H0} = 1/nec$ is the classical value of the Hall coefficient, and we introduce the dimensionless variables

$$t = \frac{T}{T_c}, \quad \varepsilon = \frac{\pi(1-k^2)\delta^2}{4T_c \nu_0} \gg 1, \quad \Omega = \tau\omega_H \left(\frac{\delta}{\nu_0} \right)^2. \tag{35}$$

Let us mention a useful formula for the tangent of the Hall angle, which can be used to estimate the parameter $\tau\omega_H$ from experimental data:

$$\frac{E_y}{E} = \frac{\tau\omega_H + \dfrac{\varepsilon}{t} \operatorname{Im} \dfrac{1}{\sqrt{1-i\Omega}}}{1 + \dfrac{\varepsilon}{t} \operatorname{Re} \dfrac{1}{\sqrt{1-i\Omega}}}.$$

The temperature and magnetic-field dependences described by formulas (33) and (34) for the resistivity and Hall coefficient can be compared with the available experimental data (see Ref. 9 and the references cited therein). For this we should eliminate from consideration the anomalies observed in a narrow fluctuational neighborhood of the critical temperature T_c of the superconducting transition, which are not described by the self-consistent field approximation.[1] The interval of reasonable values of the temperature is $1 < t < 3$. In those experimental papers there is unfortunately no detailed information about the magnetic-field dependences of the quantities in Eqs. (33) and (34). Their temperature dependence has been measured at two or three values of the magnetic field, including zero field.

A straightforward analysis shows that the resistivity (33), in agreement with experiment, is monotonically increasing $(\partial(\rho/\rho_0)/\partial t > 0)$ with temperature in a practically linear manner at not-too-high temperatures. The behavior of the Hall coefficient, or the so-called Hall "resistance," is more interesting: $\rho_{xy}/\rho_0 = \tau\omega_H R_H/R_{H0}$. By differentiating expression (34) with respect to temperature, one can establish that this quantity reaches a maximum at the point

$$t_0 = \varepsilon I \frac{\sqrt{1+(I/R)^2}}{1 + \sqrt{1+(I/R)^2}} \left(\frac{I/R}{1 + \sqrt{1+(I/R)^2}} - \tau\omega_H \right)^{-1}, \tag{36}$$

$$(R, I) \equiv (\operatorname{Re}, \operatorname{Im}) \frac{1}{\sqrt{1-i\Omega}},$$

$$\Omega \ll 1; \quad t_0 = \varepsilon, \qquad \max\left(\frac{\rho_{xy}}{\rho_0} \right) \approx \frac{\Omega}{8};$$

$$\Omega \gg 1: \quad t_0 \approx \frac{\varepsilon}{\sqrt{\Omega}}, \quad \max\left(\frac{\rho_{xy}}{\rho_0} \right) \approx \frac{1}{2(1+\sqrt{2})} \tag{37}$$

[see Fig. 1, which shows the results of numerical calculations according to formula (34)]. The condition $t_0 > 1$ and formulas (37) imply a restriction on the value of the magnetic field: $\Omega < \varepsilon^2$. Theoretical estimates of the orders of magnitude of
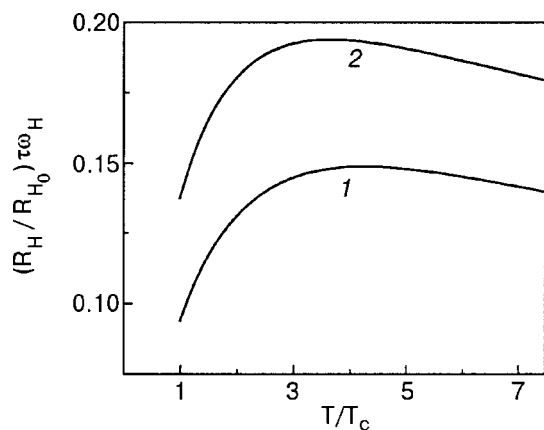
FIG. 1. Temperature dependence of the Hall resistance: $\tau\omega_H = 0.05$ (1), $\tau\omega_H = 0.1$ (2). $\delta/\nu_0 = 6$, $\varepsilon = 5$.

these model parameters, consistent with inequalities (2) and (29), make it possible to use them for estimating the characteristic magnetic fields for the theory under consideration: $H \sim 10^3 - 10^4$ Oe. These values of the magnetic field do indeed correspond to the magnetic field at which the temperature dependence of the conductivity and Hall coefficient were measured in Ref. 9.

We see from expressions (36) and (37) and Fig. 1 that at low fields the maximum decreases in height and shifts to higher temperatures, to beyond the limits of applicability of the theory, while at high fields it reaches the experimentally observed values at moderate temperatures. These behaviors agree with experiments.[10]

Thus we find that the model of Ref. 1 correctly conveys the main features of the behavior of two different electronic orbital effects in HTSC metal oxides in the normal state: the ac resistivity, and the Hall effect.

The authors thank E. V. Bezuglyi for fruitful discussions and help with the organization of this paper.

[1)]Formulas (20)[1] contain an error: a term $-i\omega_n \left(\begin{smallmatrix} 1 & 0 \\ 0 & 1 \end{smallmatrix}\right)$ is missing from the expression for g_0^{-1}.

[1] V. P. Galaĭko, Fiz. Nizk. Temp. **19**, 123 (1993) [Low Temp. Phys. **19**, 87 (1993)].

[2] V. P. Galaĭko, Fiz. Nizk. Temp. **13**, 1102 (1987) [Sov. J. Low Temp. Phys. **13**, 627 (1987)].

[3] V. P. Galaĭko, E. V. Bezuglyĭ, and V. S. Shumeĭko, Fiz. Nizk. Temp. **13**, 1301 (1987) [Sov. J. Low Temp. Phys. **13**, 732 (1987)].

[4] V. M. Dmitriev, M. N. Ofitserov, and N. N. Prentslau, Fiz. Nizk. Temp. **16**, 387 (1990) [Sov. J. Low Temp. Phys. **16**, 214 (1990)].

[5] V. P. Galaĭko, V. M. Dmitriev, M. N. Ofitserov, and N. N. Prentslau, Fiz. Nizk. Temp. **19**, 135 (1993) [Low Temp. Phys. **19**, 96 (1993)].

[6] A. A. Abrikosov, L. P. Gor'kov, and I. E. Dzyaloshinskiĭ, *Methods of Quantum Field Theory in Statistical Physics*, Prentice-Hall, Englewood Cliffs, N.J. (1963), Fizmatgiz, Moscow (1962).

[7] L. P. Kadanoff and G. Baym, *Quantum Statistical Mechanics: Green's Function Methods in Equilibrium and Nonequilibrium Problems* [Benjamin, New York (1962); Mir, Moscow (1964)].

[8] G. H. Wannier, Rev. Mod. Phys. **34**, 645 (1962).

[9] A. L. Solovjov, Fiz. Nizk. Temp. **24**, 161 (1998) [Low Temp. Phys. **24**, 215 (1998)].

[10] A. L. Solovjov, private communication.

Translated by Steve Torstveit

LOW TEMPERATURE PHYSICS

VOLUME 28, NUMBER 5

MAY 2002

Characteristics of the electric field accompanying a longitudinal acoustic wave in a metal. Anomaly in the superconducting phase

Yu. A. Avramenko, E. V. Bezuglyi, N. G. Burma, I. G. Kolobov, V. D. Fil',* and O. A. Shevchenko

B. Verkin Institute for Low Temperature Physics and Engineering, National Academy of Sciences of Ukraine, pr. Lenina 47, 61103 Kharkov, Ukraine

V. M. Gokhfeld

A. A. Galkin Donetsk Physicotechnical Institute, ul. R. Lyuksemburg 72, 83114 Donetsk, Ukraine

The temperature dependence of the amplitude and phase of the electric potential arising at a plane boundary of a conductor when a longitudinal acoustic wave is incident normally on it is investigated theoretically and experimentally. The surface potential is formed by two contributions, one of which is spatially periodic inside the sample, with the period of the acoustic field; the second is aperiodic and arises as a result of an additional nonuniformity of the electron distribution in a surface layer of the metal. In the nonlocal of parameters region the second contribution is dominant. The phases of these contributions are shifted by approximately $\pi/2$. For metals found in the normal state the experiment is in qualitative agreement with the theory. The superconducting transition is accompanied by catastrophically rapid vanishing of the electric potential, in sharp contrast to the theoretical estimates, which predict behavior similar to the BCS dependence of the attenuation coefficient for longitudinal sound. © *2002 American Institute of Physics.* [DOI: 10.1063/1.1480239]

1. INTRODUCTION

When an elastic wave propagates in a metal, a perturbation of its electron subsystem occurs which compensates the tendencies of the ionic displacements to disrupt the charge neutrality or the balance between the ion and electron currents. At high temperatures or in dirty samples (the so-called local limit, determined by the condition $ql \ll 1$, where q is the acoustic wave vector and l is the electron mean free path) the electron collision frequency is high enough to maintain local equilibrium at any point of the deformed lattice. In the limit $ql \ll s/v_F$ (s and v_F are the sound velocity and Fermi velocity) the electric field arising in the metal has a purely inertial nature—the acoustic analog of the Stewart–Tolman effect.

In the opposite limiting case ($ql \gg 1$, nonlocal limit) the collisions can no longer maintain local equilibrium, and additional electric fields are produced in the metal, bringing about the required adjustment of the electrons to the moving lattice. In zero magnetic field, the polarization of the electric field of an elastic wave propagating in an isotropic metal or along a high-symmetry direction is parallel to the ionic displacements. When a magnetic field is turned on, the Lorentz force exerted on the electrons moving with the lattice gives rise to a Hall component of the alternating electromagnetic field, the existence of which is no longer dependent on strict requirements on the purity or temperature of the sample.

The opposite process also occurs: the generation of acoustic vibrations when a polarized electromagnetic field is excited in the metal in a suitable way. On the whole, these phenomena—the acoustoelectric and electroacoustic transformations—are well known and widely used both in scientific experiments and for contactless excitation of sound in technical applications (see, e.g., the review[1]).

However, as far as the authors are aware, the experimental studies have always been done for electromagnetic fields in which the electric field vector was orthogonal to the wave vector of the elastic wave.[1] The latter is apparently due to the fundamental differences in the behavior of the fields of transverse and longitudinal polarization at the interface between the metal and free space (or an insulating medium). For normal incidence of a transverse elastic mode on the interface the electromagnetic field in the metal is naturally "matched" with the electromagnetic field in the vacuum (insulator). In other words, in this geometry an electromagnetic wave is radiated from the metal; this wave can easily be detected by a suitably oriented antenna of the flat-coil type. This same antenna can also be used to generate a transverse elastic wave in the metal.

An electromagnetic wave with electric field polarized along the wave vector does not exist. Therefore, in the case of normal incidence of a longitudinal acoustic wave on the interface, electromagnetic radiation from the sample is absent in principle. Nevertheless, it is possible to detect the electric field **E** due to a longitudinal acoustic wave. Since div **E** $\neq 0$ in a longitudinal wave, uncompensated charge and the accompanying potential appear both in the bulk of the metal and on its surface.[4] This potential can be detected by a voltmeter of suitable sensitivity. One of the authors (V.M.G.) long ago had analyzed a method of linear electroacoustic conversion with the use of a contactless capacitive driver.[5] Here, when an alternating voltage is applied to the exciting plate of the capacitor, an electric charge is induced beneath it

on the surface of the metal, and the nonlocal interaction of this charge with the lattice excites a longitudinal elastic wave of the same frequency. A detailed experimental check of Ref. 5 has not been made, possibly because of the rather stringent requirements on the purity of the metal. The limiting case of a capacitive driver (receiver) is a galvanic contact, which is what was mainly used in the present study. Finally, the presence of the contact on the interface alters the boundary conditions for the elastic deformations; however, it turns out that the latter leads to a slight increase in the conversion efficiency and in general relaxes the requirements on the purity of the material under study. For this reason it is possible to carry out an experiment on practically all reasonably pure metals provided that some relatively simple requirements are met as to the nonlocality of the interaction of the electrons with the elastic field ($ql>1$).

The structure of this paper is as follows. In Sec. 2 a theory of the acoustoelectric conversion is given for the simplest case—a conducting half space (one-dimensional problem) in the approximation of an isotropic dispersion relation for the carriers and their "specular" reflection by the interface. The electric potential accompanying an elastic wave in the metal is a sum of two contributions. Besides the well-known forced solution, which repeats the profile of the elastic deformations, in the nonlocal limit there is also a substantial quasiperiodic term due to the perturbation of the ballistic motion of the electrons by the surface of the sample.

In Sec. 3 we present the results of experimental studies of the temperature dependence of the aforementioned electric potential in metals of different degrees of purity (Ga, W, Al) in the normal state. On the whole, the temperature dependences of the amplitude and phase of the potential show an acceptable qualitative agreement with the theoretical estimates; this can be regarded as experimental confirmation of the theoretical ideas proposed here.

In Sec. 4 we discuss the evolution of the measured electric potential at the superconducting transition. Contrary to the expectation of a rather slow decrease in the recorded value below T_C (like the behavior of the longitudinal sound attenuation coefficient), a much sharper decrease in the amplitude of the potential is observed.

2. THEORY OF ACOUSTOELECTRIC CONVERSION IN THE CASE OF NORMAL INCIDENCE OF A SOUND WAVE ON AN INTERFACE

Let us consider a metallic half space $x \geq 0$. Suppose that a longitudinal elastic wave $u_x = u_0 \exp(-i\omega t - iqx)$ comes in from the interior of the sample and is reflected from the sample boundary with a reflection coefficient R (we neglect the sound attenuation). Near the boundary the displacement field and the deformation field are formed as a result of the interference of the incident and reflected waves, independently of the regime (pulsed or continuous). The resultant field is conveniently expressed in terms of the amplitudes of the displacement $u(0)$ and deformation $u'(0)$ at the interface. In particular, for the deformation field that we will be interested in below we can write

$$\frac{du_x(x)}{dx} \equiv u_{xx}(x) = u'(0)\cos qx - qu(0)\sin qx. \tag{1}$$

The relation between $u(0)$ and $u'(0)$ is determined by the boundary conditions

$$\frac{qu(0)}{iu'(0)} = \frac{1+R}{1-R} \equiv C. \tag{2}$$

For a contact with an elastically uniform, nonattenuating medium the parameter C is equal to the ratio of the acoustic impedances of the metal and of the medium in contact with it (in particular, $C=\infty$ for a contact with the vacuum). In the case of an attenuating medium the parameter C can be complex-valued.

The deformation-induced deviation $\psi(x,v_x)\partial f_0/\partial\varepsilon$ of the electron distribution function from its equilibrium f_0 is described by the kinetic equation[6] (we are neglecting the inertial field):

$$v_x\frac{\partial}{\partial x}(\psi - e\varphi) - i\tilde{\omega}\psi = -i\omega\Lambda_{xx}u_{xx}. \tag{3}$$

Here $\tilde{\omega} \equiv \omega + i/\tau$ (ω is the angular frequency, and τ is the electronic relaxation time), Λ_{xx} is the corresponding component of the deformation potential tensor $\Lambda_{ik} = \lambda_{ik} - \langle\lambda_{ik}\rangle/\langle 1\rangle$, λ_{ik} is the "bare" deformation potential, $\varphi(x)$ is the electric potential in the field of the elastic wave, v_x is the x component of the Fermi velocity v_F of the electron, and the angle brackets denote averaging over the Fermi surface with a weight v_F^{-1}:

$$\langle A\rangle \equiv \frac{2}{(2\pi\hbar)^3}\int\frac{A\,dS}{v_F}.$$

It is important to note that the quantity $e\varphi(x)$ appearing in Eq. (3) is actually the total electrochemical potential of the electrons, including, in addition to the "true" electric potential, the change of the chemical potential $u_{xx}\langle\lambda_{xx}\rangle/\langle 1\rangle$ due to the change of the electron spectrum in the elastic deformation field.[6] The difference of the electrochemical potentials at different points of the sample is a source of real emf that can be registered by a voltmeter, and it, of course, vanishes at equilibrium, e.g., in the limit of a static deformation ($\omega \rightarrow 0$). At the same time, the gradient of the "true" electric potential, which compensates the deformation contribution to the electrochemical potential and brings about an adjustment of the electron density to the spatial variations of the ion density is always nonzero in a nonuniformly deformed sample (physically this effect is analogous to a contact potential difference). The presence of this potential in a nonuniformly deformed metal (including in the elastic field of a sound wave) gives rise to uncompensated charges with a density $\delta n = r_D^2\langle\lambda_{xx}\rangle\nabla^2 u_{xx} \sim (qr_D)^2 qun$, where n is the total electron density, q is the characteristic wave number of the deformation, and r_D is the screening radius of the longitudinal field ($r_D^{-2} = 4\pi e^2\langle 1\rangle$), which in "good" metals is of the order of magnitude of the lattice constant. Such a "charge density wave" accompanying the propagation of a sound wave in the general case contains a nonequilibrium contribution due to the disruption of the spatial uniformity of the electrochemical potential $e\varphi(x)$; this contribution is proportional to the frequency of the sound (see below) but in the majority of cases is small ($\sim s/v_F$) compared to the "adiabatic" component mentioned above. To avoid misunderstandings we should say that, because of the small value of

the uncompensated charge ($\delta n \ll n$) the potential $\varphi(x)$ can, of course, be calculated from the condition of electrical neutrality $\langle \psi \rangle = 0$, where $\langle \psi \rangle$ has the meaning of a nonequilibrium admixture to the charge density which is "adiabatically" modulated by the elastic field.

Far from the boundary ($x \gg l$) one can assume that the unknown functions $\psi(x)$ and $\varphi(x)$ are periodic, with the same spatial period as $u(x)$,[6] and in this case Eq. (3) reduces to an algebraic equation. Near the interface (at distances $x \lesssim l$ from it) the electron distribution differs substantially from periodic, and the problem of finding $\psi(x)$ and $\varphi(x)$ is complicated. It can be solved relatively simply by the Fourier method if the so-called specular boundary condition is imposed on the function $\psi(x)$:

$$\psi(+0, v_x) = \psi(+0, -v_x). \tag{4}$$

We emphasize that the condition of "specular" reflection from the moving boundary can be written in the form (4) only in a comoving reference frame, in which there is no current through the boundary ($\langle v_x \psi(0, v_x) \rangle = 0$), and the scattering of the electrons is elastic. Since the potential measurement is actually done at a moving boundary, all of the calculations below pertain to the comoving system, in which the form (3) of the linearized kinetic equation is preserved.

Let us continue the functions $u_{xx}(x)$ and $\varphi(x)$ evenly onto the semiaxis $x < 0$ (this will be denoted below by a superscript S). Then from the form of Eq. (3) (in view of the evenness of $\Lambda_{xx}(v_x)$ it is symmetric with respect to a simultaneous change of the signs of x and v_x) and condition (4) it follows that the unknown function $\psi(x)$ should be continued to $x < 0$ without a discontinuity. As a result, its transform is equal to

$$\psi_k = \frac{k v_x (\varphi^S)_k - \omega \Lambda_{xx}(u_{xx}^S)_k}{k v_x - \widetilde{\omega}}. \tag{5}$$

The Fourier transform of the electric potential $(\varphi^S)_k$ of interest is found from the condition of electrical neutrality of the metal, $\langle \psi_k \rangle = 0$:

$$(\varphi^S)_k = (u_{xx}^S)_k \left\langle \frac{\omega \Lambda_{xx}}{k v_x - \widetilde{\omega}} \right\rangle \left\langle \frac{k v_x}{k v_x - \widetilde{\omega}} \right\rangle^{-1} \equiv (u_{xx}^S)_k R_k, \tag{6}$$

where

$$(u_{xx}^S)_k = q \left(\frac{q u(0) - i u'(0)}{k^2 - (q+i0)^2} + \frac{q u(0) + i u'(0)}{k^2 - (q-i0)^2} \right) \tag{7}$$

is the transform of the deformations (1).

Integration over the Fermi surface in (6) leads to branch points $k = \pm K$ ($K = \widetilde{\omega}/v_F$) of the kinetic coefficient R_k; these singularities are in addition to the "acoustic" poles $k = \pm (q \pm i0)$ of expression (7). Undoing the Fourier transform, we find that in addition to the purely periodic forced solution mentioned above, which is determined by the poles (the q contribution), the function $\varphi(x)$ also contains an aperiodic term, whose amplitude is a complicated function of x and whose phase ($\sim \omega x/v_F$) is determined by the Fermi velocity (K contribution).

The asymptotics of the solutions of this type at large depths have been discussed previously on more than one occasion in the analysis of the propagation of electron quasiwaves in a metal.[5,7,8] In the present paper we will be interested in the relationship of the K and q contributions to the electric potential $\varphi(0)$ measured at the boundary of the metal and their respective temperature dependences.

Let us see what the solution (6) gives in the simple case of a quadratic isotropic dispersion relation of the charge carriers, $\varepsilon = p^2/2m$, when the deformation potential can be represented in the form[6]

$$\Lambda_{xx} = L(3 v_x^2/v_F^2 - 1). \tag{8}$$

In this case the kinetic factor in (6) is easily calculated and is equal to

$$R_k = \frac{\omega L}{\widetilde{\omega}} \Phi(z); \quad \Phi(z) = \frac{3}{z^2} - \frac{\ln \dfrac{1-z}{1+z}}{2z + \ln \dfrac{1-z}{1+z}},$$

$$z = \frac{k v_F}{\widetilde{\omega}} \equiv \frac{kl}{\omega \tau + i}. \tag{9}$$

To find the coefficient of proportionality between $u_{xx}(x)$ [see Eq. (1)] and the q contribution to $e \varphi(x)$, it is sufficient to substitute $k = q$ in (9); thus, in the x representation we obtain

$$e \varphi_q(x) = R_q u_{xx}(x); \quad R_q = L \frac{s}{v_F} a \Phi(a),$$

$$a \equiv \frac{v_F}{s} \frac{\omega \tau}{\omega \tau + i}. \tag{10}$$

Let us now evaluate the K contribution. According to what we have said, it is given by the integral

$$e \varphi_K(x) = \int_C \frac{dk}{2\pi} (u_{xx}^S)_k R_k \exp(ikx) \tag{11}$$

over a contour C passing along the edges of the branch cut $k = y \widetilde{\omega}/v_F$ ($1 \leqslant y < \infty$) in the complex k plane. Using formulas (6), (7), and (9), we can write this integral in the form

$$e \varphi_K(x) = i \omega u(0) \frac{L}{v_F} \int_1^\infty dy \frac{y a^2}{a^2 - y^2} \left[\left(y + \frac{1}{2} \ln \frac{y-1}{y+1} \right)^2 \right.$$

$$\left. + \frac{\pi^2}{4} \right]^{-1} \exp\left(\frac{i y \widetilde{\omega} x}{v_F} \right) \equiv i \omega u(0) \frac{L}{v_F} J(a, x). \tag{12}$$

We note that the K contribution at any x is proportional to the displacement of the surface, $u(0)$, while the q contribution is proportional to the local deformation $u'(x)$. This means that upon a variation of the surface potential by means of a capacitor with a vacuum (gas-filled) gap—an elastically free surface—we can record only the K contribution. In the general case, by adding (10) and (12) together we obtain for the potential measured on the surface:

$$\varphi(0) = \varphi_q(0) + \varphi_K(0)$$

$$= -i \frac{L}{e v_F} \left(\frac{2I}{\rho s} \right)^{1/2} \left[\frac{a \Phi(a)}{C} - J(a, 0) \right], \tag{13}$$

where I is the energy flux in the sound beam, and ρ is the density of the conducting medium.

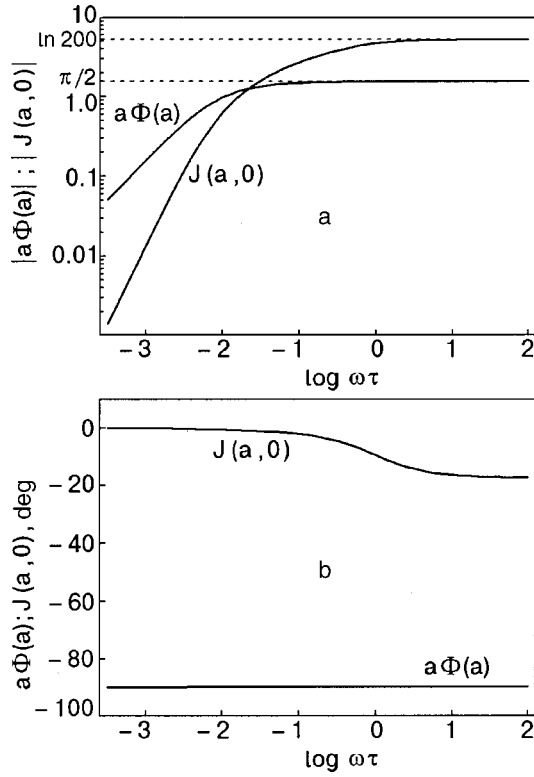Let us estimate the expected value of the effect. The coefficient in formula (13) at $L \sim 10$ eV and $I \sim 10$ W/cm^2

FIG. 1. Theoretical dependence of the amplitude (a) and phase (b) of the periodic (Φ) and aperiodic (J) contributions to the surface electric potential, as functions of the scattering parameter.

has a value close to $\simeq 1\ \mu$V. The dependence of the functions $|a\Phi(a)|$ and $|J(a,0)|$ on the parameter $\omega\tau$ is presented in Fig. 1. In the nonlocal region of frequencies and temperatures ($ql>1$) the first of these rapidly approaches its limiting value $|a\Phi(a)|=\pi/2$, whereas the second varies as $\ln|a|$; for $\omega\tau\gg1$ its limiting value $|J(v_F/s,0)|\approx\ln(v_F/s)$, which is practically always greater than $\pi/2$ (the curves in Fig. 1 were constructed for the parameter value $v_F/s=200$ ($\ln v_F/s=5.3$), which is typical of gallium). Thus the expected value of the effect is at the level of a few microvolts, i.e., quite amenable to measurement.

In Fig. 1 we see that for $C\sim1$ the contributions under discussion become equal at $ql\sim1$. The phases of these contributions, however, are shifted by $\pi/2$, and therefore on the curves of the temperature dependence of $\varphi(T)$ one should expect an appreciable change in the phase of the signal in the temperature region where the mean free path becomes comparable to the wavelength of the sound.

Of course, the specular boundary condition used does not fully correspond to the experimental situation; however, it is known that taking more realistic boundary conditions (the diffuseness of the boundary) into account in nonlocal problems of acoustoelectronics complicates the calculations significantly without leading to any substantial changes in the results.[9] It can be hoped that in the given case the behavior of $\varphi(0)$ will correspond qualitatively to the behavior that follows from (13).

At the parameter values used, the amplitude of the adiabatic component of the charge density wave accompanying the propagation of a sound wave in a metal is of the order of $10^8\ \mathrm{cm}^{-3}$. Let us now estimate the contribution of the non-

equilibrium potential $\varphi(x)$ to the amplitude of the wave of uncompensated charge density. In the general case one can find its value by solving Eq. (5) jointly with Poisson's equation $k^2\varphi_k=4\pi e\langle\psi_k\rangle$. As a result, for the nonequilibrium admixture to the charge density we obtain

$$\langle\psi_k\rangle=-(u^S_{xx})_k\left\langle\frac{\omega\Lambda_{xx}}{kv_x-\widetilde{\omega}}\right\rangle\left(1+\frac{4\pi e^2}{k^2}\left\langle\frac{kv_x}{kv_x-\widetilde{\omega}}\right\rangle\right)^{-1}. \tag{14}$$

The final answer depends on the relationship between the squares of the inverse screening radius and the actual wave number. For the periodic component of the charge density wave ($qr_D\ll1$) the 1 in the denominator of (14) can be neglected at any distance from the surface of the metal, i.e., the answer reduces to a double differentiation of the potential φ_q found previously from the condition of electrical neutrality. As a result, the amplitude of this component turns out to be small ($\sim s/v_F$) in comparison with the adiabatic contribution. To estimate the K contribution at distances $x\gg r_D$ from the surface this approximation is again applicable, since in this case the convergence of the integrand in (12) (which acquires an additional factor of k^2 after the double differentiation with respect to x) at large k is provided by the exponential factor, and the 1 in the denominator of (14) can again be neglected. This allows us to obtain the following estimate for the uncompensated charge of the K component at distances from the surface which are small compared to the mean free path and the wavelength of the sound:

$$\delta n(x)=-i\omega u(0)\frac{L}{v_F}\frac{q^2}{4\pi e^2}\ln\frac{v_F}{x\widetilde{\omega}}. \tag{15}$$

Thus the uncompensated charge of the K component increases logarithmically as $x\to0$, reaching a maximum value in the surface region $x\lesssim r_D$. The density of this surface charge can be estimated to logarithmic accuracy by employing a cutoff at $k\sim r_D^{-1}$ in the total denominator of expression (14) and making the substitution $x\to r_D$ in Eq. (15); this leads to a value $\delta n\sim10^8\ \mathrm{cm}^{-3}$, which is comparable to the amplitude of the adiabatic component.

We conclude this Section by verifying the applicability of the reciprocity theorem for the "exotic" mechanism of acoustoelectric coupling under consideration. In this case the acoustoelectric converter would be of the electrostatic type, in which the ponderomotive forces are due to the interaction of the electric charges. For converters of this type the electromechanical reciprocity theorem can be formulated as[10]

$$\frac{\partial F}{\partial g}=\frac{\partial\varphi}{\partial u}, \tag{16}$$

where F is the density of the mechanical force, which is causally related to the uncompensated charge density g, while the remaining components are the same as those already used. The relation between the electric field and the periodic elastic displacement is written in the form $\mathbf{u}=B\mathbf{E}$. Since $F=\rho s^2 d^2u/dx^2$ and $g=\mathrm{div}\,\mathbf{E}/4\pi$ (since we are seeking an harmonic component of the displacements, differentiation with respect to x reduces to multiplication by q), and, using formula (12) for a free surface ($C=\infty$), we find $B\approx L\ln(v_F/s)/(4\pi\rho sev_F)$, which agrees exactly with the result obtained in Ref. 5.
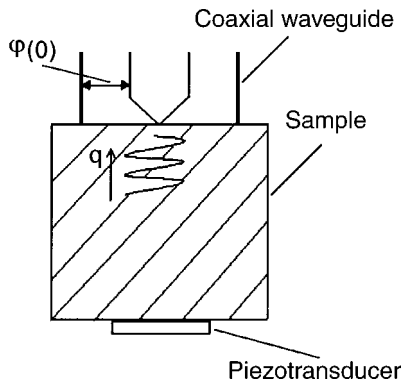
FIG. 2. Diagram of the experiment.

3. EXPERIMENTAL STUDY OF THE SOUND-GENERATED SURFACE POTENTIAL IN CONDUCTORS FOUND IN THE NORMAL STATE

The basic scheme of the experiment is illustrated in Fig. 2. The sample under study is used to short a coaxial feeder, the outer conductor of which is in contact with the sample outside the region of incidence of the sound beam. The inner, spring-loaded conductor is a fragment of a hemisphere of rather large radius (~ 1 cm). Thus the experiment measures the amplitude and phase of the potential difference between the central part of the "hot" spot created by a sound beam of diameter ~ 4 mm and the remote parts of the surface of the sample at zero potential. In some experiments the galvanic contact of the inner conductor of the coaxial feeder with the sample was replaced by a capacitive coupling ($C \sim 5$ pF), or in some cases a flat (planar) coil displaced relative to the axis of symmetry of the sound beam was used to detect the magnetic field of the currents spreading out from the "hot" spot (this will be referred to below as an asymmetric coil).

An rf oscillator ($\omega/2\pi \sim 55$ MHz) and a lithium niobate piezotransducer were used, giving a maximum acoustic power per pulse of up to 50–100 W/cm^2. The pulse duration ($\sim 5 \times 10^{-7}$ s) and the pulse repetition rate (~ 17 Hz) were chosen so that the heating of the sample at a temperature $T \sim 1$ K did not exceed $(2$–$3) \times 10^{-2}$ K.

Gallium. Single-crystal samples of high-purity gallium were used, ensuring a parameter value $\omega\tau \sim 5$ at the working frequency in the region of impurity scattering.

When the potential was registered using the galvanic contact, in addition to the signal coincident in time of arrival with the acoustic pulse, an electron-sound signal, passing through the sample at the Fermi velocity, was also observed (for temporal separation of the latter from the signal appearing at the time of the probe pulse, a germanium delay line, not shown in Fig. 2, was used). Analysis of the nature of the electron sound is proposed as the subject of a separate study; in this paper we discuss only the electric potential arising on the surface of the sample at the time of arrival of the sound pulse.

The maximum response at a fixed excitation power could be attained only for freshly ground surfaces; prolonged storage of a sample led to a falloff of the signal amplitude, apparently because of diffusion of impurities into the subsurface region. At $T = 1.5$ K the value of $|\varphi(0)|$ at the maximum excitation power reached 30–50 μV. The characteristic

value of the Fermi velocity on the main sheets of the Fermi surface of gallium is $v_F \approx 7 \times 10^7$ cm/s,[11] and therefore in accordance with the estimate (13) a large value of the deformation potential ($L \approx 20$ eV) is required in order to obtain such values of $\varphi(0)$. It is also possible that the main contribution to the effect is given by sheets of the Fermi surface on which the Fermi velocity is low, which are known to exist in gallium.[11]

Typical curves of the temperature dependence of the amplitude and phase of the potential measured with the use of a galvanic contact are presented in Fig. 3. The data for $|\varphi(0)|$ are corrected for the change in sound attenuation in the sample. The resultant phase of the signals is determined not only by the phase of $\varphi(0)$ but also, and mainly, by the acoustic delay. However, in the investigated temperature interval the corrections due to the change in the sound velocity did not exceed a few percent of the measured total variations of the phase.

For Ga the temperature dependence of the relaxation time is known quite well,[12] and therefore in Fig. 3 we also show the calculated curves obtained at $C = 1$. The calculations were done on the assumption that low-angle scattering is efficient $[(\omega\tau)^{-1} = 0.2 + 0.05T^2 + 0.15T^3]$, although this question requires separate investigation. Without going into the details of the anisotropy of the effect, which is clearly seen on the experimental curves, we will mention the two circumstances that we think are essential.

1. As expected from the analysis given above, the phase of $\varphi(0)$ experiences significant ($\sim \pi/2$) variation in the temperature region corresponding to the transition from the non-
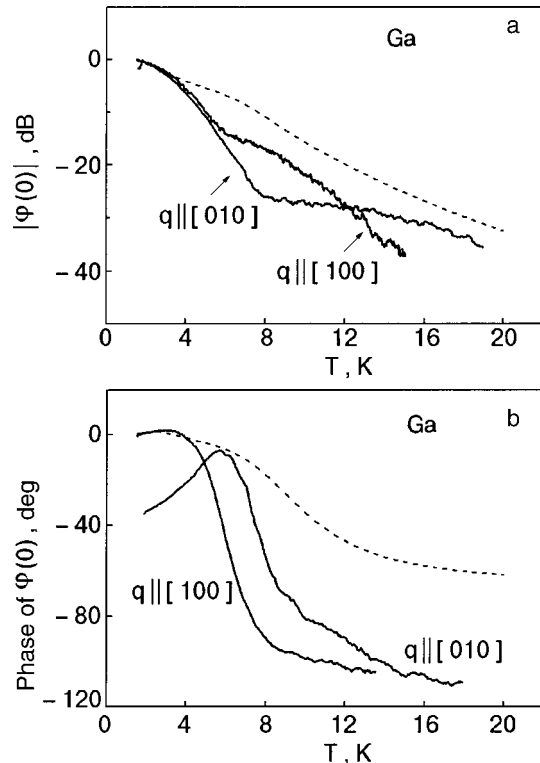

FIG. 3. Amplitude (a) and phase (b) of the potential $\varphi(0)$ measured with a galvanic contact on Ga in the propagation of sound along different crystallographic directions (solid curves) at a frequency of 55 MHz. The dashed curve shows the result of a calculation according to Eq. (13) for $C = 1$, $(\omega\tau)^{-1} = 0.2 + 0.05T^2 + 0.15T^3$, $v_F/s = 200$.

local to the local regime. On the whole, the scale of the variations of the amplitude and phase of $\varphi(0)$ agree with the calculation. There is justification for thinking that the stated theoretical ideas about the nature of the origin of $\varphi(0)$ and the decisive role of the K contribution at large values of ql are in qualitative agreement with experiment.[2)]

2. The calculation gives a much smoother variation of the amplitude and phase of $\varphi(0)$ in the crossover region than is observed in experiment. The kink in the temperature dependence of the amplitude, which coincides with the center of the "jump" in phase, cannot be described using Eq. (13), even when the model parameters are varied over wide limits. Apparently, the rate of decrease of the K contribution in the crossover region is substantially higher than is predicted by Eq. (13). This circumstance is probably due to the "specularity" and isotropicity of the dispersion relation which were imposed on the model, and the solution for a more realistic case will be closer to the observed behavior of $\varphi(0)$.

Let us also mention some other features of the behavior of the phase of $\varphi(0)$. For $q\|[010]$ at $T<6$ K the phase of the signal increases with increasing temperature (Fig. 3b). This behavior occurs only in that geometry, and it is most likely due to the broad flattening on the Fermi surface of Ga in the $\mathbf{q}\cdot\mathbf{v}=0$ region.[13] It is easy to see from the relations given above that in this case, for $\omega\tau\sim1$, the increase in the scattering leads to growth of the phase of the q contribution while having practically no effect on the K contribution. The model calculation according to Eq. (13) with the actual relative area of the flat part taken into account ($\sim2-4\%$; Ref. 13) gives a good description of both the scale of this effect and its temperature dependence.

It follows from Fig. 3b that the change in phase of the signal in the crossover region is assuredly in excess of $\pi/2$. This is possible due to the complex nature of the parameter C in the case of reflection of sound from a contact region of small size. If C in Eq. (13) has the form $C=C_0(1+i\beta)$ ($\beta>0$), then in the nonlocal parameter region, where the contribution from the first term in (13) predominates, the influence of β is insignificant. However, on going to the local limit the phase of the harmonic component turns out to be lower than the calculated value by an amount $\arctan(\beta)$.

In the proposed conception of the origin of $\varphi(0)$ the variation of the phase of the recorded signal is due to the fact that the interface in the contact region is elastically non-free ($u'(0)\neq0$, i.e., $C^{-1}\neq0$). To check this idea, we replaced the galvanic contact with a capacitor with a vacuum gap (more precisely, a gap filled with a heat-exchange gas). The result is shown in Fig. 4. In view of the small value of the capacitance (as we were striving to avoid edge effects, the electrode forming the capacitor had a diameter of ~2 mm) we were unable to make measurements in the same temperature interval as in Fig. 3. Nevertheless, it is reliably established that in this case there is no significant decrease of the phase of the signal. We assume that this result, taken together with the data of Fig. 3b, is unambiguous evidence in support of the approach developed here. Moreover, relation (12) also predicts a certain increase in the phase of the K contribution with increasing scattering even in the purely isotropic approximation; this is apparently registered by the capacitive sensor, although on a larger scale (Fig. 4b).
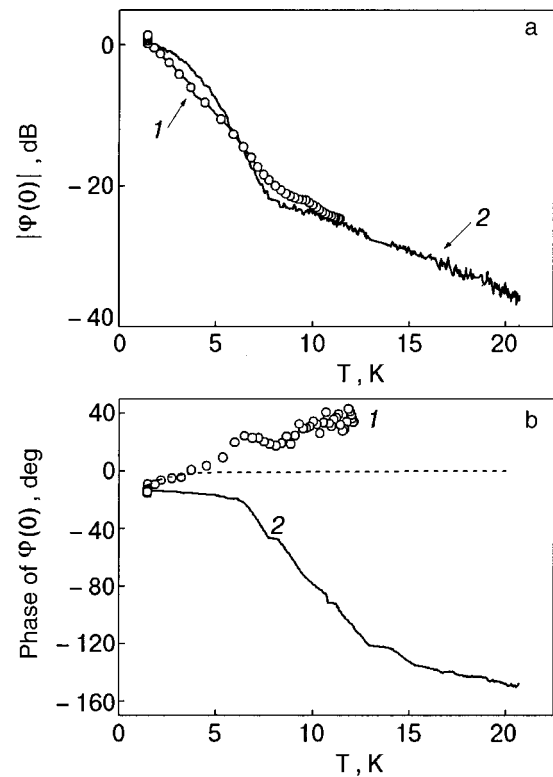

FIG. 4. Amplitude (a) and phase (b) of the potential $\varphi(0)$ measured on Ga with a capacitive sensor (*1*) and an asymmetric coil (*2*) (solid curves). The dashed curves show the results of a calculation according to Eq. (12) (the parameters used in the calculation were the same as in Fig. 3).

The presence of excess surface charge in the region of the "hot" spot presupposes the existence of currents spreading out from the center of the sample toward the periphery. To detect them we used a flat coil asymmetrically shifted relative to the center of the sample. The plane of the turns of this coil were oriented perpendicular to the interface and parallel to the radial direction, the surface of the sample in the region of the "hot" spot was left elastically non-free. The results of this experiment are also presented in Fig. 4. The amplitude of the signal behaves analogously to that shown in Fig. 3a, while the phase of the signal deviates even more to the high side of $\pi/2$. Most likely this is due to the fact that the rf conductivity of the metal, being a complex quantity, varies in phase on going to the local limit, thereby altering the phase of the rf current as well, so that the total shift increases.

Tungsten and aluminum. In tungsten in the impurity-scattering region the value of the parameter $\omega\tau$ is approximately equal to 1, while in aluminum $\omega\tau\approx0.3$. It should be noted, however, that our estimates of the impurity scattering were obtained from a study of the bulk characteristics and can be somewhat overestimated for the surface regions. The values of $|\varphi(0)|$ measured in these metals turned out to be substantially smaller than in gallium ($\sim1\ \mu$V). This is clearly due to the small value of the deformation potential, since a slight (see Fig. 1) increase in the scattering (i.e., decrease in the parameter $\omega\tau$ in comparison with gallium) should not lead to a substantial decrease in $|\varphi(0)|$.

Curves of the temperature dependence of the amplitude and phase of $\varphi(0)$ for W and Al are shown in Fig. 5. In spite
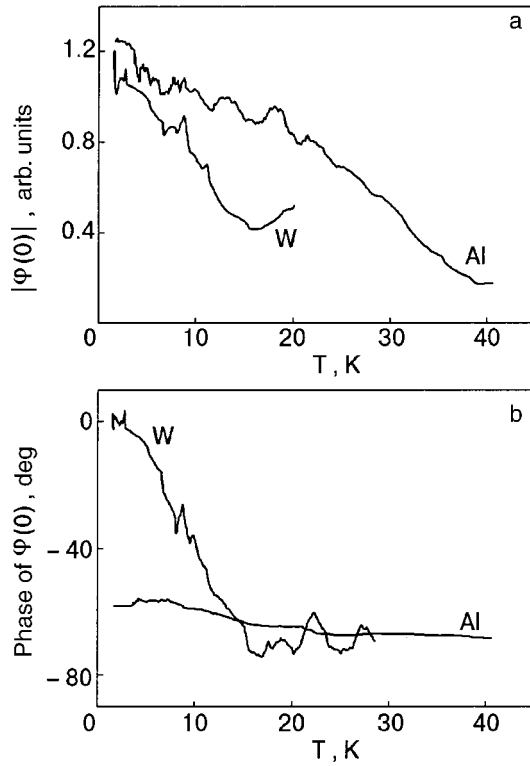
FIG. 5. Amplitude (a) and phase (b) of the potential $\varphi(0)$ measured with a galvanic contact on W and Al.

of the small value of the detected signal, the curves for tungsten qualitatively repeat the behavior of $\varphi(0)$ in Ga, the most salient feature of which, in our view, is the significant variation of the phase of the signal. In Al the phase of the signal is practically unchanging. It can be supposed that, as in Ga, the more rapid (in comparison with Eq. (13)) falloff of the K contribution has led to its nearly complete suppression already at the starting (impurity) value of $\omega\tau$.

4. INFLUENCE OF THE SUPERCONDUCTING TRANSITION ON $\varphi(0)$

Before turning to a description of the experimental results, let us briefly present the theoretical scheme for estimating the possible behavior of $\varphi(0)$ below T_C. It follows from the above discussion that the existence of a measurable potential $\varphi(0)$ is due to the deformation interaction of the electrons with the elastic field of a longitudinal wave. In a superconductor only normal excitations interact with sound through the deformation potential. The "freezing out" of the normal excitations leads to the situation that for $T \ll T_C$ the potential $\varphi(0)$ is due solely to the Stewart–Tolman inertial field, which we are neglecting in this paper. Consequently, our problem consists in estimating the decay law of $\varphi(0)$ below T_C.

In a superconductor the electromagnetic field is customarily described by a gradient-invariant combination of Φ (the electrochemical potential of the excitations) and $\mathbf{p}_s$ (the momentum of the superconducting condensate) and the spatial and time derivatives of the phase of the order parameter χ and the electromagnetic potentials φ and $\mathbf{A}$:

$$\Phi = \frac{1}{2}\frac{\partial}{\partial t}\chi + e\varphi, \quad \mathbf{p}_s = \frac{1}{2}\nabla\chi - \frac{e}{c}A. \tag{17}$$

In Ref. 14, which is devoted to the general theory of elasticity in superconductors, a relation is obtained between the fields Φ and $\mathbf{p}_s$ and the elastic displacements $\mathbf{u}$. In the case of longitudinal sound and an isotropic one-dimensional model, one can, using Ref. 14, write the following relations for the Fourier components of Φ and p_s:

$$-a\Phi = cp_{sx} + i\omega c^{(d)}mu,$$
$$-(ab + c^2)p_{sx} = i\omega(ab^{(d)} = cc^{(d)})mu. \tag{18}$$

The solution of the boundary-value problem analogous to that considered above but for superconductors meets with considerable difficulties due to the energy dependence of the velocity of normal excitations,[15] and therefore for making estimates we limit consideration to the q contribution only, for which the wave vector of the Fourier component coincides with the wave vector of the sound. Asymptotic expressions for the polarization coefficients a, b, and c of the electron subsystem and the electroacoustic coefficients $c^{(d)}$ and $b^{(d)}$, which were all found in Ref. 14 in the limit of strong spatial dispersion ($ql \gg 1$), have the form

$$a = 1 + i\frac{\pi}{2}\frac{s}{v_F}f(\Delta), \quad b = \frac{L}{m}\left(\rho_S - \frac{3\pi}{2}i\frac{s}{v_F}\frac{\Delta/4T}{\cosh^2(\Delta/4T)}\right),$$

$$c = s(1 - \rho_S), \quad b^{(d)} = i\frac{\pi}{2}\frac{s}{v_F}\frac{L}{m}\left(1 + \frac{\Delta}{2T}\ln\frac{Tv_F}{\Delta s}\right),$$

$$c^{(d)} = -i\frac{\pi}{2}\frac{L}{mv_F}f(\Delta), \tag{19}$$

where $\rho_s \approx 2(T_C - T)/T_C$ is the density of the superconducting condensate, $f(\Delta) = 2/(\exp(\Delta/T) + 1)$ is the Fermi function, and $\Delta(T)$ is the superconducting gap.

Restricting consideration in (18) and (19) to the first nonvanishing terms of the expansion in the small parameter s/v_F and assuming that the inequalities $\rho_s, \Delta/T > (s/v_F)^2$ hold, we find

$$\Phi = i\omega\frac{cb^{(d)} - bc^{(d)}}{ad + c^2}mu = -i\omega c^{(d)}mu,$$

$$p_s = -i\omega\frac{ab^{(d)} + cc^{(d)}}{ab + c^2}mu = -i\omega\frac{b^{(d)} + sc^{(d)}}{b}mu. \tag{20}$$

In the case of longitudinal sound the vector potential in (17) can be dropped, and we obtain for the electric potential

$$e\varphi(x) = \Phi(x) - sp_s(x). \tag{21}$$

It follows from (19)–(21) that the contribution p_s to the periodic component of the potential is small in the parameter s/v_F and can also be dropped, and the relation between the amplitudes of the potential and the normal (n) and superconducting (sc) states has the form

$$(e\varphi)_{sc} = (e\varphi)_n f(\Delta), \tag{22}$$

i.e., the q contribution should fall off with decreasing temperature in the same way as the sound attenuation coefficient. In addition, it follows from (22) that the phase of the potential should not change on transition through T_C. Since
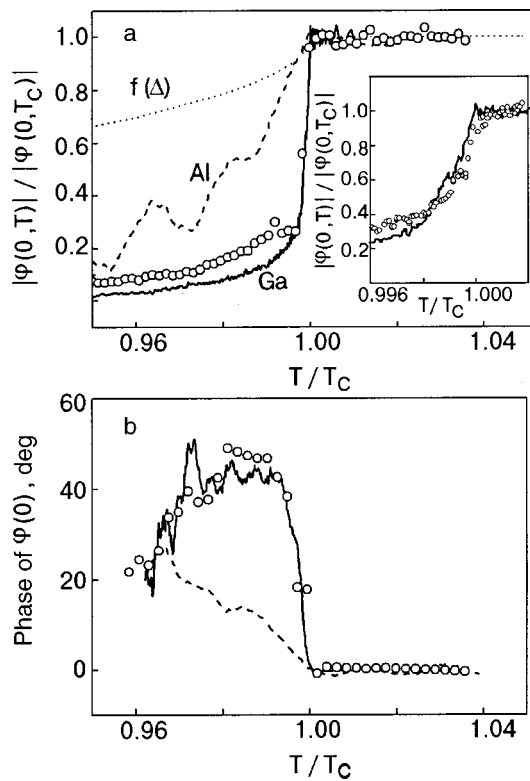
FIG. 6. Effect of the superconducting transition on the electric potential: amplitude $|\varphi(0)|$—the solid and dashed curves are for a galvanic contact (Ga and Al), the circlets are for an asymmetric coil (Ga), and the upper dotted curve shows $f(\Delta)$. Inset: the behavior of $|\varphi(0)|$ in Ga (galvanic contact) for different excitation amplitudes: solid curve—+10 dB, circlets—0 dB (a); the variation of the phase $\varphi(0)$ below T_C: the solid and dashed curves are for a galvanic contact (Ga and Al), and the circlets are for an asymmetric coil (b).

the K component of the potential is also due to the deformation interaction, there is no reason to think that its law of variation will be substantially different from (22).

The experimental results presented in Fig. 6 strongly contradict the estimates given above. Even in Al, in which apparently only the periodic component of the signal is present to a significant degree, the amplitude of $\varphi(0)$ changes much more sharply than $f(\Delta)$, and the phase undergoes a rather rapid rise. These features are more pronounced in Ga, in which one might suspect a manifestation of some sort of nonlinearity, since a nonlinearity is expressed quite clearly in the sound attenuation.[16] For an excitation intensity close to the maximum, nonlinear behavior of $\varphi(0)$ was indeed observed, associated with both overheating and a sharp drop in the sound attenuation coefficient below T_C, with a corresponding decrease in the heat release. The data presented in Fig. 6a pertain to the region of amplitudes in which these effects are practically absent (inset in Fig. 6a).

The following "simplified" line of reasoning is also possible. In the experiments described, the potential difference between the "hot" spot and the remote parts of the sample is recorded in the regime of spreading surface currents. Therefore, the value of the potential that is registered can depend on the spreading resistance. In other words, in a superconductor the rapid growth of the diamagnetic contribution to the conductivity ($\sim \rho_s v_F / s$) can lead to "short-circuiting" of the source of the electromotive force, and that is what is

detected in the experiment. In Fig. 6 we also show the signal taken from the asymmetric coil, which registered the amplitude and phase of the spreading currents specifically. We see that the amplitude of this signal falls off just as rapidly as does $|\varphi(0)|$, and the phase also increases practically in a jump. Therefore, from the standpoint of the "simplified" explanation a rapid growth of the "resistance" of the source of emf must also be assumed, and that is hard to imagine.

From the results presented in Fig. 6a for Ga we see that beyond the region of very rapid drop of $|\varphi(0)|$ comes a more gradual "tail," reminiscent of the evolution of $f(\Delta)$. This suggests another hypothesis: for some reason that we have not discussed, the K contribution in a superconductor actually vanishes very rapidly, and the remaining q contribution falls off as follows from the theory. We recall, however, that the phase of the q contribution is different from the phase of the K contribution by more than $\pi/2$ (Fig. 3b), and so this scenario should be accompanied by a downward phase jump of corresponding amplitude. The data of Fig. 6b are inconsistent with this hypothesis as well.

At present the authors do not have any reasonable explanation for the described behavior of $\varphi(0)$ near T_C. On the whole, the picture looks as if either a state in which an uncompensated charge cannot exist develops with catastrophic rapidity in a superconductor which is found in the normal phase, at least in the nonlocal limit, or else below T_C the electric potential just as rapidly transforms to a quantity that cannot be measured by a voltmeter. We add that a jump in the phase of $\varphi(0)$ by approximately $\pi/4$ can be evidence that the surface impedance has some relation to the observed effect, since the penetration depth of the field at the transition through T_C changes from a complex quantity with approximately equal real and imaginary parts (their relative sizes depend on whether the normal or anomalous skin-effect regime is realized) to the purely real London penetration depth.

5. CONCLUSION

In summary, we have for the first time carried out a theoretical analysis and experimental observation and study of the electric potential arising when a longitudinally polarized elastic wave is incident normally on a metal surface. The potential under study is the sum of two contributions. The first of them, the q contribution, is due to forced oscillations of the electric field, which is proportional to the elastic deformation u', i.e., it can be detected only on a non-free boundary, where $u'(0) \neq 0$. The second, K contribution is due to the presence of the metal boundary itself, which distorts the ballistic motion of nonequilibrium carriers in a subsurface layer of thickness $\sim l$; its amplitude turns out to be proportional to the displacement of the surface, $u(0)$. In the nonlocal limit the amplitude of the K contribution is markedly greater than that of the q contribution, while in the local limit it is the other way around. The phase of the K contribution leads the phase of the q contribution by approximately $\pi/2$, and therefore in the crossover region the phase of the recorded potential varies quite sharply. The experimental observation of just such behavior is, in the opinion of the authors, an unambiguous qualitative confirmation of the correctness of the ideas developed in this paper about the origin of the potential in question.

At the superconducting transition the amplitude of the potential falls in a catastrophically rapid manner, and the phase just as rapidly increases by approximately $\pi/4$. This behavior is inconsistent with the theoretical concepts, which predict a much smoother decrease of the amplitude, close to the BCS dependence of the longitudinal sound attenuation coefficient, and the absence of any phase variations.

[*]E-mail: fil@ilt.kharkov.ua

[1]This is not strictly accurate. Applications of electroacoustic conversion often make use of the circumstance that in a quasistatic electric field the surface of a conductor is subjected to an additional pressure. In an alternating field this pressure excites elastic displacements of the surface, including longitudinal ones. This effect is widely used in low-frequency acoustic experiments with vibrating reeds,[2] and it is also the basis of the ESAT (electrostatic acoustic transformation) mechanism.[3] Because the response is quadratic in the field amplitude, in this case the reciprocity principle is, of course, not obeyed, and this effect can be used for acoustoelectric conversion only with additional ''linearization.'' In the present paper we discuss only linear effects.

[2]We note that for the customary way of representing the elastic field $[\sim\exp(-i\omega t+i\mathbf{q}\cdot\mathbf{r})]$, in comparing the measured phase variations with those calculated using relation (13), the sign of the latter should be changed.

[1] A. N. Vasil'ev and Yu. P. Gaĭdukov, Usp. Fiz. Nauk **141**, 431 (1983) [Sov. Phys. Usp. **26**, 952 (1983)].

[2] P. Esquinazi, J. Low Temp. Phys. **85**, 3/4, 139 (1991).

[3] H. Shimizu and A. J. Bahr, IEEE Ultrasonic Symp. Proc. 17 (1976).

[4] V. M. Gokhfel'd and V. D. Fil', Fiz. Tekh. Vysokikh Davlenii **11**, 4, 76 (2001).

[5] A. N. Vasil'ev, V. M. Gokhfel'd, and M. I. Kaganov, Zh. Éksp. Teor. Fiz. **92** 2283 (1987) [Sov. Phys. JETP **65**, 1286 (1987)].

[6] V. M. Kontorovich, Zh. Éksp. Teor. Fiz. **45**, 1638 (1963) [Sov. Phys. JETP **18**, 1125 (1964)].

[7] V. M. Gokhfel'd, M. A. Gulyanskiĭ, and M. I. Kaganov, A. G. Plyavenek, Zh. Éksp. Teor. Fiz. **89**, 985 (1985) [Sov. Phys. JETP **62**, 566 (1985)].

[8] A. I. Kopeliovich and M. S. Churyukin, Fiz. Nizk. Temp. **19**, 176 (1993) [Low Temp. Phys. **19**, 125 (1993)].

[9] V. M. Gokhfel'd and M. I. Kaganov, Fiz. Nizk. Temp. **11**, 517 (1985) [Sov. J. Low Temp. Phys. **11**, 282 (1985)].

[10] V. V. Furduev, *Electroacoustics* [in Russian], OGIZ, Moscow (1948).

[11] E. V. Bezuglyĭ, N. G. Burma, E. Yu. Deĭneka, and V. D. Fil', Fiz. Nizk. Temp. **19**, 667 (1993) [Low Temp. Phys. **19**, 477 (1993)].

[12] E. V. Bezuglyi, N. G. Burma, E. Yu. Deyneka, A. I. Kopeliovich, and V. D. Fil, J. Low Temp. Phys. **91**, 179 (1993).

[13] E. V. Bezuglyĭ, A. M. Stepanenko, and V. D. Fil', Fiz. Nizk. Temp. **13**, 246 (1987) [Sov. J. Low Temp. Phys. **13**, 140 (1987)].

[14] E. V. Bezuglyi, Fiz. Nizk. Temp. **9**, 15 (1983) [Sov. J. Low Temp. Phys. **9**, 6 (1983)].

[15] E. V. Bezuglyi and A. V. Boichuk, Fiz. Nizk. Temp. **23**, 676 (1997) [Low Temp. Phys. **23**, 507 (1997)].

[16] V. D. Fil', V. I. Denisenko, and P. A. Bezuglyĭ, JETP Lett. **21**, 329 (1975).

LOW-TEMPERATURE MAGNETISM

Low-temperature domain-wall dynamics in weak ferromagnets

A. P. Kuz'menko*

Khabarovsk State Technical University, ul. Tikhookeanskaya 136, 680035 Khabarovsk, Russia

The nonlinear and multidimensional supersonic dynamics of domain walls in weak ferromagnets—orthoferrites and iron borate—are investigated experimentally at low temperatures in magnetic fields much less than the spin-flop field. A qualitative physical model of the observed effects is presented, and an elastically induced spin-reorientation mechanism of magnetization reversal is observed and investigated. This mechanism is accompanied by the unsteady motion of the domain walls, the velocity of which is considerably higher than the limiting velocity for their steady-state motion. © *2002 American Institute of Physics.*
[DOI: 10.1063/1.1480240]

INTRODUCTION

Weak ferromagnetic (WFM) materials such as the orthoferrites $RFeO_3$ (R^{3+} is a rare-earth ion or Y), hematite α-Fe_2O_3, and iron borate $FeBO_3$, in which the main magnetic ion is Fe^{3+}, have a number of magnetic properties in common. The crystalline and magnetic structure of these compounds and the corresponding fields of the symmetric H_E and antisymmetric H_D exchange interactions and magnetic anisotropy H_A cause a slight canting of the antiferromagnetic (AFM) sublattices (0.5° in $RFeO_3$ and 0.9° in $FeBO_3$) at temperatures below the Néel point T_N. In these materials the WFM moment M also has values of the same order of magnitude (5.8–11.4 T). In orthoferrites the WFM moment vector **M** has a pronounced anisotropic character, and for $T_{SR} < T < T_N$ (T_{SR} is the spin reorientation temperature) it is directed along the [001] axis (along [100] in $SmFeO_3$). On this basis they are classed as weak ferromagnets with anisotropy of the easy axis type. The presence of the ions R^{3+} in orthoferrites leads to an additional magnetic ordering in the rare-earth sublattice. In $FeBO_3$ there are two types of anisotropy fields: out-of-plane H_A and in-plane H_a, the values of which are 3×10^3 and 0.2 kOe, respectively. In the temperature interval $T_R < T < T_N$ (T_R is the compensation temperature) the in-plane anisotropy field in $FeBO_3$ holds the magnetic moments M and L in the basal plane (111), i.e., it is an easy-plane weak ferromagnet.[1,2] The influence of temperature, external magnetic field, or elastic stresses on the effective anisotropy constants will bring about the onset of various orientation phase transitions in easy-plane and easy-axis weak ferromagnets.[1–3]

A number of $RFeO_3$ compounds at low temperatures ($T \leqslant T_{SR}$) exhibit a spin reorientation of the vector **M** from the main direction along the easy axis [001] (except for $SmFeO_3$) to the [100] axis.[1] This reorientation is due to a change of the signs and magnitudes of the first and second anisotropy constants, K_1 and K_2. For example, in $TmFeO_3$ the reorientation is accompanied by a change in sign of K_1, and for $K_2 > 0$ it takes place as two second-order phase tran-

sitions in the temperature interval 86 K $\leqslant T_{SR} \leqslant$ 92 K, while for $K_2 < 0$ this reorientation occurs discontinuously as a first-order phase transition. Analogous changes of the spin configurations take place in the Er, Nd, Ho, and Sm orthoferrites. As the temperature is lowered, in the Er, Nd, Gd, and Sm orthoferrites a compensation point appears at a temperature T_R as a result of the superposition of the magnetizations of the rare-earth and iron sublattices, which are of different sign. The highest compensation temperature T_R is observed for the Er orthoferrite: $T_R = 45$ K. In $DyFeO_3$ at a temperature $T_M = 40$ K the WFM moment vanishes discontinuously,[1] AFM ordering arises, and a so-called Morin transition is observed. In the easy-plane weak ferromagnet $FeBO_3$ the compensation point occurs at $T_R = 5$ K; it is due to a change in sign of the effective field of the in-plane magnetic anisotropy H_a (Ref. 2). Below the compensation temperature T_R (in the absence of external interactions and without allowance for the demagnetizing fields) it is energetically favorable for the system to be in a state with the AFM vector **L** parallel to one of the C_2 axes in the easy plane (111).

The tipping of the magnetic sublattices (spin flop) in a weak ferromagnet occurs in rather high magnetic fields, below which the main mechanism of magnetization reversal of a weak ferromagnet is domain-wall (DW) motion. For example, for $RFeO_3$ the expression for the spin-flop field has the form $H_{SF} = -H_D/2 + ((H_D/2)^2 + H_E H_A)^{1/2}$, and its value is 75 kOe.[1] The external magnetic field enhances the role of magnetic ordering in the rare-earth sublattice of the orthoferrites. In combination with the lowering of the temperature, this substantially alters the boundary and character of the spin reorientation transition. In $TmFeO_3$ in an external magnetic field the second second-order phase transition at $T_2 = 86$ K is observed to vanish, and the boundary of the first transition is shifted to $T_1 = 90$ K.[1]

Spin reorientation transitions in weak ferromagnets can be induced by elastic pressure with a certain orientation, and a change of the temperature T_{SR} occurs in this case also. For

example, in $TmFeO_3$ a unidirectional pressure $p_c = 1.5$ kbar along the easy axis increases T_{SR} by 10 K.[1]

The DW dynamics in the orthoferrite $YFeO_3$ have been the most thoroughly studied both experimentally and theoretically.[3–11] It was found that it is only in weak ferromagnets that the limiting velocity of steady DW motion C is substantially faster than the transverse and longitudinal sound velocities V_t and V_l (for $YFeO_3$, $V_t = 4.2$ km/s and $V_l = 7.2$ km/s). For an estimate of the value of C one can use the long-wavelength approximation of the spin-wave dispersion relation: $C \propto \gamma (2H_E A / M_0)^{1/2}$. The value of C calculated for $YFeO_3$ using the values of the inhomogeneous exchange constant A, sublattice magnetization M_0, and gyromagnetic ratio γ comes out to be 19.74 km/s, in good agreement with the experimentally measured[10] and theoretically calculated[11] values.

The dependence of the DW velocity $V(H)$ on the amplitude of the driving magnetic field in $YFeO_3$ slabs consists of a discrete series of "shelves"—magnetic field intervals ΔH_i within which the DW velocity V_i remains practically constant. The relationships governing their formation were determined in Ref. 6. At DW velocities equal to V_t and V_l, the formation of the shelves on the curves is due to magnetoelastic interactions.[3–5] The formation of intervals ΔH_i at supersonic DW velocities ($C > V_i > V_{t,l}$) is accompanied by resonant braking on the characteristic bending (near-wall) vibrations of the DWs. In $TmFeO_3$ at the point of transition of the DW through the sound barrier the separation of a dynamic deformation from the DW has been observed visually and studied in Ref. 7; the formation of this deformation was justified theoretically in Ref. 4. In this transition a shock-wave mechanism operates which causes a renormalization of the effective anisotropy constants.[3–5] The DW in $YFeO_3$ at supersonic velocities becomes multidimensional.[3] Under certain conditions the onset of an elastically induced spin renormalization transition has been detected, at which the motion of the less stable, ab type of DWs becomes energetically favorable to that of the usual ac type of DWs.[3,8] The phenomena observed in supersonic DW motion in WFM slabs have been explained on the basis of a description of the dynamic DW as a self-organizing system.[9]

The magnon and phonon oscillations are ordinarily studied by the methods of microwave or ultrasonic spectroscopy, light scattering, or neutron scattering. In particular, in $ErFeO_3$ at a temperature of ~ 4 K these methods have revealed a giant decrease (by up to 25%) in the sound velocity,[12] and a light-scattering experiment at this same temperature first revealed the separation from the DW of a dynamic elastic deformation, excited by the latter to near-sonic velocities.[13]

In this paper we present the results of a low-temperature study of the dynamics of DWs by the method of double-exposure high-speed photomicrography[3,6] in rare-earth orthoferrites (REOs) of different composition and in iron borate. Using a supersonic DW as a natural dynamic microprobe,[14] we studied the magnetization reversal process at different temperatures under the influence of pulsed magnetic fields and the dynamic deformations of the shock type excited during the transition of a DW through the sound barrier.

METHODS AND RESULTS

These studies were done on thin, optical transparent slabs of the yttrium, lutetium, dysprosium, europium, and thulium orthoferrites and iron borate with thicknesses ranging from 35 to 120 μm. The samples were oriented perpendicular to the optic axis, making it possible to obtain magnetooptical contrast sufficient for visualization of the domain structure in transmitted light.

Depending on the orientation of the plane of the $RFeO_3$ slab with respect to the crystallographic axes, three types of DWs can exist. For example, Block and Néel DWs are detected if the plane of the slab is perpendicular to the easy axis [001]. In a slab cut perpendicular to the optic axis, which lies in the ac plane and is directed at an angle of 52° to the [001] axis, a tilted DW is formed—an intermediate analog of the Néel DW. For all of these types of DWs it is energetically favorable for the vectors of the AFM and WFM moments to rotate in the ac plane. The absence of birefringence in this geometry makes for the highest magnetooptical contrast of the domain structure.

The easy-plane weak ferromagnet $FeBO_3$ has a more complicated configuration of the magnetic anisotropy fields, making for considerable diversity in the possible types of domain structure. The magnetostatic energy in this weak ferromagnet is decreased when the magnetic moments of the sublattices lie in the basal plane (111). Two types of DWs are energetically favorable in this case: DW∥[001] and DW⊥[001], i.e., Néel and Bloch DWs, respectively. The optic axis in $FeBO_3$ is perpendicular to the (111) plane, and therefore a projection of **M** on the light propagation direction was created by a deviation of the light rays from the optic axis of the crystal by an angle of 15–20°. In an $FeBO_3$ sample in the absence of external fields and elastic stresses, domain structure is formed not only in the (111) plane but also in the direction of the [001] axis. Here the domain structure becomes layered. A high-contrast domain structure in $FeBO_3$ with a single DW in each individual layer was observed when a compressive stress (~ 1 Pa) and a gradient field (700 Oe/cm) were applied simultaneously.[3] Under these conditions, despite the high magnetooptical quality of the $FeBO_3$, the resulting angle of rotation of the plane of polarization of the light wave amounted to $\sim 1°$.

All of the $RFeO_3$ samples investigated were chemically polished in superheated acid H_3PO_4, which permitted decreasing the coercivity to 0.1 Oe. A pulsed magnetic field produced by two Helmholtz coils was applied to the samples; the coils had a diameter of 1 mm for $RFeO_3$ ($H \perp$ plane) and 5 mm for $FeBO_3$ ($H \parallel$ plane).[3] The rise time of these pulses was less than 20 ns, and the amplitude reached 4.8 kOe. The pulse repetition rate was not more than a few hertz. Before the start of the motion, an isolated rectilinear DW in $RFeO_3$ was held in place by a gradient magnetic field at a distance of 0.15 mm from the inner edge of the coil. The value of the gradient field varied, depending on temperature and the composition of the REO. For example, the DW dynamics in $TmFeO_3$ was studied in a static field with a gradient of 2500 Oe/cm at a temperature of 168 K, whereas in $YFeO_3$, $LuFeO_3$, and $EuFeO_3$ it was 500 Oe/cm or less at all temperature.
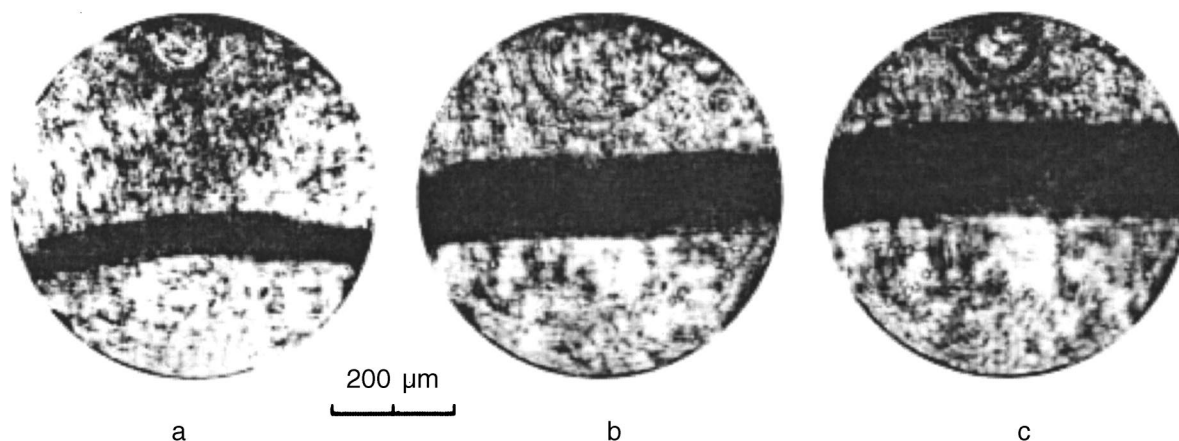
To study the DW dynamics we used the double-exposure

FIG. 1. Photomicrographs of the twin dynamic domain structures at 4.2 K in yttrium orthoferrite at a delay of 15 ns between light pulses for different domain-wall velocities V [10^3 m/s]: 4.12 (a), 12 (b), and 18 (c). The domain wall is moving from bottom to top.

method.[3,6] The source of the pulsed laser radiation was a transverse-discharge nitrogen laser pumping a dye laser. The wavelength of the dye laser was chosen to lie in the quasi-window of optical transparency for the weak ferromagnets studied: 630 nm for $RFeO_3$, and 553 nm for $FeBO_3$. This made it possible to detect high-contrast dynamic domain structures and DWs on photographic film or a video camera without the need for brightness enhancers. The error of determination of the DW velocity in $RFeO_3$ was around 2% at a velocity of 20 km/s and was actually determined solely by the duration of the subnanosecond light pulses. In $FeBO_3$ the error of determination of the DW velocity V was somewhat greater because of the lower contrast of the domain structure and the features of the dynamic behavior of the DWs in this easy-plane weak ferromagnet.

　　For studying the DW dynamics in weak ferromagnets at low temperatures we used an optical helium cryostat developed at the P. N. Lebedev Physics Institute, Russian Academy of Sciences. The samples were immersed directly in liquid helium or nitrogen, and the temperature was varied by pumping on the products of boiling. In addition, we used an optical nitrogen cryostat in which the sample was mounted on a cold finger, and also a supercooled mixture of a solvent with liquid nitrogen and dry ice.

　　The temperature of the sample was measured by a copper–Constantan thermocouple attached to the sample by a heat-conducting paste. Cooling of the WFM samples led to a slight increase in their transparency and an increase in the magnetooptical contrast. Figure 1 shows a photomicrograph of twin dynamic DWs in $YFeO_3$ at the boiling temperature of helium for various DW velocities. Bubbles of gaseous helium can be seen inside the coil. The dynamic DWs in $EuFeO_3$ at $T=4.2$ K have a similar appearance.

　　From the displacements $x(\omega)$ of an isolated DW under the influence of an alternating magnetic field at different temperatures we determined the DW mobility μ in all the weak ferromagnets studied. For the $x(\omega)$ curves obtained in this way we found the relaxation frequency ν_R, at which the amplitude of the DW oscillations decreases by a factor of $\sqrt{2}$. The values of ν_R in easy-plane and easy-axis weak ferromagnets are substantially different: 5.7 and ~1 MHz, respectively. The mobility of an isolated DW in the weak ferromag-

nets under study was calculated in analogy with Ref. 15 from the DW relaxation frequencies found at different temperatures and amplitudes of the alternating magnetic field with allowance for the static-field gradient restoring the DWs to the equilibrium position. The temperature dependence of the DW mobility μ for the easy-plane $FeBO_3$ and the easy-axis $TmFeO_3$, $EuFeO_3$, $DyFeO_3$, and $YFeO_3$ are shown in Fig. 2. The DW mobility in the $TmFeO_3$ samples is maximum at a temperature of 168 K, where it equals 860 cm/(s·Oe). Below that temperature the DW mobility in $TmFeO_3$ decreases to zero already at 115 K. With decreasing temperature the DW mobility μ in $EuFeO_3$ increases, reaching 5800 cm/(s·Oe) at 4.2 K. The mobility $\mu(T)$ is found to be proportional to $1/T^2$ (Ref. 15). In $DyFeO_3$ samples with thicknesses of 25 and 90 μm the DW mobility at room temperature is 343 and 295 cm/(s·Oe), respectively. When the temperature is decreased to 77 K, μ decreases to 50 cm/(s·Oe). The highest DW mobility in the $YFeO_3$ samples studied was observed at a temperature of around 100 K. Its
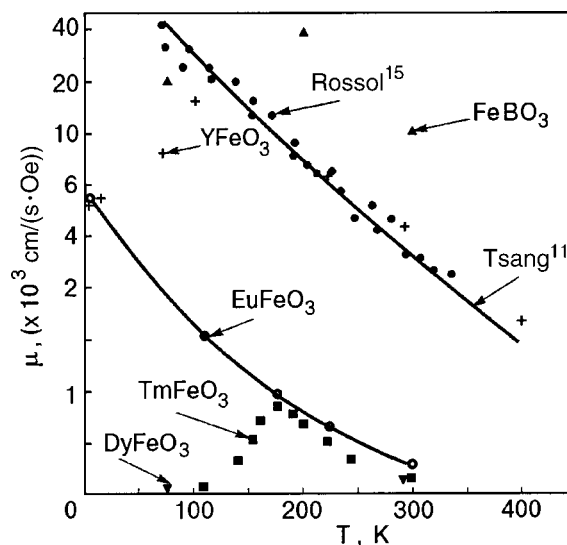

FIG. 2. Temperature dependence of the domain-wall mobility (indicated by arrows) in $EuFeO_3$, $TmFeO_3$, $YFeO_3$, $DyFeO_3$, and $FeBO_3$ (determined from the data of Ref. 2). Also shown are the data from the papers by Rossol[15] and the calculated curve of Tsang *et al.*[11]
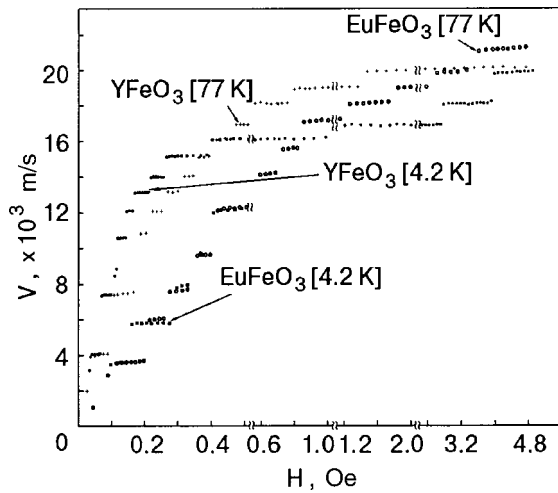
FIG. 3. Field dependence of the domain-wall velocity in slab samples of the orthoferrites $EuFeO_3$ and $YFeO_3$ at 4.2 and 77 K.
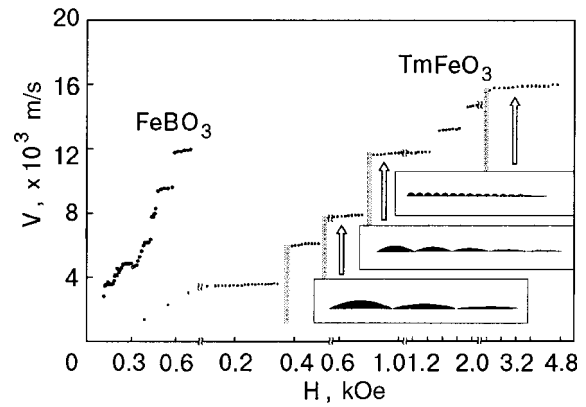

FIG. 4. Field dependence of the domain-wall velocity in slab samples of $TmFeO_3$ at 168 K and $FeBO_3$ at 200 K.[2] Also shown is the qualitative field dependence of the period of the multidimensional formations and their amplitude for different domain-wall velocities in $TmFeO_3$.

value for different samples varied in the range $(20–40) \times 10^3$ cm/(s·Oe). When the temperature was decreased further to $T = 2.1$ K, the DW mobility decreased in all the $YFeO_3$ samples (see Fig. 2). The single crystals of all these orthoferrites were grown by the the floating zone method with optical heating. Samples of the orthoferrite $LuFeO_3$ grown by the spontaneous crystallization from the flux do not exhibit spin reorientation, i.e., the DW mobility μ should have increased with decreasing temperature. The DW mobility in this sample at room temperature reached 350 cm/(s·Oe), after which it fell practically to zero at a temperature of 80 K.

The DW mobility in $FeBO_3$, calculated according to the data of Ref. 3 for various temperatures, is also shown in Fig. 2. It is seen that at 200 K the DW mobility μ reaches a maximum of 45×10^3 cm/(s·Oe). Increasing the external compressive stress p on an $FeBO_3$ slab above $p_{cr} = 1$ Pa led to a decrease in the DW mobility. The insufficient contrast and, as a result, the reduced accuracy in the investigation of the DW dynamics in this material did not permit a determination of whether the temperature or the compressive stress has the dominant influence on the value of μ.[3]

The DW mobility was also determined from the initial part of the $V(H)$ curve. The magnetic field at which the DW starts to move was taken equal to the coercivity of the particular WFM sample.[6] The value of the coercivity did not exceed 1–2 Oe. The value of the coercivity was somewhat higher for the $LuFeO_3$ sample, attesting to the high quality of the samples grown by spontaneous crystallization from the flux. The values of the DW mobilities determined from the $V(H)$ and $x(\omega)$ curves agreed with each other.

Figure 3 shows the magnetic-field dependence of the DW velocity V in samples of the orthoferrites $EuFeO_3$ and $YFeO_3$ at temperatures of 4.2 and 77 K. The fact that these $V(H)$ curves are analogous to those obtained previously[6] for $YFeO_3$ samples at room temperature attests to their underlying commonality. The $V(H)$ curve for $EuFeO_3$, like that for $YFeO_3$, is nonlinear. It consists of a discrete set of DW velocities V_i which remain constant in certain magnetic field intervals ΔH_i (a series of "shelves"). The first constant DW velocities on the $V(H)$ curve were equal to the velocities of

transverse and longitudinal bulk sound waves, $V_t(\Delta H_t)$ and $V_l(\Delta H_l)$. For example, in $EuFeO_3$ the first two shelves on the $V(H)$ curve were observed at velocities of 3.5 and 5.8 km/s, and those in $YFeO_3$, at 4.12 and 7.2 km/s. Similar shelves were observed on the $V(H)$ curves in the other REOs. In particular, in $TmFeO_3$ at the temperature 168 K at which the DW mobility is maximum, the $V(H)$ curves also had shelves ΔH_t and ΔH_l at velocities $V_t = 3.6$ km/s and $V_l = 6.5$ km/s (Fig. 4).

Along with the shelves ΔH_t and ΔH_l, for all the $RFeO_3$ samples at different temperatures (including low temperatures) additional shelves ΔH_i appeared on the $V(H)$ curves at supersonic DW velocities $V = V_i$. For example, in $EuFeO_3$ at 4.2 K in fields up to 0.5 kOe (at the highest DW mobility) the $V(H)$ curve had shelves at velocities of 3.5, 5.8, 7.5, and 14 km/s. For this same sample at 77 K the $V(H)$ curves in fields of up to 4.8 kOe had shelves at velocities of 3.5, 5.8, 7.5, 12, 14, 15.5, 17, 18, 19, 20, and 21.5 km/s (see Fig. 3). The $V(H)$ curve for $TmFeO_3$ also consists of a series of shelves appearing in fields up to 4.8 kOe at the following DW velocities: 8, 11.9, 13.5, 15, and 16.8 km/s (Fig. 4). The values of the limiting velocities for steady-state motion of the DW in the thulium and europium orthoferrites at the fields studied (see Figs. 3 and 4) are equal to 17 and 21.5 km/s, respectively, somewhat different from the corresponding value in $YFeO_3$.

The formation of the DW braking intervals in REOs, as in $YFeO_3$,[3] had the following regularities of a resonance character:

— the dependence of $V(H)$ at $V_t < V_i < C$ consisted of a discrete series of intervals ΔH_i, the number and size of which increased with increasing thickness of the samples, with $V(H)$ becoming increasingly more continuous in nature;

— As $V_i \rightarrow C$ the difference $V_{i+1} - V_i$ decreased, and the size of the interval ΔH_i increased.

In the easy-plane weak ferromagnet $FeBO_3$ at 200 K, as in the easy-axis weak ferromagnet $RFeO_3$, the formation of shelves—field intervals $\Delta H_{t,l}$—occurred at near-sonic velocities (see Fig. 4). According to the theoretical results of Ref. 12, in $FeBO_3$ the values of V_t varied by 8–10%, depending on the polarization. For V_l this change was $\sim 1\%$.
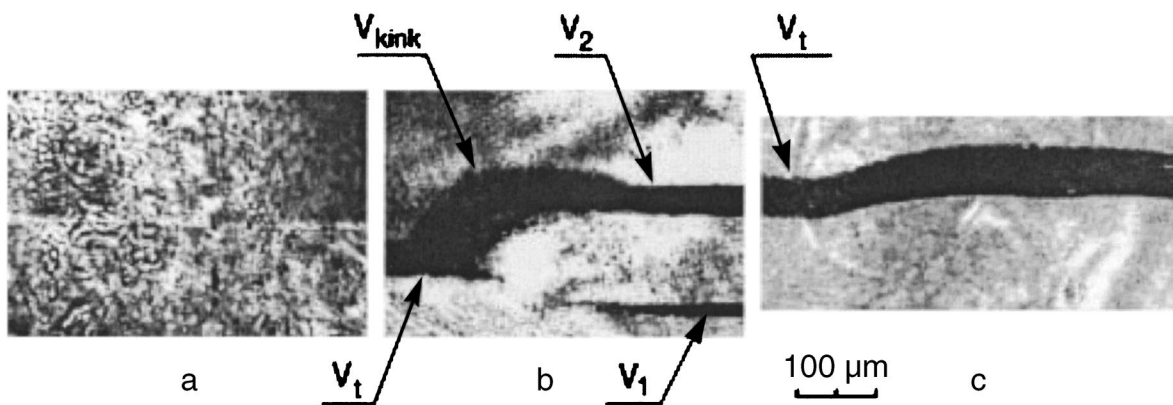
FIG. 5. Photomicrographs of the unsteady twin dynamic domain structure at 300 K in YFeO$_3$ with varied conditions on the surface (a); at 168 K in TmFeO$_3$ at $V \gg V_t$ (b) and at 80 K in LuFeO$_3$ (c) with a delay of 15 ns between light pulses. The domain wall is moving from bottom to top.

Two shelf intervals are seen on the $V(H)$ curve, with transverse velocities of 4.2–4.8 km/s and 5.9–6.2 km/s, corresponding to shelves $\Delta H_{t,1}$ and $\Delta H_{t,2}$. At a temperature of ~ 80 K the $V(H)$ curves for FeBO$_3$ had another shelf in addition to those mentioned above; it occurred at a velocity of 9.5 km/s, which, because of dispersion, varied to 10.2 km/s. This velocity agrees with the calculated value of V_l. In addition, the $V(H)$ curve at this temperature goes to saturation at $V = 11.8$ km/s. This value, in analogy with the limiting velocity C of steady-state DW motion in orthoferrites, practically coincides with the minimum phase velocity of spin waves in FeBO$_3$, equal to 11.2 km/s at a temperature of ~ 80 K. An analogy with the $V(H)$ curves in orthoferrites and FeBO$_3$ was also observed in the formation of a shelf on the DW velocity curve below the first transverse sound velocity (3.6 km/s). However, a more complete correspondence between the nonlinear supersonic DW dynamics in FeBO$_3$ and RFeO$_3$ could not be established because of the low magnetooptical contrast of the observed domain structures (Fig. 5c).

In all the orthoferrites RFeO$_3$ studied, the DW motion at supersonic velocity became multidimensional. Multidimensional formations arose on the DWs independently of the value of their mobility, as is demonstrated by the photomicrographs of the DWs in LuFeO$_3$ at room temperature (Fig. 5c), where the mobility was only 350 cm/(s·Oe). The typical twin multidimensional domain structures observed at a temperature of 168 K at supersonic velocities in TmFeO$_3$

had an oval shape (see Fig. 6). The behavior of these formations repeated the previously observed[3] features of the multidimensional motion of DWs in YFeO$_3$. The multidimensional formations had a characteristic period of λ and arose less than 1 ns after the transition of the DW through the sound barrier at all DW velocities from $V_{t,l}$ to C. The transition of a DW through the sound barrier to V_i occurred in an unsteady manner. Furthermore, the transition between supersonic DW velocities (equal to 8, 11.9, and 16 km/s for TmFeO$_3$; see Fig. 4) was unsteady also. At those velocities V_i at the end of the corresponding shelf, in an interval δH of around 1 Oe, the DW velocity jumped upward: $V_i \rightarrow V_{i+1}$. At the same time, the period of the half-oval formations decreased ($\lambda_i \rightarrow \lambda_{i+1}$). The value of the period λ_i of the half-oval formation remained constant at a supersonic DW velocity. At the end of an interval ΔH_i the DW straightened out, and its motion became unsteady. Here the amplitude of the multidimensional formations A_i decreased continuously to zero at the end of a shelf ΔH_i, as is illustrated schematically in Fig. 4. In TmFeO$_3$ at a DW velocity equal to 16 km/s the value of the period of the multidimensional formation was 0.4×10^{-4} m, as it appeared in transillumination of the domain wall by the first pulse in Fig. 6c. In this same orthoferrite the periods of the multidimensional formations at DW velocities of 8 and 11.9 km/s were 3.3×10^{-4} m and 1.8×10^{-4} m, respectively (Figs. 6a and 6b). The smallest period of the multidimensional formations in YFeO$_3$ was equal
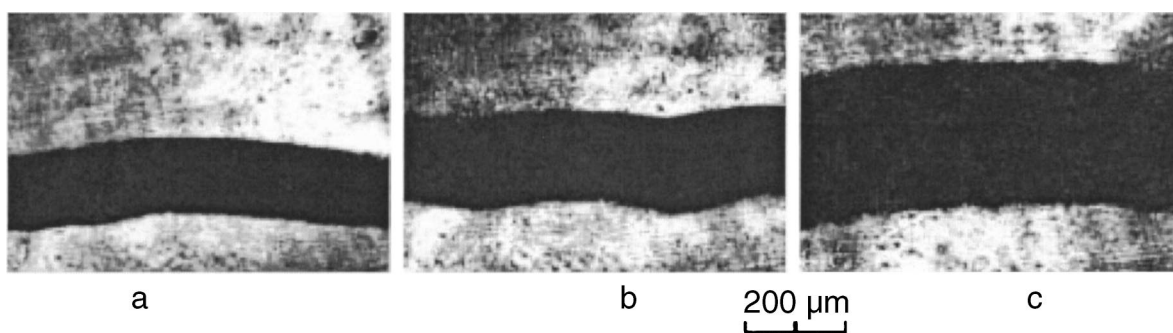

FIG. 6. Photomicrographs of the twin dynamic domain structures at 168 K in TmFeO$_3$ at a delay of 15 ns between light pulses, with different sizes λ_i of the multidimensional formations [10^{-6} m]: 330, $V = 8 \times 10^3$ m/s (a), 280, $V = 11.9 \times 10^3$ m/s (b), and 40, $V = 16 \times 10^3$ m/s (c). The domain wall is moving from bottom to top.

to 2.5×10^{-4} m, which was found at a DW velocity of 16 km/s.[3]

At a velocity $V < V_t$ in EuFeO$_3$ (at 4.2 K) and DyFeO$_3$ (at 77 K) the multidimensional formations on the DWs acquired a somewhat different, trapezoidal shape. The lateral sides of the trapezoid had smeared outlines and moved practically perpendicular to the main direction of motion to the right and to the left of the center of the DW. The motion of the leading edge of the trapezoidal DW was unsteady.

Unsteady motion of DWs was also observed when the DW velocity changed between the values V_i indicated above, which were slightly different in different orthoferrites, and was accompanied by an instantaneous (in less than 1 ns) change in the magnetooptical contrast over the entire region under study in the sample, as is demonstrated by the photomicrograph of this situation (see Fig. 5a). The newly arising magnetooptical contrast had an intermediate value in comparison with the contrast typical for orthoferrites (see Figs. 5 and 6). This contrast was typical for the unsteady motion of the dynamic domain structures and was observed only at the end of the interval ΔH_i corresponding to V_i. The domain structure with this contrast was observed several times in 50 ns when the delay between the magnetic field pulse and the first (or second) illumination pulse was changed. A slight increase in the amplitude of the pulsed magnetic field ($\Delta H_i + \delta H$, where $\delta H = 1$ Oe) led to a sharp increase in the DW velocity: $V_i \rightarrow V_{i+1}$. The DW motion with velocity V_{i+1} as the magnetic field changed within the interval ΔH_{i+1} again became steady all the way to the end of this interval, but the shape of the DW remained multidimensional but with a smaller period, equal to λ_{i+1}. This scenario was repeated at all the velocities V_i indicated.

The unsteady motion of a DW observed at low temperatures was also detected when the boundary conditions at the surfaces of the orthoferrite samples were changed (when the samples were placed in different liquid media, including liquid helium and nitrogen) or when compressive stresses were applied. It was accompanied by the formation of intermediate contrast and occurred at the same temporal and field parameters.[8]

In the REOs of europium, lutetium, and dysprosium, as in TmFeO$_3$,[7] at all temperatures the transition to supersonic DW motion was accompanied by simultaneous light diffraction on the dynamic elastic deformations separating off from the DWs. The existence time of these deformations determined from the observed diffraction patterns (several tens of nanoseconds) and also their size (several microns) turned out to be similar in order of magnitude for all the REOs investigated. We note that in YFeO$_3$ the separation of dynamic elastic deformations at the time when the DW breaks the sound barrier was not observed.

In the TmFeO$_3$ sample (Fig. 5b) during the transition of the DW through the sound barrier a dynamic rearrangement of the domain structure was observed in which the original two-domain structure with a single DW becomes complex. A new magnetic phase arose in the form of a flexible DW having diffuse outlines and moving from right to left (along the [010] axis). The velocity of a bend on the DW, determined from the direction of the normal to the plane of the bend, was equal to the longitudinal sound velocity $V_l = 6.5$ km/s. The

shape of this bend on the DW was similar to that of the kink observed previously in YFeO$_3$.[3] In contrast to the REOs, in YFeO$_3$ the solitary bending waves on a supersonic domain wall arises solely under the influence of an artificially created nonuniformity of the magnetic field.[16]

Simultaneously with this, as is seen on the right in the photomicrograph in Fig. 5b, two rectilinear parts of the DW, with distinct outlines, appeared. The DW in each of them moved along the [100] axis in the same direction as before (from bottom to top). The velocities of these DWs were $V_1 = 0.9$ km/s and $V_2 = 2.7$ km/s. A vector addition of velocities, $\mathbf{V}_t = \mathbf{V}_1 + \mathbf{V}_2$, is in fact observed. To the left in the photomicrograph we see a preserved fragment of the original dynamic domain structure. The velocity of the DW in it remained equal to $V_t = 3.6$ km/s.

An analogous rearrangement of the domain structure occurred in this sample at the transition through the sound barrier in the vicinity of the longitudinal sound velocity and at velocities of 8, 11.9, and 16 km/s. This type of rearrangement of the domain structure, in which multivaluedness appeared in the DW velocity as a function of the amplitude of the driving magnetic field, occurred in a very narrow region of magnetic fields, equal to a few oersteds. Beyond this region the DW motion became steady, and the velocity relation became single-valued, as can be seen by comparing Fig. 5b to Fig. 6. Such a rearrangement of the domain structure was observed at $T = 4.2$ K in EuFeO$_3$ at near-sonic velocities of the DW (for $V \sim V_{t,l}$).

The presence of a segment of DW motion with a velocity equal to V_t on the left in Fig. 5b indicates that all of the domain-structure rearrangement processes occur simultaneously during the motion of the DW in the time delay between the two illumination pulses (15 ns). The region in which the new magnetic phase arose had dimensions of 6.5 $\times 10^{-4}$ m along the horizontal (along the direction of motion of the flexible DW) and 1.8×10^{-4} m along the vertical (along the direction of motion of the two parts with a rectilinear DW). The rate of ''growth'' of the new magnetic phase in these directions was more than 40 km/s and 12 km/s, respectively. The value of the first velocity in TmFeO$_3$ was substantially greater than the above-mentioned limiting value of the velocity of steady DW motion $C = 17$ km/s. The value of the second velocity was the same as the velocity at which a shelf was observed on the $V(H)$ curve (Fig. 4) in this orthoferrite, a fact which serves as indirect confirmation of the correctness of such a determination of the velocities of the domain-structure rearrangement.

DISCUSSION OF THE RESULTS

From a phenomenological point of view the magnetic ordering which arises in noncollinear antiferromagnets is different from the ordinary spontaneous magnetization. To describe the magnetization-reversal processes in two-sublattice weak ferromagnets of the RFeO$_3$ type, besides taking into account the resultant magnetization vector $M = M_1 + M_2$ we must also take into account the AFM vector $L = L_1 - L_2$ $\times (M \ll L)$. In a weak ferromagnet under the influence of an external field or elastic strains an exchange enhancement effect arises in which $H_E/(H + H_D)$ is multiplied by a coefficient of the order of 10^3 (Ref. 17).

In the studies below we shall take into account the well-known expression for the thermodynamic potential for a weak ferromagnet:[1]

$$\Phi = \Phi_0 + K_2 \cos 2\varphi + K_4 \cos 4\varphi - M_z H_z \cos \varphi, \quad (1)$$

where K_2 and K_4 are the anisotropy constants. The value of K_2 is determined by the interaction between the R^{3+} and Fe^{3+} ions, while the main contribution to K_4 is from the exchange interaction between Fe^{3+} ions alone. The components M_z and H_z in (1) are directed along the [001] axis, which actually coincides with the geometry of our experiment. Under real conditions the dynamic properties of REOs are influenced most strongly by the low-temperature growth of the magnetoelastic coupling coefficients[1,12] and dynamic deformations of the DW at the time it breaks the sound barrier,[4,5,7,9,13] and the magnetic inhomogeneities originating in the growth of the crystals.[3,6,18]

The temperature-induced spin reorientation transitions are governed mainly by the variations of the anisotropy constant K_2, which is explained by the fact that it is more strongly T-dependent than K_4 (Ref. 1). For example, the first-order phase transition of the type $G_X F_Z \rightarrow G_Y$ (in $DyFeO_3$) occurs at $K_2(T) = 0$. The influence of elastic strains on L (the magnitude of $|\mathbf{L}| \cong 2M_0$) turns out to be more substantial than the influence of the external field H. At the transition of the DW through the sound barrier under conditions of "overheating" of the elastic subsystem it is possible that there are structural changes inside the DW. An ordinary 180° DW with rotation of the vectors $\mathbf{M}$ and $\mathbf{L}$ in the ac plane is transformed to a DW without rotation of $\mathbf{M}$. In the central part of such a DW the vector $\mathbf{M}$ vanishes, and the vector $\mathbf{L}$ is oriented along the [010] axis. A DW region with a transition of the "Morin type" acts as a nucleus for a new magnetic phase in the subsequent rearrangement of the domain structure, as has been observed at $T = 155$ K from the NMR spectra in $DyFeO_3$ ($T_M = 40$ K). In a weak ferromagnet the fine structure of the DW can be quite complex, containing an alternation of DWs of the ac type (the rotation of $\mathbf{M}$) and DWs of the ab type (without rotation of $\mathbf{M}$).[19–21]

The mobility of a Néel DW is determined, according to Refs. 3 and 15, as $\mu_N \approx \gamma \alpha^{-1}[A/(K + 2\pi M^2)]$, where K is an effective anisotropy constant. The differences in the mobilities $\mu(T)$ for $EuFeO_3$ and $YFeO_3$ (see Fig. 2) can be explained by stronger temperature dependence of K and the onset of a magnetoelastic interaction in the REO. This conclusion is also confirmed by the decrease in the DW mobility in $DyFeO_3$ at 80 K ($T_M = 40$ K) and in $TmFeO_3$ at 168 K. The $\mu(T)$ curve in $FeBO_3$ is analogous to the $\mu(T)$ curve in $RFeO_3$. At the same time, the value of μ decreases rather sharply at compressive stresses greater than $p_{cr} \sim 1$ Pa, indicating a substantial magnetoelastic coupling in $FeBO_3$. The $\mu(T)$ curves shown in Fig. 2 can be used to compare the contributions to the braking of DWs by three-magnon scattering processes and magnon conversion in $YFeO_3$ and the REOs of thulium and europium at the same temperatures. For example, at temperatures of 300 and 168 K the DW mobility in the REOs are close in value and equal ~ 870 and 345 cm/(s·Oe), whereas in $YFeO_3$ the DW mobility is more than an order of magnitude higher, a fact that can be directly linked to the larger effective values of the Dzyaloshinskiĭ

superexchange interactions $d_1 - d_3$ in the REOs. This strong difference in the DW mobilities in $YFeO_3$ and REOs, as was noted in Ref. 22, is caused by the anisotropy of the susceptibility of the rare-earth ions, which is approximately the same in the REOs. On the other hand, the solitonlike character of the DW in magnets, as follows from the results of Ref. 23, leads to a situation where the coefficients of dynamic drag of the DW on account of magnon scattering processes and magnon conversions can be compared with the phonon drag forces. As a result, at temperatures $T \ll 1$ K and $T > 100$ K the phonon scattering processes can give the main contribution. These conclusions are confirmed by experimental data: at helium temperatures and above room temperature it is observed that the intervals of constant $\Delta H_{t,l}$ on the $V(H)$ curve at $V_{t,l}$ become larger[14] and that the DW mobility decreases at $T < 4.2$ K (Fig. 2). The previously observed difference in the value of the mobility ratio, $\mu_B / \mu_N = 1.75$ in thin samples and $\mu_B / \mu_N = 1.06$ in ordinary samples of $YFeO_3$, agrees with the ratio of the frequencies of activationless spin oscillations $\omega_1 = 11 - 13$ cm^{-1} and $\omega_2 = 15 - 20$ cm^{-1} determined from light scattering on spin waves,[3] the variation of which lies within the limits 1.15 $< \omega_1 / \omega_2 < 1.82$. For $RFeO_3$ and $FeBO_3$ in Ref. 24 the difference in the uniaxial anisotropy constants as a function of the orientation of the DW relative to the crystallographic axes was taken into account. On this basis it was concluded from the differences in the values of the mobilities that the Bloch DW is transformed to a Néel DW, which is indirect evidence of the possibility of internal structural transformations of a DW.

The changes of the magnetooptical contrast observed in real time with the aid of the Faraday magnetooptic effect and the rearrangement of the dynamic domain structure in weak ferromagnets (Figs. 5 and 6), in analogy with Refs. 20 and 21, are possibly be due to rotation of the vector $\mathbf{M}$ and the corresponding changes of the magnetic symmetry. The reason for their appearance may be dynamic deformations and shock waves excited as the DW is breaking the sound barrier.[7] The value of these deformations increases in a resonant manner at sonic DW velocities:[3–5]

$$U_t = - \delta_t \sin \theta \cos \theta / C(1 - V^2/V_t^2),$$

$$U_l = - \delta_l \sin^2 \theta / C(1 - V^2/V_l^2), \quad (2)$$

where θ is the angle between the easy axis and the direction of motion of the DW. In Refs. 7 and 13 the difference in U_t and U_l was determined experimentally. For the DWs under study, which are close to the being of the Néel type, the dynamic deformations at the transverse sound velocity had a rather distinct leading edge and a smeared trailing edge, in agreement with the results of Refs. 4 and 5.

The value of the interval ΔH_t for $V = V_t$ depends substantially on the excitation by the DW of shock waves, which can propagate inside the interval $V_{\pm} \approx V_{t,l}(1 \pm 2(\delta_{t,l}\alpha_{t,l}\Delta_0 / \eta_{t,l}V_{t,l}))^{1/2}$ (Ref. 9). Here Δ_0 is the width of a nonmoving DW, $\alpha_{t,l}$, $\delta_{t,l}$, and $\eta_{t,l}$ are the linear elastic moduli and the magnetoelastic interaction coefficients, and the acoustic attenuation coefficient, all corresponding to the velocities $V_{t,l}$. The size of these shock waves is close to Δ_0

($\sim 2\ \mu$m).[7] The value of $\Delta H_{t,l}^m$ with only the magnetoelastic interactions taken into account is given, according to Ref. 5, as

$$\Delta H_{t,l}^m = \Delta_0 \delta_{t,l}^2 (1 - (V_{t,l}/C)^2)^{-1/2} / \eta_{t,l} V_{t,l} M_0. \tag{3}$$

The contributions $\delta_{t,l}$ and $\eta_{t,l}$ to the width $\Delta H_{t,l}^m$ are in competition with each other. The actually observable value of ΔH_t for all the REOs (see Figs. 3 and 4) increases with decreasing temperature all the way down to $T = 4.2$ K. This can be explained by an increase in the magnetoelastic interaction with decreasing T on account of the magnetic ordering in the R^{3+} ion.

In solving problems of magnetodynamics the theoretical results are constructed on the basis of the strong- or weak-dissipation approximations.[3–5] Strong dissipation of the elastic energy leads to an S-shaped form, with negative differential mobility and multivaluedness of the DW velocities as a function of the driving magnetic field: to each value of the magnetic field there correspond several values of the DW velocities. Under conditions of ''overheating'' of the elastic subsystem under the influence of the dynamic deformation at the time when the DW breaks the sound barrier a renormalization of the anisotropy constants may be sufficient for the formation of regions in which the domain structure is rearranged in accordance with conservation of topological charge, as is seen in Fig. 5b. In the region where these changes of the domain structure occur, there may be weak dissipation of elastic vibrations. This hypothesis is supported by the data of Ref. 7, in which light diffraction is observed specifically in this region for a TmFeO$_3$ sample. The motion of a DW at the instant of breaking the sound barrier is, according to the results of Refs. 3–5, accompanied by a strong instability, as is confirmed by the data of Ref. 8. Such critical behavior of the DW at the transition to supersonic motion makes it hard to distinguish the approximations of strong- and weak-dissipation.

A new approach to the description of the DW dynamics was developed in Refs. 3 and 9, where the influence of shock waves on the DW dynamics was taken into account. The observed rearrangement of the domain structure obeys Maxwell's rule. The variation of the DW velocity is of the nature of elastically induced fluctuations and is a typical example of a nonequilibrium first-order phase transition. The DW braking occurs through magnetoelastic interactions and shock waves. The resulting value of the ''shelf'' $\Delta H_{t,l}$ on the $V(H)$ curves consists of a sum $\Delta H_{t,l}^m + \Delta H_{t,l}^s$. The DW braking on shock waves depends most importantly on the values of $\alpha_{t,l}$, $\delta_{t,l}$, and $\eta_{t,l}$ and on the DW mobility μ_0 obtained on the initial part of the $V(H)$ curve. In all cases the width of the interval $\Delta H_{t,l}^s$ varies as $1/\eta_{t,l}^2$. The value of $\Delta H_{t,l}^s(\eta_{t,l})$, unlike $\Delta H_{t,l}^m(\eta_{t,l})$ (3), is of a rapidly changing character, especially at low temperatures. At small values of the acoustic damping ($\eta_{t,l} < 0.15$ erg·s/cm^3) the shock mechanism of braking begins to prevail. This conclusion is confirmed experimentally by inverting the DW direction at near-sonic velocities, when the width of the resulting $\Delta H_{t,l}$ decreases by just the quantity $\Delta H_{t,l}^s$ (Ref. 3).

The largest contribution to $\Delta H_{t,l}^s$ is from $\delta_{t,l}$ and initial mobility. For example, when $\delta_{t,l}$ is increased by 1 $\times 10^7$ erg/cm^3, the value of $\Delta H_{t,l}^s$ increases by a factor of

two.[9] This is confirmed experimentally and theoretically by the fact that only in REOs, and predominantly at low temperatures, is the separation of a dynamic deformation (shock wave) from the domain wall detected at DW velocities in the range $V_- < V < V_+$ (Refs. 4 and 7). The lifetime of these formations in TmFeO$_3$ is 20 ns, somewhat shorter than the estimate ~ 40 ns obtained in Ref. 9. From the width of the interval of constant $\Delta H_{t,l}$ on the $V(H)$ curve one can estimate the value of the power delivered by the DW to the elastic subsystem:

$$P = M_0 \Delta H_{t,l} V_{t,l}. \tag{4}$$

It has a value of several microwatts, which, on conversion to a unit surface area of the DW completely confirms the theoretical results[3–5] that the anisotropy constants (1) can be renormalized and their sign can change when the DWs break the sound barrier. This may be responsible for the change in size and structure of the DW in weak ferromagnets, the nonlinearity of $V(H)$, and the multidimensionality of the supersonic motion of the DWs.

When a pressure is applied along certain crystal axes, the spin reorientation temperature T_{SR} can be raised by an amount

$$\Delta T = -LpT_{SR}/2KE, \tag{5}$$

where L and E are the magnetoelastic constants and Young's modulus, and p is the applied pressure.[1] The dynamic rearrangement of the domain structure in TmFeO$_3$ samples, according to Fig. 5b, occurs at a temperature of 168 K, which differs from the upper boundary T_{2SR} of the reorientation temperature by $\Delta T = T - T_{2SR} = 70$ K. According to Eq. (5), such a shift in temperature can occur upon a change of the pressure created by the dynamic deformations of DWs in the region of near-sonic velocities by an amount of the order of 10 kbar. This is only an order of magnitude higher than the pressure (1.5 kbar) along the [001] axis which, according to Ref. 1, was applied to the TmFeO$_3$ samples and caused an increase by 10 K in the upper boundary T_{2DR}. The formation of such large dynamic deformations during the breaking of the sound barrier is also indicated by the previously observed fracture of YFeO$_3$ samples in a study of the relaxation curves of the displacement of the stripe domain structure in the region of sonic velocities.[25]

Another mechanism for the braking of DWs and the formation of intervals ΔH_i operates at $V > V_t$. This corresponds most completely to the model of parametric-resonance braking of DWs at near-wall (Winter) magnons (WMs).[3,6,18,26] This braking mechanism can occur in real single crystals with periodic nonmagnetic inclusions of Fe^{2+} and Fe^{3+} arising during their synthesis. Here the dispersion relation of the WMs and the phononic vibrations coincide, which facilitates the formation of their combined oscillations.[3] According to the proposed scenario,[18,26] the Winter bending oscillations of the DWs are absent or negligibly small at velocities far from the parametric resonance, and here the DW remains planar. Velocities corresponding to parametric resonance are separated by an energy gap, the surmounting of which is accompanied by a loss of stability of the DW. The velocities V_i at which, according to the theoretical results,[18] the formation of the ΔH_i features is observed have the values

$$V_i = (iC\lambda/d)(1+2i\lambda/d)^{-1/2}. \tag{6}$$

The set of values of V_i according to (6) is determined by the ratio of the period of the inhomogeneity λ to the thickness d of the slab. The best agreement between the experimentally observed and calculated values of the velocities V_i is achieved, according to (6), for a period of the inhomogeneity of 30 μm in a slab of thickness $d = 10$ μm, and this also suggests a resonance character of the interaction of the DWs with the WMs. It follows from the theoretical results[18] that in this case the field curve of $V(H)$ will have intervals ΔH_i with velocities V_i,

$$\Delta H_i = \frac{3m_0\tau(CQ\varepsilon)^2 A_i V_i}{32M_s}[1-(V_i/C)^2]^{1/2}, \tag{7}$$

where τ is the relaxation time of the WMs, $\varepsilon_i = 10^{-2}$ is the modulation depth of the spectrum of oscillations of the WMs with the spatial frequency, and $Q = 10^5$ is the Q of the WMs. As the mass m of a moving DW we take a value equal to $\pi\Delta_0^3\delta_{t,l}^3/(\eta_{t,l}^2\nu_{t,l}^3)(\rho/M\Delta H_{t,l})^{1/2}$ (ρ is the resistivity of the REO). The width of the interval ΔH_i increases substantially $\propto\lambda/d$, in agreement with the experimental data. From the width ΔH_i we estimate the WM relaxation time τ_i as $\sim 10^{-7}$ s. The parametric resonance of the DW braking by a WM should satisfy the condition $\omega_n\tau_n \gg 1$, which establishes the lower threshold of the WM frequency as 10^8 Hz.

This model for the braking of a DWs on WMs has been confirmed experimentally in model experiments on samples of orthoferrites with artificially created periodic magnetic inhomogeneities. For this purpose, periodic magnetic strips of an ultradisperse ferromagnetic powder were specially deposited on the surface of a YFeO$_3$ sample. The ferromagnetic grains were of submicron size. From these grains periodic "rolls" of different sizes and orientations with respect to the plane of the DW were formed, i.e., parallel or perpendicular to the [100] axis. The influence of the artificially created magnetic inhomogeneities were manifested on the $V(H)$ curves as visible changes in ΔH_i. The increase and decrease of the width of the intervals or the formation of new ΔH's were registered. For example, as was reported earlier,[6] under these conditions the appearance of an additional interval ΔH_9 on the $V(H)$ curve was observed at a velocity equal to 9 km/s. More active conversions are observed on the $V(H)$ curve when the inhomogeneities are perpendicular to the plane of the DW, creating an additional in-plane field perpendicular to the direction of motion of the DW. The excitation of WMs by other methods has not been detected experimentally.

The acceleration of a DW to any supersonic velocity V_i inevitably involves breaking the sound barrier. Estimates obtained for the relaxation time of WMs agree in order of magnitude with the existence time of the dynamic deformations (~ 20 ns).[7] In view of this, it can be assumed that the elastic deformations have enough time to "adjust" to changes in the magnetic subsystem. Consequently, superimposed on the mechanism of parametric excitation of WMs will be a mechanism of magnetoelastic interaction of a DW with the phonon subsystem. The simultaneous action of these two mechanisms substantially complicates the theoretical description of the DW dynamics.

A feature of the supersonic motion of a DW is its multidimensionality,[3] with a jumplike decrease in the period λ_i with increasing velocity V_i as the amplitude of the driving fields increases. The behavior of the multidimensional formations exhibits regularities typical of self-organizing systems and is determined solely by the internal properties of the dynamic DW under study.[9] The multidimensional formations on the DW (see Fig. 6) are an additional channel of energy dissipation.

The fact that the $V(H)$ curve taken in a field whose amplitude varies from H_{max} to $H = 0$, i.e., in the reverse direction, coincides with the usual $V(H)$ curve (Figs. 3 and 4) attests to the absence of velocity hysteresis, which is at odds with the theoretical results based on the strong-dissipation approximation to the description of the supersonic dynamics of DWs in weak ferromagnets.[3,5] The nonsteady nature of the DW motion,[8] accompanied by changes in the sizes of the multidimensional formations, are also not described by the theoretical models. To explain all of these features, a probabilistic approach to the consideration of the nonlinear and multidimensional DW dynamics in weak ferromagnets was proposed in Ref. 9. A Lyapunov function was introduced as

$$L = \mathcal{P}^2/2\tau - 2MH\mathcal{P} - \int F(\xi)d\xi, \tag{8}$$

where $\mathcal{P}$ is the generalized momentum density, and $F(\xi)$ is the density of the additional DW braking force due to resonant quasiparticle excitations. The function $L(\mathcal{P})$ is similar to the potential energy of a DW. Its maximum corresponds to the unsteady motion of a DW, and its minimum to the stable motion of a DW with one of the velocities V_i. The velocities of steady-state motion of DWs in such a description correspond to extrema of this function. Its maximum corresponds to absolutely unstable motion, and its minimum to stable motion.

However, this approach is applicable only for an ideal dynamical system, devoid of damping, in which the principle of maximum slowing is operative. Fluctuations of the growth-related magnetic inhomogeneities and the resonant increase in the dynamic deformations at the time when the DW breaks the sound barrier transform it into a nonequilibrium system. To describe it we use Maxwell's principle. The usual equation of motion of a DW[3] is replaced by the Fokker–Planck equation for the probability density distribution function $W(t,\mathcal{P})$:[9]

$$\partial W/\partial t = \partial(W\partial\Phi/\partial\mathcal{P})/\partial\mathcal{P} + \partial^2(DW)/\partial\mathcal{P}^2, \tag{9}$$

where D takes into account the jumps of the magnetic inhomogeneities along the path of the DW motion and the fluctuations of the dynamic deformations. This actually means that their combined influence leads to a situation where for each velocity of steady-state DW motion V_i the value of D turns out to be modulated. One can speak of a correspondence of V_i and D_i. From the parametric field dependence of the Lyapunov function $L(\mathcal{P})$ it follows that the solution of equation (9) (Ref. 9) corresponds to a series of values $W_i(t,\mathcal{P})$ for which the DW motion takes on a steady-state character with supersonic frequencies V_i:

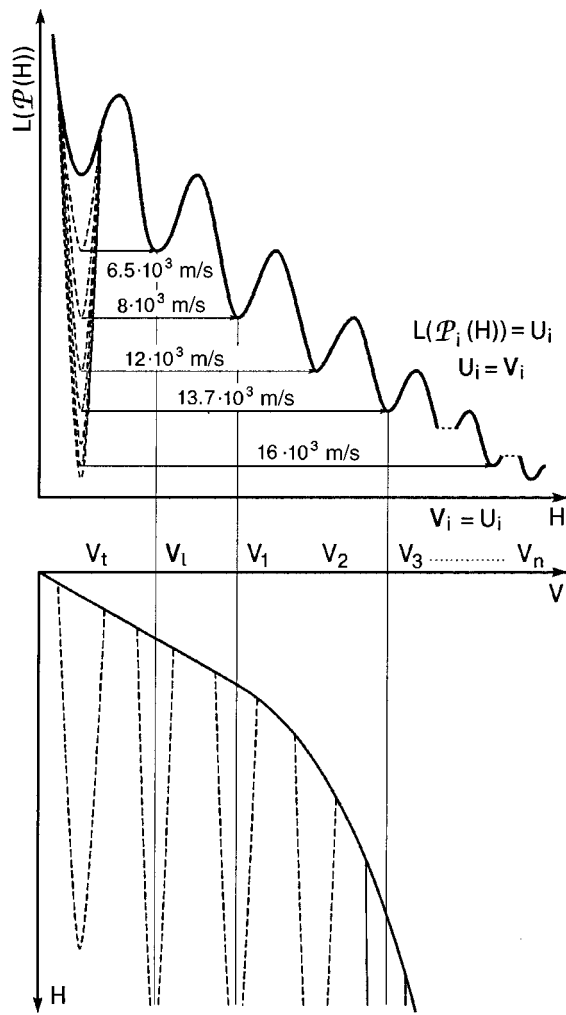$$W_i(t,\mathcal{P}) = N\exp(-L(\mathcal{P})/D_i). \tag{10}$$

FIG. 7. Qualitative field dependence of the Lyapunov function $L(\mathcal{P}(H))$ and of the domain-wall velocity $V(H)$.

The highest probability density $W_i(t,\mathcal{P})$ corresponds to the minima of $L(\mathcal{P})$, i.e., to a minimum of the potential energy of the DW. The qualitative dependence of $L(\mathcal{P})$ on H for different D_i follows the function $L(\mathcal{P}(H))$. The corresponding curves of $V(H)$ and $L(\mathcal{P}(H))$ are presented in Fig. 7. Here the $V(H)$ curve is free of velocity hysteresis, and under conditions such that the minima of the DW energy are equal, the DW velocity changes discontinuously (Fig. 7). In such a treatment the role of the control parameter is played by the DW velocity and not by the magnetic field driving the DW.

In thin-slab samples of $YFeO_3$ a velocity jump occurs from $V = V_t$ to $V_i = 16.2$ km/s.[6] The decrease of the minimum of the DW energy in this case is due to growth of the acoustic attenuation. Similarly, the jumps in the DW velocity observed on the $V(H)$ curve at temperatures of 100 and 4.2 K for $YFeO_3$ upon the transition to supersonic motion can also be explained by a low-temperature decrease of $\eta_{t,l}$. A jumplike transition of the DW motion between velocities of steady-state motion (on the $V_i(H)$ curve) has an analogy with the tunneling of a DW through a potential barrier. The intervals ΔH_i observed on the $V(H)$ curves correspond to minima of the DW potential energy (Fig. 7), the depth of the minima being determined by the state of the phonon and magnon subsystems.

The dynamic behavior of the DWs in REOs, as we have

said, is due to a competition between the influences of $\eta_{t,l}$ and $\delta_{t,l}$. The increasing role of the rare-earth ordering as the temperature is lowered leads to an increase of $\delta_{t,l}$ (Refs. 1 and 12), which, according to Eq. (3), leads to an increase of the interval $\Delta H_{t,l}$ and to a decrease of the minimum of the DW energy. For example, in $TmFeO_3$, in contrast to $YFeO_3$, such a change of $\delta_{t,l}$ is accompanied by a dynamic rearrangement of the domain structure[8] (Fig. 5b). The DW motion at $V = V_t$, V_l, and V_i becomes unstable. Fluctuations of this nature in the critical conditions for the transition of a DW through the sound barrier disrupt the single-valuedness of $V(H)$: the DW decays and can move with several velocities (according to Fig. 5b, with four velocities). As was shown in Ref. 9, obedience to Maxwell's principle leads to a rather slow transition of the DW motion from one velocity to another. As a result, the amplitude of the dynamic deformations excited by the DW have time to grow very strongly, and this is one of the reasons for the observed dynamic rearrangement of the domain structure and the change in the spin reorientation temperature (5). This is a typical example of a nonequilibrium first-order phase transition.

The critical behavior of a DW upon transition to supersonic motion makes it difficult to separate the strong- and weak-dissipation approximations. In the case of strong dissipation of the elastic energy an S-shaped $V(H)$ curve arises, with a negative differential mobility and multivaluedness of the DW velocities as a function of the driving magnetic field. Figure 4 shows the initial part of the experimental and calculated $V(H)$ curves for $TmFeO_3$. It is seen that in the region of negative differential mobility, to each value of the magnetic field there correspond several values of the DW velocity. Under conditions of "overheating" of the elastic subsystem under the influence of the dynamic deformation, at the instant the DW breaks the sound barrier the renormalization of the anisotropy constants can be sufficient for the formation of regions in which the domain structure is rearranged (Fig. 5b).

In $DyFeO_3$ slabs cut perpendicular to the optic axis the coexistence of WFM and AFM phases was observed experimentally in the vicinity of the Morin phase transition, and the AFM–WFM transition was studied.[20,21] The influence of nucleation within the DW was observed, and a second-order phase transition was observed in which metastable AFM domains having an intermediate magnetooptical contrast arose from the 180° DW between the WFM domains. Under the influence of a pulsed magnetic field $H_u = 3.5$ kOe with a rise rate of 200 to 450 Oe/μs the propagation of an AFM–WFM transition front with a maximum velocity of 10 km/s was observed and investigated.[21] The results of that study agree with the effects observed here—unsteady DW motion accompanied by the formation of intermediate contrast (Fig. 5a). These results indicate that in addition to the main mechanism of magnetization reversal through the displacement of DWs, which is characteristic for orthoferrites, the role of the inducing of a magnetic moment, characteristic for an AFM phase, is strongly increasing. An important role in this begins to be played by the exchange enhancement effect,[17] which possibly explains the scale of the observed dynamic rearrangement and its anomalously high rates of development. The unsteady motion of the DWs in $RFeO_3$

can be interpreted as an elastically induced spin reorientation transition.[8]

Previously[27] an elastically induced spin reorientation phase transition was observed in a study of the DW motion at near-sonic velocities in the easy-plane weak ferromagnet $FeBO_3$. It was accompanied by the decay of the initial $180°$ DW into two $90°$ walls. In $RFeO_3$, unlike $FeBO_3$, the elastically induced spin reorientation transition begins inside the DW (see Fig. 5b) and is accompanied only by a transition from an ac type of DW to the less stable ab type.[8,19]

Using the relations which determine the periodicity λ and the amplitude A of the multidimensional formations A (Ref. 9)

$$\lambda = (1 - (\nu/C)^2)^{1/2}(\tau C^2/\mu)$$

$$\times \int_{-\pi/2}^{\pi/2} (H - H(\nu \cos \varphi))^{-1} \cos \varphi \, d\varphi, \qquad (11)$$

$$A = \tau(\nu^2 - C)^2 \nu^{-1} \ln|1 - \nu/(\mu H)|, \qquad (12)$$

one can trace the basic regularities of their variations. Here τ is the lifetime of the magnetic oscillations, and φ is the angle between the normal to the plane of the DW and its velocity. The qualitative forms of the functions $\lambda(H)$ and $A(H)$ obtained according to (11) and (12) are presented in Fig. 4. The period of the multidimensional formation decreases abruptly at the transition of the DW velocity from V_i to V_{i+1}, and their amplitude falls off linearly with increasing driving magnetic field within the interval ΔH_i, which corresponds to the experimentally observed dynamic changes of the multidimensional formations on the DW. At the end of each interval ΔH_i the dissipative structure with the given size λ_i no longer has time to get rid of its energy, and the DW becomes rectilinear (in the interval $\delta H \sim 1$ Oe). The "overheating" of the dynamical system leads to the inclusion of new, stronger mechanisms of energy dissipation, including dissipation due to rearrangement of the domain structure, which is manifested in the unsteady motion of the DW and the formation of intermediate magnetooptical contrast.

The elastic dynamic deformations arising ahead of the moving DW when its velocity has not yet reached the value V_t act as a potential barrier for the DW itself, the amplitude of this barrier increasing as the DW velocity approaches the speed of sound. At the same time, the energy of the DW itself is also growing. As the DW velocity approaches the limiting velocity, quasirelativistic effects arise, leading to a decrease in the width and an increase in the mass of the DW. Such a decrease in the interaction region and interaction time of the DW with the dynamic deformations can turn out to be sufficient for the DW to overcome the potential barrier formed by them. This scenario explains the fluctuation mechanism for the breaking of the sound barrier by the DW and, in our view, has a certain analogy with DW depinning effects in $RFeO_3$.

CONCLUSION

Low-temperature studies of the domain-wall dynamics in weak ferromagnets (the easy-plane $FeBO_3$ and the easy-axis $TmFeO_3$, $EuFeO_3$, $DyFeO_3$, and $YFeO_3$) have permitted us to determine the conditions and mechanisms for the

onset of energy dissipation from the DW to magnetoelastic and bending (Winter) oscillations and to estimate their parameters.

We have shown that a spin reorientation transition is observed at the time that the DW breaks the sound barrier under conditions of strong elastically induced renormalization of the anisotropy constants in the field of a shock wave. The conditions for the onset of this transition are determined in real time.

The domain wall in weak ferromagnets at supersonic velocities becomes multidimensional and is a dynamic self-organizing object. We have proposed a qualitative model within which the evolution of the observed rearrangement of the domain structure was successfully described.

*E-mail: kap@tiis.khstu.ru

[1] K. P. Belov, A. K. Zvezdin, A. M. Kadomtseva, and R. Z. Levitin, *Orientational Transitions in Rare-Earth Magnets* [in Russian], Nauka, Moscow (1979).

[2] M. N. Seavey, Solid State Commun. **10**, 219 (1962).

[3] V. G. Bar'yakhtar, M. V. Chetkin, B. A. Ivanov, and S. N. Gadetskii, *Dynamics of Topological Magnetic Solitons. Experiment and Theory*, Vol. 129 of Springer Tracts in Modern Physics, Springer-Verlag, Berlin (1994).

[4] V. G. Bar'yakhtar, B. A. Ivanov, and A. L. Sukstanskiǐ, Pis'ma Zh. Tekh. Fiz. **6**, 1497 (1980) [Sov. Tech. Phys. Lett. **6**, 645 (1980)].

[5] A. K. Zvezdin, A. A. Mukhin, and A. F. Popkov, "Magnetoelastic anomalies in domain-wall dynamics in weak ferromagnets," FIAN Preprint No. 108, P. N. Lebedev Physics Institute, Academy of Sciences of the USSR SSSR, Moscow (1982).

[6] M. V. Chetkin, A. P. Kuz'menko, A. V. Kaminskiǐ, and V. N. Filatov, Fiz. Tverd. Tela (St. Petersburg) **40**, 1656 (1998) [Phys. Solid State **40**, 1506 (1998)].

[7] A. P. Kuz'menko, A. V. Kaminskiǐ, E. A. Zhukov, and V. N. Filatov, Fiz. Tverd. Tela (St. Petersburg) **43**, 666 (2001) [Phys. Solid State **43**, 692 (2001)].

[8] A. P. Kuz'menko, V. K. Bulgakov, and V. D. Tereshchenko, Fiz. Met. Metalloved. **43**, 12 (2001).

[9] S. V. Gomonov, A. K. Zvezdin, and M. V. Chetkin, Zh. Éksp. Teor. Fiz. 94(11), 133 (1988) [Sov. Phys. JETP **67**, 2250 (1988)].

[10] M. V. Chetkin and A. De la Kampa, JETP Lett. **27**, 157 (1978).

[11] C. H. Tsang, R. L. White, and R. M. White, J. Appl. Phys. **49**, 6063 (1978).

[12] V. D. Buchel'nikov, N. K. Dan'shin, L. T. Tsymbal, and V. G. Shavrov, Usp. Fiz. Nauk **166**, 585 (1996).

[13] S. D. Demokritov, A. I. Kirilyuk, N. M. Kreines, V. I. Kudinov, V. B. Smirnov, and M. V. Chetkin, J. Magn. Magn. Mater. **104**, 663 (1992).

[14] M. V. Chetkin, V. K. Bulgakov, and A. P. Kuz'menko, Izvestiya Vyssh. Uchebn. Zaved. Fiz. 7, 1522 (2001).

[15] F. C. Rossol, J. Appl. Phys. **40**, 1082 (1969).

[16] M. V. Chetkin and Yu. N. Kurbatova, Phys. Lett. A **260**, 108 (1999).

[17] E. A. Turov, *Kinetic, Optical, and Acoustic Properties of Antiferromagnets* [in Russian], Urals Branch of the Academy of Sciences of the USSR, Sverdlovsk (1990).

[18] A. K. Zvezdin and A. F. Popkov, Pis'ma Zh. Tekh. Fiz. **10**, 449 (1984) [Sov. Tech. Phys. Lett. **10**, 188 (1984)].

[19] M. M. Farztdinov, M. A. Shamsutdinov, and A. A. Khalfina, Fiz. Tverd. Tela (Leningrad) **21**, 1522 (1979) [Sov. Phys. Solid State **21**, 878 (1979)].

[20] V. V. Eremenko, N. F. Kharchenko, Yu. G. Litvinenko, and V. M. Naumenko, *Magnetooptics and Spectroscopy of Antiferromagnets* [in Russian], Naukova Dumka, Kiev (1989).

[21] S. L. Gnatchenko, A. B. Chizhik, and N. F. Kharchenko, JETP Lett. **51**, 324 (1990).

[22] I. V. Bar'yakhtar and B. A. Ivanov, "Dynamic braking of domain walls in a weak ferromagnet" [in Russian], Preprint ITF-83-111R, Institute of Theoretical Physics, Academy of Sciences of the UkrSSR, Kiev (1983).

[23] A. V. Zuev and B. A. Ivanov, Fiz. Tverd. Tela (Leningrad) **24**, 2458 (1982) [Sov. Phys. Solid State **24**, 1395 (1982)].

[24] N. Papanicolaou, Phys. Rev. B **55**, 12290 (1997).

[25] P. D. Kim and D. Ch. Khvan, Fiz. Tverd. Tela (Leningrad) **24**, 2300 (1982) [Sov. Phys. Solid State **24**, 1306 (1982)].

[26] V. V. Makhro, Fiz. Tverd. Tela (St. Petersburg) **40**, 1855 (1988) [Phys. Solid State **40**, 1681 (1998)].

[27] M. V. Chetkin, V. V. Lykov, and V. D. Tereshchenko, Fiz. Tverd. Tela (Leningrad) **32**, 939 (1990) [Sov. Phys. Solid State **32**, 555 (1990)].

Translated by Steve Torstveit

Magnetic properties of a lead-doped BKBO single crystal

S. N. Barilo, V. I. Gatal'skaya,* S. V. Shiryaev, and T. V. Smirnova

Institute of Solid State and Semiconductor Physics, National Academy of Sciences of Belarus, ul. P. Brovki 17, 220072 Minsk, Belarus

H. Szymczak, R. Szymczak, and M. Baran**

Institute of Physics of the Polish Academy of Sciences, Al. Lotnikow 32/46, 02-668 Warsaw, Poland

A single crystal of $Ba_{0.65}K_{0.35}Pb_{0.2}Bi_{0.8}O_3$ (BKPBO) grown by the method of electrochemical deposition is investigated. The crystal is single-phase with the cubic perovskite structure. The isotherms of the field dependence of the magnetization for $0.1T_c \leq T \leq 0.72T_c$ are well described by the collective pinning theory. The temperature dependence of the collective pinning length $L_c(T)$ agrees with the mechanism of δl pinning, which is due to spatial fluctuations of the mean free path of the charge carriers. The magnetic properties of BKPBO are compared with those for crystals of the BKBO system. © *2002 American Institute of Physics.*
[DOI: 10.1063/1.1480241]

INTRODUCTION

By now the crystal structure and properties of oxide superconductors based on $BaBiO_3$ have been quite well studied. This crystal belongs to the class of distorted cubic perovskites ABO_3, the framework of which consists of nonequivalent BiO_6 octahedra. The distortion of the structure is due to a static rotation of the octahedra around the [110] axes and an alternation of large and small octahedra, the size difference being due to the different Bi–O lengths. The periodic variation of the Bi–O bond lengths (the averaged values differ by 0.16 Å (Ref. 1)—the distortions of a so-called "breathing" phonon mode) lead to a periodic alternation of the charge on the bismuth ions $[2Bi^{4+}(6s^1) \rightarrow Bi^{3+}(6s^2) + Bi^{5+}(6s^1)]$. As a consequence of this, a charge density wave (CDW) arises, the compound $BaBiO_3$ exhibits insulating properties, and the value of the optical gap is ~ 2 eV.[1] Partial substitution of the electrically inactive Ba (in the A position) by potassium or of the electrically active Bi (in the B position) by lead will lead, at a certain doping level, to the appearance of superconductivity with $T_c = 30$ K (Ref. 2) and 12 K (Ref. 3) in the first and second cases, respectively. This is accompanied by a decrease of both the rotational distortions and the "breathing" mode distortions and, consequently, suppression of the CDW. In both systems the superconductivity arises near the boundary of the metal–insulator transition.[4,5] However, the mechanism of superconductivity in these systems is still not completely clear. Band-structure calculations[6] have shown, for example, that the degree of charge transfer between the two different bismuth ions is negligible. In Ref. 7, based on the results of EXAFS spectroscopy, the valence state of bismuth in $BaBiO_3$ was described as $Bi^{3+} + Bi^{3+}L^2$, where L^2 means that there are two holes in the $2p$ orbitals of O, and the electronic structure consists of a system of local electron (BiO_6) and hole (BiL^2O_6) pairs, separated both in space and energy. Partial substitution of the Ba by K ions decreases the number of electrons, and a fraction of the BiO_6 complexes go into the

state BiL^2O_6. At optimum doping a continuous BiL^2O_6 cluster appears, the local electron pairs with BiO_6 complexes move freely through the BiL^2O_6 clusters, and a transition to the superconducting state occurs.[7] The system $BaPbO_3$, consisting of PbL^2O_6 hole complexes, is nonsuperconducting, and only when it is doped with bismuth ($0.05 < x < 0.35$) do electron pairs arise on the BiO_6 complexes and move freely through the $BiL^2O_6 + PbL^2O_6$ clusters, which leads to the onset of superconductivity.[7]

It is known[4] that the dependence of T_c on the potassium concentration in the BKBO system has a dome-shaped form, with a maximum at $x \approx 0.35–0.4$. For $x > 0.4$ the value of T_c decreases noticeably, which may be linked to growth of the number of BiL^2O_6 hole complexes and the absence of electron complexes upon the complete substitution of the barium by potassium. In the case when the bismuth is partially substituted by lead in the system BKBO with the optimum ratio Ba/K ($T_c \approx 30$ K), according to the model of Ref. 7, additional PbL^2O_6 complexes should arise, and the number of BiO_6 electron complexes should decrease; this leads to a weakening of the coherent transfer of pairs in the dynamic exchange $BiL^2O_6 \leftrightarrow BiO_6$ and $PbL^2O_6 \leftrightarrow BiO_6$, i.e., to degradation of the superconductivity (lowering of T_c).

In this paper we investigate the magnetic properties of a $Ba_{0.65}K_{0.35}Pb_{0.2}Bi_{0.8}O_3$ single crystal with the goal of studying the influence of the Pb doping on the superconducting properties and the pinning mechanism of the vortex lattice in the BKBO system at the optimum potassium concentration ($T_c \approx 30$ K).

SAMPLES AND EXPERIMENTAL METHODS

Single crystals of the systems BKBO and BKPBO were grown the method of electrochemical deposition, the details of which are given in Ref. 8. The phase composition and lattice parameters were determined by the x-ray diffraction method. The x-ray diffraction measurements of powders of the crystalline material BKPBO revealed that the single crys-
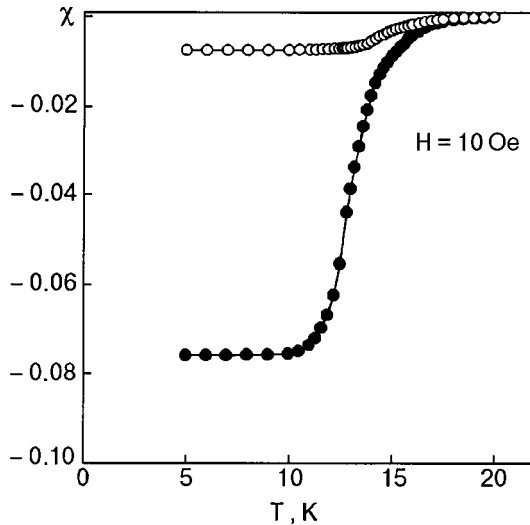
FIG. 1. Temperature dependence of the susceptibility in the FC (○) and ZFC (●) regimes for a BKPBO single crystal.

FIG. 2. Fragments of hysteresis loops for a BKPBO single crystal for various temperatures.

tal with $x=0.35$ (K) and $y=0.2$ (Pb) is single-phase, with the cubic perovskite structure ($a=b=c=4.27$ Å).

Measurements of the magnetization of the BKPBO single crystal in low fields and the $M(H,T)$ hysteresis in fields up to 50 kOe were made with a Quantum Design MPMS-5 SQUID magnetometer. The magnetization isotherms $M(H)$ were obtained at temperatures of 2–14 K. The susceptibility of the single crystal in the normal state was determined in a field of 50 kOe, and then this contribution was subtracted from the $M(H,T)$ curves in order to isolate the response due to the superconducting state of the single crystal.

EXPERIMENTAL RESULTS AND DISCUSSION

The temperature dependence of the susceptibility of the BKPBO single crystal measured under field-cooling (FC) and zero-field cooling (ZFC) conditions in a field of 10 Oe are given in Fig. 1. The superconducting transition temperature $T_c=19.5$ K and the transition width $\Delta T \approx 3$ K; practically complete screening is observed in the crystal and only a 12% Meissner signal. The latter is due to the strong pinning in low fields and is typical of HTSC materials. In low fields the hysteresis loops (Fig. 2) exhibit a comparatively narrow magnetization peak, the value of which is temperature dependent and decreases in the temperature interval 5–11 K by a factor of approximately 3. The small width of this magnetization peak (and, consequently, of the peak of the critical current J_c) in low fields has been observed in single crystals[9] and thick films[10] of BKBO and is explained by either a strong field dependence of J_c (due to the vanishing of the repulsion between vortices) or to strong deformations of the vortex lattice by pinning centers.[11] The value of J_c for 5 K at zero field is 4×10^3 A/cm^2. As the field increases, the value of J_c decreases monotonically; the peak effect[10,12,13] is not observed in the crystal (Fig. 2).

Measurements of the irreversibility field $H_{irr}(T)$ and the upper critical field $H_{c2}(T)$ near T_c showed (Fig. 3) that both these temperature dependences obey a law of the form $H(T) \sim H(0)(1-T/T_c)^n$, with $n=1.4$ for $H_{irr}(T)$ and
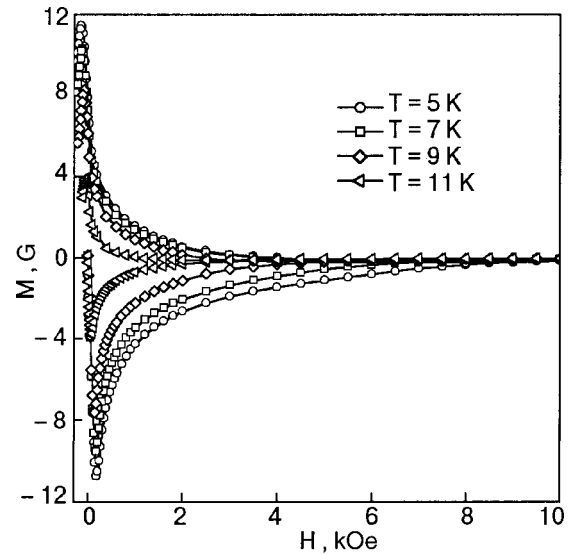
$n=1.23$ for $H_{c2}(T)$. A linear extrapolation agrees with the Ginzburg–Landau theory and gives $H_{c2}(0) \approx 39.65$ kOe, $H_{irr} \approx 29.1$ kOe.

The field dependence $J_c(B)$ at different temperatures (in our case $B=H$) can be described in the framework of the collective pinning theory.[11] For sufficiently low fields a regime of isolated vortices is realized in the crystal, and $J_c \sim (\xi/L_c)^2$, where ξ is the coherence length, and L_c is the characteristic longitudinal size of the vortex. With increasing magnetic field the distance a_0 between vortices decreases, the vortices begin to interact with one another, forming bundles with a characteristic transverse size R_c which depends on the elastic constants of the vortex lattice.[11] For the case of a small bundle size, $a_0 < R_c < \lambda$ (λ is the penetration depth of the magnetic field)

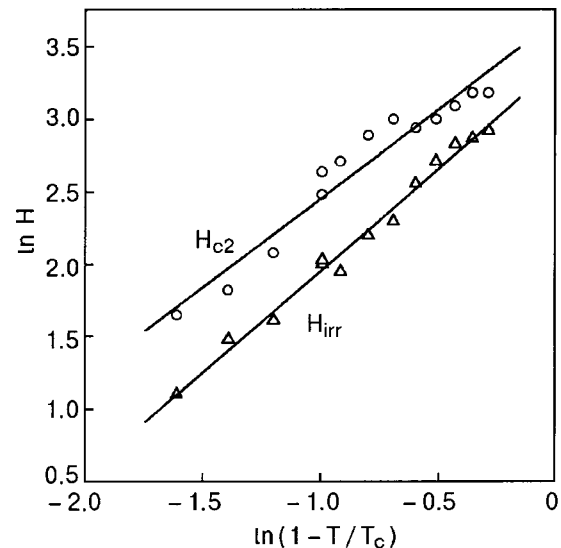$$J_c \sim B \exp[-2(L_c^2(T)B/\varphi_0)^{3/2}] \tag{1}$$

FIG. 3. Temperature dependence of the irreversibility field H_{irr} and upper critical field H_{c2} for a BKPBO single crystal.
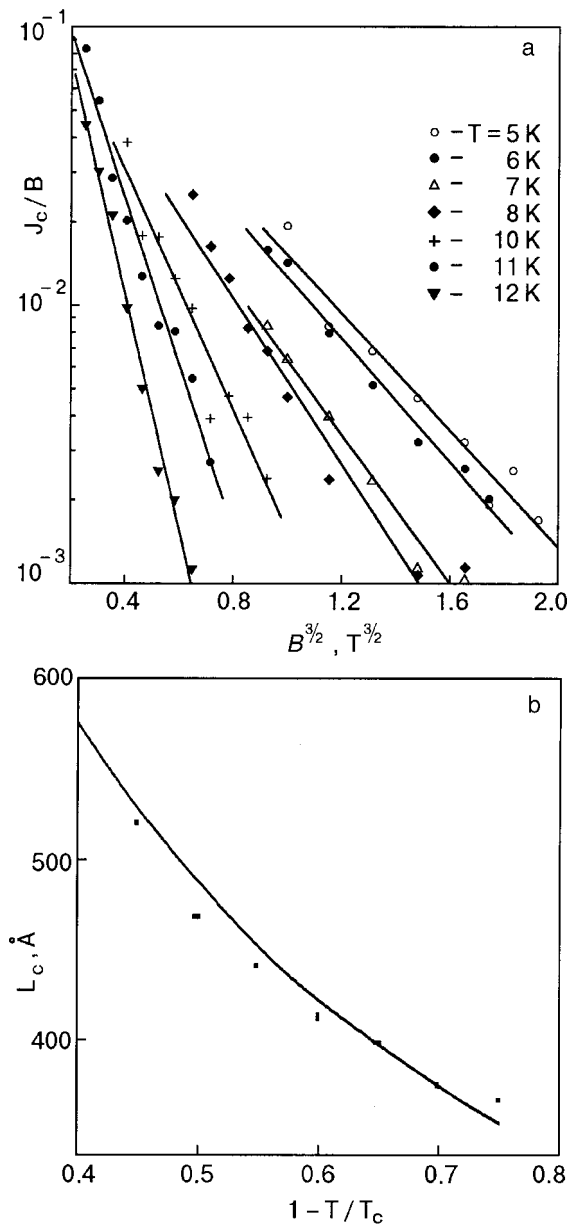
FIG. 4. Curves of J_c/B versus $B^{3/2}$ for a BKPBO single crystal for different temperatures (a) and the function $L_c = 283(1 - T/T_c)^{-0.77}$ (b) (■—experimental data).

FIG. 5. Dependence of the normalized pinning force $F_p/F_{p\,max}$ on the reduced field H/H_{max} (a) and H/H_{irr} (b) for BKPBO.

with a maximum at $B \approx B_{sb}/2$, where B_{sb} $(= \varphi_0/L_c^2(T)$, where φ_0 is the flux quantum) is the crossover field between the regime of pinning of single vortices and pinning of bundles of small-size vortices.

The form of the $M(B)$ curves for BKBO is undistorted by the flux creep only in a certain temperature interval,[14] and we shall therefore limit our analysis to $T \leqslant 14$ K, i.e., $0.1T_c \leqslant T \leqslant 0.72T_c$. The semilog plot of J_c/B versus $B^{3/2}$ (Fig. 4a) can be used to determine the temperature dependence of $L_c(T)$, which can be approximated by the expression $L_c(T) = L_c(0)(1 - T/T_c)^n$ with $L_c \approx 283$ Å and $n = -0.77$ (Fig. 4b).

Exceptionally important information about the pinning mechanism can be obtained by studying the bulk pinning force in the crystal, $F_p = J_c B$. Whereas in conventional type-II superconductors H_{c2} is chosen as the scaling field, for HTSC the irreversibility field H_{irr} may also be used for
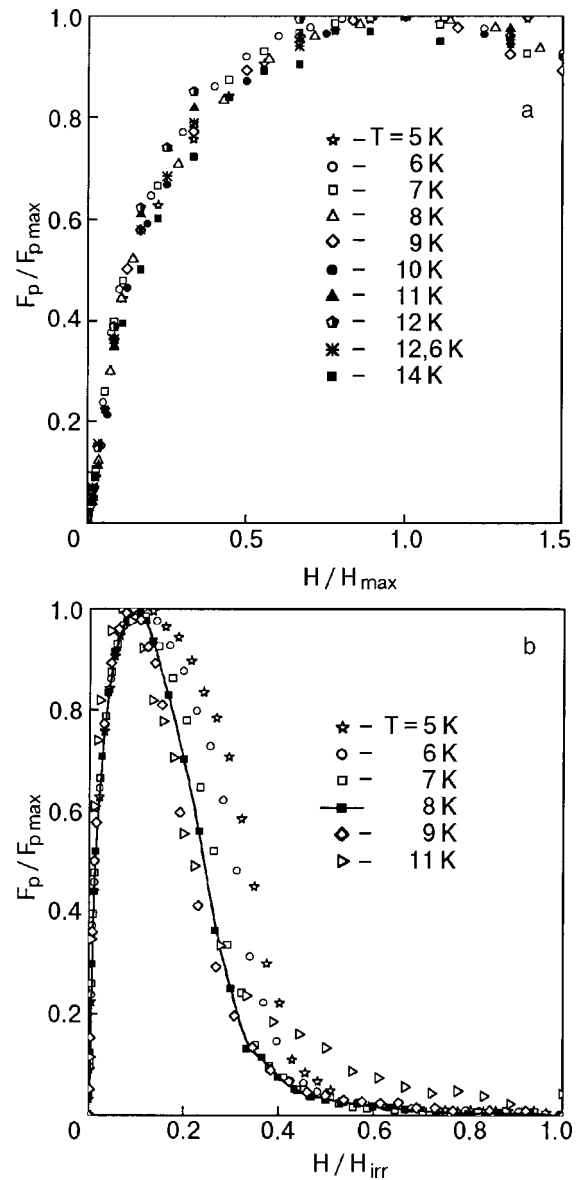
this.[15] Figure 5 shows the experimental values of the normalized pinning force in a BKPBO single crystal as a function of the reduced field $b = H/H_{max}$ (a) and H/H_{irr} (b) for various temperatures. The value of H_{max} corresponds to the maximum pinning force $F_{p\,max}$. The function $F_p/F_{p\,max} = f(H/H_{max})$ has a broad, diffuse maximum in the neighborhood of $b = 1$ (Fig. 5a). At the same time, approximating the experimental data, in accordance with Ref. 16, in the form $F_p \sim b^p(1-b)^q$, where $b = H/H_{irr}$, gives a pronounced peak at $b_{max} = p/(p+q) = 0.10-0.12$ in the temperature interval 5–11 K. In particular, for 5 K the values $p = 0.5$ and $q = 4$ are obtained. Following the model of Ref. 16, one can reach a conclusion about the character of the pinning centers in the superconductor. In classical superconductors the values $p = 1$ and $q = 2$ are characteristic of pinning of the vortex lattice by randomly distributed point defects, while the values $p = 0.5$ and $q = 2$ are characteristic of pinning by planar defects. For HTSCs, in addition to the indicated values of q and q, large values $q = 3$ (Refs. 17–20) and $q = 4$ (Refs. 10

and 21) have also been noted. The pinning force depends on the elastic properties of the vortex lattice, and the value $q = 3$ can be explained[19] by the combined contributions of the elastic constants C_{66} and C_{44}. The reason for the appearance of values $q > 3$ is unclear. Many factors must be taken into account, e.g., the interaction of the vortex lattice with pinning centers and the behavior of the elastic constants of the vortex lattice, which are insufficiently well understood for HTSCs.

It is useful to compare the results obtained for a BKPBO crystal having a concentration $Pb_{0.2}$ with the data for the $Ba_{0.5}K_{0.5}BiO_3$ single crystal.[17] Both crystals have the cubic perovskite structure with close values of the lattice parameters $a \approx b \approx c \approx 4.24$ Å. The transition to the superconducting state occurs at $T_c \approx 20$ K, and the peak effect is absent in both crystals. It is worthy of note that in the BKBO system the optimum Ba/K ratio gives $T_c = 30$ K,[12] and doping by only $Pb_{0.2}$ lowers T_c to 10 K. We also note that the compound $BaPb_{0.2}Bi_{0.8}O_3$ is nonsuperconducting.[1]

The pinning mechanism of the vortex lattice in a type-II superconductor can be described by the so-called δT_c and δl pinning models. The first is due to fluctuations of the superconducting transition temperature, and the second is due to the scatter of the values of the mean free path of the charge carriers.[11] Knowledge of the temperature dependences of the collective pinning length $L_c(T)$ and of the coherence length $\xi(T)$ enables one to determine the pinning mechanism in HTSCs. It was shown in Ref. 11 that $L_c = \xi \delta^{-1/3}$, where δ is a dimensionless pinning parameter, and $L_c(T) \sim \xi^2$ for δl pinning, and $L_c \sim \xi^{2/3}$ for δT_c pinning. Thus one can compare the temperature dependence $L_c(T)$ obtained by us from relation (1) (Fig. 4) with the $L_c(T)$ curve extracted from measurements of $H_{c2}(T) \sim \varphi_0 / \xi^2(T)$. In Ref. 22 it was shown, based on direct measurements of $H_{c2}(T)$ with a force magnetometer for a $Ba_{0.5}K_{0.5}BiO_3$ single crystal, that for temperatures of 2–15 K the pinning of the vortex lattice is described well by the δl pinning model. Pinning of the δl type is also characteristic for BKPBO, as follows from Fig. 6, where the data for the temperature interval $0.1T_c \leqslant T \leqslant 0.72T_c$ are given. We note that in BKBO single crystals with a potassium concentration of 0.34–0.41 and $T_c \approx 30$ K in the temperature interval interval $0.1T_c \leqslant T \leqslant 0.8T_c$ a crossover between δT_c and δl pinning is observed; this is a possible cause of the peak effect in these single crystals.[12,13,17] We stress once again that the peak effect does not arise in BKPBO and BKBO ($x = 0.5$), which are characterized by δl pinning.

CONCLUSION

We have studied the magnetic properties of a $Ba_{0.65}K_{0.35}Pb_{0.2}Bi_{0.8}O_3$ single crystal with $T_c = 19.5$ K, grown by the method of electrochemical deposition. The critical current density J_c (5 K, ~ 0 T) is 4×10^3 A/cm². The field curves of $J_c(B)$ in the temperature interval $0.1T_c \leqslant T \leqslant 0.72T_c$ are well described by the collective pinning theory; with the onset of the regime of bundles of small-size vortices a sharp drop in $J_c(B)$ is observed. The pinning mechanism of the vortex lattice is in agreement with the δl pinning model, which involves a variation of the mean free path of the charge carriers. A comparison of the BKPBO and BKBO
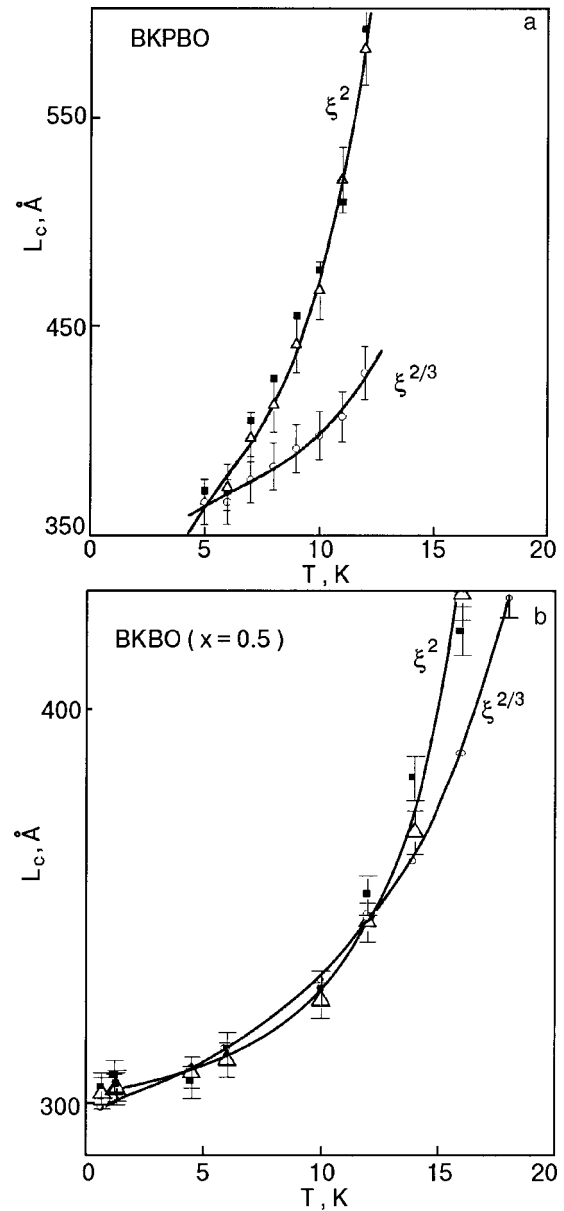

FIG. 6. Temperature dependence of $L_c(T)$ for single crystals of BKPBO (a) and BKBO (b). The solid curves show the approximations $L_c(T) \sim \xi^2$ and $L_c(T) \sim \xi^{2/3}$; ■—experimental data.

($x = 0.5$) crystals shows that they have close values of T_c and of the lattice parameters, that the peak effect is absent in both crystals, and that both have δl pinning of the vortex lattice.

*E-mail: v_gatal@ifttp.bas-net.by
**E-mail: baran@ifpan.edu.pl

[1] D. E. Cox and A. W. Sleight, Solid State Commun. **19**, 969 (1976).
[2] L. F. Mattheiss, E. M. Gyorgy, and D. M. Johnson, Phys. Rev. B **37**, 3475 (1988).
[3] A. W. Sleight, J. L. Gillson, and P. E. Bierstedt, Solid State Commun. **17**, 27 (1975).
[4] Sh. Pei, J. D. Jorgensen, B. Dabrowski, D. E. Hinks, D. R. Richards, A. W. Mitchell, J. M. Newsam, E. K. Sinha, D. Vaknin, and A. J. Jacobson, Phys. Rev. B **41**, 4126 (1990).
[5] D. E. Cox and A. W. Sleight, Acta Crystallogr., Sect. B: Struct. Crystallogr. Cryst. Chem. **35**, 1 (1989).

[6] L. F. Mattheiss and D. R. Hamann, Phys. Rev. B **23**, 4227 (1983).

[7] A. P. Menushenkov, Poverkhnost **12**, 56 (1999).

[8] S. N. Barilo, S. V. Shiryaev, V. I. Gatalskaya, D. I. Zhigunov, A. V. Push-karev, V. V. Fedotova, H. Szymczak, R. Szymczak, M. Baran, J. W. Lynn, N. Rosov, and S. Skanthakumar, J. Cryst. Growth **198/199**, 636 (1999).

[9] V. I. Gatalskaya, G. V. Gatalskii, L. A. Kurochkin, S. L. Kurochkin, and S. V. Shiryaev, Phys. Status Solidi A **143**, 123 (1994).

[10] S. N. Barilo, V. I. Gatalskaya, S. V. Shiryaev, T. V. Smirnova, H. Szymc-zak, R. Szymczak, and M. Baran, Phys. Status Solidi A **181**, 471 (2000).

[11] G. Blatter, M. V. Feigelman, A. I. Larkin, and V. M. Vinokur, Rev. Mod. Phys. **66**, 1125 (1994).

[12] S. N. Barilo, V. I. Gatalskaya, S. V. Shiryaev, A. S. Shestac, L. A. Kuroch-kin, T. V. Smirnova, V. N. Koyava, N. S. Orlova, and A. V. Puskarev, Physica C **254**, 181 (1995).

[13] S. N. Barilo, S. V. Shiryaev, V. I. Gatalskaya, J. W. Lynn, M. Baran, H. Szymczak, R. Szymczak, and D. Dew-Hughes, Phys. Rev. B **58**, 12355 (1998).

[14] W. Harneit, T. Klein, L. Baril, and C. Escribe-Filippini, Europhys. Lett. **36**, 141 (1996).

[15] L. Niel, Cryogenics **32**, 975 (1992).

[16] D. Dew-Hughes, Philos. Mag. **30**, 293 (1974).

[17] R. Prozorov, A. Tsameret, J. Jeshurun, C. Koren, M. Konczykowski, and S. Bouffard, Physica C **234**, 311 (1994).

[18] E. Mezetti, R. Gerbaldo, G. Gigo, L. Gozzelino, B. Minetti, and R. Cheru-bini, J. Appl. Phys. **82**, 6122 (1997).

[19] J. J. Jun, B. R. Zhao, B. Xu, S. Q. Guo, B. Yin, J. W. Li, and L. Li, Phys. Status Solidi A **157**, 115 (1996).

[20] M. Baran, H. Szymczak, R. Szymczak, S. N. Barilo, V. I. Gatalskaya, and S. V. Shiryaev, J. Magn. Magn. Mater. **166**, 124 (1997).

[21] J. N. Li, F. R. De Boer, L. W. Loeland, M. I. V. Menken, K. Kadowaki, A. A. Menovsky, J. J. M. Franse, and P. H. Kes, Physica C **169**, 81 (1990).

[22] S. N. Barilo, D. Hall, V. I. Gatalskaya, T. V. Smirnova, S. V. Shiryaev, and J. E. Crow, Physica B **294−295**, 383 (2001).

Translated by Steve Torstveit

LOW-DIMENSIONAL AND DISORDERED SYSTEMS

Aging effect on the magnetic and transport properties of laser-deposited La$_{0.5}$Sr$_{0.5}$CoO$_{3-\delta}$ films

V. G. Prokhorov* and G. G. Kaminskiĭ

Institute of Metal Physics of the National Academy of Sciences of Ukraine, pr. Vernadskogo 36, 03680 Kiev, Ukraine

V. M. Ishchuk and I. N. Chukanova

Institute of Single Crystals of the National Academy of Sciences of Ukraine, pr. Lenina 60, 61001 Kharkov, Ukraine

Y. P. Lee

Department of Physics, Hanyang University, Seoul 133-791, Korea

K. W. Kim

Department of Physics, Sunmoon University, Asan, Chungnam 336-840, Korea

Magnetic and transport studies are carried out on laser-deposited films of La$_{0.5}$Sr$_{0.5}$CoO$_{3-\delta}$ and La$_{0.65}$Sr$_{0.35}$CoO$_3$. It is shown that prolonged aging (for up to one year) of La$_{0.5}$Sr$_{0.5}$CoO$_{3-\delta}$ films leads to a decrease of the oxygen concentration to a deficit $\delta \approx 0.08$. The oxygen deficit that forms is accompanied not only by a redistribution of the charge between the cobalt ions of different valences but also by the formation of topological disorder in the Co–O–Co conducting channel as a result of the accumulation of oxygen vacancies. The observed growth of the resistivity with decreasing temperature is more accurately described in a model of weak localization of the carriers than by a thermally activated conduction mechanism. In addition to the usual ferromagnetic transition at $T_C \approx 240$ K, in the "aged" La$_{0.5}$Sr$_{0.5}$CoO$_{2.92}$ film an additional transition, typical of a magnetic transition in a spin glass, is observed at $T_M \approx 50$ K. Analysis of the temperature behavior of the resistivity of La$_{0.5}$Sr$_{0.5}$CoO$_3$ and La$_{0.65}$Sr$_{0.35}$CoO$_3$ films found in the metallic state show that in addition to the quadratic term proportional to T^2, the temperature dependence of the resistivity contains an exponential term of the form $\propto \exp(-T_0/T)$, which is due to the opening of a spin gap in the conducting channel at low temperatures. © *2002 American Institute of Physics.* [DOI: 10.1063/1.1480242]

1. Interest in the study of cobalt-based lanthanide oxides (La$_{1-x}$Sr$_x$CoO$_3$) is due to their high electrical and ionic conductivity, which permits them to be used as electrodes for ferroelectric (Pb–Zr–Ti–O) capacitors instead of costly platinum and also in other electrochemical devices.[1,2] The ideal compound La$_{0.5}$Sr$_{0.5}$Co$_3$ (LSCO) has a pseudocubic perovskite structure (with a crystal lattice constant $a \approx 0.3834$ nm) and a metallic behavior of the resistivity in the low-temperature region.[3,4] The large negative magnetoresistance R_m recently observed in the compound La$_{1-x}$Sr$_x$CoO$_3$ in the concentration range $0.15 < x \le 0.4$ has attracted still more attention to the study of these perovskite systems.[5–7] On the other hand, it has been shown that the temperature dependence of the resistivity of epitaxial films of LSCO is very sensitive to the conditions of their preparation and subsequent heat treatment. For example, when the oxygen pressure in the chamber during the deposition of the films is decreased, a transition is observed from a metallic to a semiconductor type of conduction.[8–11] In spite of the fact that the

transport properties of the LSCO films have been studied for quite some time, the mechanism of conduction in these objects is still a topic of discussion.

In the present paper we report a study of the influence of prolonged aging on the magnetic and transport properties of LSCO films obtained by the pulsed laser deposition. It is shown that the oxygen deficit caused by the aging effect leads to significant changes in the magnetic and transport properties of the LSCO films which cannot be explained by a simple redistribution of charge between the Co^{3+} and Co^{4+} ions. The observed features in the temperature dependence of the resistivity and magnetization are discussed in the framework of modern theoretical models.

2. Films of La$_{0.5}$Sr$_{0.5}$CoO$_{3-\delta}$ were prepared by the method of pulsed laser deposition on single-crystal substrates of SrTiO$_3$ (STO) with a (001) working plane. The parameters of the Nd-YAG laser used for the deposition were: wavelength 1064 nn, pulse duration 7.8–10.5 ns, energy per pulse 0.3–0.4 J/pulse, and pulse repetition rate 12 Hz. The sub-
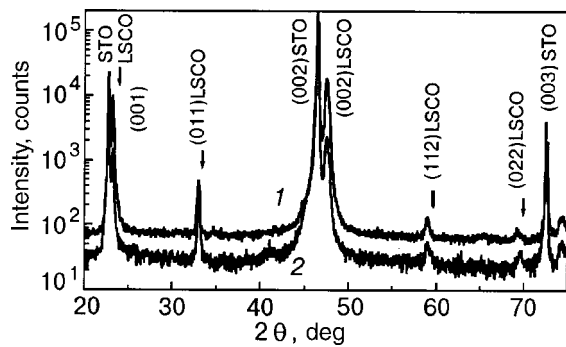
FIG. 1. $\theta - 2\theta$ x-ray diffraction curves for the as-deposited (*1*) and aged (*2*) $La_{0.5}Sr_{0.5}CoO_{3-\delta}$ films.

FIG. 2. Temperature dependence of the resistivity of $La_{0.5}Sr_{0.5}CoO_{2.92}$ (1), $La_{0.65}Sr_{0.35}CoO_3$ (2), and $La_{0.5}Sr_{0.5}CoO_3$ (3) films, measured at zero magnetic field (black circlets) and in a field of 5 T (white circlets). The insets show the relative magnetoresistance R_m for the aged $La_{0.5}Sr_{0.5}CoO_{2.92}$ film (a) and the as-deposited $La_{0.65}Sr_{0.35}CoO_3$ film (b) in a perpendicular magnetic field of 5 T.

strate temperature during the deposition of the films was 850 °C. The oxygen pressure in the chamber was maintained at a level of 450 mtorr during the deposition and 750 torr during the cooling of the films. The thickness of the deposited films was 200 nm. Diffractograms of the $\theta - 2\theta$ type were obtained on a Rigaku diffractometer with a Cu-K_α source and an angular scanning step of $0.01°$. The parameters of the crystal lattice were determined from a linear extrapolation of the experimental data to a value $\cos^2 \theta / \sin \theta = 0$, which made it possible to reduce the influence of instrumental errors. The resistivity was measured by the usual four-contact method in the temperature interval 4.2–300 K in a magnetic field of up to 5 T. The absolute value of the resistivity ρ was determined by the van der Pauw method. The magnetization curves of the films cooled in zero field (ZFC) and in a field of 100 Oe applied parallel to the surface of the films (FC) were obtained with a Quantum Design SQUID magnetometer in the temperature interval 4.2–300 K.

3. Figure 1 shows the x-ray diffractograms for an as-deposited $La_{0.5}Sr_{0.5}CoO_{3-\delta}$ film (curve *1*) and one that had been aged in air for a year (curve *2*). We see that both types of film have mainly a *c*-axis growth texture, which is characterized by a high intensity of the (00*l*) peaks. In addition, however, in both films there are also reflections of low intensity: (011), (022), and (112). An analysis shows that both the initial and the aged films have a pseudocubic crystal lattice with the following parameters: $c \approx 0.3835$ nm (the as-grown film) and $c \approx 0.3842$ nm (the aged film). The increase in the lattice parameter c in the perovskitelike compound $La_{0.5}Sr_{0.5}CoO_{3-\delta}$, as a rule, is accompanied by a decrease in the oxygen content.[12] Based on the data of this study, a simple linear dependence between the lattice parameter c and the concentration of oxygen vacancies can be assumed in the region $0 < \delta < 0.4$: $c[nm] = c_{\delta=0}[nm] + 8.5 \times 10^{-3}\delta$, where c is the actual value of the lattice parameter and $c_{\delta=0}$ is the value of the lattice parameter for the compound with the stoichiometric oxygen composition ($\delta = 0$). Assuming that in our case the stoichiometric composition corresponds to the as-deposited film, we can conclude that in the aged sample $La_{0.5}Sr_{0.5}CoO_{3-\delta}$ the oxygen deficit is $\delta \approx 0.08$. Thus the effect of prolonged aging of LSCO films amounts to a loss of oxygen to a deficit $\delta \approx 0.08$.

Figure 2 shows the temperature dependence of the resistivity $\rho(T)$ for the as-deposited (*3*) and aged (*1*) LSCO films. It is seen that the as-deposited film has a metallic trend of the
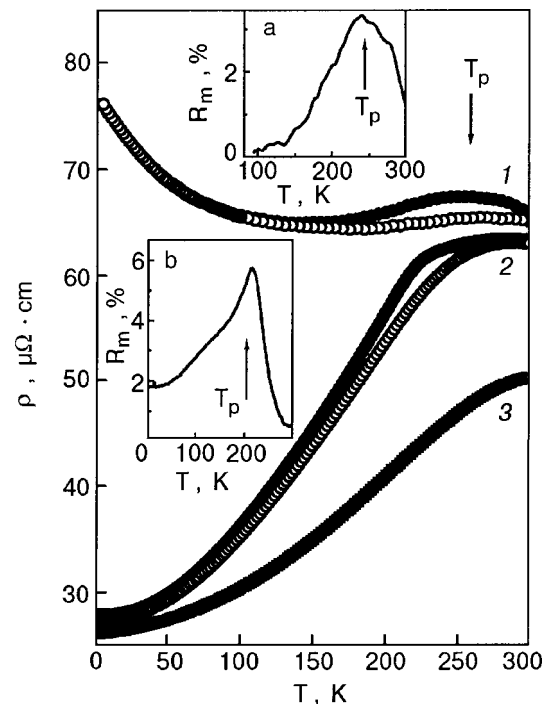
resistivity throughout the investigated temperature range and that the value of the resistivity is practically independent of the applied magnetic field (up to 5 T) within the experimental error. For the aged film, on the contrary, the $\rho(T)$ curve has a pronounced nonmonotonic behavior, with a maximum at $T_p \approx 240$ K and a minimum at $T \approx 140$ K. Applying an external magnetic field leads to a decrease of the resistivity in the region of the maximum and to a shift in the position of the maximum to higher temperatures. Inset "a" shows the temperature dependence of the negative magnetoresistance for the aged LSCO film, defined as $R_m(\%) = 100\% [R(0) - R(H)]/R(0)$, which reached a value of $\approx 3.6\%$. Here $R(0)$ and $R(H)$ are the resistances of the samples in the absence of magnetic field and in a magnetic field of 5 T. The negative-R_m effect has been observed previously for LSCO films of this composition. However, the value of R_m either increased monotonically as the temperature was lowered[12] or changed sign.[8] In our case the curve has the shape of a pronounced peak, which is ordinarily observed in $La_{1-x}Sr(Ca)_xCoO_3$ compounds with a lower concentration of the divalent (Sr or Ca) ions.[13,14] There is nothing surprising in this if one considers the fact that the oxygen deficit formed as a result of the aging of the film should lead to a redistribution of the valence of the cobalt ions.

The ionic (charge) relation for the compound $La_{0.5}Sr_{0.5}CoO_{3-\delta}$ with allowance for the oxygen vacancies (V_δ^0) should be written in the following form:[15]

$$La_{1-x}^{3+}Sr_x^{2+}Co_{1-x+2\delta}^{3+}Co_{x-2\delta}^{4+}O_{3-\delta}^{2-}V_\delta^0.$$
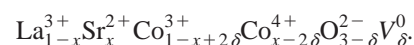
As was shown above, the degree of the oxygen deficit in the aged film as compared to the as-deposited film is $\delta = 0.08$.
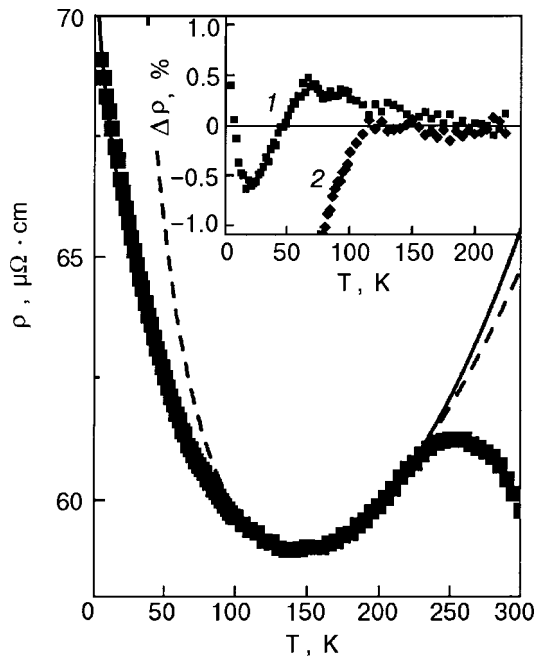
FIG. 3. Temperature dependence of the resistivity of $La_{0.5}Sr_{0.5}CoO_{2.92}$ film at zero magnetic field. The solid and dashed curves correspond to the theoretical curves for the weak-localization and hopping-conduction models, respectively. The inset shows the relative difference between the experimental and calculated data for the weak-localization model (1) and hopping-conduction model (2).

Thus the real ratio of the cobalt ions of different valence, $Co^{3+}:Co^{4+}$, for the aged film will be not 0.5:0.5 but 0.66:0.34. A similar ratio of the cobalt ions of different valence can be achieved in films with the optimum oxygen composition by decreasing the concentration of the Sr^{2+} ions in them. To check this conjecture we deposited, under similar conditions, a film with the composition $La_{0.65}Sr_{0.35}CoO_3$, which had a $Co^{3+}:Co^{4+}$ ratio of 0.65:0.35, i.e., close to the ratio of the cobalt ions of different valence for the aged $La_{0.5}Sr_{0.5}CoO_{2.92}$ film. As is shown in Fig. 2 (curve *2*), the $La_{0.65}Sr_{0.35}CoO_3$ film exhibits a metallic trend of $\rho(T)$ in the entire range of temperatures investigated, unlike the aged $La_{0.5}Sr_{0.5}CoO_{2.92}$ film, which has a marked growth of the resistivity at $T \lesssim 140$ K, in spite of the close values of the $Co^{3+}:Co^{4+}$ ratio. Thus we can conclude that the growth of the resistivity with decreasing temperature observed in the $La_{0.5}Sr_{0.5}CoO_{2.92}$ film with the oxygen deficit is determined not by a decrease in the concentration of the Co^{4+} ions below the percolation threshold but is of a different physical nature. In inset "b" we see that, first, the negative R_m has a peak at $T_p = 220$ K, the value of which is larger than for the $La_{0.5}Sr_{0.5}CoO_{2.92}$ film ($\approx 3.6\%$), and, second, that R_m has a nonzero value even in the region of very low temperatures.

In Fig. 3 it is seen that below $T_p \approx 240$ K the temperature behavior of the resistivity for the aged film $La_{0.5}Sr_{0.5}CoO_{2.92}$ can be described to good accuracy by the following empirical formula:

$$\rho(T) = \rho_0 + \alpha T^2 - \beta T^{1/2}, \tag{1}$$

with the fitting parameters $\rho_0 = 72.7 \ \mu\Omega \cdot cm$, $\alpha = 2.1 \times 10^{-4} \ \mu\Omega \cdot cm \cdot K^{-2}$, and $\beta = 1.5 \ \mu\Omega \cdot cm \cdot K^{-1/2}$. The theoretical curve is shown by the solid curve in Fig. 3. The quadratic term in expression (1) usually pertains to an

electron–electron (or Baber) scattering mechanism.[16] The negative term $\beta T^{-1/2}$, which makes for growth of the resistivity with decreasing temperature, has a form reminiscent of the quantum correction to the conductivity of electrons in the weak-localization model.[17] On the other hand, the observed growth of the resistivity in the low-temperature region cannot be described in the framework of a model of thermally activated or hopping conduction.[11,18] The dotted curve in Fig. 3 corresponds to an expression for the temperature dependence of the resistivity that includes the Mott term describing hopping conduction: $\rho(T) = \rho_0 + \alpha T^2 + \gamma \exp(T_0/T^{1/4})$, with the fitting parameters $\rho_0 = 47.9 \ \mu\Omega \cdot cm$, $\alpha = 1.24 \times 10^{-4} \ \mu\Omega \cdot cm \cdot K^{-2}$, $\gamma = 0.8 \ \mu\Omega \cdot cm$, and $T_0 = 4500$ K. As we see from the inset in Fig. 3, the relative difference between the experimental values of the resistivity and the theoretical curve obtained from Eq. (1) does not exceed $\pm 0.5\%$ in the entire temperature interval (curve *1*), whereas the hopping conduction model, even with the optimal values of the fitting parameters, leads to a strong deviation of $\rho(T)$ from the experimental curve for $T < 100$ K (curve *2*).

It is well known that any type of disorder in the conducting channel (or conduction band) can lead to localization of the electrons.[19] Let us suppose that the oxygen vacancies introduce a slight disorder into the conducting channel of the aged film $La_{0.5}Sr_{0.5}CoO_{2.92}$. This type of topological disorder not only leads to a change in the electron spectrum, which is characteristic of a disordered Fermi liquid, but also makes the electron system unstable with respect to the metal–insulator transition.[20] An increase in the electron density of states near the Fermi level is typical for a system of strongly correlated electrons near a metal–insulator transition and should lead to enhancement of the role of electron–electron scattering in the conduction mechanism of these materials.

Let us do a more detailed analysis of expression (1) on the basis of the weak localization model. For the contribution to the resistivity due to the electron–electron scattering of the carriers, one can write the following expression: $\rho_{ee}(T) \approx (mE_F/ne^2\hbar)(T/E_F)^2$, where m, n, and e denote the electron mass, concentration, and charge, and E_F is the Fermi energy.[21] The quantum correction to the electronic conductivity in the weak localization model can also be reduced to the simple form: $\rho_{WL}(T) \approx -(mE_F/ne^2\hbar)(T/E_F)^{1/2}$ if the electron localization condition $l \approx \hbar/p_F$ is used, where l is the electron mean free path and p_F is the Fermi momentum.[21] Knowing the values of the coefficients α and β in expression (1), we can estimate the order of magnitude of the Fermi energy. The value obtained in this way, $E_F \approx 10^3$ K, is entirely reasonable for this class of compounds.[18] Consequently, we may conclude that the oxygen deficit accompanying aging of LSO films leads to the onset of disorder in the conduction channel and to the appearance of a weak localization effect on the temperature dependence of the resistivity.

Figure 4 shows the temperature dependence of the normalized resistivity, $\Delta\rho_{norm}(T) = [\rho(T) - \rho_0]/(\rho_{250} - \rho_0)$, for the as-deposited $La_{0.5}Sr_{0.5}CoO_3$ (*1*) and $La_{0.65}Sr_{0.35}CoO_3$ (*2*) films. We see that in the high-temperature region ($T \geq 150$ K) the two experimental curves practically coincide, but when T is lowered their behavior begins to diverge sub-
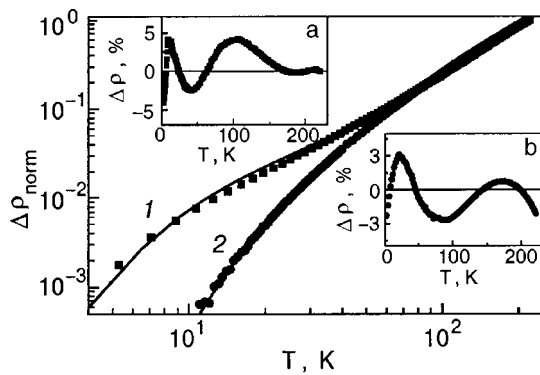
FIG. 4. Temperature dependence of the normalized resistivity for the as-deposited films of $La_{0.5}Sr_{0.5}CoO_3$ (1) and $La_{0.65}Sr_{0.35}CoO_3$ (2). The solid curves are theoretical. Insets "a" and "b" show the relative difference between the experimental data and the theoretical curves for films 1 and 2.

FIG. 5. Temperature dependence of the magnetization for the as-deposited $La_{0.5}Sr_{0.5}CoO_3$ film (1), the aged $La_{0.5}Sr_{0.5}CoO_{2.92}$ film (2) and the as-deposited $La_{0.65}Sr_{0.35}CoO_3$ film (3), cooled in the absence of magnetic field (ZFC) and in a magnetic field of 100 Oe applied parallel to the surface (FC).

stantially. This analysis has shown that in the approximation of one-channel conduction the behavior of $\Delta\rho_{norm}(T)$ for both films can be described by the empirical expression $\Delta\rho_{norm}(T) = \alpha T^2 \exp(-T_0/T) + \beta \exp(-T_0/T)$ (the solid curves) with the fitting parameters $\alpha = 2 \times 10^{-5}$, $\beta = 0.05$, and $T_0 = 20$ K (for $La_{0.5}Sr_{0.5}CoO_3$) and $\alpha = 3 \times 10^{-5}$, $\beta = 0.001$, and $T_0 = 25$ K (for $La_{0.65}Sr_{0.35}CoO_3$). Insets "a" and "b" in Fig. 4 show that the difference between the experimental and theoretical curves is not more than $\pm 5\%$.

The existence of exponential terms of this form in the temperature dependence of the resistivity of itinerant ferromagnets in the metallic state had been predicted previously for explaining the behavior of $\rho(T)$ for rare-earth metals and alloys.[22–24] There it was assumed either that an energy gap opens in the spectrum of spin-wave excitations on account of the strong magnetic anisotropy, or that the nuclear levels are twofold degenerate on account of the influence of the intracrystalline field. The latter assumption appears to be the more likely for the given class of compounds, as it is known that the Co^{3+} ions can be found in low-spin ($t_{2g}^6 e_g^0$) and high-spin ($t_{2g}^4 e_g^2$) states, which are separated by a small energy gap.[18] Recently it was shown that the value of the spin gap can determine the low-temperature behavior of the resistivity of the compound $La_{1-x}Sr_xCoO_3$ with a low concentration of strontium ions ($x \leq 0.15$).[13] It is known that in this region of concentrations x the compound has a semiconductor trend of the resistivity $\rho(T)$, since it decomposes into noninter-coupled ferromagnetic clusters with metallic conduction in a nonmetallic matrix, the volume concentration of the clusters being below the percolation threshold.[25,26] Our analysis shows (see Fig. 4) that a spin gap can also appear on the temperature dependence of the resistivity in heavily strontium-doped $La_{1-x}Sr_xCoO_3$ compounds found in a ferromagnetic metallic state. It should be noted that the values of T_0 obtained here for the concentrations $x = 0.35$ and 0.5 are in good agreement with the values of the spin gap predicted for this compound.[13]

Figure 5 shows the temperature dependence of the magnetization (FC and ZFC) for the three films studied–as-deposited $La_{0.5}Sr_{0.5}CoO_3$ (curve *1*), aged $La_{0.5}Sr_{0.5}CoO_{2.92}$ (curve *2*), and as-deposited $La_{0.65}Sr_{0.35}CoO_3$ (curve *3*). It is seen from the curves that, first, the transition to the ferromagnetic state occurs at $T_C \approx 250$ K for the $La_{0.5}Sr_{0.5}CoO_3$
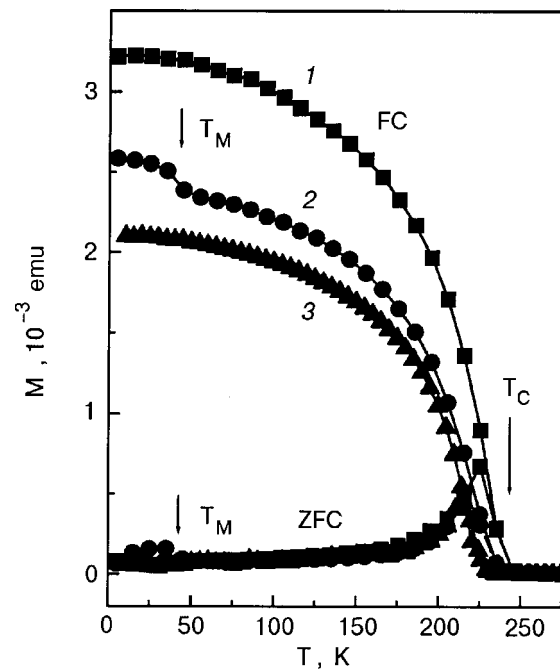
film, at $T_C \approx 240$ K for $La_{0.5}Sr_{0.5}CoO_{2.92}$, and at $T_C \approx 230$ K for $La_{0.65}Sr_{0.35}CoO_3$, in agreement with the data in the literature.[11,25] Second, the oxygen deficit that appears as the LSCO films are aged (curve *2*) or when the strontium concentration is decreased, i.e., for the $La_{0.65}Sr_{0.35}CoO_3$ film; curve *3*) in both cases leads to a decrease of the value of the magnetic moment when the samples are cooled in a magnetic field $H = 100$ Oe and, hence, to a possible decrease of the FM phase in them. Third, for the aged $La_{0.5}Sr_{0.5}CoO_{2.92}$ film, as the temperature is decreased to $T_M \approx 50$ K one observes yet another magnetic transformation, which is accompanied by a slight increase of the magnetic moment of the sample. It should be noted that although the general characteristic of the temperature dependence of the additional contribution to the magnetization for the FC and ZFC states remains the same as for the main transition, it is more reminiscent of the magnetic transitions observed in spin glasses than of those in homogeneous magnetic materials. For example, the growth of the magnetic moment with increasing temperature for the ZFC case begins long before the phase transition temperature. A similar type of dependence of $M(T)$ at temperatures close to $T_M \approx 50$ K was observed for a compound of this type with a very low strontium concentration ($x = 0.06$), and T_M was identified as the freezing temperature of a spin glass.[25] Fourth, the too-large difference between the FC and ZFC magnetization curves $M(T)$ presupposes a substantial non-uniformity in the distribution of the intrinsic magnetic moment in the investigated films and confirms the existence of ferromagnetically ordered regions separated by a matrix of disordered spins (the cluster glass state).[25,26]

One can draw the following conclusions.

1. The long-term aging (one year) of $La_{0.5}Sr_{0.5}CoO_{3-\delta}$ leads to loss of oxygen by an amount $\delta \approx 0.08$. The accumulation of oxygen vacancies brings about not only a redistri-

bution of charge between cobalt ions of different valence but also the formation of topological disorder in the conducting channel of the Co–O–Co chains.

2. The observed growth of the resistivity as the temperature is lowered in the oxygen-deficient $La_{0.5}Sr_{0.5}CoO_{2.92}$ films is governed not by a thermally activated conduction mechanism but by the effect of weak localization of carriers due to the vacancy-related disorder in the position of the oxygen ions.

3. Analysis of the temperature behavior of $\rho(T)$ for $La_{0.5}Sr_{0.5}CoO_3$ and $La_{0.65}Sr_{0.35}CoO_3$ films found in the metallic state shows that in addition to the quadratic term $\propto T^2$ the temperature dependence of the resistivity contains an exponential term of the form $\propto \exp(-T_0/T)$ due to the opening of a spin gap in the conducting channel at low temperatures.

[*]E-mail: pvg@imp.kiev.ua

[1] J. Mizusaki, J. Tabuchi, T. Matsuura, S. Yamauchi, and K. Fueki, J. Electrochem. Soc. **136**, 2082 (1989).
[2] B. Yang, S. Aggarwal, A. M. Dhote, T. K. Song, R. Ramesh, and J. S. Lee, Appl. Phys. Lett. **71**, 356 (1997).
[3] Z. L. Wang and J. Zhang, Phys. Rev. **54**, 1153 (1996).
[4] S. Yamaguchi, Y. Okimoto, and Y. Tokura, Phys. Rev. **54**, R11022 (1996).
[5] T. Saitoh, T. Mizokawa, A. Fujimori, M. Abbate, Y. Takeda, and M. Takano, Phys. Rev. **56**, 1290 (1997).
[6] M. R. Ibarra, R. Mahendiran, C. Marquina, B. Garcia-Landa, and J. Blasco, Phys. Rev. **57**, R3217 (1998).
[7] R. Caciuffo, D. Rinaldi, G. Barucca, J. Mira, J. Rivas, M. A. Senaris-Rodriguez, P. G. Radaelli, D. Fiorani, and J. B. Goodenough, Phys. Rev. **59**, 1068 (1999).
[8] G. P. Luo, Y. S. Wang, S. Y. Chen, A. K. Heilman, C. L. Chen, C. W. Chu, Y. Liou, and N. B. Ming, Appl. Phys. Lett. **76**, 1908 (2000).
[9] J.-M. Liu and C. K. Ong, Appl. Phys. Lett. **73**, 1047 (1998).
[10] S. Madhukar, A. Aggarwal, A. M. Dhote, R. Ramesh, A. Krishnan, D. Keeble, and E. Poindexter, J. Appl. Phys. **81**, 3543 (1997).
[11] W. Wu, K. H. Wong, and C. L. Choy, Thin Solid Films **385**, 298 (2001).
[12] J.-M. Liu and C. K. Ong, J. Appl. Phys. **84**, 5560 (1998).
[13] V. Golovanov, L. Mihaly, and A. R. Moodenbaugh, Phys. Rev. **53**, 8207 (1996).
[14] A. V. Samoilov, G. Beach, C. C. Fu, and N.-C. Yeh, J. Appl. Phys. **83**, 6998 (1998).
[15] G. H. Jonker and J. H. Van Santen, Physica **19**, 120 (1953).
[16] W. G. Baber, Proc. R. Soc. London, Ser. A **158**, 383 (1937).
[17] B. L. Altshuler and A. G. Aronov, Sov. Phys. JETP **50**, 968 (1979).
[18] M. Imada, A. Fujimori, and Y. Tokura, Rev. Mod. Phys. **70**, 1039 (1998).
[19] J. M. Ziman, *Models of Disorder*, Cambridge University Press, Cambridge (1971).
[20] T. R. Kirkpatrick and D. Belitz, in *Electron Correlation in the Solid State*, edited by N. H. March, Imperial College Press, London (1999), p. 297.
[21] A. A. Abrikosov, *Fundamentals of the Theory of Metals*, North-Holland, Amsterdam (1988), Nauka, Moscow (1987).
[22] A. R. Mackintosh, Phys. Lett. **4**, 140 (1963).
[23] S. V. Vonsovskiĭ, *Magnetism*, Vols. 1 and 2, Wiley, New York (1974), Nauka, Moscow (1971).
[24] L. V. Meisel and P. J. Cote, J. Phys. F **7**, L321 (1977).
[25] M. Itoh, I. Natori, S. Kubota, and K. Motoya, J. Phys. Soc. Jpn. **63**, 1486 (1994).
[26] M. A. Senaris-Rodriguez and J. B. Goodenough, J. Solid State Chem. **118**, 323 (1995).
[27] K. Asai, O. Yokokura, N. Nishimori, H. Chou, J. M. Tranquada, G. Shirane, S. Higuchi, Y. Okajima, and K. Kohn, Phys. Rev. **50**, 3025 (1995).

Translated by Steve Torstveit

Low-frequency quantum oscillations of the impedance of layered conductors at high magnetic field

O. V. Kirichenko* and I. V. Kozlov

B. Verkin Institute for Low Temperature Physics and Engineering, National Academy of Sciences of Ukraine, pr. Lenina 47, 61103 Kharkov, Ukraine
(Submitted December 17, 2001)

The propagation of electromagnetic waves in layered conductors is investigated by the method of the quantum kinetic equation. The quantum oscillations of the impedance for elastic scattering on impurities is calculated. An expression is obtained for the low-frequency oscillations of the impedance over a wide range of frequencies of the electromagnetic wave. © *2002 American Institute of Physics.* [DOI: 10.1063/1.1480243]

By studying the propagation of waves in organic conductors placed in a high magnetic field **B**, one can investigate in detail the energy spectrum and relaxation properties of the charge carriers.[1] In conductors having a layered structure the electron energy spectrum has a quasi-two-dimensional character, and the electron energy $\varepsilon(\mathbf{p})$ depends weakly on the momentum projection $p_z = \mathbf{p} \cdot \mathbf{n}$ on the normal **n** to the layers. Layered conductors at low temperatures exhibit the clearest manifestations of the de Haas–van Alphen (dHvA) and Shubnikov–de Haas (SdH) quantum oscillation effects.[2–11] The study of the SdH oscillations of the dc resistivity of layered conductors is the subject of a great number of theoretical and experimental papers (see, e.g., the reviews[12] and the references cited therein). The experimental study of the propagation of electromagnetic waves in organic conductors has received much less attention,[13–17] even though the kinetic phenomena in alternating fields carry rich information about the electron systems in conducting media. Among the papers mentioned is a study of tetrathiafulvalene-based compounds of the form (BEDT–TTF)$_2$X (X stands for a set of various anions) in which the wave vector **k** and the static magnetic field were directed along the normal to the layers. Below we shall examine the propagation of electromagnetic waves in quasi-two-dimensional layered conductors in a geometry used in some of the studies cited, i.e., in which the Poynting vector and the magnetic field are parallel to **n**. In this case the alternating electromagnetic field is orthogonal to the vector of the quantizing magnetic field, and it is extremely important to take into account the quantum oscillations of the kernel of the scattering operator for the charge carriers. Here the amplitude of the SdH oscillations of the surface impedance is of a substantially different order of magnitude than in the approximation in which a magnetic-field-independent relaxation time τ is used in the quantum kinetic equation for the collision integral.[18] In contrast to the dHvA oscillations, the period of which is determined by the extremal-area (S_{extr}) cross sections of the Fermi surface, the SdH oscillations contain combination frequencies of the type

$$\nu = \frac{(n S_{\text{max}} + n' S_{\text{min}})c}{e\hbar},$$

where n and n' are any integers, c is the speed of light, e is the charge of the electron, and $\hbar$ is Planck's constant.

The distribution of the electric field of frequency ω in the conductor is easily found from Maxwell's equations

$$\left(\frac{\partial^2}{\partial z^2} + \frac{\omega^2}{c^2} \right) E_\alpha + \frac{4\pi i \omega}{c^2} j_\alpha = 2 E'_\alpha(0),$$

supplemented by the constitutive relation connecting the current density $\mathbf{j}(z,t)$ with the electric field. To determine the current density

$$\mathbf{j} = e \operatorname{Tr}(\hat{\mathbf{v}}\hat{f}) = \frac{2e^2 B}{c(2\pi\hbar)^2} \sum_{n,n'=0}^{\infty} \int dp_z \mathbf{v}_{n'n} \hat{f}_{nn'} \tag{1}$$

it is necessary to find the density matrix $f_{nn'}$ with the use of the quantum kinetic equation;[19] here $\mathbf{v}_{n'n}$ is a matrix element of the velocity operator. Solely for the sake of brevity in the calculation we will use a rather simple dispersion relation for the charge carriers, in the form

$$\varepsilon_n(p_z) = \left(n + \frac{1}{2} \right) \hbar\Omega - A \cos\left(\frac{ap_z}{\hbar} \right), \quad n = 0,1,2,3..., \tag{2}$$

where a is the distance between layers, $\Omega = eB/mc$ is the cyclotron frequency, m is the effective mass of the conduction electrons, $A = \eta\varepsilon_f$, and the quasi-two-dimensionality parameter η will be assumed not too small,

$$\frac{\hbar\Omega}{\varepsilon_f} \ll \eta \ll 1,$$

so that there are sufficient Landau levels on the Fermi surface $\varepsilon(\mathbf{p}) = \varepsilon_f$ that one may use a quasiclassical approximation for calculating the impedance. We limit consideration to the case of the normal skin effect, when the relation between the current density $j_i = e \operatorname{Tr}(\hat{v}_i \hat{f})$ and the electric field **E** can be treated, to sufficient accuracy, as local:

$$j_i(\mathbf{r},t) = \sigma_{ij} E_j(\mathbf{r},t).$$

The approximation of a local relation is completely admissible when the drift of the conduction electrons along the wave vector **k** over the mean free time τ of the charge carriers is much less than the skin depth δ, i.e.,

$$\eta v\tau \ll \delta. \tag{3}$$

Thanks to the symmetry of the spectrum it is sufficient to consider only the components of the conductivity tensor in the plane of the layers. For circular polarization of the wave, $E^\pm = E_x \pm i E_y$, the conductivity tensor becomes diagonal.

In order for the quantum oscillations to be substantial, the mean free time of the charge carriers must be much greater than the period of gyration of the electron along its orbit ($\Omega\tau \gg 1$). We shall take into account only the elastic scattering on impurities, assuming that the range of the scattering potential is much less than the de Broglie wavelength of the electrons. This allows us to calculate the conductivity tensor without having to assume that the interaction potential of the electron with the impurity is small. The calculation is done by the method of the quantum kinetic equation, following Refs. 18–20.

The electron gas is described by a density matrix which satisfies the quantum kinetic equation. We write the latter in the form proposed in Ref. 19:

$$-i\omega\hat{f}_1 + \frac{i}{\hbar}[\hat{\varepsilon};\hat{f}_1] + \frac{i}{\hbar}n_{\text{imp}}\text{Tr}_\alpha[\hat{V};\hat{F}_0(\hat{f}_1)]$$

$$= \frac{i}{\hbar}\left[\frac{e\mathbf{E}\cdot\hat{\mathbf{v}}}{i\omega};\hat{f}^{(0)}\right] - \frac{i}{\hbar}n_{\text{imp}}\text{Tr}_\alpha[\hat{V};\hat{F}_1]; \qquad (4)$$

$$\frac{\partial\hat{F}_0(\hat{f})}{\partial t} + \frac{i}{\hbar}[\hat{\varepsilon}+\hat{V};\hat{F}_0(\hat{f})] = -\frac{i}{\hbar}[\hat{V};\hat{f}];$$

$$\frac{\partial\hat{F}_1}{\partial t} + \frac{i}{\hbar}[\hat{\varepsilon}+\hat{V};\hat{F}_1] = \frac{i}{\hbar}\left[\frac{e\mathbf{E}\cdot\hat{\mathbf{v}}}{i\omega};\hat{F}_0(\hat{f}^{(0)})\right],$$

where $\hat{f}^{(0)}$ is the Fermi–Dirac distribution function, $\hat{f}_1$ is the correction linear in the field to the density matrix, $\hat{V}$ is the impurity operator, $\hat{F} = \hat{F}_0 + \hat{F}_1$ is the binary correlation operator of the electron and one impurity, n_{imp} is the impurity concentration, the trace Tr_α is taken over the states of the impurity, and α is the set of quantum numbers characterizing the state of the impurity; from now on, the subscript α will be dropped from all notations except Tr_α. The system of equations (4) is a chain of Bogolyubov equations broken off at the two-impurity correlation operator. The impurity is assumed to be uniformly distributed and infinitely heavy. We use the gauge

$$\mathbf{A} = (0, Bx, 0) + \frac{c\mathbf{E}}{i\omega}, \quad \varphi = 0.$$

The energy of the electron in the field of the wave has the form $\hat{H}_1 = -(e\mathbf{E}\cdot\hat{\mathbf{v}})/(i\omega)$ and contains the velocity operator, which we write in the $|n, P_y, P_z\rangle$ representation, which is the natural one for the given gauge. P_y determines the coordinate of the center of the electron orbit $x_0 = (cP_y)/(eB)$, and P_z is the same as the kinematic momentum component p_z. Unlike the coordinate operator, which enters the Hamiltonian through the use of the gauge $\mathbf{A} = (0, Bx, 0)$, $\varphi = -\mathbf{E}\cdot\mathbf{r}$, the matrix elements of the velocity operator do not depend on P_y:

$$v_x \pm i v_y = v^\pm = v_0^\pm - \frac{eE^\pm}{i\omega m}, \qquad (5)$$

where

$$v_{0nn'}^+ = -\frac{i\hbar}{m}\left(\frac{2eB\hbar}{c}n'\right)^{1/2}\delta_{n+1,n'},$$

$$v_{0nn'}^- = \frac{i\hbar}{m}\left(\frac{2eB\hbar}{c}n\right)^{1/2}\delta_{n-1,n'}.$$

Thus, taking the electric field into account through the use of a vector potential allows one to avoid an additional summation in the expressions for the density matrix and substantially simplifies the calculations.

Equations (4) can be written in the form

$$-i\omega\hat{X} + \frac{i}{\hbar}[\hat{\varepsilon}+\hat{V};\hat{X}] = \hat{Y}, \qquad (6)$$

where $\hat{X}$ is the operator which we are seeking, and $\hat{Y}$ is the right-hand side of the equation. It was shown in Ref. 19 that Eq. (6) has a solution of the form

$$\hat{X} = \frac{\hbar}{2\pi}\int dz\,\hat{G}^+\left(z + \frac{\omega}{2} + \hat{V}\right)\hat{Y}\hat{G}^-\left(z - \frac{\omega}{2} + \hat{V}\right). \qquad (7)$$

The Green's function $\hat{G}^\pm$ satisfies the relation

$$\hat{G}^\pm(z-\hat{V}) = \hat{G}^\pm(z) + \hat{G}^\pm(z)\hat{T}^\pm(z)\hat{G}^\pm(z), \qquad (8)$$

where $T_{\nu\mu} = \langle\varphi_\nu|\hat{V}|\psi_\mu\rangle$ is the T matrix, φ_ν is the eigenfunction of the Hamiltonian without the impurity, and ψ_ν is the wave function of the electron in the presence of the impurity.

We now calculate the Green's function for a layered conductor. Following Ref. 20, one can show that for a short-range impurity at

$$x, y \ll \frac{r_L}{n_f}, \quad z \ll a, \qquad (9)$$

where $n_f = \varepsilon_f/(\hbar\Omega)$ and r_L is the Larmor radius, the Green's function can be written in the form

$$G^\pm(r, r', E) = \sum_\nu \frac{\phi_\nu(r)\phi_\nu^*(r')}{E - \varepsilon_\nu \pm i\delta}$$

$$= \Phi(r, r')[G_{\text{cl}}(r - r', E) + G_q^\pm], \qquad (10)$$

where

$$\Phi(r, r') = \exp\left[\frac{i\hbar c}{2eB}(x+x')(y-y')\right];$$

G_{cl} is the real part of the Green's function in the absence of magnetic field, and the dependence of G_q on $(r - r')$ can be neglected. In the case of a quasi-two-dimensional spectrum, G_{cl} is rather complicated for explicit calculation. Unlike the case of the quadratic spectrum, G_{cl} depends on E and also depends on $(r - r')$ in a complicated way. However, the explicit form will not be needed in the calculations that follow. For calculating G_q we use the Poisson summation formula, as a result of which the expression for G_q takes the form

$$G_q^\pm(\varepsilon) = \mp \frac{im}{2\hbar^2 a}$$

$$\times \left[1 + 2 \sum_{k=1}^\infty (-1)^k \exp\left(\pm \frac{2\pi i k \varepsilon}{\hbar \Omega} \right) J_0\left(\frac{2\pi k A}{\hbar \Omega} \right) \right],$$ (11)

where J_0 is the Bessel function. The series appearing in Eq. (11) is conditionally convergent, but it can be shown that when the Dingle broadening of the Landau levels is taken into account, a small factor $C_D^k = \exp(-k/\Omega\tau)$ will appear in the oscillatory part of the Green's function, and then the series becomes absolutely convergent.

As was shown in Ref. 20, the electron wave function in the field of the impurity satisfies Dyson's equation

$$\psi_\nu(r) = \varphi_\nu(r) + \int G(r,r',E)V(r')\psi_\nu(r')d^3r'.$$

When the Green's function in the form (11) is substituted in, the wave function $\psi_\nu(r)$ in the region specified by inequalities (9) can be represented in the form

$$\psi_\nu(r) = \frac{\varphi_\nu(R_{\text{imp}})}{1 - (2\pi\hbar^2/m)f_{\text{imp}}G_q^\pm(E)} \psi_0(r),$$ (12)

where $\psi_0(r)$ satisfies the equation

$$\psi_0(r) = 1 + \int G_{\text{cl}}(r,r',E)V(r')\psi_0(r')d^3r',$$

R_{imp} is the coordinate of the impurity; the total scattering amplitude f_{imp} is given by the expression

$$f_{\text{imp}} = \frac{m}{2\pi\hbar^2} \int V(r)\psi(r)d^3r;$$ (13)

$G_{\text{cl}}(r,E)$ is a smooth function of E and varies substantially over energy intervals $\Delta E \sim \varepsilon_f$. However, for calculating the galvanomagnetic coefficients, only the energy region near the Fermi level is important, where

$$\Delta E = E - \varepsilon_f \sim \max(\hbar\Omega, \hbar\omega) \ll \varepsilon_f.$$

Thus the dependence on E of $G_{\text{cl}}(r,E)$ and $\psi_0(r)$ can be neglected, taking $E \simeq \varepsilon_f$. The expression for the T matrix in the case of a quasi-two-dimensional spectrum can be written in the form

$$T_{\mu\nu}^\pm(E) = t^\pm(E)\varphi_\mu^*(R_0)\varphi_\nu(R_0),$$

$$t^\pm(E) = \frac{(2\pi\hbar^2/m)f_{\text{imp}}}{1 - (2\pi\hbar^2/m)f_{\text{imp}}G_q^\pm(E)},$$ (14)

which agrees with formula (7) of Ref. 20 for the case of a quadratic dispersion relation. Essentially, the energy dependence enters only in the kernel of the T matrix.

In calculating the oscillatory part of the conductivity tensor, only the off-diagonal elements of the velocity operator are important. The contribution from the diagonal part of $\hat{v}$ in the formula for the current,

$$\mathbf{j}_{\text{diag}} = e\,\text{Tr}(\hat{\mathbf{v}}_{\text{diag}}\hat{f}) = -\frac{e^2\mathbf{E}}{i\omega m}\text{Tr}(\hat{f}) = -\frac{e^2\mathbf{E}}{i\omega m}n_e,$$

is expressed in terms of the electron density n_e and cannot oscillate as the magnetic field varies. In the expression for the density matrix the diagonal part of $\hat{v}_\pm$ can also be neglected. In fact, $\hat{\mathbf{v}}$ enter the expression for $\hat{f}$ only in the form

of the combination $e\mathbf{E}\cdot\hat{\mathbf{v}}/i\omega$, but because the diagonal components of the velocity are linear in the field $\mathbf{E}$, the corresponding correction to $\hat{f}$ will be quadratic in the field. Since we are neglecting the diagonal components of $\hat{\mathbf{v}}$ in the equation for the current, we will be interested only in the off-diagonal part of the density matrix $\hat{f}$. As was shown in Ref. 19, for the off-diagonal components of the density matrix the collision integral $in_{\text{imp}}\text{Tr}_\alpha[V_\alpha; F_0(f_1)]_{nm}/\hbar$ appearing in the system of equations (4) reduces to multiplication of f_1 by the quantity

$$\frac{1}{\tau_{nm}} = \frac{i}{\hbar}n_{\text{imp}}[t^+(\varepsilon_m + \hbar\omega) - t^-(\varepsilon_n - \hbar\omega)].$$ (15)

The right-hand side of the equation for $\hat{F}_0$ in system (4) contains the commutator with the impurity operator. Therefore, in the explicit expression for $\hat{F}_0$, the operator $\hat{V}$ will appear together with the T matrix, but it can be canceled out by reduction with Dyson's equation:

$$\hat{T}^\pm = \hat{V} + \hat{V}\hat{G}^\pm\hat{T}^\pm = \hat{V} + \hat{T}^\pm\hat{G}^\pm\hat{V},$$ (16)

where now the expression for $\hat{F}_0$ can be written as

$$\hat{F}_0 = \frac{i}{2\pi}\int dz[-\hat{G}^+(z)\hat{T}^+(z)\hat{f}^{(0)}\hat{G}^-(z)$$

$$+ \hat{G}^+(z)\hat{f}^{(0)}\hat{T}^-(z)\hat{G}^-(z)$$

$$- \hat{G}^+(z)\hat{T}^+(z)\hat{f}^{(0)}\hat{G}^-(z)\hat{T}^-(z)\hat{G}^-(z)$$

$$+ \hat{G}^+(z)\hat{T}^+(z)\hat{G}^+(z)\hat{f}^{(0)}\hat{T}^-(z)\hat{G}^-(z)].$$ (17)

We note that $\hat{F}_0(\hat{f}^{(0)})$ has the meaning of an impurity correction to the Fermi–Dirac function:

$$\hat{f}^{(0)}(\hat{\varepsilon} + \hat{V}) = \hat{f}^{(0)}(\hat{\varepsilon}) + \hat{F}_0(\hat{f}^{(0)}).$$

The calculation of $\hat{f}_1$ can be reduced to the evaluation of $\hat{F}_1$. For this we write $\hat{F}_1$ and $\hat{f}_1$ in the form of a sum:

$$\hat{F}_1 = \hat{F}_a + \hat{F}_b, \quad \hat{f}_1 = \hat{f}_a + \hat{f}_b,$$

for which the system of equations (4) will take the form

$$-i\omega\hat{F}_a + \frac{i}{\hbar}[\hat{\varepsilon};\hat{F}_a] = \frac{i}{\hbar}\left[\frac{e\mathbf{E}\cdot\hat{\mathbf{v}}}{i\omega};\hat{F}_0\right],$$

$$-i\omega\hat{F}_b + \frac{i}{\hbar}[\hat{\varepsilon};\hat{F}_b] = -\frac{i}{\hbar}[\hat{V};\hat{F}_1],$$

$$-i\omega\hat{f}_a + \frac{i}{\hbar}[\hat{\varepsilon};\hat{f}_a] + \hat{\tau}^{-1}\hat{f}_a = \frac{i}{\hbar}\left[\frac{e\mathbf{E}\cdot\hat{\mathbf{v}}}{i\omega};\hat{f}^{(0)}\right],$$

$$-i\omega\hat{f}_b + \frac{i}{\hbar}[\hat{\varepsilon};\hat{f}_b] + \hat{\tau}^{-1}\hat{f}_b = -\frac{i}{\hbar}n_{\text{imp}}\text{Tr}_\alpha[\hat{V};\hat{F}_1].$$ (18)

It is not hard to see that

$$f_{nm}^b = \frac{-i\omega + i(\varepsilon_n - \varepsilon_m)/\hbar}{-i\omega + i(\varepsilon_n - \varepsilon_m)/\hbar + 1/\tau_{nm}}n_{\text{imp}}\text{Tr}_\alpha F_{nm}^b.$$ (19)

It can be shown that $\hat{F}_a$ corresponds to a shift of the energy level due to the presence of the impurity and can be neglected. Indeed, the corresponding contribution to the conductivity

$$\sigma_{F_a} \sim \mathrm{Tr}[\hat{v};\hat{F}_0]\hat{v} \sim \int d\bar{P}_z \sum_n (\bar{F}^0_{n+1,n+1} - F^0_{n,n})n$$

$$\sim \int d\bar{P}_z \sum_n \bar{F}^0_{n,n} \sim \mathrm{Tr}(\hat{f}^{(0)}(\hat{\varepsilon}+\hat{V}) - \hat{f}^{(0)}(\hat{\varepsilon}))$$

is proportional to the difference of the electron densities in the presence and absence of the impurity, i.e., it does not depend on the magnetic field **B**. Thus we obtain

$$f^1_{nm} = \frac{\dfrac{i}{\hbar}\left[\dfrac{e\mathbf{E}\cdot\hat{\mathbf{v}}}{-i\omega};f^{(0)}\right]_{nm}}{-i\omega + \dfrac{i}{\hbar}(\varepsilon_n - \varepsilon_m) + \dfrac{1}{\tau_{nm}}}$$

$$+ \frac{-i\omega + \dfrac{i}{\hbar}(\varepsilon_n - \varepsilon_m)}{-i\omega + \dfrac{i}{\hbar}(\varepsilon_n - \varepsilon_m) + \dfrac{1}{\tau_{nm}}} n_{\mathrm{imp}}\mathrm{Tr}_\alpha F^b_{nm}. \tag{20}$$

Since only some of the terms appearing in $\hat{F}^b$ are important, we write it in the following form:

$$\hat{F}_b = \frac{i}{2\pi}\int dz_1\left\{\hat{G}^+\left(z_1 + \frac{\omega}{2}\right)\left[\frac{e\mathbf{E}\cdot\hat{\mathbf{v}}}{i\omega};\hat{F}_0(\hat{f}^{(0)})\right]\right.$$

$$\times \hat{G}^-\left(z_1 - \frac{\omega}{2}\right) + \hat{G}^+\left(z_1 + \frac{\omega}{2}\right)\hat{T}^+\left(z_1 + \frac{\omega}{2}\right)$$

$$\times \hat{G}^+\left(z_1 + \frac{\omega}{2}\right)\left[\frac{e\mathbf{E}\cdot\hat{\mathbf{v}}}{i\omega};\hat{F}_0(\hat{f}^{(0)})\right]\hat{G}^-\left(z_1 - \frac{\omega}{2}\right)$$

$$+ \hat{G}^+\left(z_1 + \frac{\omega}{2}\right)\left[\frac{e\mathbf{E}\cdot\hat{\mathbf{v}}}{i\omega};\hat{F}_0(\hat{f}^{(0)})\right]$$

$$\times \hat{G}^-\left(z_1 - \frac{\omega}{2}\right)\hat{T}^-\left(z_1 - \frac{\omega}{2}\right)\hat{G}^-\left(z_1 - \frac{\omega}{2}\right)$$

$$+ \hat{G}^+\left(z_1 + \frac{\omega}{2}\right)\hat{T}^+\left(z_1 + \frac{\omega}{2}\right)\hat{G}^+\left(z_1 + \frac{\omega}{2}\right)$$

$$\times\left[\frac{e\mathbf{E}\cdot\hat{\mathbf{v}}}{i\omega};\hat{F}_0(\hat{f}^{(0)})\right]\hat{G}^-\left(z_1 - \frac{\omega}{2}\right)$$

$$\times \hat{T}^-\left(z_1 - \frac{\omega}{2}\right)\hat{G}^-\left(z_1 - \frac{\omega}{2}\right)\Bigg\}. \tag{21}$$

The first term in (21) corresponds to a shift of the energy level due to the presence of the impurity, and it can be neglected. The next term contains an expression of the form $\hat{T}\hat{v}\hat{T}$, which vanishes upon summation over P_y in (20) as a consequence of the orthogonality of the Hermite polynomials. For the same reason, only the part with the commutator $[e\mathbf{E}\cdot\hat{\mathbf{v}}/i\omega;\hat{F}_0]$ is important in the rest of the terms.

The expression for $\hat{f}_1$ simplified in this way must be substituted into the equation for the current (1). We note that the T matrix is nondiagonal in P_y and P_z, and each appearance of it in formula (21) leads to the necessity of summing over these quantum numbers. Thus, to simplify the calculations that follow it would be desirable to reduce expression (21) to a form in which the T matrix enters each term only once. This can be done by employing the following arguments.

1. As we know, the scattering tensor obeys the optical theorem, which in our case is conveniently written in the form

$$\hat{T}^+(a)(\hat{G}^+(a) - \hat{G}^-(b))\hat{T}^-(b) = \hat{T}^+(a) - \hat{T}^-(b);$$

$$-2\pi i\hat{T}^+(a)\delta(\hat{\varepsilon} - a)\hat{T}^-(a) = \hat{T}^+(a) - \hat{T}^-(a), \tag{22}$$

which can easily be obtained from the Born expansion of the T matrix or by substituting the Green's function and T matrix in explicit form.

2. It follows from the explicit form of the T matrix that it obeys the relation

$$\hat{T}^\pm(a) = \frac{t^\pm(a)}{t^+(b)}\hat{T}^+(b), \tag{23}$$

which together with the optical theorem gives an efficient way of simplifying the tensor expressions.

After all the transformations have been done, the expression for the density matrix becomes extremely awkward, and we will not write it out. After some calculations, the conductivity tensor can be written in the form $\sigma^\pm = \sigma_a^\pm + \sigma_b^\pm$, where

$$\sigma_a^\pm = \pm\frac{ie^2}{2\pi^2\hbar^2\omega}\sum_n\int dP_z\frac{n[f^{(0)}(\varepsilon_n \pm \hbar\Omega) - f^{(0)}(\varepsilon_n)]}{\omega \mp \Omega - \dfrac{n_{\mathrm{imp}}}{\hbar}[t^+(\varepsilon_n + \hbar\omega) - t^-(\varepsilon_n - \hbar\omega)]}, \tag{24}$$

$$\sigma_b^\pm = \pm\frac{ie^2 n_{\mathrm{imp}}}{2\pi^2\hbar^2\omega(\omega \mp \Omega)}\sum_n\int dP_z\frac{n}{\omega \mp \Omega - \dfrac{n_{\mathrm{imp}}}{\hbar}[t^+(\varepsilon_n + \hbar\omega) - t^-(\varepsilon_n - \hbar\omega)]}\left[-\frac{i}{2\pi}(\omega \pm \Omega)\right.$$

$$\times \int dz\frac{t^+(z) - t^-(z)}{\varepsilon_n + \omega \mp \Omega - z + i\delta}\frac{f^{(0)}(z) - f^{(0)}(\varepsilon_n)}{z - \varepsilon_n - i\delta} + \frac{i}{2\pi}(\omega \pm \Omega)\int dz\frac{t^+(z) - t^-(z)}{\varepsilon_n - \omega \pm \Omega - z - i\delta}\frac{f^{(0)}(z) - f^{(0)}(\varepsilon_n)}{z - \varepsilon_n + i\delta}\right], \tag{25}$$

where n_e is the electron density, and $\sigma_a^{\pm}$ and $\sigma_b^{\pm}$ correspond to $\hat{f}_a$ and $\hat{f}_b$ in the density matrix. For brevity in the writing of these formulas we have omitted certain terms which are important for the classical part of $\sigma^{\pm}$ but do not contribute to the oscillatory part of the conductivity. The given expression can be used to calculate the conductivity for any values of ω, although elementary estimates of the penetration depth of the electromagnetic wave into the conductor show that for the layered conductors under study, the resonance region ($\omega - \Omega \sim 1/\tau$) corresponds to the case of the anomalous skin effect and cannot be treated in the local-coupling approximation. In the absence of resonance and for $\omega \neq 0$ the main contribution to the quantum oscillations of the conductivity tensor is given by the correction linear in $1/\tau$. The second-order correction in $1/\tau$ becomes important only for the static case $\omega \ll \Omega$, and therefore in the expressions quadratic in the inverse relaxation time one can set $\Omega - \omega \approx \Omega$. We note that for taking the trace Tr in expressions (24) and (25), the density of states $\nu(\varepsilon)$ appearing in the trace in the formula for the current (1) is expressed in terms of the Green's function (11) as

$$\frac{eB}{c(2\pi\hbar)^2} \sum_n \int dP_z \dots = \frac{1}{(2\pi\hbar)^3} \int \nu(\varepsilon) d\varepsilon \dots$$

$$= \int \frac{d\varepsilon}{2\pi i} [G_q^- - G_q^+] \dots \quad (26)$$

To simplify the remaining calculations somewhat, let us assume that the oscillations of the scattering tensor are small, i.e.,

$$\frac{f_{\text{imp}}}{a} \left(\hbar \frac{\Omega}{A} \right)^{1/2} C_D \ll l, \quad (27)$$

and we will keep only the leading terms in the expansion in powers of $\hbar\Omega/\varepsilon_f$ and $1/\Omega\tau$, assuming that $1/\Omega\tau \gg \hbar\Omega/\varepsilon_f$. After (11), (14), and (26) have been substituted into (24) and (25), the expression for the conductivity will contain products of series:

$$\sum_k^{\infty} (-1)^k \exp\left(\frac{2\pi i k\varepsilon}{\hbar\Omega} \right) J_0\left(\frac{2\pi kA}{\hbar\Omega} \right)$$

$$\times \sum_l^{\infty} (-1)^l \exp\left[\frac{2\pi i l}{\hbar\Omega}(\varepsilon + \Delta) \right] J_0\left(\frac{2\pi lA}{\hbar\Omega} \right)$$

$$= \sum_{k,l}^{\infty} (-1)^{k+l} \exp\left(\frac{2\pi i l\Delta}{\hbar\Omega} \right) \exp\left[\frac{2\pi i\varepsilon}{\hbar\Omega}(k+l) \right]$$

$$\times J_0\left(\frac{2\pi kA}{\hbar\Omega} \right) J_0\left(\frac{2\pi lA}{\hbar\Omega} \right), \quad \Delta = 0, \pm \hbar\omega, \quad (28)$$

the required absolute convergence of which, as we have said, is ensured by the Dingle broadening of the Landau levels. The terms of the series with $k, l \neq 0$ in Eq. (28) contain the Bessel function, which gives an additional small factor of $\sqrt{\hbar\Omega/A}$. Thus the main contribution to the high-frequency oscillations of the conductivity will come from the part of the sum (28) with $k \neq l = 0$ and $l \neq k = 0$. In addition, we drop the products with $k + l = 0$, the phase of which does not depend on ε (they cause oscillations at the difference frequencies). As will be seen from the calculations below, this will

cause the phase of the oscillations of the corresponding part of the conductivity tensor to be independent of ε_f, with the result that its amplitude will not be suppressed by the usual temperature smearing but it will be hit twice by the Dingle factor C_D. Thus, in the absence of resonance ($\omega - \Omega \gg 1/\tau$) the quantum correction to the conductivity tensor due to the presence of an impurity has the form

$$\sigma_q^{\pm} = \frac{2e^2 n_e}{m\tau} \frac{1}{(\omega \mp \Omega)^2}$$

$$\times \left\{ \left(1 \pm \frac{3i}{\Omega\tau} \right) \sum_{k=1}^{\infty} \exp\left(\frac{2\pi i k\omega}{\Omega} \right) J_0^2\left(\frac{2\pi kA}{\hbar\Omega} \right) C_D^2 \right.$$

$$+ \left(1 \pm \frac{3}{2} \frac{i}{\Omega\tau} \right) \sum_{k=1}^{\infty} \frac{(-1)^k i\Omega}{\pi k\omega} \cos\left(\frac{2\pi k\varepsilon_f}{\hbar\Omega} \right)$$

$$\left. \times \left(\exp\left(2\pi i k\frac{\omega}{\Omega} \right) - 1 \right) J_0\left(\frac{2\pi kA}{\hbar\Omega} \right) C_D C_t \right\}, \quad (29)$$

where $C_t = [2\pi^2 k_B T/(\hbar\Omega)]/[\sinh(2\pi^2 k_B T/(\hbar\Omega))]$ is a factor causing temperature smearing,

$$\frac{1}{\tau} = \frac{4\hbar\pi^2 C_{\text{imp}} n_{\text{imp}} f_{\text{imp}}^2}{ma}$$

is the relaxation time due to the impurity[19] and is numerically equal to the nonoscillatory part of expression (15); f_{imp} is the total scattering amplitude (13), $C_{\text{imp}} = 1$ if $f_{\text{imp}} \ll a$ and $C_{\text{imp}} = (a/f_{\text{imp}})^2$ if $f_{\text{imp}} \gg a$.

As was noted in Ref. 20, the quantum oscillations of the impedance and the quantities characterizing the propagation of an electromagnetic wave in a conductor are determined mainly by the quantum nature of the collision integral associated with scattering on impurities. In the collisionless limit the impedance oscillations are due to oscillations of the magnetization. In Ref. 20 only the oscillations at the fundamental harmonics were considered. Low-frequency oscillations at the combination frequencies do not appear in the magnetization oscillations. Thus, to a sufficient degree of accuracy one can assume that the total conductivity tensor has the form $\sigma^{\pm} = \sigma_{\text{cl}}^{\pm} + \sigma_q^{\pm}$, where $\sigma_{\text{cl}}^{\pm} = n_e e^2/[m(-i\omega \pm i\Omega + 1/\tau)]$ is the classical, nonoscillatory part of the conductivity tensor.

Since we are considering only the case of the normal skin effect, the expressions given for the conductivity completely describe the process of electromagnetic wave propagation. In the approximation of local coupling of the current density with the electric field, the latter is damped exponentially in the sample:

$$E^{\pm}(z,t) = E_0^{\pm} \exp(ik_z^{\pm} z - i\omega t),$$

where

$$k_z^{\pm} = \left(\frac{4\pi i\omega\sigma_{\pm}}{c^2} \right)^{1/2}.$$

The impedance and the penetration depth of the field into the conductor are related to $k_z^{\pm}$ by the relations

$$Z_{\pm} = \frac{4\pi}{c^2} \frac{\omega}{k_z^{\pm}}, \quad \delta_{\pm} = (\text{Im } k_z^{\pm})^{-1}.$$

When the smallness of the amplitude of the quantum oscillations is taken into account, the expression for the impedance can be rewritten as

$$
\begin{aligned}
Z_{\pm} = Z_{\pm}^{cl} \Bigg\{ 1 &- \frac{i}{(\omega \mp \Omega)\tau} \Bigg[\left(1 \pm \frac{3i}{\Omega\tau}\right) \\
&\times \sum_{k=1}^{\infty} \exp\left(2\pi i k \frac{\omega}{\Omega}\right) J_0^2\left(\frac{2\pi k A}{\hbar\Omega}\right) C_D^2 \\
&+ \left(1 \pm \frac{3}{2}\frac{i}{\Omega\tau}\right) \sum_{k=1}^{\infty} \frac{(-1)^k i\Omega}{\pi k \omega} \cos\left(\frac{2\pi k \varepsilon_f}{\hbar\Omega}\right) \\
&\times \left[\exp\left(\frac{2\pi i k \omega}{\Omega}\right) - 1 \right] J_0\left(\frac{2\pi k A}{\hbar\Omega}\right) C_D C_t \Bigg] \Bigg\}, \quad (30)
\end{aligned}
$$

where $Z_{\pm}^{cl}$ is the part of the impedance which is nonoscillatory in the inverse magnetic field.

The unusual temperature dependence of the low-frequency oscillations has a simple physical explanation. The low-frequency oscillations of the impedance are formed by the interference of the oscillations from two extremal cross sections, giving rise to a factor

$$
\cos\left(\frac{S_1 - S_2}{eB\hbar/c}\right) + \cos\left(\frac{4\pi A}{\hbar\Omega}\right),
$$

where $S_{1,2} = 2\pi m(\varepsilon_f \pm A)$, which results in a dependence of the low-frequency contribution on the magnetic field. If the overlap integral of the wave functions of electrons belonging to neighboring layers is nearly independent of energy, i.e., $A(\varepsilon) \simeq \mathrm{const}$, then taking the temperature smearing of the Fermi function into account will not lead to a decrease in the amplitude of the oscillations. Even if $A(\varepsilon)$ does depend on the energy of the charge carriers, then $dA(\varepsilon)/d\varepsilon \simeq \eta$, and with increasing temperature the oscillation amplitude, which is proportional to $\exp[-(2\pi^2 k_B T)(|dA/d\varepsilon|)/(\hbar\Omega)]$, falls off much more slowly than do the amplitudes of the remaining harmonics. This gives reason to hope that low-frequency quantum oscillations of the impedance might be observed in synthetic complexes based on tetrathiafulvalene even at liquid hydrogen temperature, where their fundamental harmonics are utterly small. In spite of the fact that the low-frequency oscillations of the impedance at the combination frequencies appear in higher orders in the magnetic small parameter $\hbar\Omega/(\eta\varepsilon_f)$, these oscillations have been successfully observed at liquid helium temperatures for the case of the static magnetoresistance,[22] and Prof. V. G. Peschansky has informed us that these observations agree with the theoretical calculation.[23]

[*]E-mail: kirichenko@ilt.kharkov.ua

[1] O. V. Kirichenko, Yu. A. Kolesnichenko, and V. G. Peschansky, Phys. Rev. **18**, 4 (1998).

[2] M. V. Kartsovnik, V. N. Laukhin, and V. N. Nizhankovskiĭ, A. A. Ignat'ev, JETP Lett. **47**, 363 (1988).

[3] M. V. Kartsovnik and P. A. Kononovich, V. N. Laukhin, I. F. Shchegolev, JETP Lett. **48**, 541 (1988).

[4] I. D. Parker, D. D. Pigram, R. H. Friend, M. Kurmo, and P. Day, Synth. Met. **27**, A387 (1988).

[5] K. Oshima, T. Mori, H. Inokuchi, H. Urayama, H. Yamochi, and C. Sato, Phys. Rev. B **38**, 938 (1988).

[6] W. Kang, G. Montanbaux, J. R. Cooper, D. Jerome, P. Batail, and C. Lenoir, Phys. Rev. Lett. **62**, 2559 (1989).

[7] I. F. Schegolev, P. A. Kononovich, M. V. Kartsovnik, V. N. Laukhin, S. I. Pesotskii, B. Hilti, and C. W. Mayer, Synth. Met. **39**, 537 (1990).

[8] R. Yagi, Y. Iue, T. Osada, and S. Kagoshima, Phys. Soc. Jpn. **59**, 3069 (1990).

[9] N. D. Kurshch, L. I. Buravov, M. V. Kartsovnik, V. N. Laukhin, S. I. Pesotskii, R. P. Rozenberg, E. B. Jagubskii, and A. V. Zvarikina, Synth. Met. **46**, 271 (1992).

[10] A. E. Kovalev, M. V. Kartsovnik, R. P. Shibaeva, R. P. Rozenberg, and I. F. Shcegolev, Solid State Commun. **89**, 575 (1994).

[11] M. V. Kartsovnik, A. E. Kovalev, V. N. Laukhin, I. F. Shchegolev, H. Ito, T. Ishiguro, N. D. Kushch, H. Mori, and G. Saito, Synth. Met. **70**, 811 (1995).

[12] J. Wosnitza, *Fermi Surfaces of Low-Dimensional Organic Metals and Superconductors*, Springer-Verlag, Berlin (1996); M. V. Kartsovnik and V. N. Laukhin, J. Phys. I **6**, 1753 (1996); J. Singelton, Rep. Prog. Phys. **63**, 1111 (2000).

[13] J. Singleton, F. L. Pratt, M. Dorotto, T. J. B. M. Janssen, M. Kurmoo, J. A. A. J. Perenboom, W. Hayes, and P. Day, Phys. Rev. Lett. **68**, 2500 (1992).

[14] S. V. Demishev, N. E. Sluchanko, A. V. Semeno, and N. A. Samarin, JETP Lett. **61**, 313 (1995).

[15] S. V. Demishev, A. V. Semeno, N. E. Sluchanko, N. A. Samarin, I. B. Voskoboinikov, V. V. Glushkov, J. Singleton, S. J. Blundell, S. O. Hill, W. Hayes, M. V. Kartsovnik, A. E. Kovalev, M. Kurmoo, P. Day, and N. D. Kushch, Phys. Rev. B **53**, 12794 (1996).

[16] A. Polisski, J. Singleton, and N. Kushch, Czech. J. Phys. **46**, 2623 (1996).

[17] S. V. Demishev, A. V. Semeno, N. E. Sluchanko, N. A. Samarin, I. B. Voskoboĭnikov, M. V. Kartsovnik, and A. E. Kovalev, N. D. Kushch, Zh. Éksp. Teor. Fiz. **111**, 979 (1997) [JETP **84**, 540 (1997)].

[18] A. M. Kosevich, V. V. Andreev, Zh. Éksp. Teor. Fiz. **38**, 882 (1960) [Sov. Phys. JETP **11**, 637 (1960)].

[19] V. V. Andreev, A. M. Kosevich, Zh. Éksp. Teor. Fiz. **43**, 1061 (1962).

[20] V. G. Skobov, Zh. Éksp. Teor. Fiz. **39**, 689 (1960) [Sov. Phys. JETP **12**, 483 (1961)].

[21] V. G. Peschanskiĭ, I. V. Kozlov, K. Jiasemides, Fiz. Nizk. Temp. **26**, 225 (2000) [Low Temp. Phys. **26**, 169 (2000)].

[22] T. G. Togonidze, M. V. Kortsovnik, J. A. A. J. Perenboom, N. D. Kurshch, and H. Kobayashi, Physica B **294–295**, 435 (2001).

[23] P. D. Grigoriev, M. V. Kartsovnik, W. Biberacher, and P. Wyder, cond-mat/0108352 (2001).

Translated by Steve Torstveit

PHYSICAL PROPERTIES OF CRYOCRYSTALS

Orientational order parameter in α-N$_2$ from x-ray data

N. N. Galtsov,* O. A. Klenova, and M. A. Strzhemechny

B. Verkin Institute for Low Temperature Physics and Engineering of the National Academy of Sciences, 47 Lenin Ave., Kharkov 61103, Ukraine

A method is suggested and validated for the deduction of orientational order parameter values η in molecular crystals consisting of diatomics directly from integrated x-ray diffraction intensities. This method is applied to pure solid nitrogen in its α phase. It is shown that to within a good accuracy the integrated intensity of a superstructure reflection is proportional to η^2. The η values determined from x-ray powder diffraction measurements agree well with the values obtained by NQR and NMR. © *2002 American Institute of Physics.* [DOI: 10.1063/1.1480244]

1. INTRODUCTION

Experimental determination of the orientational order parameter is an important issue for the physics of phase transitions in molecular crystals. In pure molecular crystals made up of linear molecules (N$_2$, CO$_2$, N$_2$O, etc.), the order parameter η is defined as a thermodynamic average of the spherical harmonic of second order in the suitable reference frame,

$$\eta = \langle P_2(\cos \theta) \rangle, \tag{1}$$

where P_2 is the Legendre polynomial; θ is the angle made by the molecular axis with the $\langle 111 \rangle$ direction of the $Pa3$ structure. Much effort has been spent on investigating the problem of the temperature dependence of the order parameter and its role in the α-β phase transition (for an exhaustive overview see Ref. 1). In order to determine η values from experimental data, the resonance techniques of NMR and NQR are employed (for more details see Refs. 1 and 2). If the disordering factor is not only temperature but positional randomness as well (as is the case in binary alloys), resonance methods can became inefficient. Reconstruction of η values in CO$_2$-Ar solid mixtures directly from electron diffraction intensities was attempted in Ref. 3. This approach possesses sufficient generality for application to the case of pure crystals, e.g., nitrogen. First attempts to use the integrated intensities of superstructure reflections as a measure of orientational order and to evaluate the effect of large-amplitude librations date back to the sixties in diffraction measurements of Sándor and coworkers[4,5] on solid DCl and DBr. Later, with the coming of the computer era, it became feasible to construct and probe models for the calculation of the molecular scattering factors, but the procedure is still cumbersome and is all the more difficult the larger the rotational and other anharmonicities. In this connection the method suggested here does not involve any models but directly interrelates the (specifically) x-ray integrated intensities with the correctly and rigorously defined order parameter.

Although both the structure and the orientational order parameter have been thoroughly studied[6,7] over the entire domain of existence of the low-temperature α phase of N$_2$, determination of η directly from diffraction data is nevertheless of interest for the following reasons. First, this is an independent method on a par with the NMR and NQR techniques.[2,7] Second, reconstruction of this kind will allow assessment of the method's efficiency and its applicability for orientational ordering of another nature and symmetry.

In Sec. 2 of this paper we present an improved modification of the method suggested previously[3] and its validation. Section 3 contains details of a powder x-ray experiment. In the last Section we deduce η values, compare them with the results available from NQR measurements, and draw conclusions.

2. THEORY

The integrated intensity of scattered x-ray radiation can be represented in the form[8,9]

$$I \propto \Phi(\theta) \left| \sum_s F_s(\mathbf{q}) \exp(2\pi i \mathbf{q} \cdot \mathbf{R}_s) \right|^2, \tag{2}$$

where the summation runs over positions $\mathbf{R}_s$ occupied by nitrogen atoms in the unit cell; $\mathbf{q}$ is the momentum transfer; θ is the diffraction angle; and F_s is the scattering amplitude. Summing over pairs of nitrogen atoms within each molecule (sublattice), we obtain for the structure factor

$$F(\mathbf{q}) = 2 f_N \sum_c \exp(2\pi i \mathbf{q} \cdot \mathbf{R}_c) \cos \xi(\mathbf{q} \cdot \mathbf{m}_c). \tag{3}$$

Here, specifically for α-N$_2$, f_N is the atomic scattering factor for the nitrogen atom; the summation runs over the four sublattices c of the $Pa3$ structure with $\mathbf{R}_c$ being the centers of the four molecules in the four sublattices; $\mathbf{m}_c$ is the instantaneous direction of the unit vector along the respective molecular axis in sublattice c; $\xi = 2\pi d/a$, where $d = 0.54895$ Å is half of the interatomic spacing in the nitrogen molecule; a is the lattice parameter, which is in principle

temperature dependent. For $T=0$ and $a=5.648$ Å, ξ $=0.61058$. Further we expand the cosine in Eq. (3) in spherical harmonics by making use of the known formula[10]

$$\cos[\xi(\mathbf{q}\cdot\mathbf{m}_c)]$$
$$= \sum_{\text{even } l\geqslant 0} -\frac{l}{2}(2l+1)j_l(\xi q)(\mathbf{C}_l(\mathbf{n})\cdot\mathbf{C}_l(\mathbf{m}_c)). \quad (4)$$

Here $j_l(y)$ are the spherical Bessel functions; the summation is over even l;

$$(\mathbf{C}_l(\mathbf{n})\cdot\mathbf{C}_l(\mathbf{m}_c)) = \sum_{m=-l}^{l} C^*_{lm}(\mathbf{n})C_{lm}(\mathbf{m}_c), \quad (5)$$

where $C_{lm}(\mathbf{n})$ and $\mathbf{C}_l(\mathbf{n})$ are Racah's spherical harmonics and the respective spherical tensors;[10] $\mathbf{n}$ is the unit vector along $\mathbf{q}$, while q is the length of the momentum transfer vector. As will be shown below, the expansion in Eq. (4) when truncated at the second term agrees reasonably well (typically to within 0.5–3%) with the exact results, i.e., the terms with $l\geqslant 4$ can be treated as rather small corrections. It can be shown (see Appendix) that the $l=2$ term after averaging yields precisely the orientational order parameter in Eq. (1):

$$\overline{C_{2m}(\mathbf{m}_c)} = \eta C_{2m}(\mathbf{m}_{c0}), \quad (6)$$

where $\mathbf{m}_{c0}$ are the unit vectors along the corresponding cube diagonals in the $Pa3$ structure. Finally,

$$\overline{\cos[2\pi x(\mathbf{q}\cdot\mathbf{m})_c]} \simeq j_0(\xi q) - 5\eta j_2(\xi q)(\mathbf{C}_2(\mathbf{n})$$
$$\cdot\mathbf{C}_2(\mathbf{m}_{c0})). \quad (7)$$

The scalar product in the right hand side can be expressed in standard angular variables:

$$(\mathbf{C}_2(\mathbf{n})\cdot\mathbf{C}_2(\mathbf{m}_{c0})) \equiv G_c(\mathbf{q}) = \frac{3(\mathbf{n}\cdot\mathbf{m}_{c0})^2-1}{2}. \quad (8)$$

Thus, the total scattering factor $F(\mathbf{q})$ can be approximated as

$$F(\mathbf{q}) \simeq 2f_N\left[j_0(\xi q)\sum_c \exp(2\pi i\mathbf{q}\cdot\mathbf{R}_c)\right.$$
$$\left. -5\eta j_2(\xi q)\sum_c G_c(\mathbf{q})\exp(2\pi i\mathbf{q}\cdot\mathbf{R}_c)\right], \quad (9)$$

where $G_c(\mathbf{q})$ is defined in Eq. (8). The function $G_c(\mathbf{q})$ is just the Legendre polynomial $P_2(\cos\theta_{\mathbf{m,n}})$, where $\theta_{\mathbf{m,n}}$ is the angle between $\mathbf{q}$ and the respective axis $\mathbf{m}_{c0}$. It is well known (see, for example, Ref. 11) that summing of $P_2(\cos\theta_{\mathbf{m,n}})$ over the first coordination sphere of cubic symmetry yields zero. Hence, for regular reflections, for which all factors $\exp(2\pi i\mathbf{q}_c\cdot\mathbf{R}_c)$ are unity, the second term in Eq. (9) will be absent. It can be also easily shown that for the structure under consideration the sum of the same exponential factors for superstructure reflections will yield zero in the first term in Eq. (9). Thus, the structure factor F can be represented in the form

$$F = 8f_N F_0, \quad (10)$$

where

$$F_0^{\text{reg}} = j_0(\xi q) \quad (11)$$

for regular reflections and

$$F_0^{\text{sup}} = -\frac{5}{4}j_2(\xi q)\sum_c G_c(\mathbf{q})\exp(2\pi i\mathbf{q}\cdot\mathbf{R}_c) \quad (12)$$

for superstructure reflections. The quantity ξ depends but weakly on temperature due to variations of the lattice parameter.

Let us now evaluate the error introduced when the truncation in Eq. (9) is used instead of the exact expansion in Eq. (4). To estimate the error for the simplest case $\eta=1$ we take a few strong reflections at relatively small diffraction angles, viz., the regular reflections (111), (002), and (022) and the superstructure reflections (102) and (112). We find that the error amounts to -0.35% for (111), 1.08% for (002), and 1.52% for (002) and to 2.97% for (102) and -0.54% for (112). Thus the approximate expression is good to within an error of 3% or better, which permits use of this expression for deducing the orientational order parameter directly from integrated diffraction intensities. Since the integrated intensity I, Eq. (2), is proportional to the respective total structure factor squared, we conclude that the integrated intensity of a superstructure line is, to a good accuracy, proportional to η^2.

3. EXPERIMENT

There were integrated intensity ratios available[12] from x-ray studies on N_2 published previously.[6] However, the accuracy of those old data was insufficient for our purposes, for which reason we had to measure the powder x-ray intensities anew.

For calculations we used the data of x-ray measurements carried out in the iron radiation on a powder diffractometer DRON-3M equipped with a special-purpose helium cryostat.[13] Samples of solid nitrogen were grown by depositing the gas under study in small bursts onto a copper substrate cooled to 6–8 K. Such a condensation procedure precluded formation of a pronounced texture, which could be a serious disadvantage in obtaining reliable data on the integrated intensities. To remove internal strains, the polycrystalline samples obtained (0.1 or 0.2 mm thick, with a grain size of about 10^{-4} cm) were annealed for 1 hour at $T=28$–30 K. Except for the first pattern at 5 K, all other patterns were taken for diffraction angles that included only the reflections (002), (102), (112), and (022). The temperature range of these studies was from 5 K to the α-β transition temperature. The temperature during a single data-taking run was stabilized to within ±0.005 K. The errors in the determination of lattice parameters and total integrated intensities were respectively $\pm0.02\%$ and 1%. Typical diffraction patterns are shown in Fig. 1.

4. RESULTS AND DISCUSSION

The integrated intensities of Bragg reflections for a particular momentum transfer $\mathbf{q}$ (or diffraction angle θ) were calculated using the formula[9]

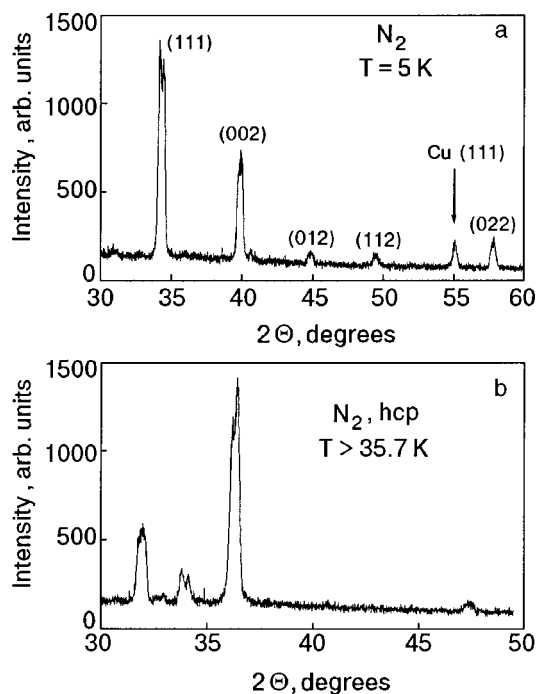$$I = Af_N(\theta)P(\mathbf{q})\Phi(\theta)|F|^2. \quad (13)$$

FIG. 1. Typical powder x-ray patterns for α-N_2 at 5 K (a) and slightly above the transition point, where the structure is hexagonal (b).
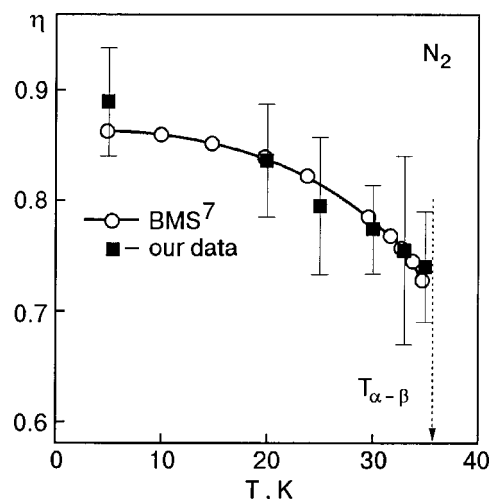

FIG. 2. Orientational order parameter as a function of temperature. The filled squares are our data; the empty circles are the data of Brookeman, McEnnan, and Scott.[7] The solid line is a guide for the eye, which virtually coincides with the self-consistent theory[14] that takes into account anharmonic and correlation effects in the rotational subsystem. The error bars for our results are mainly due to the texture of our polycrystalline samples.

Here A is a parameter, the same for all data taken during a single run; $f_N(\theta)$ is the atomic scattering factor for the nitrogen atom; $P(\mathbf{q})$ is the reflection repetition number;

$$\Phi(\theta) = \frac{1 + \cos^2\theta}{\sin^2\theta\cos\theta} \qquad (14)$$

for the diffraction method used; and F is the structure factor as defined in Eq. (3). To remove the poorly defined coefficient A in Eq. (13) from further consideration, we take the ratio of the integrated intensity of a superstructure reflection (subscript s) to that of a regular one (subscript r)

$$R(\mathbf{q}_s, \mathbf{q}_r) \simeq \frac{B(\mathbf{q}_s)}{B(\mathbf{q}_r)} \left| \frac{F_0(\mathbf{q}_s)}{F_0(\mathbf{q}_r)} \right|^2 \eta^2. \qquad (15)$$

Here F_0 are the functions defined in Eqs. (11) and (12); and $B(\mathbf{q}) = f_N(\mathbf{q})P(\mathbf{q})\Phi(\mathbf{q})$. Equation (13) allows us to obtain η values as

$$\eta \simeq \frac{F_0(\mathbf{q}_r)}{F_0(\mathbf{q}_s)} \left[R(\mathbf{q}_s, \mathbf{q}_r) \frac{B(\mathbf{q}_r)}{B(\mathbf{q}_s)} \right]^{1/2}. \qquad (16)$$

We point out here that absolute η values are obtained in this way.

Our calculation procedure was as follows. From diffraction patterns for every temperature point, we determined the rms lattice parameter as well as the integrated intensities and angular positions of reflections (111), (002), (102), (112), and (022). Those data allowed us to calculate all the pertinent quantities involved in Eq. (2).

Since, as was shown above, the integrated intensities of regular reflections depend weakly on the order parameter, we can use them to assess the texture factor of our polycrystalline samples. The intensity ratios between regular reflections (111), (002), and (022) give evidence that the texture was not very pronounced, amounting to about 10% with a preference

for the axes of type $\langle 100 \rangle$. The η values were calculated from three or four superstructure-to-regular reflection intensity ratios. An average of the η values for every temperature point are plotted in Fig. 2 as solid squares. These values compare fairly well with the η values calculated from NQR frequencies.[7] The rather large scatter of our order parameters as compared to those derived from NQR data is mainly due to the rather appreciable texture factor. We did not try to recalculate η with allowance for the texture. It is obvious that this factor will be nonexistent if diffraction data are taken on a single crystal.

In conclusion, we have shown that the orientational order parameter can be successfully calculated directly from diffraction data, either polycrystalline or single-crystal. The method applied to the orientational phase of solid nitrogen yielded results in good agreement with those obtained with resonance techniques and with the most advanced theory. Being simple and straightforward, this method allows control at every step of the calculations, and the intrinsic errors can be easily taken into account. The method can be elaborated on other types of orientational order. Moreover, this approach can be extended to other techniques (for example, optical) where the response is sensitive to the orientational order in the sample under investigation.

APPENDIX

The spherical harmonics $C_{2m}(\mathbf{m}_c)$ in Eq. (7), where $\mathbf{m}_c$ are the unit vectors along the instantaneous orientations of the molecular axes in sublattice c, should be transformed

Galtsov *et al.*

from the laboratory frame to the same proper axis, for example, $\langle 111 \rangle$. Then the harmonics in the two frames will be related as

$$C_{2m}(\mathbf{m}_c) = \sum_n D_{mn}^{(2)*}(\chi) C_{2n}(\mathbf{m}_c'), \qquad (A1)$$

where $\mathbf{m}_c'$ is the vector in the old (laboratory) frame and $\mathbf{m}_c$ is the same vector in the new (proper) frame; $D_{mn}^{(2)}(\chi)$ is the Wigner function, and χ is the set of angles that determine the rotation of the frame. In the absence of defects of any kind it is quite natural to assume that the molecular axes are distributed axisymmetrically[15] around the chosen z axis (direction $\langle 111 \rangle$) both in time and from site to site within the same sublattice. This means that after averaging of Eq. (A1) only the $m=0$ component will survive, namely (remembering that $C_{20}(\mathbf{m}_c) = P_2(\cos\theta)$),

$$\overline{C_{2n}(\mathbf{m}_c')} = \eta \delta_{n0}. \qquad (A2)$$

Since by the definition of the angles involved $D_{m0}^{(2)*}(\chi) = C_{2m}(\mathbf{m}_{c0})$, from Eq. (A1) we obtain within an arbitrary frame

$$\overline{C_{2m}(\mathbf{m}_c)} = \eta C_{2m}(\mathbf{m}_{c0}). \qquad (A3)$$

We point out once again that $\mathbf{m}_{c0}$ is the direction $\langle 111 \rangle$ (around which the unit vectors $\mathbf{m}_c$ fluctuate) expressed in an arbitrary (laboratory) frame.

*E-mail: galtsov@ilt.kharkov.ua

[1] V. G. Manzhelii, Yu. A. Freiman, M. L. Klein, and A. A. Maradudin (Eds.), *Physics of Cryocrystals*, AIP Publishers, Woodbury (1997).
[2] T. A. Scott, Phys. Rev. C **27**, 89 (1976).
[3] M. A. Strzhemechny, A. A. Solodovnik, and S. I. Kovalenko, Fiz. Nizk. Temp. **24**, 889 (1998) [Low Temp. Phys. **24**, 669 (1998)].
[4] E. Sándor and M. W. Johnson, Nature (London) **223**, 730 (1969).
[5] E. Sándor and R. F. C. Farrow, Disc. Faraday Soc. **48**, 78 (1969).
[6] I. N. Krupskii, A. I. Prokhvatilov, and A. I. Erenburg, Fiz. Nizk. Temp. **1**, 359 (1975) [Sov. J. Low Temp. Phys. **1**, 178 (1975)].
[7] J. R. Brookeman, M. M. McEnnan, and T. A. Scott, Phys. Rev. B **4**, 3661 (1971).
[8] M. A. Krivoglaz, *Theory of Scattering of X-Rays and Thermal Neutrons by Real Crystals*, [in Russian] Nauka, Moscow (1967).
[9] L. I. Mirkin, *Handbook on X-ray Analysis of Polycrystals* [in Russian], GIFML, Moscow (1961).
[10] D. A. Varshalovitch, A. N. Moskalev, and V. K. Khersonskii, *Theory of Angular Momentum*, World Scientific, Singapore (1988).
[11] J. Van Kranendonk, *Solid Hydrogen*, Plenum, New York (1983).
[12] A. I. Erenburg, private communication.
[13] A. I. Prokhvatilov, I. N. Krupskii, L. D. Yantsevich, and A. S. Barylnik, *Prib. Tekhn. Experim.* 3, 261 (1981).
[14] T. N. Antsygina, V. A. Slusarev, Yu. A. Freiman, and A. I. Erenburg, J. Low Temp. Phys. **56**, 331 (1984).
[15] J. Felsteiner and Z. Friedman, Phys. Rev. B **6**, 2491 (1972).

LOW-TEMPERATURE PHYSICS OF PLASTICITY AND STRENGTH

Features of the low-temperature plasticity of Pb–In single crystals

N. V. Isaev,* V. S. Fomenko, V. V. Pustovalov, and I. S. Braude

B. Verkin Institute for Low Temperature Physics and Engineering, National Academy of Sciences of Ukraine, pr. Lenina 47, 61103 Kharkov, Ukraine

The temperature dependence of the plasticity parameters of Pb–In single crystals with indium concentrations of 1–20 at. % are investigated under tensile deformation at a constant strain rate in the temperature interval 4.2–295 K. From an analysis of the experimental data, empirical estimates are obtained for the main parameters of the dislocation–impurity interaction and the dynamic drag coefficient of the dislocations. The calculated values of these parameters are consistent with the idea of a gradual transition on cooling, from a thermally activated motion of dislocations through local impurity barriers to a thermal–inertial motion. With increasing indium concentration (to 20 at. %) the low-temperature mechanisms of dislocation motion begin to be affected substantially by regions of short-range order (clusters), the presence of which is detected by the diffuse x-ray scattering method. © *2002 American Institute of Physics.* [DOI: 10.1063/1.1480245]

1. INTRODUCTION

Point defects formed by impurity atoms in a crystal lattice are the main barriers for mobile dislocations in the plastic deformation of fcc solid solutions. In the region of moderately low temperatures the depinning of dislocations from impurity barriers is substantially influenced by thermal fluctuations: the lower the temperature, the longer the time that a dislocation must wait for a favorable thermal fluctuation and the larger the stress that must be applied to the crystal to maintain a given strain rate.[1]

By analyzing the experimental data on the dependence of the flow stress on the deformation temperature and impurity concentration, one can estimate the main parameters of the thermally activated plasticity and obtain information about the parameters of the impurity barriers and the statistics of their distribution along the dislocation line. This analysis technique, developed in Refs. 1 and 2, permits reliable estimation of the corresponding parameters only if a number of experimental conditions are met. In the case of fcc crystals, these include: 1) a wide interval of deformation temperatures in which the deformation occurs through dislocation slip, while the influence of diffusion processes is unimportant; 2) measurement not only of the temperature dependence of the critical shear stress $\tau_0(T)$ but also of the differential characteristics of the plasticity (the sensitivity of the stress to the strain rate, $\delta\tau/\delta\ln\dot\varepsilon$, and to the deformation temperature, $\delta\tau/\delta T$); 3) a wide interval of impurity concentrations and their homogeneous distribution in the volume of the crystal. This last condition presupposes that the concentration of local barriers is known beforehand and corresponds to the atomic concentration of the impurity.

Under the above conditions it has been shown previously that the plasticity of a number of lead-based solid solutions is actually governed by thermally activated depinning of dislocations from impurity atoms at deformation temperatures below 140–170 K.[3–5] Meanwhile, since the impurity concentration in the alloys studied did not exceed 6 at. %, it remains unclear how a further increase in the concentration will affect the mechanisms of low-temperature plastic deformation in them. This paper is devoted to answering this question.

2. EXPERIMENTAL METHOD

The Pb–In system is a convenient object of study. First, its elements have a high mutual solubility.[6] Second, alloys with indium concentrations of 10–20 at. % can have regions of short-range order appearing in them, and these can affect the plasticity. Finally, because of the marked difference in the atomic scattering coefficients of lead and indium, those regions can be detected by such methods as diffuse x-ray scattering.[7]

In the present study we have investigated Pb–In single crystals with In concentrations of 1, 5, 10, and 20 at. %. The purity of the starting materials for preparation of the alloys was 99.999% for Pb and 99.997% for In. The single crystals were grown by the Bridgman method in a knock-down graphite form,[8] which made it possible to obtain a series of 10 samples of a given orientation from a single seed. The dimensions of the working part of the sample were $15\times3\times1$ mm. The orientation of the axis of tension was close to the [110] direction for all the samples.

The strain-hardening curves $\tau(\varepsilon)$ (τ is the shear stress and ε is the shear strain) were calculated from the load versus time curves obtained in the tensile deformation of the sample at a constant strain rate $\dot\varepsilon = 1.1\times10^{-4}$ s^{-1} in the temperature range $T = 4.2–295$ K on a low-temperature straining machine with a ^{4}He cryostat. The temperature of the sample was monitored by means of three resistance ther-

mometers attached to different points on the sample. The relative error for the measurement of the sample temperature was not more than 10^{-2}.

The value of the critical shear stress τ_0 was determined from the deviation of the initial part of the $\tau(\varepsilon)$ curve from Hooke's law. By making use of the significant extent of the easy-slip stage, in a number of cases a sample was loaded 3 or 4 times to τ_0 at different temperatures. With allowance for the hardening during each loading, the values of τ_0 corresponded to the values determined from the $\tau(\varepsilon)$ curve at a fixed temperature.

At $T<T_c \cong 7$ K (T_c is the critical temperature of the superconducting transition of the alloy) the sample was placed in the magnetic field of a superconducting solenoid, permitting measurements to be made in the normal and superconducting states.

In addition to τ_0, in the deformation process we also measured the increment of the deforming stress $[\Delta\tau(\dot{\varepsilon})]_T$ upon an abrupt increase in the strain rate by a factor of 10 or 100 in comparison with $\dot{\varepsilon}=1.1\times 10^{-5}$ s^{-1}. To reduce the uncontrolled influence of deformation defects, the value of $\Delta\tau$ was determined by extrapolation of the $\Delta\tau(\tau)$ curve to the point $\tau=\tau_0$. The error of measurement of the stress was ± 1 kPa.

X-ray structural studies of alloys with different impurity concentrations were made on powders obtained from undeformed single crystals. The diffraction curves were taken on a DRON-2.0 diffractometer in Cu–K_α radiation from the anode (with a Ni filter) at room temperature in a θ–2θ scheme with the use of collimating slits. The scattering intensity was measured point-by-point at steps of $\Delta(2\theta) = 0.01°$ in the angle interval $10<2\theta<25°$ by summing the number of counts detected in 40 s at each step.

3. EXPERIMENTAL RESULTS AND DISCUSSION

3.1. Temperature dependence of the plasticity parameters

The experimental curves of the temperature dependence of the critical shear stress $\tau_0(T)$ and the rate sensitivity of the deforming stress $\Delta\tau(T)$ for Pb–In single crystals are presented in Figs. 1 and 2.

For all of the alloys studied, the $\tau_0(T)$ curves have three distinct parts (Fig. 1): as the temperature is lowered in the interval $T=295$–150 K the value of τ_0 remains practically constant; at $T=150$–30 K it increases, reaching a maximum value $\tau_0(T_i)$; at $T<T_i$ it falls off. The temperature boundaries of these intervals and the absolute values of $\tau_0(T)$ depend on the concentration C of impurity atoms.

Below the critical temperature of the superconducting transition, T_c, the well-known softening effect is observed: the transition of the sample from the normal to the superconducting state is accompanied by a drop in the critical shear stress (CSS) by approximately 10%. The temperature dependence of this effect turned out to be similar to that which was observed and discussed previously in Refs. 4 and 5 for other lead alloys, and for that reason it is not shown in Fig. 1.

The temperature dependence of the sensitivity of the stress $\Delta\tau(T)$ for all of the alloys studied is a curve with a maximum at $T_m \simeq 90$–110 K (Fig. 2). With increasing impurity concentration the value of $\Delta\tau(T_m)$ increases substan-
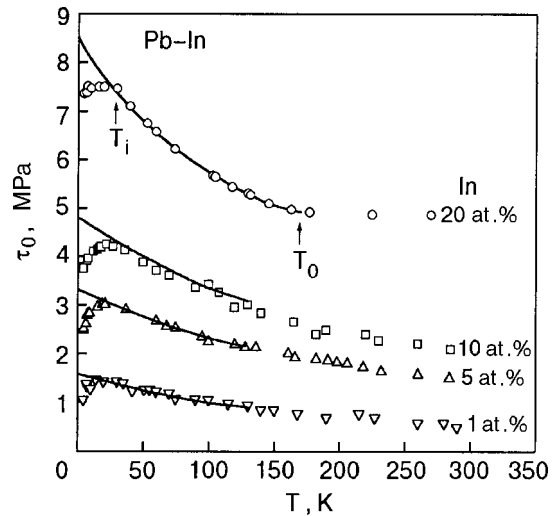

FIG. 1. Temperature dependence of the critical shear stress τ_0 of Pb–In single crystals (the orientation of the axis of tension is along [110]); the data below T_c were obtained in a magnetic field to bring the samples to the normal state. The solid curves correspond to the theoretical expression (3). T_0 and T_i are the threshold temperatures.

tially, but the temperature T_m changes only slightly.

In the region $T>200$ K the value of $\Delta\tau(T)$ decreases and becomes negative, and the $\tau(\varepsilon)$ curves show signs of unstable (jumplike) plastic flow, indicative of the influence of diffusion on the inelastic deformation and of deformation aging at higher temperatures.

The temperature curves of the plasticity parameters $\tau_0(T)$ and $\Delta\tau(T)$ recorded in this study for Pb–In alloys with different impurity concentrations are qualitatively similar to those observed for Pb–Sn,[3] Pb–Sb,[4] and Pb–Bi.[5]

3.2. Thermally activated plasticity

Over the entire range of concentrations of impurity atoms studied here the experimental curves of $\tau_0(T,C)$ and $\Delta\tau(T,C)$ for Pb–In single crystals deformed at a constant rate at temperatures 30 K$<T<$150 K are typical for dislocation-related plastic deformation occurring as a result
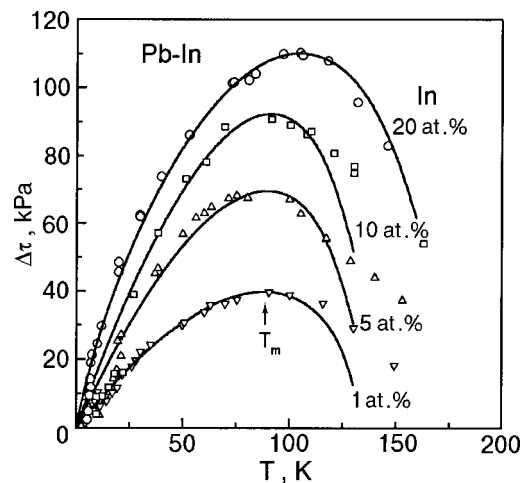

FIG. 2. Temperature dependence of the sensitivity of the stress $\Delta\tau$ to a change of the strain rate by a factor $\dot{\varepsilon}_1/\dot{\varepsilon}_2=10$. The solid curves correspond to the theoretical expression (4). T_m is the temperature of maximum sensitivity.

TABLE I. Empirical values of the theoretical parameters.

C, at. %	T_0, K (4)	T_0, K (3)	p	q	A	τ_c, MPa (4)	τ_c, MPa (3)	τ_i MPa	H_0, eV	T_i, K
1	132	132	0.67	1	21	0.6	0.6	0.8	0.22	14
5	134	138	0.67	1	25	1.05	0.95	2.14	0.25	25
10	135	137	0.67	1	25	1.4	1.4	3.10	0.26	27
20	165	170	0.62	1.2	36	3.4	3.5	4.92	0.50	26

of the thermally activated motion of dislocations through local barriers formed by impurity atoms. In such cases the relation connecting the rate of plastic deformation $\dot{\varepsilon}$, the deforming stress τ_0, and the temperature T is given by the classic Arrhenius equation:

$$\dot{\varepsilon} = \dot{\varepsilon}_0 \exp\left[-\frac{H(\tau^*)}{kT} \right], \qquad (1)$$

where $\tau^* = \tau_0 - \tau_i$ is the effective stress, equal to the difference between the deforming stress τ_0 and the long-range (internal) stress τ_i, and $H(\tau^*)$ is the effective activation energy (enthalpy), the specific form of which depends on the force law for the interaction between a dislocation and a pinning center and the statistics of the distribution of the pinning centers along the dislocation line.

For different models of solid-solution hardening the dependence of the activation enthalpy on the stress is well approximated by the general expression[1]

$$H(\tau^*) = H_0 \left[1 - \left(\frac{\tau^*}{\tau_c} \right)^p \right]^q, \qquad (2)$$

where H_0 is the energy parameter of the dislocation–impurity interaction for the particular impurity, and τ_c is the critical stress for activationless motion of a dislocation through the impurity barriers. The exponents p and q are numerical parameters of the order of unity, the concrete values of which depend on the type of barriers and the statistics of their distribution along the dislocation line.

For analysis of the experimentally investigated plasticity characteristics one can obtain explicit expressions for them from relations (1) and (2):

$$\tau_0(T) = \tau_i + \tau_c \left[1 - \left(\frac{T}{T_0} \right)^{1/q} \right]^{1/p}; \qquad (3)$$

$$\left(\frac{\Delta\tau}{\Delta \ln \dot{\varepsilon}} \right)_T = \left(\frac{\tau_c}{pqA} \right) \left(\frac{T}{T_0} \right)^{1/q} \left[1 - \left(\frac{T}{T_0} \right)^{1/q} \right]^{1-p/p}. \qquad (4)$$

Here we have used the notation $A = \ln(\dot{\varepsilon}_0/\dot{\varepsilon})$, $T_0 = H_0/kA$.

Using the scheme of thermal activation analysis proposed in Ref. 1 and refined in Ref. 2, let us compare relations (3) and (4) with the experimental curves presented in Figs. 1 and 2 and calculate the optimal empirical values of the parameters of the theory: p, q, τ_i, τ_c, A, H_0.

First we analyze the experimental curve of $\Delta\tau(T)$, for which expression (4) does not contain the parameter τ_i. This allows us to avoid the errors due to the lack of reliable methods of measuring $\tau_i(T)$ in the low-temperature region.[9] Calculations have shown that at all impurity concentrations expression (4) (the solid curves in Fig. 2) satisfactorily

describes the experimental data if the empirical values listed in Table I are used for the parameters. It is seen from Table I that for alloys of Pb with 1, 5, or 10 at. % In the values of p and q are the same, and the values of T_0 are close. At the same time, for alloys of Pb with 20 at. % In the optimal values of a number of the parameters are quite distinctive, particularly the high value of T_0.

According to expression (4), from the ratio τ_c/A one can calculate τ_c if the parameter A is estimated independently. For this we numerically differentiate the $\tau_0(T)$ curves shown in Fig. 1 to find the empirical values of the derivative $d\tau_0/dT$. Since the temperature dependence $\tau_i(T)$ for lead alloys is weak, we shall assume that $d\tau_i/dT \ll d\tau_0/dT$ and use the relation

$$A = -T \left(\frac{\Delta\tau}{\Delta \ln \dot{\varepsilon}} \right)_T^{-1} \left(\frac{d\tau_0}{dT} \right)_{\dot{\varepsilon}}. \qquad (5)$$

Estimates of the parameter A with the use of expression (5) for different temperatures have shown that in the interval 30–150 K the value of A is practically independent of temperature and varies weakly with impurity concentration in the interval from 1 to 10 at. %. The temperature-averaged values of A corresponding to this interval are given in Table I. Values $A \cong 20$–25 are typical for the majority of fcc solid solutions,[1,3–5] and the absence of temperature and concentration dependence of the parameter A is one of the criteria of applicability of Eqs. (1) and (2) for describing the plastic deformation process. The calculated values of A for the alloy with 20 at. % indium, on the contrary, are substantially larger than the typical values for fcc solid solutions.

For the different temperature-averaged values of A, Table I lists the corresponding values of the parameter τ_c, which is the critical stress for activationless depinning of dislocations from barriers, and of the characteristic energy parameter of the barriers, $H_0 = kT_0A$.

For comparison of the experimental data with expression (3) we take the values $\tau_i = \tau_0(T_0)$ as the empirical values of the internal stress and calculate for each concentration the empirical values $\tau^*(T)$ and the critical shear stress $\tau_0(T) = \tau_i + \tau^*(T) = \tau_0(T_0) + \tau^*(T)$. As is shown in Fig. 1, in the region of moderately low temperatures expression (3) (solid curves) satisfactorily describes the experimental dependence $\tau_0(T)$ for the values of p and q chosen previously. The values of the parameters T_0 and H_0 and of $\tau_c = \tau^*(T=0)$ that are obtained from expression (3) are in good agreement with the values of these parameters obtained from expression (4).

As we see from Table I, at indium concentrations between 1 and 10 at. % the temperature H_0 does not vary substantially, and its value correlates with estimates made pre-

viously for other lead-based solid solutions. For example, in Pb–Sn alloys H_0 equals 0.22–0.24 eV,[3] in Pb–Bi it is 0.25 eV,[5] and in Pb–Sb it is 0.33 eV.[4] These values agree with the values of the strength of the impurity barriers in lead solid solutions estimated by other methods.[10,11] The observed correlation of the values of the characteristic energy parameter H_0 suggests that, as in the papers cited, impurity atoms are effective barriers for dislocations in single crystals of Pb alloys with 1–10 at. % In Meanwhile, the high value $H_0 = 0.5$ eV for the solid solution of Pb with 20 at. % In contradicts this conclusion. As was the case for the values given above for the parameters A and T_0, the value of H_0 is atypical for point barriers formed by substitutional impurity atoms. According to expression (2), it can be assumed that the characteristic barriers for for mobile dislocations in the concentrated alloy are of a different type.

Finally, it should be noted that the tabulated values of the critical stress $\tau_c = \tau^*(T=0)$ and internal stress τ_i, which were obtained as a result of a joint analysis of expressions (3) and (4), depend substantially on the impurity concentration.

An additional test by which one can assess the correctness of the choice of numerical values of p and q is provided by the correlation between the values of the temperatures T_m and T_0 obtained from formula (4). A study of formula (4) at the maximum leads to the relation $T_m = p^q T_0$. For the values of p and q given in Table I this relation holds to an accuracy of 10%.

The value of the parameter p and the shape of the $\tau_c(C)$ curve can give us an idea of the statistics of the distribution of barriers along the dislocation line. The value $p = 2/3$ refers to a situation in which the average length of the dislocation segments L depends on the stress τ^* acting on the dislocation (Friedel statistics). To a first approximation the expression for L can be written as[12]

$$L \approx \left(\frac{2 E_L b}{\tau^* C} \right)^{1/3} \tag{6}$$

and the stress for the activationless breaking away of a dislocation from a barrier is given by

$$\tau_c = \left(\frac{2 E_L}{b^2} \right) \delta^{3/2} C^{1/2}, \tag{7}$$

where E_L is the linear tension of the dislocation, b is the Burgers vector, and $\delta = f_m/2 E_L$ is the dimensionless barrier "strength" (f_m is the maximum force necessary to overcome a barrier without the assistance of thermal activation). The straight line in Fig. 3a shows that the empirical dependence $\tau_c(C)$ does in fact obey expression (7) in the interval $C = 1 - 10$ at. %. From the slope of the straight line we can estimate the force f_m:

$$\left(\frac{2 E_L}{b^2} \right) \delta^{3/2} = \frac{f_m^{3/2}}{b^2 (2 E_L)^{1/2}} = 4.5 \times 10^6 \text{ Pa.} \tag{8}$$

Using relation (8), the standard estimate $2 E_L = G b^2$, and the values of the shear modulus $G = 10^{10}$ Pa and Burgers vector $b = 3.5 \times 10^{-10}$ m for the easy-slip system in lead, we obtain a value $f_m = (0.9 - 1.2) \times 10^{-11}$ H. These values of f_m are also in good agreement with those for the solid solutions Pb–Bi, Pb–Sn, and Pb–Sb.[3–5]
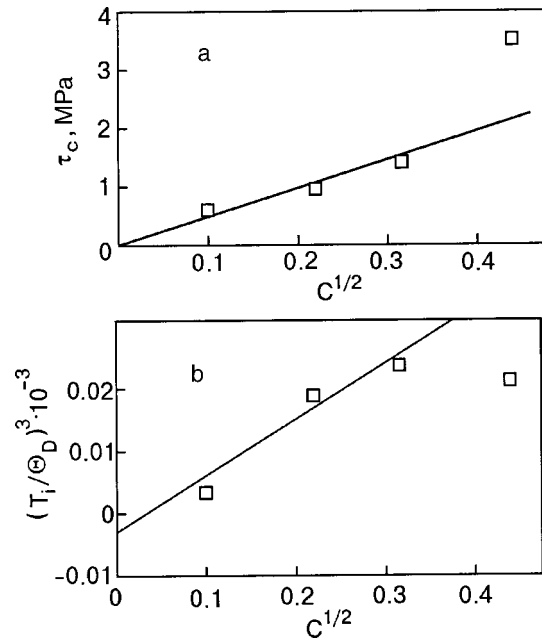

FIG. 3. Concentration dependence of the critical stress for activationless depinning of the dislocations, $\tau_c = \tau^*(T=0)$; the straight line corresponds to the theoretical expression (7) (a), and of the threshold temperature of the anomaly, T_i; the straight line corresponds to expression (12) with $\nu = 3$ (b). The concentration C is given in absolute units.

Thus the optimal value of the parameter p and the form of the concentration dependence $\tau_c(C)$ for Pb–In solid solutions is evidence that in the concentration interval $C = 1 - 10$ at. % the distribution of barriers along the dislocation line corresponds to Friedel statistics. The value of the energy parameter H_0, maximum force f_m, and limiting temperature T_0 are characteristic for barriers formed by substitutional atoms in lead. At $T > T_0$ a contribution to the deforming stress from long-range barriers comes into play.

When the impurity concentration is increased to 20 at. % In the overall shape of the experimental curves of $\tau_0(T)$ and $\Delta\tau(T)$ and, hence, the thermally activated character of the plastic deformation, remain as before. However, as a thermal activation analysis shows, the concentrated alloy apparently contains additional barriers characterized by high values of the parameters τ_c, T_0, and H_0. Their concentration does not correspond to the initial atomic concentration of the impurity and requires an independent estimate, and their distribution along the dislocation is not described by Friedel statistics.

3.3. Low-temperature anomalies of the plasticity

At low temperatures the interrelationships obeyed in the plastic flow of Pb–In alloys are no longer as described above. At $T < 30$ K the temperature dependences of the measured characteristics of the plasticity $\tau_0(T)$ and $\Delta\tau(T)$ deviate from the theoretical dependences (3) and (4), which are typical of a thermally activated process described by Eqs. (1) and (2) (see Figs. 1 and 4). Such deviations are called low-temperature anomalies of the plasticity.

For example, in the deformation of a Pb–In single crystal cooled to a temperature below a certain characteristic temperature T_i, contrary to expression (3), the sign of the derivative $(d\tau_0/dT)_{\dot{\varepsilon}}$ changes, and the dependence of the
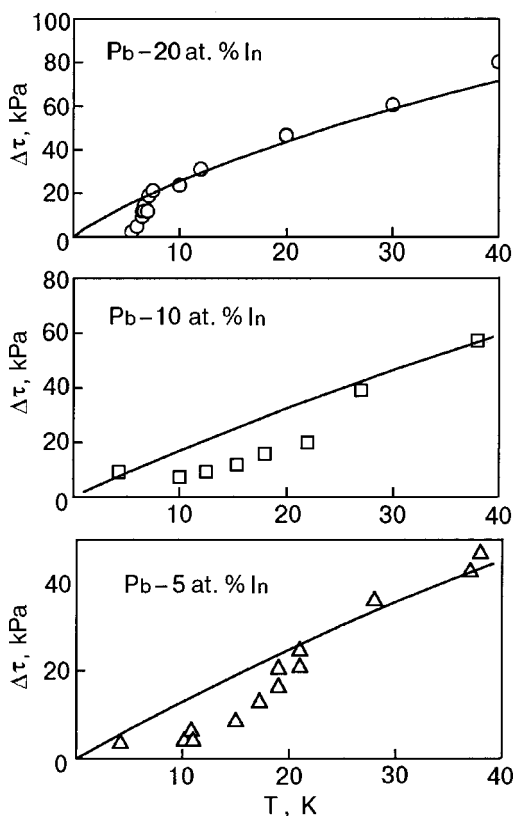
FIG. 4. Temperature dependence of the sensitivity of the stress $\Delta\tau$ to a change in the strain rate in the region of anomalous plasticity. The solid curves correspond to the theoretical expression (4).

sensitivity of the deforming stress $\Delta\tau(T)$ to a change in the strain rate falls off faster than predicted by Eq. (4) (see Fig. 4). The threshold temperature T_i for this anomalous plasticity, according to the experimental curves, increases with increasing impurity concentration (see Table I).

Physical mechanisms whose action might account for the low-temperature anomalies of the plasticity have been analyzed in a monograph.[13] Since the character of the anomalies observed in the present study is typical for lead-based fcc solid solutions, let us discuss the relevant hypotheses that have recently found experimental confirmation.

One of the main causes of the low-temperature anomalies of the plasticity observed in the temperature interval 20–40 K is the inertial properties of the dislocations.[14,15] Having an intrinsic mass, a dislocation segment can go from an overdamped to underdamped state as the temperature is lowered. This occurs through an increase in the effective stress $\tau^*(T)$ and a decrease of the phonon component $B_{ph}(T)$ of the dynamic drag on the dislocations, $B(T) = B_{ph}(T) + B_e$ (B_e is the athermal contribution to the braking of dislocations by conduction electrons). In the underdamped state the decay time of the characteristic vibrations of a dislocation segment is a significant fraction of the waiting time for a favorable thermal (or quantum) fluctuation. As a result, the fluctuation-related depinning of a dislocation from an individual barrier is accompanied by an activationless depinning of the dislocation from several neighboring barriers (unzipping). The condition for a dislocation segment of length L to be underdamped is the simultaneous satisfaction of two inequalities:

$$\tau_0 - \tau_i = \tau^* > 0.5\tau_c, \tag{9}$$

$$BL < 2\pi(ME_L)^{1/2}, \tag{10}$$

where M is the mass per unit length of the dislocation.

The hypothesis of a gradual transition from a thermally activated to a thermal–inertial and then to a quantum–inertial mechanism of motion of dislocations through impurity barriers has made it possible to describe completely the low-temperature anomalies of the plasticity of the solid solutions Pb–Sn, Pb–Sb, and Pb–Bi.[3–5]

It is easy to check that for $T \approx T_i$ conditions (9) and (10) hold for all of the alloys investigated in the present study. The condition $\tau^* > 0.5\tau_c$ holds below $T \approx 50$ K. To check condition (10) we use the rough estimates $E_L \cong 0.5b^2$, $M \approx 0.5\rho b^2$ (ρ is the density of the crystal). Taking for the drag coefficient in the low-temperature region the typical value for lead alloys $B = (3-4) \times 10^{-5}$ nm^{-2} s (Ref. 16) and again assuming that $G \approx 10^{10}$ Pa, $b \approx 3.5 \times 10^{-10}$ m, and $\rho \approx 10^4$ kg/m^3, we find that condition (14) holds for $L < 10^{-7}$ m. According to relations (6) and (7), for $\tau^* \approx 0.5\tau_c$ the segment length has a value $L \approx 10^{-7}$ m already at the minimum impurity concentration $C = 0.1$ at. %.

The combined influence of inertial effects and thermal fluctuations on the motion of dislocations through barriers has been treated most consistently by computer simulation methods in Ref. 17. According to the thermal–inertial model constructed there, the signs that the dislocations are beginning to manifest inertial properties as the temperature is lowered are: the derivative $d\tau^*/dT$ decreases to zero and changes sign; the rate sensitivity of the deforming stress decreases (the activation volume increases) as a consequence of the quasidynamic character of the motion; anomalies appear only in the presence of impurity barriers; the threshold temperature T_i for the anomaly increases with increasing impurity concentration. The low-temperature features of the plasticity observed in the present study for Pb–In alloys agree qualitatively with the signs indicating a thermal–inertial mechanism. The only thing that doesn't fit is that the threshold temperature T_i does not increase as predicted by the model when the indium concentration is raised to 20 at. %.

Thus, in the concentration region 1–10 at. % the low-temperature anomalies of the plasticity of Pb–In alloys are determined by those physical mechanisms that have been invoked to explain the plasticity anomalies observed at $T < 20$–30 K in Pb–Sn, Pb–Sb, and Pb–Bi alloys[3–5]—in particular, the thermal–inertial mechanism for the motion of dislocations through impurity barriers. The contradictory low value of T_i in the case of the concentrated alloy may be evidence of the formation of additional barriers in its structure which violate conditions (9) and (10) for the transition of the dislocations to an underdamped state.

3.4. Dynamic drag coefficient of the dislocations

The model of thermal–inertial motion of the dislocations and the experimental data on the threshold temperature for anomalous plasticity $T_i(C)$ can be used to estimate the value and temperature dependence of the dynamic drag coefficient $B(T)$ of the dislocations. The scheme for making such an estimate, proposed in Ref. 18, has been successfully applied to lead- and aluminum-based fcc solid solutions in Ref. 19.

According to the thermal–inertial model, the threshold temperature T_i increases with increasing concentration of impurity barriers. When the inequality $\tau^* > 0.5\tau_c$ holds, the function $T_i(C)$ should satisfy the condition

$$B(T)L(\tau^*, C) = 2\pi(ME_L)^{1/2},$$

in which the temperature dependence $B(T)$ is determined by the phonon component of the drag. For $T < \Theta_D$ (Θ_D is the Debye temperature) the phonon contribution to the dynamic drag of the dislocations is approximated rather well by a power law,[20] and we can therefore use the following expression for $B(T)$:

$$B(T) = B_e + \eta \left(\frac{T}{\Theta_D} \right)^\nu, \tag{11}$$

where $\eta = \text{const}$ and the value of the exponent ν depends on the specific mechanism of phonon drag. Taking into account that in our case $L(\tau^*, C)$ is given by Eq. (6), making the assumption that $\tau^* \approx \tau_c$, and using the functional form of $\tau_c(C)$ from Eq. (7), we expect the following relation to hold:

$$\eta \left(\frac{T}{\Theta_D} \right)^\nu = \alpha C^{1/2} - B_e, \tag{12}$$

where $\alpha = 2\pi(ME_L \delta / b^2)^{1/2}$. The corresponding straight line in Fig. 3b illustrates how relation (12) holds for all of the T_i except the value for the alloy with 20 at. % In if the values $\Theta_D = 94 - 98$ K,[19] $\nu = 3$, and $\eta = 10\alpha$ are used. The value $\nu = 3$ corresponds to the case when the braking of the dislocations is governed by the inelastic scattering of thermal phonons by dislocation lines (the flutter effect).[20] For the coefficient η in formula (11) we obtain the empirical estimate $\eta = 10\alpha \cong 7 \times 10^{-3}$ Pa·s. Extrapolating the straight line in Fig. 3b to its intercept with the vertical axis, we obtain an empirical value of the electron drag coefficient: $B_e = 2 \times 10^{-5}$ Pa·s. This value is in good agreement with the experimental estimates of the electron drag coefficient in the normal state for a Pb alloy with 10 at. % In: $B_{eN} = 3.6 \times 10^{-5}$ Pa·s.[16]

3.5. Intensity of diffuse x-ray scattering

Analysis of the experimental data on the low-temperature plastic deformation has shown that the Pb alloy with 20 at. % In has a number of distinguishing features which are atypical for lead alloys with lower impurity concentrations. It can be supposed that these features are due to additional barriers arising in the structure of the concentrated alloys which disrupt the low-temperature mechanisms of dislocation–impurity interaction in the ideal solid solution. To elucidate the nature of these barriers we did an x-ray structural study.

The distribution of the intensities of the diffuse x-ray scattering by the solid solutions is shown in Fig. 5. Because of the substantial difference in the atomic scattering coefficients of lead and indium, it is seen that for scattering angles in the region $\theta < 25°$ for $C = 5$ at. % and 20 at. % indium a high level of intensity of the diffuse halo is observed. At low scattering angles the reduced intensity of the diffuse halo, $I - I_{bg}$ (I_{bg} is the background intensity), is higher for the alloys with $C = 20$ at. %. As a consequence, the integral of
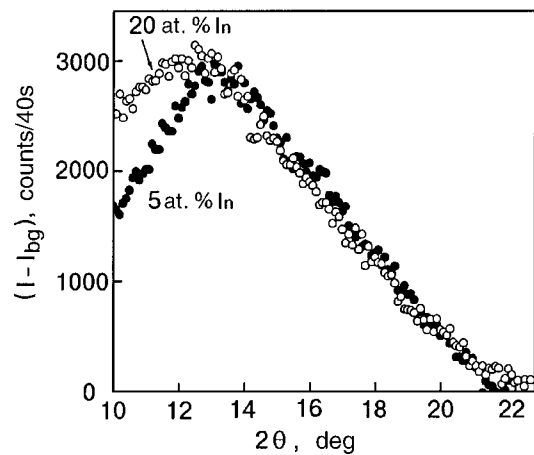

FIG. 5. Distribution of the intensity of the diffuse halo in Pb alloys with 5 at. % and 20 at. % In. I_{bg} is the background scattering intensity.

the scattering intensity distribution for Pb with 20 at. % In has a value 7–10% larger than for Pb with 5 at. % In.

The observed increase in the intensity of the diffuse halo may be due to a local ordering of the atoms, to size, thermal, and Compton effects, and also to static displacements. In view of the fact that in our case the indium concentration does not exceed the solubility limit and the masses of the irradiated samples are the same, as a first approximation we can assume that at small θ the contribution of the thermal and Compton scatterings does not depend on the concentration. The intensity of the diffuse scattering due to static displacements, as a rule, is also small at low scattering angles. The role of the size mismatch of the atoms (the ratio of atomic diameters) depends on how much this ratio differs in the alloy from the ratio of the atomic diameters in the pure metals. An analysis of the diffuse x-ray scattering for the Pb–In system at indium concentrations of 20–60 at. % in Ref. 7 showed that the contribution of the size effect, like that of the thermal, Compton, and static effects, is insignificant. The diffuse scattering intensity at low angles in this system is due mainly to local ordering of the atoms. Calculations showed that the short-range order parameter takes on negative values, corresponding to the formation of clusters in the alloy, with the number of clusters per unit volume increasing along with the impurity concentration.

The increase of the integrated intensity of the diffuse scattering for Pb–20 at. % In observed in the present study also confirms the increasing role of clusters in the scattering of x rays. Such clusters are effective barriers for mobile dislocations and could be the cause of the features of the low-temperature plastic deformation observed in the concentrated alloy.

4. CONCLUSIONS

1. The parameters of the low-temperature plasticity of the Pb–In single crystals investigated in this study depend on the deformation temperature in a complex way. Analysis of the temperature dependences of these parameters showed that in the temperature interval $T_i < T < T_0$ the interaction of the dislocations with impurity barriers is of a thermally activated character in the entire range of indium concentrations studied.

2. In the concentration interval $C = 1 - 10$ at. % the distribution of the barriers to be overcome with the aid of thermal fluctuations are distributed along the dislocation line according to Friedel statistics, and their energy parameters are typical of barriers formed by individual substitutional atoms. In the concentrated alloys (at impurity concentrations up to 20 at. % In) the motion of the dislocations can be influenced substantially by additional barriers in the form of clusters, the number of which increases with increasing impurity concentration.

3. For $T < T_i$ the low-temperature anomalies of the plasticity of Pb–In alloys is explained by the manifestation of the inertial properties of the dislocations and are in agreement with a thermal–inertial model of their motion through impurity atoms. The anomalies of the plasticity in the concentrated alloy containing clusters are not described in the framework of the thermal–inertial theory developed for point barriers of a single type.

*E-mail: Isaev@ilt.kharkov.ua

[1] U. F. Kocks, A. S. Argon, and M. F. Ashby, Progr. Mater. Sci. Oxford, Pergamon Press. **19**, 288 (1975).

[2] V. D. Natsik and H.-J. Kaufmann, Phys. Solid State **65**, 571 (1981).

[3] I. A. Shepel', L. N. Zagoruǐko, V. D. Natsik, and V. V. Pustovalov, V. P. Soldatov, Fiz. Nizk. Temp. **17**, 390 (1991) [Sov. J. Low Temp. Phys. **17**, 202 (1991)].

[4] N. V. Isaev, V. D. Natsik, V. V. Pustovalov, I. A. Shepel', and S. É. Shumilin, Fiz. Nizk. Temp. **18**, 911 (1992) [Low Temp. Phys. **18**, 641 (1992)].

[5] N. V. Isaev, V. D. Natsik, V. V. Pustovalov, V. S. Fomenko, and S. É. Shurnilin, Fiz. Nizk. Temp. **24**, 786 (1998) [Low Temp. Phys. **24**, 593 (1998)].

[6] M. Hansen and K. Anderko, *Constitution of Binary Alloys*, McGraw-Hill, New York (1958).

[7] Y. Koike, J. Phys. Soc. Jpn. **29**, 1235 (1970).

[8] Yu. G. Kazarov, in *Condensed Matter Physics* [in Russian], Vol. 11, Kharkov (1973), p. 100.

[9] V. I. Dotsenko, Phys. Status Solidi B **54**, 99 (1979).

[10] I. Van der Planken and A. Deruyttere, J. Mater. Sci. **4**, 499 (1969).

[11] V. P. Soldatov, V. D. Natsik, and L. G. Ivanchenko, Fiz. Nizk. Temp. **22**, 1087 (1996) [Low Temp. Phys. **22**, 740 (1996)].

[12] J. Friedels, *Dislocations*, Pergamon Press (1964).

[13] V. I. Dotsenko, A. I. Landau, and V. V. Pustovalov, *Topical Problems of Low-Temperature Plasticity of Materials* [in Russian], Naukova Dumka, Kiev (1987).

[14] A. V. Granato, Phys. Rev. B **4**, 2196 (1971).

[15] Schwarz, R. D. Isaak, and A. V. Granato, Phys. Rev. Lett. **38**, 554 (1977).

[16] V. R. Parameswaran and J. Weertman, Met. Trans. **2**, 1233 (1971).

[17] A. I. Landau, Phys. Status Solidi A **61**, 555 (1980); **65**, 119 (1981).

[18] V. A. Moskalenko, V. N. Kovaleva, V. D. Natsik, V. V. Pustovalov, and S. É. Shumilin, Fiz. Nizk. Temp. **22**, 1459 (1996) [Low Temp. Phys. **22**, 1108 (1996)].

[19] N. V. Isaev, V. D. Natsik, and V. S. Fomenko, Fiz. Nizk. Temp. **25**, 987 (1999) [Low Temp. Phys. **25**, 740 (1999)].

[20] V. I. Al'shits and V. L. Indenbom, Usp. Fiz. Nauk **115**, 3 (1975) [Sov. Phys. Usp. **18**, 1 (1975)].

Translated by Steve Torstveit